Modeling Landslide-Induced Flow Interactions with Structures using the Material Point Method

Carter M. Mast

A dissertation
submitted in partial fulfillment of the
requirements for the degree of

Doctor of Philosophy

University of Washington

2013

Reading Committee:

Pedro Arduino, Chair

Peter Mackenzie-Helnwein, Chair

Gregory R. Miller

Program Authorized to Offer Degree:
Civil and Environmental Engineering

©Copyright 2013
Carter M. Mast

University of Washington

Abstract

Modeling Landslide-Induced Flow Interactions with Structures using the Material Point Method

Carter M. Mast

Co-Chairs of the Supervisory Committee:
Professor Pedro Arduino
Civil & Environmental Engineering

Research Associate Professor Peter Mackenzie-Helnwein
Civil & Environmental Engineering

Keywords: finite deformation, large displacement, granular flow, impact, contact, reaction force, locking, porous media, multiphase, landslide, avalanche, debris flow, soil-structure interaction

Landslides cause significant damage and loss of life around the world each year. To help protect people, infrastructure, and lifelines against such disasters, it is critical to: a.) control the path and/or redirect flow when potential interaction with the built environment exists, and b.) have engineered structures that are capable of resisting the loads imparted by a landslide. Capturing the mechanical behavior and structural interaction is challenging—as these flow events are highly dynamic, unpredictable, and inherently complex in nature.

This dissertation presents the Material Point Method (MPM) as a continuum-based tool for modeling landslides and other flow-like events, with an emphasis on capturing the force interaction between the flow and rigid structures. Key challenges arising in this context are the ability to: a.) model the transition between solid and fluid-like behavior within a single numerical environment, b.) develop constitutive frameworks that can accommodate extremely large deformations while remaining computationally efficient and numerically stable, and c.) account for the different phases and constituents that comprise these events This research addresses these challenges and includes an anti-locking enhancement designed to improve kinematics and the quality of the stress field, a volume constraint for multiphase simulations, and an evaluation of different elasto-plastic material models suitable for large deformation analyses of granular materials. The current implementation is used to model several examples from both the solid and fluid mechanics regime, including incompressible fluid flow, the response of an elastic cantilever beam, three fully saturated porous media analyses, a ductile hyper-velocity Taylor bar impact, a parametric investigation of planar granular flow, snow avalanche simulation, and three landslide applications evaluating the nature of the force interaction with structures.

TABLE OF CONTENTS

Page

List of Figures iii

List of Tables ix

Chapter 1: Introduction and Overview 1
1.1 Scope of Work 2

Chapter 2: The Material Point Method 5
2.1 What is the Material Point Method? 5
2.2 Traditional Implementation 7
2.3 Comparison to Other Numerical Methods 13
2.4 Literature Review 15
2.5 Summary 24

Chapter 3: Material Models 25
3.1 Elasto-plastic Materials 25
3.2 Rate-Independent Plasticity 26
3.3 General Considerations 38
3.4 Notation and Key Relationships 42
3.5 J_2 Material Model 44
3.6 Two Surface Drucker-Prager Material Models 48
3.7 Two Surface Matsuoka-Nakai Material Model 58
3.8 Model Verification 61
3.9 Summary 67

Chapter 4: Anti-Locking Strategy 68
4.1 Introduction and Background 68
4.2 Theoretical Overview 69
4.3 Anti-Locking Approaches 72
4.4 Numeric Implementation 74
4.5 Algorithmic Overview 80
4.6 Summary 81

Chapter 5: A Volume Constraint Approach and Other Considerations 82
5.1 Building an Appropriate Weak Formulation 84
5.2 Incorporating the Volume Constraint in the MPM 87
5.3 Algorithmic Overview 92
5.4 Limitations of the Volume Constraint 95
5.5 Conclusions 98

Chapter 6: Example Problems 1: Linear Elastic Simulations 99
6.1 Applications to Fluid Dynamics 99
6.2 Application to Solid Mechanics: Vibrating Cantilever Beam 109
6.3 Volume Constraint Validation 115

Chapter 7: Example Problems 2: Finite Deformation Elastoplastic Simulations 131
7.1 Taylor Bar Impact 131
7.2 Planar Sand Column Collapse 140
7.3 Avalanche Control: Energy Dissipation Using Earthen Embankments 164
7.4 Soil-Column Impact: Granular Flow into a Single Column/Wall 173
7.5 Soil-Column Impact: Varying Approach Angle 199

Chapter 8: Conclusions 206
8.1 Summary 206
8.2 Key Findings 207
8.3 Moving Forward 211

Bibliography 214

Appendix A: Yield Surface Examples 226
A.1 Generating Points on a Yield Surface 226
A.2 Directional Derivatives of the Yield Surface 229

Appendix B: Computational Framework 233
B.1 Overview 233
B.2 Pre-Processing 234
B.3 Model Analysis 250
B.4 Post-Processing 255

Appendix C: Sample Files 259

LIST OF FIGURES

Figure Number — Page

2.1 Computational cycle for the standard Material Point Method. 6

2.2 Simulating granular matter using the Material Point Method, Smoothed Particle Hydrodynamics, and the Discrete Element Method. 14

2.3 Relationship between the particle characteristic function, $\boldsymbol{\chi}_p$, and MPM, GIMP, and CPDI. 22

3.1 Multiplicative decomposition of the deformation gradient. 35

3.2 J_2 yield surface. 45

3.3 Drucker Prager yield surface. 48

3.4 Smooth cap Drucker Prager yield surface. 52

3.5 Relationship between the effective friction angle, ϕ_F, critical state angle, ϕ_{cs}, and the plastic dilation angle, ψ_G. (a), (b), and (c) are consistent with a dense, moderately dense, and loose arrangement of a granular medium (dry sand for example). 57

3.6 Matsuoka Nakai yield surface. 59

3.7 Failure points for dense and loose sand. Different yield criteria are plotted for comparison purposes only. The primed axes denote the deviatoric plane. Source: Lade (1972); Lade and Duncan (1975); Andrade and Tu (2009) 61

3.8 Simple shear results. (a) Shear stress σ_{12} and (b) normal stress σ_{33} as a function of shear deformation. 63

3.9 Simple shear results. (a) Relationship between pressure, p, and shear measure q. (b) Volumetric strain as a function of shear deformation. 64

3.10 Biaxial compression results. (a) q. (b) Volumetric strain. 65

3.11 Error norm of the biaxial confining stress σ_3. (a) Modified Drucker-Prager model as presented in Section 3.6.3. (b) Matsuoka-Nakai yield surface, Eq. (3.120), coupled with the two invariant plastic potential, Eq. (3.108). (c) Matsuoka-Nakai model as presented in Section 3.7. 66

4.1 Cell-Based approach for determining unknown parameters $\boldsymbol{\alpha}$ and $\boldsymbol{\beta}$. (a) Example particle configuration. (b) Particles within each cell are used to determine a cell-based $\boldsymbol{\alpha}_c$ and $\boldsymbol{\beta}_c$. (c) Each cell containing particles has unique values for $\boldsymbol{\alpha}$ and $\boldsymbol{\beta}$. 75

4.2 Node-Based approach for determining unknown parameters $\boldsymbol{\alpha}$ and $\boldsymbol{\beta}$. (a) Example particle configuration. (b) Particles within the support of each node are used to determine a node-based $\boldsymbol{\alpha}_i$ and $\boldsymbol{\beta}_i$ (shown support for center node assumes linear shape functions). (c) Each node containing particles within its support has unique values for $\boldsymbol{\alpha}$ and $\boldsymbol{\beta}$. 76

5.1 Fundamental explanation of force transfer in the context of the MPM. (a) Wave crashing in fluid simulation and (b) Accumulation of sand in the corners of a rotating box. 94

5.2 Force balance and phase interaction. (a) Three multiphase scenarios, (b) Grid decomposition for first multiphase scenario, and (c) Force equilibrium. 97

6.1 Dam break simulation: (a) Initial configuration, and (b) Configuration at normalized time T. 100

6.2 Comparison between MPM simulations and experimental data for dam break analyses. The upper row compares the run out length, while the lower row compares the run out height. Experimental data is from Martin and Moyce Martin and Moyce (1952). 101

6.3 Dam break sequence for MPM simulations with $h_0/l_0 = 2.0$. 102

6.4 Time evolution for the dam break with barrier. 104

6.5 Initial state for the tank drain analysis. (a) The particle pressure. (b) The reaction force, $\mathbf{f}_{ir}$. 105

6.6 Reaction force along tank surface for the tank drain analysis. 107

6.7 Nodal velocity for the tank drain analysis. 108

6.8 Cantilever beam with applied initial velocity field. 109

6.9 Normalized stress distribution in cantilever beam. (a) Normal stress. (b) Shear stress. All stress values are normalized to the maximum value predicted by small deformation beam theory, denoted by Σ_{11}^{max} and Σ_{12}^{max} for the normal and shear components, respectively. 111

6.10 Energy norm convergence for cantilever beam. The left side considers all particles when calculating $\mathcal{E}$, while the right side considers only those particles whose horizontal position is greater than one beam depth away from the support. 112

6.11 Amplitude ratio, $\mathcal{A}$, and period ratio, $\mathcal{T}$, as a function of Poisson's ratio. 113

6.12 Geometric description for volume constraint validation. (a) Saturated soil with foundation loading and (b) pressure drawdown schematic. 115

6.13 Pore pressure and vertical stress distribution at t_f with increasing depth. (a) Water phase ($\theta^w = 0.1$ shown), (b) solid phase ($\theta^s = 0.9$ shown), and (c) mixture vertical stress, σ_{22}^{mix}, for all mix combinations. 117

6.14 Vertical displacement history of the surface for the solid phase. (a) Raw data, (b) Simple moving average of data, and (c) relative error in the vertical displacement of the MPM hydrostatic simulations. 119

6.15 Volume fraction history for two mixtures. (a) $\theta^w = 0.1\,, \theta^s = 0.9$ and (b) $\theta^w = 0.5\,, \theta^s = 0.5$. 120

6.16 Prescribed conditions at top of chamber. (a) Variation of water height h_a as a function of time. (b) Prescribed pressure p_a as a function of time. 121

6.17 Pore pressure history at various heights, h, for a pressure drawdown time of $t_d = 0.5\ s$. Three different time-dependent permeabilities coefficients are considered: (a) $\mu = 1.0\,(10)^5$ [N-s/m^4], (b) $\mu = 5.0\,(10)^6$ [N-s/m^4], and (c) $\mu = 1.0\,(10)^7$ [N-s/m^4]. 124

6.18 Vertical pore pressure distribution in the chamber at $t = 5.0\ s$. The particle locations are shown as circular points. The upper row is the actual value and the lower row is normalized to the initial pressure, p_{w0}. Each column represents a different drawdown time, t_d. 125

6.19 Pore pressure, reaction force, and velocity distribution. (a) Using the volume constraint outlined in Chapter 5. The nodal vector field shows the relative velocity between the solid and fluid phases. (b) The $u-p$ CMPM formulation by Zhang et al. (2008). The velocity field is for the mixture. 128

6.20 Comparison of pore pressure and displacement between the volume constraint outlined in Chapter 5, $u-p$ CMPM formulation by Zhang et al. (2008), and a FEM $u-p$ formulation from McGann et al. (2012). (a) Vertical pressure distribution under load at $t = 1.00\ s$. (b) surface displacement profile at $t = 1.00\ s$. 129

7.1 Taylor bar geometric description. (a) Initial configuration. (b) Final configuration for Standard MPM. (c) Final configuration using an anti-locking strategy. 132

7.2 Comparison of various anti-locking strategies to the standard MPM. (a) Normalized height as a function of normalized time. (b) Normalized radius as a function of normalized time. (c) and (d) are zoomed in of (a) and (b), respectively. 134

7.3 $\|\mathbf{s}\|$ at $T = 0.25$ for different MPM strategies. (a) The standard MPM [STD] (b) Cell-based full approximation [CB-FA] (c) Node-based volumetric approximation [NB-VA] and (d) Hybrid-based full approximation [HB-FA]. 136

7.4 Normal stress component σ_{33} at $T = 1.0$ for different MPM strategies. (a) The standard MPM [STD] (b) Cell-based full approximation [CB-FA] (c) Node-based volumetric approximation [NB-VA] and (d) Hybrid-based full approximation [HB-FA]. . 137

7.5 Marc nonlinear FEM results from $T = 0.95$. Isometric view of equivalent stress to yield stress, normal stress component σ_{33}, and top view comparing to the Material Point Method. 137

7.6 Average relative performance comparison. The table lists the algorithmic performance relative to the standard MPM as well as the relative time strength of each algorithm. The pie-chart provides an overview of the time strength for each method. 139

7.7 Planar sand column description. The initial and final geometry is described by the height, h, and length parameter, l. 140

7.8 Mobilized friction angle, ϕ_F. (a) Analysis A: peak strength (b) Analysis B: initial strength (c) Analysis C: residual strength 142

7.9 L_f for Cases 0–9. Case 0 is plotted in each figure for comparison purposes. 146

7.10 H_f for Cases 0–9. Case 0 is plotted in each figure for comparison purposes. 148

7.11 Log-Log plot of L_f as a function of a for Cases 0–9. (a) DP model (b) MN with DP G model and (c) All data points. 149

7.12 Log-Log plot of H_f as a function of a for Cases 0–9. (a) DP model (b) MN with DP G model and (c) All data points. 151

7.13 Evolution of sand column geometry with respect to normalized time. Plots contain all cases with $a > 2.0$. The upper row is the normalized variable $\bar{L}$ while the lower row is $\bar{H}$. Subplots (a) and (c) follow from the DP model while subplots (b) and (d) follow from the MN with DP G. material model. 153

7.14 Case 2 $\bar{H}$ compared to free fall in a gravitational field. The free fall is denoted by the dashed line. Plots contain all cases with $a > 2.0$. Subplot (a) follows from the DP model data while subplot (b) follows from the MN with DP G. data. 154

7.15 Evolution of the velocity field for $a = 2.0$, Case 2, and the MN with DP G material model. The velocity vectors are generated from nodal data and plotted alongside the particles. 155

7.16 Evolution of the velocity field for $a = 4.0$, Case 2, and the MN with DP G material model. The velocity vectors are generated from nodal data and plotted alongside the particles. 156

7.17 Evolution of the velocity field for $a = 8.0$, Case 2, and the MN with DP G material model. The velocity vectors are generated from nodal data and plotted alongside the particles. 157

7.18 Spatial comparison of particle locations for $a = 2.0$, $a = 4.0$, and $a = 8.0$. Particles whose positions correspond initially are plotted with the same color at each snapshot in time. The normalized time, T, corresponds to $a = 8.0$ data. 159

7.19 Evolution of the vertical stress, σ_{22}, for Case 2. 160

7.20 Evolution of the shear stress, σ_{12}, for Case 2. 161

7.21 Reaction force profiles for Case 2 and the MN with DP G material model. The aspect ratio is $a = 8.0$. (a) Horizontal/shear component and (b) vertical component. 162

7.22 Comparison of reaction force profiles. (a) raw data profile and (b) filtered profile. . . 163

7.23 Earthen embankments are used to protect infrastructure in the event of an avalanche. (a) Road protection in alpine setting. (b) Simulation schematic. 165

7.24 Representation of a sloped domain in a regular grid space. The desired environment is shown on the left while the computational representation is depicted at right. . . . 166

7.25 Evolution of avalanche flow from initiation to static state. The embankments prevent a majority of the flow from proceeding onto the level ground. 169

7.26 Plan view comparing velocity magnitudes. The upper row is inhibited by the earthen mounds. The lower row is a simulation without the embankments (the mound outline is shown for reference purposes only). 170

7.27 Side view comparing velocity magnitudes. The left column is inhibited by the earthen mounds. The right column is a simulation without the embankments (the mound outline is shown for reference purposes only). 171

7.28 Reaction force exerted by mounds to ensure no flow penetration. 172

7.29 Initial configuration for granular flow around column. (a) Plan view and (b) isometric view. 173

7.30 Plan view as the soil flow wraps around the column. The color map shows magnitude of the particle velocity. 176

7.31 Isometric view as the soil flow wraps around the column. The color map shows the vertical stress, σ_{22}. 177

7.32 Isometric view of plastic deformation at $t = 3.0$ s for $\phi_F = 10^\circ$ and $H_b = 3.5$ [m]. The column width increases until it forms a rigid barrier. The red particles have $|\boldsymbol{\varepsilon}_p| = 10.0$ while the blue particles have $|\boldsymbol{\varepsilon}_p| \approx 0.0$. 178

7.33 Isometric view as the soil flow wraps around the column. The color map shows the magnitude of the reaction force, $|\mathbf{f}_r|$, normal to the bounding surface. Each individual boundary node can be seen with corresponding reaction force vector. 180

7.34 Net reaction force as a function of time for $w_c = 4.0$ [m]. Positive value indicates force directed against flow. 181

7.35 Moving average of reaction force as a function of time for $w_c = 4.0$ [m]. Positive value indicates force directed against flow. The averaged value is used to obtain the steady state force measure. 182

7.36 Peak force values as a function of column width, w_c, and initial height, H_b. Each row represents a single friction angle. The center and right columns are horizontal and vertical cuts, respectively, through the contour plot shown in the left column. . . . 183

7.37 Steady state force values as a function of column width, w_c, and initial height, H_b. Each row represents a single friction angle. The center and right columns are horizontal and vertical cuts, respectively, through the contour plot shown in the left column. 185

7.38 Steady state force values as a function of friction angle, ϕ_F, and initial height, H_b. Each row represents a different column width. The center and right columns are horizontal and vertical cuts, respectively, through the contour plot shown in the left column. 186

7.39 Peak force coefficients, C_{pk}, as a function of column width, w_c, and initial height, H_b. Each row represents a single friction angle. The center and right columns are horizontal and vertical cuts, respectively, through the contour plot shown in the left column. 189

7.40 Steady state force coefficients, C_{ss}, as a function of column width, w_c, and initial height, H_b. Each row represents a single friction angle. The center and right columns are horizontal and vertical cuts, respectively, through the contour plot shown in the left column. 190

7.41 Comparison of actual contact geometry to initial values. (a) The height of soil in contact with barrier for $H_b = 3.0$ and $\phi_F = 5°$. (b) Ratio of actual contact to projected area for $H_b = 3.0$ and $\phi_F = 5°$. (c) Average ratio of actual contact to projected area for all soil depths and $\phi_F = 5°$. 191

7.42 Comparison of actual contact geometry to initial values. Average ratio of actual contact to projected area for all soil depths and all friction angles examined. 192

7.43 Comparison of actual contact geometry to initial values. Average ratio of actual contact to projected area for all soil depths and all friction angles examined. 193

7.44 Ratio of peak force to static equivalent, R_{pk}, as a function of column width, w_c, and initial height, H_b. Each row represents a single friction angle. The center and right columns are horizontal and vertical cuts, respectively, through the contour plot shown in the left column. 195

7.45 Ratio of steady state force to static equivalent, R_{ss}, as a function of column width, w_c, and initial height, H_b. Each row represents a single friction angle. The center and right columns are horizontal and vertical cuts, respectively, through the contour plot shown in the left column. 196

7.46 Peak and steady state to static force equivalent for select data points. 197

7.47 Schematic drawing of a debris flow approaching a column at an arbitrary angle. (a) Plan view. (b) Side view. 199
7.48 Plan view of the particle velocity magnitude for varying approach angles. The snapshot coincides with the time that the peak reaction force occurs. 202
7.49 Side view of impact for $\beta = 30°$. 202
7.50 Reaction force distribution for $\beta = 0.0° - 45°$. The upper row is an isometric view and the lower row a plan view. The arrow indicates the flow direction around the column. 203
7.51 Reaction force comparison. (a) Reaction force magnitude before and after smoothing as a function of time. (b) The x and z components of the reaction force as a function of time for $\beta = 30°$. (c) Peak force as a function of approach angle. 204

A.1 Needed ingredients to compute points on a yield surface. (a) Transformation from principal space to orthonormal coordinate system aligned with hydrostatic axis. (b) Slice of yield surface perpendicular to the hydrostatic axis. 227

B.1 The code components that make up the computational framework and dictate the flow of data. 234
B.2 Base keywords for input file. 235
B.3 AnalysisOptions keywords for input file. 236
B.4 Parameters keywords for input file. 239
B.5 Material keywords for input file. 241
B.6 Boundary keywords for input file. 243
B.7 OutputData keywords for input file. 246
B.8 Object relation and process flow chart. 251
B.9 Output file structure. 254
B.10 XML piece data structure for use with ParaView and VTK. This example is for a single time step and contains only particle data. 256

C.1 Sample .pvd files linking the individual particle, node, and boundary node files together for visualization in ParaView. 263

LIST OF TABLES

Table Number Page

2.1 Numerical methods and references. 13

3.1 Loading state. 29
3.2 Newton-Raphson iteration scheme. 33
3.3 Strain-driven return mapping algorithm for small deformation theory. 33
3.4 Strain-driven return mapping algorithm for finite deformation theory. 39
3.5 Sample values for constants a_{0-5}. 57

4.1 Algorithmic implementation of anti-locking strategy 81

5.1 Volume Constraint Algorithm. 93

6.1 Input parameters for dam break simulations 101
6.2 Input parameters for tank drain 106
6.3 Input parameters for plane stress beam study 110
6.4 Input parameters for plane strain beam study 113
6.5 Hydrostatic analysis geometry, material description, and MPM parameters. 116
6.6 Pressure head drawdown analysis geometry, material description, and MPM parameters. 122
6.7 Planar foundation analysis geometry, material description, and MPM parameters for use with the volume constraint algorithm in Chapter 5 and the $u-p$ CMPM formulation by Zhang et al. (2008). 127

7.1 Analysis geometry, material description, and MPM parameters. 132
7.2 Constant definitions for a_{0-4} for defining the friction angle curves in Figure 7.8. . . . 143
7.3 Best fit constants for determining $L_f(a)$ via a power law. 149
7.4 Lower and upper bound constants for determining $L_f(a)$ via a power law. 150
7.5 Best fit constants for determining $H_f(a)$ via a power law. 151
7.6 Lower and upper bound constants for determining $H_f(a)$ via a power law. 152
7.7 Initial avalanche geometry and tri-planar domain description. 167
7.8 Material and MPM parameters for avalanche simulation. 168
7.9 Column and soil mass geometry. 174
7.10 Material and MPM parameters for granular flow into a single column/wall. 175
7.11 Initial soil configuration for bi-planar domain description. 200
7.12 Material and MPM parameters for angled granular flow simulation. 201

Chapter 1

INTRODUCTION AND OVERVIEW

This document contains several color figures and plots. The reader is best served by viewing an electronic version or a color printout.

Each year landslides and avalanches cause significant damage and loss of life around the world. In the United States alone, the annual economic costs of landslides can be estimated to be between $1 and $2 billion, with an associated 25 to 50 yearly casualties (Highland, 2006). To help protect people, infrastructure, and lifelines against such disasters, it is critical to: a.) control the path and/or redirect flow when potential interaction with the built environment exists, and b.) have engineered structures that are capable of resisting the loads imparted by a landslide. Capturing the mechanical behavior and structural interaction is challenging—as these flow events are highly dynamic, unpredictable, and inherently complex in nature.

Researchers have developed both physical and numerical models in an effort to build understanding of these phenomena. Physical models typically require well-controlled, large-scale experiments (see e.g, Denlinger and Iverson (2001); Iverson and Vallance (2001); Iverson et al. (1992); Lin and Wang (2006); Reid et al. (2003); Tohari et al. (2007)). While these experiments provide valuable insight into the governing behavior and controlling mechanisms, their general effectiveness is limited due to scale restrictions and the inability to accurately recreate in-situ conditions.

Application in general contexts requires numerical models that are capable of reproducing key aspects observed in the field and the ability to represent slides at their full scale. Such models are necessary not only for prediction and design, but also for the guidance of additional experimentation as well as furthering engineering understanding and education in professional practice.

To this end various numerical simulation methodologies and techniques have been used for predicting flow initiation, evaluating flow patterns, and analyzing the general flow dynamics of avalanche and landslides. This includes depth averaging techniques (see e.g, Chen et al. (2007); Iverson and Denlinger (2001); Savage and Iverson (2003)). While these methods do reasonably well in estimating global quantities such as runout patterns, there can be limitations that make fully three-dimensional (3D) analyses cumbersome or impos-

sible, or there can be difficulties obtaining the force interaction between the flowing mass and structures. These limitations follow primarily from the two-dimensional (2D) nature of such techniques, which use depth-averaged variables. The end result is a smearing of localized 3D phenomena and an inability to accurately assess obstacle interactions with the flow. Alternately, purely Eulerian frameworks can provide a reasonable representation of granular flow and the interaction with rigid objects. This includes finite difference techniques, e.g, the work by Moriguchi et al. (2009) as well as control volume methods, e.g., Guimaraes et al. (2008). Different particle techniques, including smoothed particle methods (Ataie-Ashtiani and Shobeyri, 2008; McDougall and Hungr, 2004) and the Discrete Element Method (DEM), e.g, Teufelsbauer et al. (2011), can also be used. The primary drawback of particle methods in this context is scale—particularly for the DEM.

This work uses the Material Point Method (MPM) as a continuum-based tool for modeling landslides, and highlights the method's suitability for obtaining the dynamic reaction force interaction between the flow event and a rigid structure(s). Key challenges arising in this context are the ability to a.) model the transition between solid and fluid-like behavior within a single numerical environment, b.) develop constitutive frameworks that can accommodate extremely large deformations while remaining computationally efficient and numerically stable, and c.) account for the different phases and constituents that comprise these events.

1.1 Scope of Work

This document provides an overview of the MPM and the current literature, identifies different features and implementation strategies, and presents two enhancements designed to improve shortcomings of the traditional MPM. Multiple elasto-plastic material models suitable for both small and finite deformation analyses are explored, with an emphasis on constructing a MPM-oriented constitutive framework capable of modeling a broad range of granular material types. The current implementation is verified with examples from both the solid and fluid mechanics regime, and concludes with several landslide simulations. Each chapter contains either theoretical development, implementation details, or application related contents. A brief synopsis of each chapter is given in the remainder of this introduction.

Chapter 2

The goal for this chapter is to provide the unfamiliar reader with a basic introduction to the Material Point Method. This is accomplished using both a qualitative and theory-based

overview of the technique. A brief comparison is made to other methods and the chapter concludes with a literature survey of published work.

Chapter 3

Several elasto-plastic material models are presented following an in depth discussion of integration algorithms for both small and finite deformation computational inelasticity. The models include one, two, and three invariant formulations. Three model variants are tested in the context of granular material modeling using simple shear and biaxial compression tests. Particular attention is paid here to constructing a MPM-oriented constitutive framework capable of modeling a range of granular material types using physically meaningful and numerically reasonable parameters.

Chapter 4

When coupled with linear shape functions the standard implementation is subject to kinematic locking—the accumulation of fictitious strains that lead to errant stress field and poor kinematics. This chapter presents multiple strategies for isolating and removing kinematic locking for both elastic and elasto-plastic materials.

Chapter 5

The point-wise nature of the traditional MPM assumes the mass associated with a given integration point is confined to a singular location. Certain geometric configurations can create situations in which the implied particle volume overlaps, effectively overloading space. This chapter explores a volume constraint that develops a corrective pressure to prevent this scenario from occurring.

Chapter 6

This is the first of two chapters highlighting the capabilities of the MPM. Chapter 7 focuses on linear elastic materials and includes applications from both solid and fluid mechanics. The anti-locking framework is verified through a series of examples, including a dambreak simulation, water tank drain, and vibrating cantilever beam. The volume constraint algorithm is used to model fully saturated soil in various configurations and loading conditions.

Chapter 7

This is the second of two chapters highlighting the capabilities of the MPM. In this chapter several examples employing elasto-plastic material models are examined. This includes a Taylor Bar Impact, parametric studies of collapsing sand columns and granular flow around a stationary structure, as well as energy dissipating structures used to abate the flow of a snow avalanche.

Chapter 8

Conclusions regarding the current state of research are presented. Future avenues of study are identified with respect to the MPM, the computational framework, and the direction of the work as a whole.

Appendix A

A general procedure for computing points on a yield surface is presented in this appendix. An example calculation is performed for the three invariant Matsuoka-Nakai yield surface. The second section derives the directional derivatives for the Drucker-Prager and Matsuoka-Nakai yield functions.

Chapter B

This appendix discusses the computational framework that has been established as part of this work. Particular focus is placed on the input file structure and the various input options available to the analyst. The basic components that make up the core of the implementation are identified and discussed. The final section targets visualization related topics and provides instructions for viewing the data contained in output files.

Appendix C

Sample input files for select examples appearing in this dissertation are provided, as well as example XML files for creating animations in ParaView.

Chapter 2

THE MATERIAL POINT METHOD

The current chapter provides a qualitative overview as well as a basic discussion of the standard implementation to set the stage for the enhancements and examples presented later in this document. This basic theory is followed by a literature review, highlighting the wide range of applications the method has seen to date. This chapter provides only the basics of the method, as the mathematical foundations and underpinnings have been explored in detail and are well documented in several publications. The curious reader is encouraged to explore the supplied references for additional details.

2.1 What is the Material Point Method?

The Material Point Method (MPM) is a numerical technique that is best suited for modeling history dependent materials in a dynamic, large deformation setting. The formulation tracks moving points relative to stationary nodes, and can be used to capture the behavior of both fluids and solids in a unified framework. The standard, or traditional[1], implementation solves the governing equation of motion at fixed nodes that collectively form a grid. Each body or phase in the analysis is represented by a collection of discrete points known as *material points* or *particles*. This general concept is shown in the upper portion of Figure 2.1. Here the different components that make up an MPM simulation are classified as either Body/Phase-Based or Domain/Grid-Based, and properly understanding the role and interaction of these two categories will prove beneficial in later chapters.

The Body/Phase-Based group is comprised of the continuum body itself and the computational points that, collectively, describe the object. Each particle represents a portion of the total mass, and thus caries an implied volume as well as various state variables depending on the application. For example, in solid mechanics each material point is assigned initial values for position, velocity, stress, strain, and any other state variable needed for the constitutive relationship. That being the case, these particles form a Lagrangian frame of reference from which the state of the body is determined at any instant in time. A crucial and fundamental characteristic of the Material Point Method is the following: these

[1]The adjectives *standard* and *traditional* will be used interchangeably and represent the original framework presented by Sulsky et al. (1994, 1995)

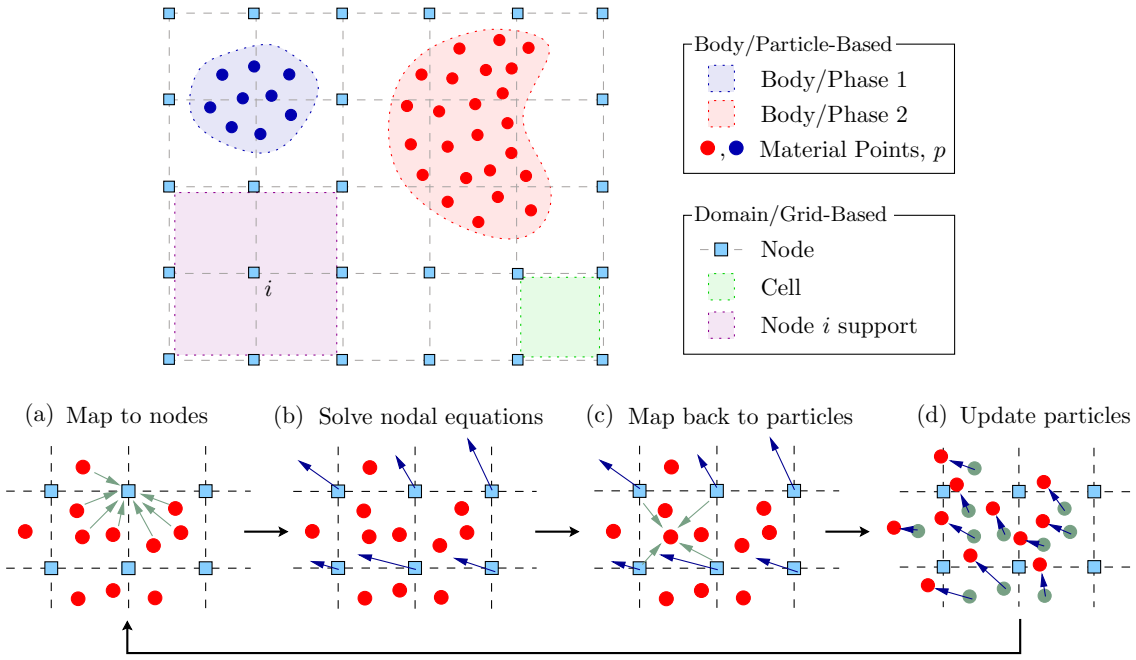

Figure 2.1: Computational cycle for the standard Material Point Method.

objects serve only as integration points for the governing equation in space (more on this shortly). As such, these entities are not physical particles, per se, and casting the MPM as a particle-based method is arguably incorrect or, at a minimum, misleading. This problem is compounded by two additional factors. The first is visualization, where viewing dynamic MPM simulations as moving material points is questionable if the true nature of the computational particles is not understood. Even simple effects like adjusting the plotting point size can severely distort the interpretation of what a material point is, can give false impressions of the implicit volume being occupied by the point, and lead to erroneous conclusions regarding the particle nature of the method. The second factor is the application of the method to discretely-based matter, such as granular materials, where the very nature of the medium lends itself to a particle description. In these applications the computational particles serve as integration points in space that contain the state of the continuum representation at that particular location, and not the individual constituent grains that make up the material.

The second category of objects, the Domain/Grid-Based entities, are responsible for defining the physical space a body moves in. The primary object is a node, and a collection of nodes forms a grid. Typically nodes are arranged in a repeating and regular pattern, forming a line in 1-dimensional (1D) applications, a rectangular pattern in 2D simulations, or a

rectangular cuboid in fully 3D environments. This repeatable structure is not a requirement of the method but is the most common scheme to date. The nodal arrangement also defines cells, or the region contained between adjacent nodes, as well as nodal supports, defined by piecewise continuous shape functions residing at each node in the domain. The interplay between the grid, nodes, cells, and nodal support (assuming linear shape functions) is shown in the upper region of Figure 2.1. Strictly speaking the nodal positions are arbitrary and can potentially change without penalty at any point in time. However, nodes are most commonly assumed to reside in a single location effectively creating a static grid. This facilitates an Eulerian frame of reference when viewed relative to the particle motion.

The sharing of information between particles and nodes is governed solely by the shape function that serve as an effective weight for determining the importance of a given particle to any node in the domain. In general this process is referred to as mapping, and can occur from particle-to-node, or in the opposite direction, from node-to-particle. The primary goal of any analyses is to track the system in time while monitoring the evolution of key quantities in both the Body and Domain categories. This is accomplished by splitting a finite time increment into many smaller time intervals, $\Delta t = t_{n+1} - t_n$, and approximating key equations over each Δt. When the governing equation is conservation of linear momentum, material point quantities of mass, momentum, and force are mapped to the appropriate nodes as indicated in Figure 2.1(a). After collecting contributions from all particles in the support, the nodal acceleration and velocity vectors are determined over Δt as observed in Figure 2.1(b). The velocity gradient and the corresponding strain increment are mapped to the particle location using the updated nodal velocity. The particle stress and material state variables are computed from the desired constitutive model as part of the third step highlighted in 2.1(c). Finally, the incremental changes in nodal velocity and position are mapped from the nodes to the particles, resulting in a fully updated system at the particle level. After 2.1(d) the procedure begins again and the computational cycle is repeated for a prescribed time duration.

2.2 Traditional Implementation

The traditional approach is built around conservation of linear momentum, which when expressed in differential form appears as follows:

$$\rho\,\dot{\mathbf{v}} = \operatorname{div}\boldsymbol{\sigma} + \mathbf{b}\ , \tag{2.1}$$

with the mass density $\rho(\mathbf{x}, t)$ at position $\mathbf{x}$ and time t, $\dot{\mathbf{v}}(\mathbf{x}, t)$ as the material time derivative of the velocity field—also known as the acceleration field—$\boldsymbol{\nabla}$ the gradient operator, $\boldsymbol{\sigma}(\mathbf{x}, t)$

is the Cauchy stress tensor, and $\mathbf{b}(\mathbf{x},t)$ is the body force per unit volume. In the present derivation the end goal is to obtain an expression for $\dot{\mathbf{v}}(\mathbf{x},t)$ consistent with the description of the MPM given in the previous section. Thus, it is necessary to build an approximation for the acceleration field in terms of the nodes and particles that make up a given analysis. It is to this end that the current discussion proceeds.

2.2.1 Building an Appropriate Weak Formulation

A weighted integral statement is constructed from (2.1) as

$$\int_{V_{\mathcal{B}}} (\rho\,\dot{\mathbf{v}} - \operatorname{div}\boldsymbol{\sigma} - \mathbf{b}) \cdot \boldsymbol{\eta}\, dV = 0 \ , \tag{2.2}$$

effectively transferring the strict, or strong, requirements of (2.1) to a weighted statement known as a weak form. Here the integration domain is over the spatial volume $V_{\mathcal{B}}$ of a continuous body, $\mathcal{B}$. The vector field $\boldsymbol{\eta}(\mathbf{x},t)$ is an arbitrary vector-valued spatial function that is kinematically consistent with the desired boundary conditions. Separating each term according to

$$\int_{V_{\mathcal{B}}} \rho\,\dot{\mathbf{v}} \cdot \boldsymbol{\eta}\, dV - \int_{V_{\mathcal{B}}} \operatorname{div}\boldsymbol{\sigma} \cdot \boldsymbol{\eta}\, dV - \int_{V_{\mathcal{B}}} \mathbf{b} \cdot \boldsymbol{\eta}\, dV = 0 \ , \tag{2.3}$$

will prove beneficial, as the product rule of differentiation yields the decomposition

$$-\int_{V_{\mathcal{B}}} \operatorname{div}\boldsymbol{\sigma} \cdot \boldsymbol{\eta}\, dV = -\int_{V_{\mathcal{B}}} \operatorname{div}(\boldsymbol{\sigma} \cdot \boldsymbol{\eta})\, dV + \int_{V_{\mathcal{B}}} \boldsymbol{\sigma} : \boldsymbol{\nabla}^s \boldsymbol{\eta}\, dV \ . \tag{2.4}$$

The modified form yields a term that can readily be transformed via the divergence theorem as

$$\int_{V_{\mathcal{B}}} \operatorname{div}(\boldsymbol{\sigma} \cdot \boldsymbol{\eta})\, dV = \int_{\mathcal{S}} (\boldsymbol{\sigma} \cdot \mathbf{n}) \cdot \boldsymbol{\eta}\, d\mathcal{S} = \int_{\mathcal{S}_{\boldsymbol{\sigma}}} \tilde{\mathbf{t}} \cdot \boldsymbol{\eta}\, d\mathcal{S} + \int_{\mathcal{S}_{\mathbf{u}}} (\boldsymbol{\sigma} \cdot \mathbf{n}) \cdot \boldsymbol{\eta}\, d\mathcal{S} \ , \tag{2.5}$$

where $\mathcal{S}$ is the surface of the body $\mathcal{B}$ (sometimes written as $\mathcal{S} = \partial V_{\mathcal{B}}$ in the literature) and $\mathbf{n}$ is the outward normal defined on $\mathcal{S}$. The terms $\mathcal{S}_{\boldsymbol{\sigma}}$ and $\mathcal{S}_{\mathbf{u}}$ correspond to the portions of the surface where loads and displacements are prescribed, respectively. These subsets collectively form the entire surface and do not overlap. The latter statement is summarized concisely as $\mathcal{S} = \mathcal{S}_{\boldsymbol{\sigma}} \cup \mathcal{S}_{\mathbf{u}}$ and $\mathcal{S}_{\boldsymbol{\sigma}} \cap \mathcal{S}_{\mathbf{u}} = 0$. The term $\tilde{\mathbf{t}} = \boldsymbol{\sigma} \cdot \mathbf{n}$ is a prescribed traction vector residing on the surface $\mathcal{S}_{\boldsymbol{\sigma}}$. Requiring that $\boldsymbol{\eta} = \mathbf{0}$ on $\mathcal{S}_{\mathbf{u}}$ removes the last integral and the remaining terms are collected to form

$$\int_{V_{\mathcal{B}}} \dot{\mathbf{v}} \cdot \boldsymbol{\eta}\, \rho\, dV = -\int_{V_{\mathcal{B}}} \boldsymbol{\sigma} : \boldsymbol{\nabla}^s \boldsymbol{\eta}\, dV + \int_{V_{\mathcal{B}}} \mathbf{b} \cdot \boldsymbol{\eta}\, dV + \int_{\mathcal{S}_{\boldsymbol{\sigma}}} \tilde{\mathbf{t}} \cdot \boldsymbol{\eta}\, d\mathcal{S} \ , \tag{2.6}$$

the very foundation of the MPM approximation scheme—not to mention several other numerical techniques. In the current form two key items need to be addressed: the arbitrary

vector-valued spatial function, $\boldsymbol{\eta}(\mathbf{x},t)$, and the integration procedure for each term arising in (2.6). These items are discussed sequentially in what follows.

The governing equations are solved at nodal points in the domain. That being the case it makes sense to build the unknown field quantities $\dot{\mathbf{v}}(\mathbf{x},t)$ and $\boldsymbol{\eta}(\mathbf{x},t)$ using the nodes themselves. These approximations are constructed as

$$\boldsymbol{\eta}(\mathbf{x},t) \approx \boldsymbol{\eta}^h(\mathbf{x},t) := \sum_i N_i(\mathbf{x})\,\boldsymbol{\eta}_i(t) \quad \text{and} \quad \dot{\mathbf{v}}(\mathbf{x},t) \approx \dot{\mathbf{v}}^h(\mathbf{x},t) := \sum_j N_j(\mathbf{x})\,\dot{\mathbf{v}}_j(t) \tag{2.7}$$

where $N_i(\mathbf{x})$ and $N_j(\mathbf{x})$ are the shape functions associated with nodes i and j, respectively. $\boldsymbol{\eta}_i(t)$ is an arbitrary, time-dependent nodal vector at a node i, and $\dot{\mathbf{v}}_j(t)$ is the time-dependent nodal acceleration vector at a node j. In this work the superscript h indicates a grid-based approximation. Closer inspection of the second integral term in Equation (2.6) reveals that $\boldsymbol{\eta}^h(\mathbf{x},t)$ must be sufficiently smooth in order to accommodate non-zero action of the differential operator, $\boldsymbol{\nabla}$. Thus, at a very minimum, the shape functions $N(\mathbf{x})$ must be linear in $\mathbf{x}$ (at least C^0 continuous).

The next task is to identify an approximation scheme for the integral terms in (2.6). Representing the total body as a collection of particles of fixed mass m_p not only satisfies conservation of mass, but also allows integrals to be computed as sums over particles as follows:

$$\int_{V_\mathcal{B}} (\bullet)\;\rho\,dV = \sum_p \int_{V_p} (\bullet)\;\rho_p\,dV_p = \sum_p \int_{m_p} (\bullet)\;dm_p \approx \sum_p (\bullet)_p\;m_p\;. \tag{2.8}$$

The symbol $\sum_p$ indicates a summation over all particles while the subscript p refers to a particle quantity. The approximation leading to the last term in (2.8) may be viewed either as a direct application of the *mean value theorem* of integration or as a single point numeric integration over the particle domain. This form is contingent upon the transformation to a mass element, defined as $dm = \rho\,dV$. Comparing to Equation (2.6), the proper mass element exists only for the first term and the terms must be modified appropriately. The notion of a *mass-specific* term is introduced using the notation $(\bar{\bullet})$, which indicates the transformation of a volume-specific quantity, i.e., $(\bullet) = \rho\,(\bullet/\rho) = \rho\,(\bar{\bullet})$ to its mass-specific counterpart. In the present example this transforms the weak form equation to

$$\int_{m_\mathcal{B}} \dot{\mathbf{v}}\cdot\boldsymbol{\eta}\,dm = -\int_{m_\mathcal{B}} \bar{\boldsymbol{\sigma}} : \boldsymbol{\nabla}^s\boldsymbol{\eta}\,dm + \int_{m_\mathcal{B}} \bar{\mathbf{b}}\cdot\boldsymbol{\eta}\,dm + \int_{\mathcal{S}_{\boldsymbol{\sigma}}} \tilde{\mathbf{t}}\cdot\boldsymbol{\eta}\,d\mathcal{S}\;, \tag{2.9}$$

where $\bar{\boldsymbol{\sigma}}$ and $\bar{\mathbf{b}}$ are the mass-specific Cauchy stress and body force, respectively. The primary integration domain has been transformed from the body volume $V_\mathcal{B}$, to the body mass $m_\mathcal{B}$.

2.2.2 Constructing the System of Equations

The discrete set of equations

$$\sum_j m_{ij}\,\dot{\mathbf{v}}_j = \mathbf{f}_i^{int} + \mathbf{f}_i^{ext}\,, \tag{2.10}$$

with

$$\mathbf{f}_i^{int} = -\sum_p \bar{\boldsymbol{\sigma}}_p \cdot \boldsymbol{\nabla} N_{ip}\, m_p\,. \qquad \text{and} \qquad \mathbf{f}_i^{ext} = \sum_p \bar{\mathbf{b}}_p\, N_{ip}\, m_p + \int_{\mathcal{S}_{\boldsymbol{\sigma}}} \tilde{\mathbf{t}}\, N_{ip}\, dS \tag{2.11}$$

is obtained for the unknown nodal accelerations $\dot{\mathbf{v}}_j$ by substituting the grid-based definitions given in listing (2.7) and the integral approximation scheme outlined in (2.8) into the weak form Equation (2.9). The resulting system utilizes $m_{ij} = \sum_p N_{ip}\, N_{jp}\, m_p$, the consistent mass matrix coefficients with N_{ip} as the shape function evaluated at the particle location, i.e., $N_{ip} = N_i(\mathbf{x}_p)$. Frequently the off diagonal coupling terms in m_{ij} are eliminated by approximating the mass matrix as a purely diagonal matrix: $m_i = \sum_p N_{ip}\, m_p$. In doing so the system in (2.10) is reduced to a series of i uncoupled equations for the i nodes describing the spatial domain.

The external surface force term in $(2.11)_2$ can be problematic in the MPM. The root of the problem lies in the fact that surface tractions must be applied on the body—a.k.a. the particles—and these objects move throughout nodal supports in time. Thus, the particle area and force orientation must be tracked appropriately so these terms can be applied at the correct nodes for any given position/orientation of the particle/surface. This is in contrast to other techniques, such as the Finite Element Method (FEM), where this term is applied directly to nodal values.

2.2.3 Putting it All Together

The primary goal of any analyses is to track the system in time while monitoring the evolution of key quantities at both the particle and nodal levels. This is accomplished in part by splitting a finite time increment, T, into many smaller time intervals, $\Delta t = t_{n+1} - t_n \ll T$. Over each time step Δt the current state is mapped to the nodes, a grid-based time integration is performed, and particle values are updated. This computational cycle is broken down and visualized as individual components in Figure 2.1. In this section the details of each step are presented.

The first step involves the transfer of particle quantities to the nodes. This is shown in

Figure 2.1(a) and is accomplished by way of

$$\mathbf{p}_{i,n} = \sum_p N_{ip}\, m_p\, \mathbf{v}_{p,n} \quad , \quad \mathbf{f}_i^{int} = -\sum_p \bar{\boldsymbol{\sigma}}_p \cdot \boldsymbol{\nabla} N_{ip}\, m_p$$
$$\text{and} \qquad \mathbf{f}_i^{ext} = \sum_p \bar{\mathbf{b}}_p\, N_{ip}\, m_p + \int_{\mathcal{S}_{\boldsymbol{\sigma}}} \tilde{\mathbf{t}}\, N_{ip}\, dS \tag{2.12}$$

for the momentum $\mathbf{p}_{i,n}$, internal force $\mathbf{f}_i^{int}$, and external force $\mathbf{f}_i^{ext}$ contributions, respectively. These values are used to solve the linear systems

$$\dot{\mathbf{v}}_i = \frac{1}{m_i}\left(\mathbf{f}_i^{int} + \mathbf{f}_i^{ext}\right) \qquad \text{and} \qquad \mathbf{v}_{i,n} = \frac{\mathbf{p}_{i,n}}{m_i}\ , \tag{2.13}$$

which yields the acceleration and velocity ($\dot{\mathbf{v}}_i$ and $\mathbf{v}_{i,n}$) at time t_n for each node in the domain. Here it is assumed that the consistent mass matrix is approximated using a diagonal, or lumped mass matrix as explained in the previous section. For the explicit integration scheme the nodal acceleration is assumed constant over the time step, resulting in the updated velocity field

$$\mathbf{v}_{i,n+1} = \mathbf{v}_{i,n} + \Delta\mathbf{v}_i \qquad \text{with velocity increment} \qquad \Delta\mathbf{v}_i = \Delta t\, \dot{\mathbf{v}}_i \tag{2.14}$$

describing the total field at the end of the time step Δt. The velocity field at the beginning and end of each time step are used to define the effective nodal velocity

$$\mathbf{v}_{i,n+\theta} = (1-\theta)\, \mathbf{v}_{i,n} + \theta\, \mathbf{v}_{i,n+1}\ , \tag{2.15}$$

where $\theta \in [0,1]$ is an integration parameter that extracts the field at an arbitrary time, $t_{n+\theta} = t_n + \theta\Delta t$, between or at t_n and t_{n+1}. The effective velocity gives way to the position increment according to

$$\Delta\mathbf{x}_i = \mathbf{v}_{i,n+\theta}\, \Delta t\ . \tag{2.16}$$

The series of computations outlined in (2.12)–(2.16) are depicted in Figure 2.1(b) and together form the grid-based time integration portion of the MPM analysis. This series of nodal equations implies the nodes themselves are moving. Strictly speaking this statement is true. However, as noted previously, the nodal position are arbitrary at the beginning of each time step. It is common practice to continuously assume nodal positions coincide with their original position at $t = t_0$ for the start of each new time step. This may be interpreted as discarding the old grid and creating a new series of nodes each time step.

At this stage in the computational cycle the motion at the nodes is well defined over the time step and will not change. Therefore the resulting deformation, incurred in an incremental fashion as a result of the change in motion, is determined based on the last

known state. This stage is represented in Figure 2.1(c). The velocity gradient is computed at the particle level according to

$$\boldsymbol{\nabla} \mathbf{v}^h_{p,n+\theta} = \sum_i \mathbf{v}_{i,n+\theta} \otimes \boldsymbol{\nabla} N_{ip} \ . \tag{2.17}$$

Multiple deformation, or strain, measures exist depending on the type of analysis. A single presentation cannot possibly accommodate all the options in this regard. This section will focus on a large deformation measure obtainable from the incremental deformation gradient:

$$\mathbf{f}_p = \mathbf{1} + \Delta t \, \boldsymbol{\nabla} \mathbf{v}^h_{p,n+\theta} \ . \tag{2.18}$$

The particle strain is updated according to

$$\boldsymbol{\varepsilon}_{p,n+1} = \tilde{\boldsymbol{\varepsilon}}(\boldsymbol{\varepsilon}_{p,n}, \mathbf{f}_p) \tag{2.19}$$

where $\tilde{\boldsymbol{\varepsilon}}$ is a general strain function of the known deformation state at t_n and the incremental change over the time step.

The particle stress is determined from

$$\bar{\boldsymbol{\sigma}}_{p,n+1} = \frac{\partial \bar{\psi}(\boldsymbol{\varepsilon}_{p,n+1})}{\partial \boldsymbol{\varepsilon}_{p,n+1}} \ , \tag{2.20}$$

where $\bar{\psi}$ is the mass specific free energy function. Much like the strain function, $\tilde{\boldsymbol{\varepsilon}}$, the free energy function is typically cast in terms of several additional variables, including state dependent quantities required for elastoplastic constitutive laws. For the time being these details are omitted. The key point to take from this presentation is the stress is a function of the updated strain. This implies a hierarchical structure that will be exploited in later chapters. For the special case of a linear elastic material, the particle stress is obtained as

$$\bar{\boldsymbol{\sigma}}_{p,n+1} = \frac{K}{\rho_0} (\operatorname{tr} \boldsymbol{\varepsilon}_{p,n+1}) \, \mathbf{1} + \frac{2\,G}{\rho_0} \operatorname{dev} \boldsymbol{\varepsilon}_{p,n+1} \tag{2.21}$$

with initial mass density ρ_0, bulk modulus K, and shear modulus G. The terms $\operatorname{tr}(\bullet)$ and $\operatorname{dev}(\bullet)$ the standard trace and deviatoric operators on a second order tensor.

Depicted in Figure 2.1(d), the final portion of the computational cycle is the particle velocity and position update

$$\mathbf{v}_{p,n+1} = \mathbf{v}_{p,n} + \sum_i N_{ip} \, \Delta \mathbf{v}_i \qquad \text{and} \qquad \mathbf{x}_{p,n+1} = \mathbf{x}_{p,n} + \sum_i N_{ip} \, \Delta \mathbf{x}_i \ , \tag{2.22}$$

obtained from the incremental change in nodal velocity and position over the time step. Upon completion of this last step the cycle repeats until the analysis time reaches a user prescribed value.

Table 2.1: Numerical methods and references.

Numerical Method	Selected References
Arbitrary Lagrangian-Eulerian (ALE)	Benson (1992); Huerta and Casadei (1994); Donea et al. (2004)
Finite Element (FEM)	Hughes (1987); Bathe (1996); Zienkiewicz et al. (2005a,c)
Meshfree or Meshless (MM)	Belytschko et al. (1996); Fries and Matthies (2003-03); Liu (2003); Liu and Liu (2003)
Finite Difference (FD)	Ghaboussi and Barbosa (1990); LeVeque (2007); Radjai and Duboi (2011)

The details provided here (as well as previous Section 2.1) highlight the very basics of the Material Point Method. Of course, this traditional form is subject to change depending on the implementation strategy or details arising due to the extension of the traditional framework, such as the enhancements described in Appendix B, and Chapters 4 and 5, or any one of the several modifications discussed in the remainder of this chapter. The current state of the literature is examined next.

2.3 Comparison to Other Numerical Methods

A thorough overview and literature review would include a detailed comparison to other numerical methods suitable for large deformation analyses. Such an approach is, however, beyond the scope of the current chapter and could likely yield a chapter of its own if presented in moderate depth. Considering the MPM is nearly 20 years old the numerical community would likely benefit from such a presentation, especially if a survey of the method's enhancements and corresponding applications were included. For the time being it suffices to say that the MPM shares many similarities with a bevy of numerical schemes, including Arbitrary Lagrangian-Eulerian (ALE) methods, both Lagrangian and Eulerian Finite Element Methods (FEM), meshless or meshfree methods, and select Finite Difference (FD) techniques. The broad list is due in part to the combination of Lagrangian (computational particles) and Eulerian (stationary grid) reference frames that make the MPM what it is. The interested reader can consult Table 2.3 for a list of references to related numerical

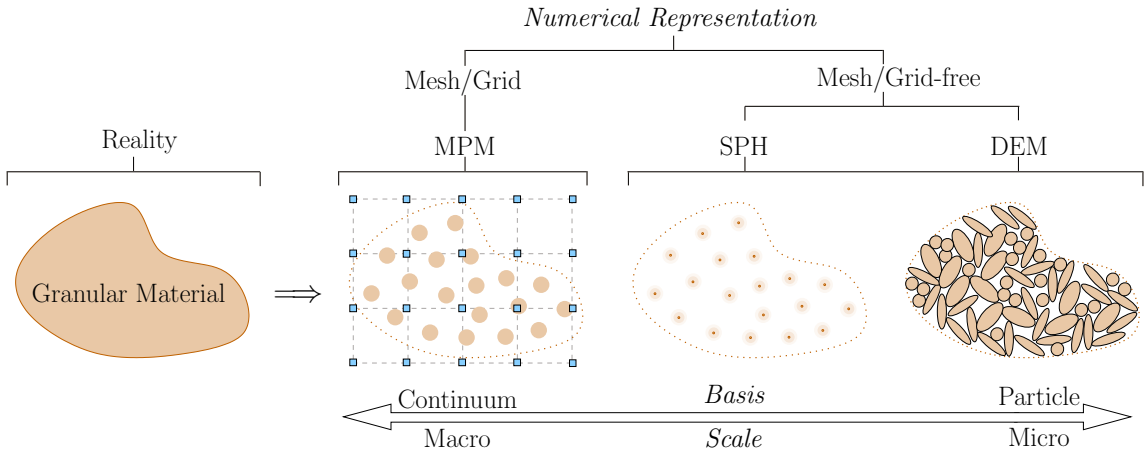

Figure 2.2: Simulating granular matter using the Material Point Method, Smoothed Particle Hydrodynamics, and the Discrete Element Method.

schemes. This table is by no means all-inclusive or even remotely indicative of the vast array of literature available on these topics. Rather, this table reflects the author's attempt to encapsulate an enormous amount of work into a smaller, less daunting list of readable references. Additional information highlighting the similarities between MPM and other numerical methods can be found in the papers by Ma et al. (2009) and Guilkey and Weiss (2003).

There is further value in discussing the MPM and the individual techniques known as Smoothed Particle Hydrodynamics (SPH), and the Discrete Element Method (DEM), as the question inevitably arises: how is MPM different from SPH and/or DEM? In terms of similarities, all three have Lagrangian-based reference frames for the material description. The distinguishing feature of the MPM is the solution of the governing equation(s) at stationary nodal points as opposed to the points that actually represent the body. Nodal shape functions span finite portions of the domain, effectively capturing the contribution of neighboring particles to a local point. Thus, the MPM is the only grid-based method of these three approaches. Both SPH and DEM solve the governing equations(s) locally at the particle position, creating a meshfree simulation environment. In both these latter cases the contribution of neighboring particles is handled as a series of individual forces arising from each particle's neighbors. In SPH, each point has a zone of influence, much like a nodal shape function, centered about the computational point. From this perspective, SPH particles function very similar to nodes in the MPM (with the major exception that SPH points move in time). Alternatively, the DEM grains interact much like one would envision actual particle-to-particle contact in a granular medium.

A natural way to link these three methods is shown in Figure 2.2 (this figure is applicable only to granular-based material descriptions). Here the MPM is depicted as being on the continuum end of the material spectrum, while the DEM serves as a particle-based representation. SPH falls somewhere in between these two extremes. The other consideration is the scale. Clearly DEM is superior for smaller scale simulations, where subtle nuances are important. As the scale increases MPM becomes more appropriate, as individual grain interactions become irrelevant and are smoothed out. Again, SPH finds itself in the middle in terms of applicable scales. This illustration serves only as a reminder as to which regime each of these numerical methods is best suited to represent. These are not hard and steadfast rules, and depending on the application all, some, or only one method may be the best approach.

A common point of confusion is the classification of MPM as either a continuum- or particle-based method. The point-wise nature of the integration scheme and body discretization instill a false sense of particle-ism. This, coupled with the other related issues such as visualization and applications to granular, constituent-based matter, leads to an erroneous classification of the MPM as a particle method. To be clear, the MPM is a continuum-method. This classification is based on the formulation and integration details. Of course, some will argue that the mere presence of particle-like objects make the technique a particle-based approach. However, when compared to other methods like SPH [2] or the DEM, it is clear that the MPM cannot and should not be classified as a true particle technique.

2.4 Literature Review

The Material Point Method was born out of a need to marry fluid-like, large deformations with a history-dependent material response. While a large body of research has focused on similar applications, much work has also been done in additional areas (many of which are explored shortly)—pushing the capabilities of the MPM and investigating new applications. In the remainder of this chapter a look at previous and current research will be examined in moderate detail. In an effort to streamline the discussion this survey has been separated into several different categories, each of which pertains to a different topic.

---

[2]Even classifying SPH as a true particle-method could be deemed as incorrect, as the particles in SPH carry a fuzzy representation and often do not represent constituents. However, the important distinction is that particles can represent constituents in SPH if need be.

2.4.1 Historical Development

The MPM follows from a more general class of numerical schemes known as PIC, or Particle-in-cell methods. The first PIC technique was developed in the early 1950's (Harlow, 1957) and was used primarily for applications in fluid mechanics. Early implementations suffered from excessive energy dissipation, rendering them obsolete when compared to other, more valid methods. In 1986, Brackbill and Ruppel solved many of the inherent problems related to energy dissipation and introduced FLIP—the Fluid Implicit Particle method. The FLIP technique was modified and tailored for applications in solid mechanics and has since been referred to as the Material Point Method.

One of the first publications on the topic was by Sulsky et al. in 1994. This pioneering work, as well as a slight variant created for specific applications in solid mechanics (Sulsky et al., 1995), successfully outlined the basic algorithmic implementation and shortly thereafter an axisymmetric form was published by Sulsky and Schreyer (1996). Using several two dimensional impact examples, these seminal works showed that elastic and perfectly plastic behavior was reasonably reproduced using the MPM. Also highlighted was the fact that no-slip impact for elastic, inelastic, and rigid bodies is handled automatically by the algorithm, further reinforcing the robustness of the proposed approach.

In the time since this initial research was published, several variations/extensions to the MPM have been proposed—many of which are application specific and discussed later in this chapter. Included in this list is one of the most prominent variants, the Generalized Interpolation Material Point (GIMP) method. This technique, as well as a related extension known as the Convected Particle Domain Interpolation (CPDI), provides an alternative representation of the particle domain. These two variants are explored at the end of this section.

2.4.2 General Implementation

The applications of the MPM vary significantly, ranging from various geotechnical implementations (Zhou et al., 1999; Wieckowski, 2004b), to anchor pullout (Coetzee et al., 2005), to the modeling of sea ice dynamics (Sulsky et al., 2007). Several large deformation, flow-like models have been reported (Wieckowski et al., 1999; Wieckowski, 2003, 2004a) while the work by York et al. (1999, 2000) emphasizes membrane analysis with a specific focus on fluid–membrane interaction. The method has even realized moderate success in the context of multicellular constructs as shown in the work by Guilkey et al. (2006) and, more recently, the numerical simulation of landslides (Andersen and Andersen, 2010b).

2.4.3 Contact, Impact/Penetration, and Material Interaction

The need to model contact and interaction of bodies has long been the focus of a significant amount of MPM research. A robust MPM contact algorithm capable of handling sliding and rolling friction, as well as separation, was first addressed in the paper by Bardenhagen et al. (2000) and later improved in the publication by Bardenhagen et al. (2001). These works introduce the idea of contact within the context of granular materials modeling and are particularly significant for two reasons: they represent the first published attempt to isolate a contact force (or traction) between interacting bodies, and they are the first to propose the use of multiple, conforming grids to model contact or interaction.

In recent years the idea of using multiple grids to model contact and body interaction has been explored by many researchers in various settings. These include the meshing process of spur gears (Hu and Chen, 2003) and the development of general, three dimensional contact algorithms by Pan et al. (2008) and Huang et al. (2011). The concept has also been extended to model the drag interaction between material phases. This latter topic is addressed by Mackenzie-Helnwein et al. (2010), where the drag force between two material phases is a function of the relative material velocities—each of which is computed on a separate grid. A similar approach is used by Zhang et al. (2008), where the treatment of several phases is handled in a multi-grid environment, and care is taken to ensure the continuity requirement is satisfied over a representative time step. Finally, in the publication by Shen and Chen (2005), a multi-grid concept is used to continuously superimpose a boundary layer in order to distribute viscous damping forces. The forces are applied along the moving computational interface between two material phases.

Contact algorithms have now been expanded to include impact and simulation of explosive phenomena. Two such examples are described in Ma and Zhang (2009) and Lian et al. (2011). The interaction between saturated soil and impacting solid bodies is explored in the work by Zhang et al. (2009). This research features the development of a *u-p* coupled Material Point Method (CMPM) and is used to predict the dynamic response of saturated soil.

2.4.4 Fracture and Material Failure

Material failure and fracture mechanics algorithms share many similar features with those from the previous section. However, enough work has been done on these additional topics to validate the creation of a separate category. Of the many similarities, perhaps the most notable is the concept of using multiple grids. In the publications from Nairn (2003) and Guo and Nairn (2006) this concept is exploited to develop separate grid velocities around

crack tip locations. This effectively serves as a discontinuity in the continuum and allows the method to capture crack propagation. An additional paper by Guo and Nairn (2004) evaluates crack parameters (e.g., the J-Integral and stress intensity factors) commonly used in fracture analysis.

The modeling of general crack geometry is complicated in the MPM since the technique is typically implemented using a regular, rectangular grid. Tan and Nairn (2001) address the issue using a hierarchical mesh refinement algorithm that allows for better geometric resolution of the discontinuity. The work by Wang et al. (2005) confronts this issue by introducing an irregular grid, and corresponding mapping scheme, to handle arbitrary crack geometry in a two dimensional framework.

Several techniques have been proposed in an effort to simulate material failure. A straightforward evaluation of the MPM's ability to capture dynamic failure with damage diffusion is addressed by Chen et al. (2002). The publication by Schreyer et al. (2002) presents a more specialized investigation into the delamination of layered composite materials by modeling the process as a strong discontinuity. The resulting framework effectively captures the propagation of delamination with no sensitivity to mesh orientation. Sulsky and Schreyer (2004) and Shen (2009) both develop decohesion constitutive models that are used to predict and assess material failure.

2.4.5 Energy and Integration Considerations

A relatively small collection of research has been published regarding the mathematical foundation of the Material Point Method. What has surfaced focuses primarily on energy conservation and integration errors in the formulation. The basic implementation of the method ensures conservation of mass and momentum by construction. However, no attention is given to the conservation of energy. This issue is addressed in the paper by Bardenhagen (2002), where it is shown that the two available options for updating the particle stress lead to dramatically different findings with respect to internal energy conservation of the system. Additional work regarding energy conservation can be found in the papers by Love and Sulsky (2006a,b). These latter two documents examine energy consistency from a thermodynamics perspective. Their findings show that the use of a consistent mass matrix results in a numerical method that inherits the energy-dissipative and momentum-conserving properties of the mesh solution.

An equal amount of attention has been given to mitigating integration errors. The first work specifically addressing this issue is by Steffen et al. (2008b). This paper examines the error associated with linear shape functions and proposes the use of quadratic B-splines basis

functions. A similar body of work by Andersen and Andersen (2010a) examines standard linear and quadratic shape functions, as well as cubic splines. They too conclude that the use of higher order basis functions leads to more accurate results. Alternatively, Htike et al. (2011) use a radial basis function (RBF) in place of the traditional linear shape functions or B-splines. The proposed RBF possesses a high degree of smoothness; thus eliminating non-physical results associated with more traditional implementations. The RBF form of the MPM is tested and validated through a series of benchmark problems from solid mechanics. Finally, the publication from Steffen et al. (2010) develops a set of criteria relating the grid size, number of particles, and time step. The premise of this research is based upon selecting a time step that balances spatial and temporal errors.

2.4.6 Computational Implementation

There is little published work on efficient implementation strategies since the MPM is a relatively young method compared to other, more established techniques. Nonetheless, there are a limited number of publications on the topic. The nature of the algorithm is well suited for parallel applications—particularly if using a lumped mass matrix as is often the case. These ideas are explored in the work by Huang et al. (2008) where researchers employ FORTRAN95 with OpenMP parallelization to investigate two separate implementation strategies. Ma et al. (2010b) examine the development of an object oriented framework for large deformation analyses. Multiple particle update strategies are investigated with an emphasis on reducing memory requirement and computational cost. The publication by Shin et al. (2010) strives to also reduce memory requirements and computational cost by presenting a dynamic meshing scheme. Their algorithm instantiates and searches only cells containing matter—effectively avoiding useless storage of empty nodes and performing unneeded computations. The efficiency of the proposed approach is measured against standard storage schemes and is shown to be quite effective.

2.4.7 Variations on the Material Point Method

Several extensions or variations have been proposed since the MPM's inception. In fact, most of the applications mentioned thus far modify or change the algorithm in one way or another. Presented in this section are representative works that significantly alter the implementation and provide noteworthy extensions.

Most implementations use a time-explicit discretization to solve dynamic problems. Sulsky and Kaul (2004) propose a time-implicit discretization and use various solution schemes to solve the resulting non-linear equations. Their study shows the potential for large com-

putational savings by using an implicit approach with appropriate time step. A quasi-static approach is developed in the research by Beuth et al. (2008,2010). These publications feature several large strain examples that are presented and compared to the FEM.

One of the problems that has long beleaguered the MPM is partially full cells and linear shape functions. In an effort to improve the kinematics an improved velocity projection is developed in the paper by Wallstedt and Guilkey (2007). Their work shows that the quality of the solution relies heavily on particle density, location, and orientation with respect to the computational grid. An enhancement to the linear projection operator is proposed that reduces the dependence on particle location and density, ultimately leading to a higher quality solution. The main issue with partially filled cells is poor and/or non-physical nodal accelerations, resulting in a numerical instability. Said instability is due in part to low nodal mass coupled with a large nodal force, and can lead to significant numerical problems. Ma et al. (2010a) have created a small mass nodal distribution coefficient matrix that attempts to eliminate this shortcoming. Their mass and momentum conserving algorithm proposes a redistribution of mass around those problematic nodes—effectively limiting the instability. The algorithm is tested and validated through one and two dimensional applications. As an alternative to nodal mass, the nodal force can be calculated differently to alleviate problematic nodal accelerations. The force is directly proportional to the shape function gradient and primarily responsible for "cell crossing" errors frequently referenced in the literature. Zhang et al. (2011) have developed an enhanced gradient for the interpolation functions to combat this issue. The enhancement eliminates the discontinuity in the gradient for linear shape functions. The approach is highlighted through bending, vibration, and projectile-target examples.

The previous paragraph provides an overview of research that aimed to fix or modify the algorithm for issues associated with linear shape functions. Although these proposed techniques effectively reduce the problem for select applications, they are unable to resolve the issue completely. In order to fully eliminate the instability, one must examine the root of the problem, which is actually the point-wise description of the body. Since any material is represented as a collection of particles, a finite portion of the body is being modeled as a singular point. Thus, the particle shape (volume), is not explicitly accounted for in the standard algorithm. Bearing this information in mind, two primary variants have been developed that take into consideration the particle shape when solving the equation of motion.

The Generalized Interpolation Material Point Method

The Generalized Interpolation Material Point (GIMP) Method was initially introduced by Bardenhagen and Kober (2004). The GIMP approach assigns a domain (typically rectangular) to each particle at the start of the analysis. In general, this leads to more accurate spatial integration. However, the technique adds additional computational cost because the overlap of particle domain and nodal support must be determined at each time step. There are effective and efficient implementation strategies as outlined in the paper by Buzzi et al. (2008).

Like the MPM, GIMP has tasted success in a wide variety of contexts and settings. These include crack propagation and modeling (Daphalapurkar et al., 2007) as well as multiscale simulation with an emphasis on molecular dynamics (Ma et al., 2006c,a). Different mesh refinement strategies are explored in the work by Ma et al. (2006b) while the paper by Wallstedt and Guilkey (2008) evaluates different time integration schemes.

It should be noted that the standard MPM algorithm is recovered by selecting a particle domain that is the Dirac delta function—implying that the Material Point Method itself is a specialization of the GIMP technique. Thus, to call the GIMP method a variation of the MPM may be a misnomer, but it is typically done so nonetheless. This relationship is outlined in additional detail in the following sections.

Convected Particle Domain Interpolation

Sadeghirad et al. (2011a) propose a procedure that includes information about the particle domain when integrating the standard weak form equations. In the Convected Particle Domain Interpolation (CPDI) technique, particles are given parallelogram-shaped domains that are constantly updated using the deformation gradient evaluated at the particle location. What separates this technique from GIMP is the following: the particle domain is described by shape vectors that evolve with the deformation gradient. Thus, shear deformations and volume changes are accounted for throughout the analysis that are not considered when using the traditional GIMP technique (although, some variants of GIMP take into account volumetric shape changes). Like GIMP, the CPDI procedure expands the support of a particle and spreads out the influence of the internal force to those nodes whose support overlaps the particle domain. Spatial integration is significantly improved and the technique reduces the number of particles needed to achieve reasonable results. A series of two dimensional numerical examples validate the proposed approach in the aforementioned reference.

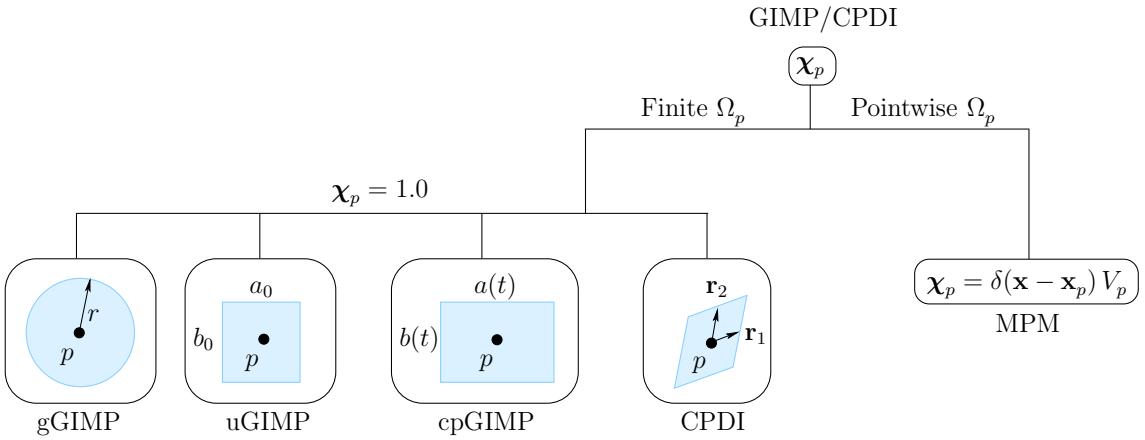

Figure 2.3: Relationship between the particle characteristic function, $\boldsymbol{\chi}_p$, and MPM, GIMP, and CPDI.

GIMP vs. CPDI vs. MPM

Although not technically a literature review there is value in further examining the the underlying relationship between the MPM, GIMP, and CPDI. The MPM as presented in this chapter assumes a general body is discretized using a collection of particles, each with mass m_p lumped at a single location $\mathbf{x}_p$. While not explicitly stated, this assumes the particle has no spatial extent. Mathematically this statement is cast using $\boldsymbol{\chi}_p(\mathbf{x} - \mathbf{x}_p) = \delta(\mathbf{x} - \mathbf{x}_p)$, where the *particle characteristic function*, $\boldsymbol{\chi}_p$, is introduced and equated to the traditional Dirac delta function. This particular choice of characteristic function is not a requirement. In fact, both CPDI and GIMP follow from a more general choice.

A generalization of the framework presented thus far is obtained by replacing N_{ip} with $\bar{N}_{ip}$ in Equation(2.11) (and corresponding discussion), where

$$\bar{N}_{ip} = \frac{1}{V_p} \int_{\Omega_p} \boldsymbol{\chi}_p(\mathbf{x} - \mathbf{x}_p)\, N_i(\mathbf{x})\, d\mathbf{x} \tag{2.23}$$

and

$$\nabla \bar{N}_{ip} = \frac{1}{V_p} \int_{\Omega_p} \boldsymbol{\chi}_p(\mathbf{x} - \mathbf{x}_p)\, \nabla N_i(\mathbf{x})\, d\mathbf{x} \tag{2.24}$$

are weighting and gradient weighting functions, respectively, and Ω_p is the support of $\boldsymbol{\chi}_p$. The term $N_i(\mathbf{x})$ is the nodal shape function previously outlined in Equation (2.7) while V_p is the volume of the particle. Additional details regarding this transformation can be found in Bardenhagen and Kober (2004) as well as Sadeghirad et al. (2011a).

The ramifications of this generalization are shown in Figure 2.3, where the underlying relationship between these methods is seen as a function of only $\boldsymbol{\chi}_p$ and the corresponding

support Ω_p. On the MPM side there is no extent to the particle domain; the Dirac delta function in the integrand ensures $N_{ip} = \bar{N}_{ip}$ and $\nabla N_{ip} = \nabla \bar{N}_{ip}$. For finite particle domains there are additional options. The classic GIMP approach utilizes $\boldsymbol{\chi}_p = 1.0$ and a rectangular particle domain described by a_0 and b_0. This approach is dubbed uGIMP by Sadeghirad et al. (2011a). The particle domain is not required to be rectangular—but doing so eases the integration process if geometrically simple shapes are used. There is nothing wrong with using circular, or ellipsoid, domains as indicated by gGIMP (the name gGIMP is not used in the literature and is assigned here to distinguish from uGIMP and cpGIMP). However, there are no published GIMP studies using non-rectangular domains to date. The volume of the particle domain can change by updating the particle dimensions with deformation, as indicated by $a(t)$ and $b(t)$ in cpGIMP (again, the name follows from Sadeghirad et al. (2011a)). Unfortunately this latter approach cannot capture particle distortion via shearing. To combat this, the CPDI technique describes the particle extent using shape vectors $\mathbf{r}_1$ and $\mathbf{r}_2$ that evolve with the deformation gradient. For CPDI the integrand in (2.23) and (2.24) is approximated based on an interpolation of the values of the traditional shape functions evaluated at the particle corners.

Coupling with Other Methods

One of the prominent trends in recent years is coupling the MPM with additional numerical techniques. Such an approach allows analysts to reap the benefits of multiple solution types and exploit each method's strengths in multiphysic simulations. One example of this is the paper by Lian et al. (2011), in which the MPM is mixed with the Finite Element Method. Their approach treats boundaries and other objects using traditional FE and does not require the meshes for the MPM and FEM to coincide. In doing so the authors leverage the benefits of MPM with regards to large deformation simulations and capture others, such as irregular shaped boundaries, with the FEM. Additional examples include the coupling with purely Eulerian finite difference or finite volume schemes, e.g., the works presented by (Zhang et al., 2008; Higo et al., 2010). In these formulations the governing equations of different materials or phases are solved by methods well suited to do so. It can be argued that coupling the MPM with other methods and exploiting each technique's strengths is far more practical for multiphysics applications than the alternative, which is trying to build a single formulation that is an all-encompassing, super-method capable of any feat. The latter may be viewed as unrealistic and an inefficient use of resources in a numerical modeling context.

2.5 Summary

This chapter provided a basic overview of the MPM, including the implementation details and the current state of the literature. In the remaining chapters the standard framework is expanded with two enhancements. As stated in the Introduction, the primary goal is to build a numerical framework capable of modeling landslides and debris flows. A key factor in doing so is the ability to capture the mechanical response of granular media as well as well other slide constituents, such as air and water. To this end several material models are presented in the next chapter.

Chapter 3

MATERIAL MODELS

Because of its continuum basis MPM must be combined with suitable constitutive relations to properly capture local state behavior at the material point level. In this chapter all the components needed to build a MPM-oriented constitutive framework are presented, including basic concepts from computational inelasticity, small and large deformation theory, and the development of specific material models capable of simulating several kinds of materials. Particular attention is paid here to developing a framework that can accommodate extremely large deformations while remaining computationally efficient and numerically stable in the context of granular media. The chapter closes with direct shear and bi-axial examples.

3.1 Elasto-plastic Materials

Material models play an invaluable role in many areas of engineering. As such, an enormous amount of research has gone into their development and application. While the complexity of these models varies significantly, the primary goal of each is the same: to capture and replicate material response observed in the field and in the laboratory. Quite often this boils down to identifying key components that are decisive or fundamental in predicting a material's behavior when subjected to a given loading. Since there is some degree of non-linearity associated with almost any material response, classifying and/or quantifying the non-linearity remains (and perhaps will always be) the central focus of material modeling. There are several techniques or methods readily available for classifying this behavior. In this chapter the focus is on elasto-plasticity, arguably among the most reliable and widely used frameworks to capture a non-linear, rate independent material response.

Elastoplastic models are used to simulate several kinds of materials, including isotropic solids, aggregates, composites, and cohesive-frictional materials—such as granular media. This chapter highlights multiple models that could be used to simulate the mechanical response of ductile metals, semi-brittle concrete, and various soils (most notably, dry sands and gravels). The purpose of this chapter is:

- Present the basic theory and implementation of computational elasto-plasticity for an

isotropic material. Particular emphasis is placed on the integration algorithm for both small and-finite deformation theory.

- Highlight several different material models and outline their formulation.

- Develop a framework that can accommodate extremely large deformations while remaining computationally efficient and numerically stable in the context of granular media.

The specific numerical integration scheme[1] and various components of the theory presented herein were made popular and documented largely by J. C. Simo; most notably in *Numerical analysis and simulation of plasticity* (Simo, 1998) and *Computational Inelasticity* (Simo and Hughes, 1998). The first of these two publications highlights and credits several historical contributors and researchers who are not directly cited here. The bulk of the material presented in this chapter is not new, nor is it intended to have the mathematical completeness to stand alone. Rather, it is presented in an effort to be provide the reader with additional details regarding the material classes as they are implemented and developed in the current coding framework. In some instances equations are simply stated without proof or with minimal explanation. For an in depth presentation the reader is referred to the aforementioned publications. Section 3.2 provides formulation details of rate-independent plasticity. This section may be skipped by any reader already familiar with the concept.

An attempt has been made to use consistent and clear notation. The notation used here largely follows Simo and that used by as R. I. Borja as well as his students, e.g., Borja et al. (2003); Andrade and Tu (2009); Tu et al. (2009).

3.2 Rate-Independent Plasticity

This discussion is ultimately split into two subsections—one for small (or infinitesimal) deformation theory and a second for finite strain theory. Prior to branching it is possible to identify and elaborate on components that are consistent between the two classes of application.

A general overview of the solution procedure is first examined in order to identify the role a material model plays in the grand scheme of numerical simulation. In the current

[1] In the literature the scheme is commonly known as a *return-map* or *return-mapping* algorithm.

context the discretized form of the equations of motion are solved iteratively using three[2] general steps (Simo and Hughes, 1998):

1. Solution of the discretized momentum equations generate incremental motions which are used to calculate the incremental strain history.

2. For a given strain history, new values of the state variables are obtained by integrating the local constitutive equations with given initial conditions.

3. The (discrete) momentum balance equation is tested for the computed stresses and, if violated, the iterative process is continued by returning to the first step.

The material itself is concerned only with the second step above. This step is regarded as the central problem of computational plasticity—as it corresponds to the primary role played by the constitutive equations. The first step above dictates the solution must proceed from a given deformation history, implying the formulation can be cast in a strain-driven context. The following ingredients are required to formulate a rate-independent plasticity model:

(i) *Decomposition of the deformation measure into elastic and plastic parts* — The decomposition is different for the infinitesimal and finite strain algorithms. Additional discussion is reserved for those specific sections.

(ii) *Stress response* — The stress is related to the elastic strain, $\boldsymbol{\epsilon}^e$, and strain-like variables, $\boldsymbol{\alpha}$, using the relationship

$$\boldsymbol{\sigma} = \frac{\partial \psi(\boldsymbol{\epsilon}^e, \boldsymbol{\alpha})}{\partial \boldsymbol{\epsilon}^e} \tag{3.1}$$

where $\boldsymbol{\sigma}$ is a general stress measure and ψ is the free energy function. If ψ can be decoupled into an elastic stored energy function and a hardening potential function, then (3.1) implies a stress relation of the form

$$\boldsymbol{\sigma} = \mathbb{C}^e : \boldsymbol{\epsilon}^e \ , \tag{3.2}$$

with $\mathbb{C}^e$ as a general, 4^{th} order tensor of elastic moduli.

---

[2]The actual number of steps required to solve the equations can vary depending on which numerical method is employed. For most continuum based methods—including the MPM—the solution procedure can be generalized in this minimalistic manner.

(iii) *Yield function and plastic potential* — The limit of the elastic deformation is captured by the yield function $F(\boldsymbol{\sigma}, \boldsymbol{\kappa})$, where $\boldsymbol{\kappa} = \partial\psi/\partial\boldsymbol{\alpha}$ is the vector of stress-like internal variables. By requiring

$$F(\boldsymbol{\sigma}, \boldsymbol{\kappa}) \leq 0\,, \tag{3.3}$$

a constraint is imposed on the elastic deformation. The locus of points in stress-space that satisfy $F(\boldsymbol{\sigma}, \boldsymbol{\kappa}) = 0$ defines the yield surface. The normal to the yield surface is obtained as

$$\mathbf{f} = \frac{\partial F}{\partial \boldsymbol{\sigma}}\ . \tag{3.4}$$

(iv) *Plastic potential and the Flow rule* — The plastic potential is denoted by the function $G(\boldsymbol{\sigma}, \boldsymbol{\kappa})$. The flow rule is defined from the relation

$$\dot{\boldsymbol{\epsilon}}^p = \gamma\, \mathbf{g}\ , \tag{3.5}$$

where $\dot{\boldsymbol{\epsilon}}^p$ is the rate of plastic deformation, the tensor

$$\mathbf{g} = \frac{\partial G}{\partial \boldsymbol{\sigma}} \tag{3.6}$$

is the plastic flow direction and γ is the consistency parameter and is discussed in additional detail shortly. A flow rule is associative if the relationship $\mathbf{g} = \mathbf{f}$ is satisfied—implying the plastic potential is the same as the yield function. This, however, is not a requirement and a non-associative flow rule is obtained if $\mathbf{g} \neq \mathbf{f}$.

(v) *Loading/Unloading and consistency condition* — The *Kuhn-Tucker* (or sometimes *Karush-Kuhn-Tucker) complimentary conditions* serve two purposes: first and foremost they establish necessary conditions for optimally solving the nonlinear system of equations that arise in elasto-plasticity . Second, these conditions provide an intuitive notion of plastic loading and unloading. The conditions are stated as

$$\gamma \geq 0\ , \quad F(\boldsymbol{\sigma}, \boldsymbol{\kappa}) \leq 0\ , \quad \text{and} \quad \gamma\, F(\boldsymbol{\sigma}, \boldsymbol{\kappa}) = 0\ . \tag{3.7}$$

From these conditions it is apparent that the consistency parameter, γ, is greater than zero only during plastic loading or unloading. The actual value of γ must be determined from the *persistency* (or sometimes *consistency*) *condition* which states

$$\gamma\, \dot{F}(\boldsymbol{\sigma}, \boldsymbol{\kappa}) = 0 \quad \text{for} \quad F(\boldsymbol{\sigma}, \boldsymbol{\kappa}) = 0 \tag{3.8}$$

The entire loading state can be ascertained from Equations (3.7) and (3.8). The possible load state conditions are listed in Table 3.1.

Table 3.1: Loading state.

Conditions	*State*
$F < 0 \Longrightarrow \gamma = 0$	Elastic response
$F = 0, \dot{F} < 0 \Longrightarrow \gamma = 0$	Elastic unloading
$F = 0, \dot{F} = 0$ and $\gamma = 0$	Neutral loading
$F = 0, \dot{F} = 0$ and $\gamma > 0$	Plastic loading

The constituents listed in (i)–(v) lead to a nonlinear system of equations that, when combined appropriately, provided the basis for computational inelasticity.

In order to solve the central problem of computational plasticity, new values of the state variables must be obtained by integrating the local constitutive equations subject to given initial conditions. In the current context this statement translates to integrating the equations of interest over the time increment $\Delta t = t_{n+1} - t_n$, where the given initial conditions correspond to the time t_n for which the state is known and well defined. In what follows the notation

$$\Delta(\bullet) = (\bullet)_{n+1} - (\bullet)_n \tag{3.9}$$

will be used, where $(\bullet)$ represents a general quantity. The formulation is now specialized for small and finite deformation theory, respectively.

3.2.1 Small Deformation

Small (or infinitesimal) deformation theory presumes the displacement gradient is small compared to unity, i.e, $\|\boldsymbol{\nabla}\mathbf{u}\| \ll 1$. In this deformation regime the deformed configuration is expressed in terms of the initial configuration. By far the most common choice for a small strain measure is

$$\boldsymbol{\epsilon} = \frac{1}{2}\left(\boldsymbol{\nabla}\mathbf{u} + \boldsymbol{\nabla}\mathbf{u}^T\right) \ , \tag{3.10}$$

and will be the deformation measure of choice for the current discussion (Malvern, 1969).

General formulation

Decomposition of the deformation measure into elastic and plastic parts is the first component of computational elasto-plasticity as outlined in the previous section. Small deformation theory achieves this split via additive decomposition of the total strain, $\boldsymbol{\epsilon}$, into the elastic and plastic parts, respectively. More formally

$$\boldsymbol{\epsilon} = \boldsymbol{\epsilon}^e + \boldsymbol{\epsilon}^p \ , \tag{3.11}$$

where $\boldsymbol{\epsilon}^e$ is the elastic strain tensor and $\boldsymbol{\epsilon}^p$ is the plastic strain tensor. The relationship defined in Equation (3.11) must hold for all times. This motivates the following expression for the elastic strain at time t_{n+1}, obtained from the known state ($\boldsymbol{\epsilon}_n$, $\boldsymbol{\epsilon}^p_n$) at time t_n:

$$\boldsymbol{\epsilon}^e_{n+1} = \boldsymbol{\epsilon}_n - \boldsymbol{\epsilon}^p_n + \Delta\boldsymbol{\epsilon} - \Delta\boldsymbol{\epsilon}^p \ . \tag{3.12}$$

In this definition the *given* strain increment $\Delta\boldsymbol{\epsilon} = \Delta\boldsymbol{\epsilon}^e + \Delta\boldsymbol{\epsilon}^p$ has also been decomposed into its elastic and plastic parts.

The final goal is to determine the state variables at time t_{n+1} from the known state at time t_n. To reach this end the given strain increment, $\Delta\boldsymbol{\epsilon}$, is initially assumed to be elastic. This crucial assumption effectively freezes the rate of plastic deformation, i.e., $\dot{\boldsymbol{\epsilon}}^p = \mathbf{0}$. This conjecture is made solely to define a *trial* elastic strain that is used in subsequent portions of the integration algorithm. This assumption has no bearing on the final result should the actual increment contain a plastic portion. With the rate of plastic deformation frozen, the elastic strain at time t_{n+1} is

$$\boldsymbol{\epsilon}^e_{n+1} = \boldsymbol{\epsilon}^{e\,,tr}_{n+1} - \Delta\boldsymbol{\epsilon}^p \ , \tag{3.13}$$

where the trial elastic strain, $\boldsymbol{\epsilon}^{e\,,tr}_{n+1}$, has been substituted for the quantity $\boldsymbol{\epsilon}_n - \boldsymbol{\epsilon}^p_n + \Delta\boldsymbol{\epsilon}$.

The stress state is a function of the elastic strain as stated in Equation (3.1). The Cauchy stress, $\boldsymbol{\sigma}$, at time t_{n+1} follows from Equations (3.2) and (3.13) as

$$\boldsymbol{\sigma}_{n+1} = \mathbb{C}^e : \boldsymbol{\epsilon}^e_{n+1} = \boldsymbol{\sigma}^{tr}_{n+1} - \mathbb{C}^e : \Delta\boldsymbol{\epsilon}^p \tag{3.14}$$

where the trial stress is a function of the trial elastic strain, i.e., $\boldsymbol{\sigma}^{tr}_{n+1} = \mathbb{C}^e : \boldsymbol{\epsilon}^{e\,,tr}_{n+1}$. From Equation (3.14) it is apparent that identifying the plastic increment, $\Delta\boldsymbol{\epsilon}^p$, is paramount for determining the final stress state, as this is the only element of (3.14) not known. To this end the plastic strain is examined in further detail.

The updated plastic strain at time t_{n+1} is

$$\boldsymbol{\epsilon}^p_{n+1} = \boldsymbol{\epsilon}^p_n + \Delta\boldsymbol{\epsilon}^p \ , \tag{3.15}$$

where the plastic increment is obtained from the integral

$$\Delta\boldsymbol{\epsilon}^p = \int_{t_n}^{t_{n+1}} \dot{\boldsymbol{\epsilon}}^p \, dt \ . \tag{3.16}$$

From the flow rule defined in Equation (3.5), the plastic increment becomes

$$\Delta\boldsymbol{\epsilon}^p = \int_{t_n}^{t_{n+1}} \gamma\,\mathbf{g}\, dt = \Delta t \ (\gamma\,\mathbf{g})|_{n+\theta} = \Delta\gamma\,\mathbf{g}_{n+\theta} \ , \tag{3.17}$$

with $\theta \in [0,1]$ as an integration parameter. The incremental consistency parameter, $\Delta\gamma$, is identified and defined from the relation $\Delta\gamma = \Delta t\, \gamma_{n+\theta}$. Note that this definition is possible by the mean value theorem of calculus and represents an integral approximation of the plastic strain increment.

The improved definition of plastic increment in terms of $\mathbf{g}_{n+\theta}$ and $\Delta\gamma$ solidifies the definition for $\boldsymbol{\sigma}_{n+1}$ given by Equation (3.14). The updated stress at time t_{n+1} is re-cast using Equation (3.17) as

$$\boldsymbol{\sigma}_{n+1} = \boldsymbol{\sigma}^{tr}_{n+1} - \Delta\gamma\, \mathbb{C}^e : \mathbf{g}_{n+\theta}\ . \tag{3.18}$$

The updated state definition at time t_{n+1} also relies on the stress-like hardening variables, $\boldsymbol{\kappa}$. Here it is assumed that these variables will follow from a prescribed hardening function—denoted by $\tilde{\boldsymbol{\kappa}}(\boldsymbol{\sigma}, \boldsymbol{\epsilon}^p, \Delta\gamma)$—that is itself a function of the current state. As labeled here it is a function of the stress, plastic strain, and the incremental consistency parameter. These are not the only options; some models may use other state variables while some may use only one or two of the three mentioned here. Nonetheless the current form suffices for this discussion and motivates the definition

$$\boldsymbol{\kappa}_{n+1} = \tilde{\boldsymbol{\kappa}}(\boldsymbol{\sigma}_{n+1}, \boldsymbol{\epsilon}^p_{n+1}, \Delta\gamma)\,. \tag{3.19}$$

At this point the key relationships between the updated state variables $\boldsymbol{\sigma}_{n+1}$, $\boldsymbol{\epsilon}^e_{n+1}$, and $\boldsymbol{\epsilon}^p_{n+1}$ have been identified. The function for $\boldsymbol{\kappa}_{n+1}$ provides the link final link between the updated state variables and the hardening parameters. The remainder of this sub-section is concerned with the algorithmic implementation and identification of special cases for small deformation, rate-independent plasticity.

Implementation

The primary goal of the return mapping integration algorithm is to determine the unknown state variables $\boldsymbol{\sigma}_{n+1}$ and $\boldsymbol{\kappa}_{n+1}$, as well as the incremental consistency parameter, $\Delta\gamma$. In doing so it is possible to uniquely identify the elastic and plastic components of the total strain. There are several strategies available for solving the non-linear system of equations that arise for the unknown state variables. Here the focus is on a single strategy that employs the well-known Newton-Raphson iteration scheme.

For implementation purposes it is assumed that tensor quantities are written as vectors. In general, a hat ($\hat{\bullet}$) is used to designate a vector representation of a symmetric tensor, i.e.,

$$\hat{\bullet} = \{\, \bullet \,\} = \{\, \bullet_{11}\,,\, \bullet_{22}\,,\, \bullet_{33}\,,\, \bullet_{12}\,,\, \bullet_{13}\,,\, \bullet_{23}\,\}^T \tag{3.20}$$

for the full tensor or, if working in principal space

$$\hat{\bullet} = \{ \bullet \} = \{ \bullet_1 , \bullet_2 , \bullet_3 \}^T \ . \tag{3.21}$$

The matrix representation of other tensors is denoted with brackets $[\bullet]$. For example, the matrix representation of the 4^{th} order elastic constitutive tensor is $[\mathbb{C}^e]$; Helnwein (2001).

The Newton-Raphson iteration linearizes the system in question and, very crudely speaking, solves for the roots of the linearized form. This technique is well documented, e.g., Rao (2002), and follows from the Taylor series expansion about the root using

$$\mathbf{r}(\mathbf{x}) \approx \mathbf{r}(\mathbf{x}_n) + \mathbf{J} \cdot \Delta\mathbf{x} \ , \tag{3.22}$$

where $\mathbf{x}$ is a vector of unknowns (the subscript $\mathbf{x}_n$ indicates the state at time t_n) and $\mathbf{r}(\mathbf{x})$ is a residual vector. The Jacobian matrix, $\mathbf{J}$, will be addressed shortly. This leads to the Newton-Raphson iteration scheme presented in Table 3.2.

In the present context the vectors take the form:

$$\mathbf{x} = \left\{ \begin{array}{c} \hat{\boldsymbol{\sigma}}_{n+1} \\ \boldsymbol{\kappa}_{n+1} \\ \Delta\gamma \end{array} \right\} \qquad \text{and} \qquad \mathbf{r}(\mathbf{x}) = \left\{ \begin{array}{l} \hat{\boldsymbol{\epsilon}}^e_{n+1} - \hat{\boldsymbol{\epsilon}}^{e\,,tr}_{n+1} + \Delta\gamma\, \hat{\mathbf{g}} \\ \boldsymbol{\kappa}_{n+1} - \tilde{\boldsymbol{\kappa}}(\boldsymbol{\sigma}_{n+1}, \boldsymbol{\epsilon}^p_{n+1}, \Delta\gamma) \\ F(\boldsymbol{\sigma}_{n+1}, \boldsymbol{\kappa}_{n+1}) \end{array} \right\} \ , \tag{3.23}$$

where the residual vector is obtained from Equations (3.18) and (3.19), as well as the yield condition. The first entry in $\mathbf{r}(\mathbf{x})$ uses Equation (3.18) and the relations

$$\boldsymbol{\epsilon}^e_{n+1} = \mathbb{C}^{e^{-1}} : \boldsymbol{\sigma}_{n+1} := \mathbb{D}^e : \boldsymbol{\sigma}_{n+1} \qquad \text{and} \qquad \boldsymbol{\epsilon}^{e\,,tr}_{n+1} = \mathbb{D}^e : \boldsymbol{\sigma}^{tr}_{n+1} \tag{3.24}$$

to formulate a residual equation relating the elastic strain to the plastic increment. Here the elastic compliance tensor, $\mathbb{D}^e$, is introduced and is the inverse of the elastic constitutive tensor.

The Newton-Raphson procedure also relies on the local Jacobian of the system. In this case the Jacobian is denoted $\mathbf{J}$ and takes the form

$$\mathbf{J}(\mathbf{x}) = \left[\frac{\partial \mathbf{r}}{\partial \mathbf{x}} \right] = \left[\begin{array}{ccc} [\mathbb{D}^e] + \Delta\gamma \left[\frac{\partial^2 G}{\partial \boldsymbol{\sigma} \otimes \partial \boldsymbol{\sigma}} \right] & \Delta\gamma \left[\frac{\partial \hat{\mathbf{g}}}{\partial \boldsymbol{\kappa}} \right] & \hat{\mathbf{g}} \\ - \left[\frac{\partial \tilde{\boldsymbol{\kappa}}}{\partial \boldsymbol{\sigma}} \right]^T & [\mathbf{1}_{n_{\boldsymbol{\kappa}}}] & - \left\{ \frac{\partial \tilde{\boldsymbol{\kappa}}}{\partial \Delta\gamma} \right\} \\ \hat{\mathbf{f}}^T & \left\{ \frac{\partial F}{\partial \boldsymbol{\kappa}} \right\}^T & 0 \end{array} \right] \ . \tag{3.25}$$

In general these are not common derivatives. They are case specific and can require the notion of a directional derivative and other techniques to evaluate. The term $[\mathbf{1}_{n_{\boldsymbol{\kappa}}}]$ is a square identity matrix of dimension $n_{\boldsymbol{\kappa}} \times n_{\boldsymbol{\kappa}}$, where $n_{\boldsymbol{\kappa}}$ is the length of the vector $\boldsymbol{\kappa}$. The

Table 3.2: Newton-Raphson iteration scheme.

1. Establish guess/initial values for unknowns: $\mathbf{x}^0$
2. Compute initial residual vector: $\mathbf{r}(\mathbf{x}^0)$
3. Set iteration counter: $k = 0$
4. While (Convergence Check) > Tolerance:
   (a) Compute Jacobian matrix: $\mathbf{J}(\mathbf{x}^k)$
   (b) Compute change in unknown values: $\Delta\mathbf{x} = -\mathbf{J}(\mathbf{x}^k)^{-1} \cdot \mathbf{r}(\mathbf{x}^k)$
   (c) Update unknown values: $\mathbf{x}^{k+1} = \mathbf{x}^k + \Delta\mathbf{x}$
   (d) Compute residual vector: $\mathbf{r}(\mathbf{x}^{k+1})$
   (e) Set $k = k + 1$

Table 3.3: Strain-driven return mapping algorithm for small deformation theory.

1. Compute the trial elastic strain: $\boldsymbol{\epsilon}^{e\,,tr}_{n+1} = \boldsymbol{\epsilon}_n - \boldsymbol{\epsilon}^p_n + \Delta\boldsymbol{\epsilon}$.
2. Compute the trial stress: $\boldsymbol{\sigma}^{tr}_{n+1} = \mathbb{C}^e : \boldsymbol{\epsilon}^{e\,,tr}_{n+1}$
3. Determine loading condition from yield function.

   If $F(\boldsymbol{\sigma}^{tr}_{n+1}, \boldsymbol{\kappa}_n) < 0$:

   Elastic response
   (a) Update Stress: $\boldsymbol{\sigma}_{n+1} = \boldsymbol{\sigma}^{tr}_{n+1}$
   (b) Update hardening variables: $\boldsymbol{\kappa}_{n+1} = \boldsymbol{\kappa}_n$
   (c) Set plastic increment: $\Delta\gamma = 0$

   Else:

   Plastic loading
   (a) Perform iteration as outlined in Table 3.2 using Equations (3.23) and (3.25)
   (b) Update $\boldsymbol{\sigma}_{n+1}$, $\boldsymbol{\kappa}_{n+1}$ and $\Delta\gamma$ with the values from the converged $\mathbf{x}^k$ vector.
   (c) Update $\boldsymbol{\varepsilon}^p_{n+1}$ using flow rule and $\Delta\gamma$.

iteration procedure is outlined in Table 3.2. The Convergence Check noted in this table is frequently a function of the residual vector. Sample target values are the L_2 vector-norm of the residual or the relative *change* in the residual vector as a percentage of some initial error. The strictness of the tolerance is can be related to which Convergence Check is used.

The iteration scheme outlined in Table 3.2 may fail for certain hardening laws, particularly those with hardening followed by softening. Convergence issues can arise near inflection points in the residual functions, or when the derivative of the residual terms approaches zero. One potential solution strategy for these cases is outlined shortly in Section 3.3.

The steps of the general return mapping algorithm are listed in Table 3.3. These steps apply only for the case of small deformation theory. The first two steps freeze the plastic flow and utilize the trial state. The yield function is evaluated under this assumption. If the elastic criterion is satisfied ($F < 0$) then the material response is elastic and the trial

values are used as the updated state for stress and elastic strain. If the elastic yield criterion is not satisfied, then the Newton-Raphson iteration procedure outlined in Table 3.2 must be performed to determine the converged value of $\mathbf{x}^k$, and hence the updated values for $\boldsymbol{\sigma}_{n+1}$, $\boldsymbol{\kappa}_{n+1}$ and $\Delta\gamma$.

The next subsection investigates the extension of the return mapping strategy for finite strain measures. The structure of the algorithm is similar to that presented in Table 3.3—permitting a seamless incorporation of both infinitesimal and finite deformation measures into a single framework.

3.2.2 Finite Deformation

There are several finite deformation measures that can be used to characterize the deformed material state; see, e.g., Malvern (1969); Holzapfel (2000). Such measures become necessary when the norm of displacement gradient is no longer small when compared to unity. Unlike small deformation theory, finite strain theories can be formulated in either the initial *or* deformed configuration. As such, there are typically additional complexities associated with constitutive laws and care must be taken to ensure frame indifference and objectivity; e.g., Truesdell and Noll (1965); Marsden and Hughes (1983). A full discussion of these topics is largely beyond the scope of this work. Here the emphasis is placed on the development and application of the left Cauchy-Green deformation tensor

$$\mathbf{b} = \mathbf{F} \cdot \mathbf{F}^T \ , \tag{3.26}$$

where $\mathbf{F}$ is the deformation gradient. With appropriate manipulations this deformation measure provides the basis for a return mapping algorithm that is remarkably similar to the framework presented for small deformation measures.

General formulation

The simplicity of the small deformation return map algorithm[3] provided in Table 3.3 is due primarily to the additive decomposition of the deformation measure, i.e., the split outlined in Equation (3.11). For finite deformations such a split is not permissible—the formulation instead must rely on multiplicative decomposition of the tensor quantity in question. The deformation gradient is decomposed using

$$\mathbf{F} = \mathbf{v} \cdot \mathbf{R} = \mathbf{F}^e \cdot \mathbf{F}^p \ , \tag{3.27}$$

[3]This statement is intended in a relative sense. A majority of the general populace likely perceive the return mapping algorithm to be quite complex regardless of which deformation measure is used.

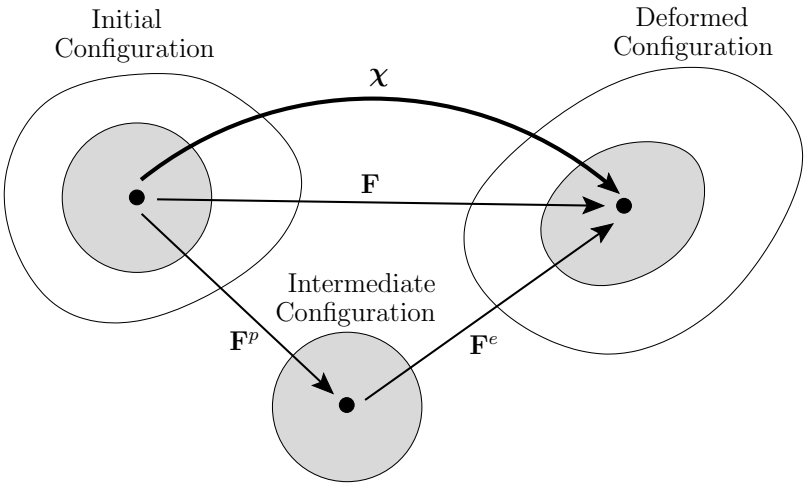

Figure 3.1: Multiplicative decomposition of the deformation gradient.

where $\mathbf{v}$ is the left stretch tensor and $\mathbf{R}$ is a rigid body rotation that satisfies the relation $\mathbf{R} \cdot \mathbf{R}^T = \mathbf{1}$ (Malvern, 1969; Geers et al., 2000) . The left stretch tensor operating on a set of vectors will induce a stretch or contraction and, in general, a rotation. A crucial exception to this is when the vectors themselves are coincident with the principal directions of $\mathbf{v}$ (Malvern, 1969; Holzapfel, 2000). For these special cases only a stretch or contraction will occur (i.e., no rotation). The other two tensors, $\mathbf{F}^p$ and $\mathbf{F}^e$, are the purely plastic and purely elastic portions of the deformation gradient, respectively. The split introduced in Equation $(3.27)_2$ implies the existence of an intermediate, stress-free configuration comprised entirely of plastic deformation. This is because the stress is only related to elastic deformations. The final deformed configuration is realized as a purely elastic mapping from the intermediate configuration (Simo, 1988; Geers et al., 2000). Since this statement is a bit abstract Figure 3.1 provides a schematic of the elastic-plastic multiplicative decomposition described above, in which the $\mathbf{F}$ is a linear map and $\boldsymbol{\chi}$ represents a general, non-linear motion.

Using Equation (3.27) the left Cauchy-Green deformation tensor is expressed in a multitude of ways:

$$\mathbf{b} = \mathbf{F} \cdot \mathbf{F}^T = \mathbf{v} \cdot \mathbf{R} \cdot \mathbf{R}^T \cdot \mathbf{v}^T = \mathbf{F}^e \cdot \mathbf{F}^p \cdot \mathbf{F}^{p,T} \cdot \mathbf{F}^{e,T} \ . \tag{3.28}$$

In light of the previously stated aspect of the rotation tensor, $\mathbf{R} \cdot \mathbf{R}^T = \mathbf{1}$, and the fact that $\mathbf{v}$ is symmetric and positive definite (Malvern, 1969), the important relation

$$\mathbf{b} = \mathbf{v}^2 \tag{3.29}$$

is identified. The left Cauchy-Green deformation tensor also has an elastic and plastic

portion; the former is related to the elastic portion of stretches $\mathbf{v}$—as well as $\mathbf{F}^e$—and given by

$$\mathbf{b}^e = \mathbf{F}^e \cdot \mathbf{F}^{e,T} . \tag{3.30}$$

As discussed at earlier, the principal stretches/contractions are not rotated by successive applications of the stretch tensor $\mathbf{v}$. As such, it is beneficial to write the tensor $\mathbf{b}^e$ as a polar decomposition of eigenvalues, b_i^e, and eigenvectors, $\mathbf{n}^{(i)}$:

$$\mathbf{b}^e = \sum_i^3 b_i^e \, \mathbf{m}^{(i)} \qquad \text{where} \qquad \mathbf{m}^{(i)} = \mathbf{n}^{(i)} \otimes \mathbf{n}^{(i)} . \tag{3.31}$$

This allows a useful relationship between the principal values of the elastic stretches, λ_i, and the elastic components, b_i^e, to be established via Equation (3.29) as

$$b_i^e = \lambda_i^2 . \tag{3.32}$$

At this point a temporary digression is made to discuss yet another strain measure, the *natural* or *Hencky* strain which is cast in terms of the principal stretches

$$\varepsilon_i^e = \log \lambda_i . \tag{3.33}$$

This measure is part of a larger family of generalized strain measures that encompass both the initial and deformed configurations and was introduced by Seth (1961) and Hill (1968a,b, 1970). It proves convenient in classifying the elasto-plastic response of a given material, particularly in the context of a numerical integration scheme (Simo et al., 1993; Simo, 1998; Holzapfel, 2000). Moreover, when taking into account the influence of the strain path, it can be shown that the natural strain provides the correct measure when the deformation takes place as a series of incremental strains—as is the case for a strain driven problem (Rees, 2006).

The natural strain tensor is obtained from the elastic deformation measure $\mathbf{b}^e$ by combining Equations (3.32) and (3.33) and by exploiting the properties of logarithmic functions. The net result is a tensor of the form

$$\boldsymbol{\varepsilon}^e = \frac{1}{2} \log \mathbf{b} = \sum_i^3 \frac{1}{2} \log b_i^e \, \mathbf{m}^{(i)} . \tag{3.34}$$

Both tensors $\mathbf{b}^e$ and $\boldsymbol{\varepsilon}^e$ are with respect to the deformed configuration in Figure 3.1. In Section 3.3 the benefits of using a logarithmic strain measure will become more apparent as specific forms of the elastic tensor $\mathbb{C}^e$ are selected. Prior to that, however, is the discussion of the return mapping integration algorithm for finite deformation elasto-plasticity.

Implementation

The implementation procedure for the return mapping algorithm is similar to the steps outlined in Table 3.3. The final goal of the integration algorithm remains the same—to determine the state variables at time t_{n+1} from the known state at time t_n—however, there are some key differences. Since the given strain increment can no longer be additively decomposed for finite deformations, it is necessary to *push forward* values at time t_n to time t_{n+1}. This is accomplished via the incremental deformation gradient, $\tilde{\mathbf{f}}$. A trial elastic state is obtained using the push forward operation applied to the last converged value of the elastic deformation measure, $\mathbf{b}_n$ as

$$\mathbf{b}_{n+1}^{e\,,tr} = \tilde{\mathbf{f}}\,\mathbf{b}_n^e\,\tilde{\mathbf{f}}^T\,. \tag{3.35}$$

This trial elastic left Cauchy-Green tensor corresponds directly to a trial elastic Hencky strain tensor via Equation (3.34), i.e.,

$$\boldsymbol{\varepsilon}_{n+1}^{e\,,tr} = \sum_i^3 \frac{1}{2}\,\log b_i^{e\,,tr}\,\mathbf{m}^{tr(i)}\,. \tag{3.36}$$

A convenient stress measure commonly used in finite deformation is the Kirchhoff stress, $\boldsymbol{\tau}$, which differs from the Cauchy stress by the volume ratio J as

$$\boldsymbol{\tau} = J\,\boldsymbol{\sigma} \qquad \text{where} \qquad J = \det\mathbf{F}\,. \tag{3.37}$$

Since it is necessary to decompose $\mathbf{b}^e$ into the principal values and directions b_i^e and $\mathbf{n}^{(i)}$, respectively, it is computationally efficient—not to mention necessary from a formulation standpoint—to work with only the principal values of the tensor quantities in question. In doing so the yield function and plastic potential are cast in terms of principal Kirchhoff stress values as opposed to the general stress measure presented in Equation (3.3). This means the following notational tweaks must also be applied in order to remain consistent:

$$\mathbf{f} = \frac{\partial F}{\partial \boldsymbol{\tau}} \Longrightarrow \hat{\mathbf{f}} = \left\{ \frac{\partial F}{\partial \tau_1}\,,\, \frac{\partial F}{\partial \tau_2}\,,\, \frac{\partial F}{\partial \tau_3} \right\}^T \tag{3.38}$$

and

$$\mathbf{g} = \frac{\partial G}{\partial \boldsymbol{\tau}} \Longrightarrow \hat{\mathbf{g}} = \left\{ \frac{\partial G}{\partial \tau_1}\,,\, \frac{\partial G}{\partial \tau_2}\,,\, \frac{\partial G}{\partial \tau_3} \right\}^T\,, \tag{3.39}$$

where the hat ($\hat{\bullet}$) notation has been used to specify a vector in principal space, i.e.,

$$\hat{\bullet} = \{\,\bullet\,\} = \{\,\bullet_1\,,\,\bullet_2\,,\,\bullet_3\,\}^T\,. \tag{3.40}$$

Using this notation the vector of unknowns, $\mathbf{x}$, and the residual vector, $\mathbf{r}(\mathbf{x})$, for use in a Newton-Raphson iteration scheme take the form

$$\mathbf{x} = \left\{ \begin{array}{c} \hat{\boldsymbol{\tau}}_{n+1} \\ \boldsymbol{\kappa}_{n+1} \\ \Delta\gamma \end{array} \right\} \qquad \text{and} \qquad \mathbf{r}(\mathbf{x}) = \left\{ \begin{array}{l} \hat{\boldsymbol{\varepsilon}}^{e}_{n+1} - \hat{\boldsymbol{\varepsilon}}^{e,tr}_{n+1} + \Delta\gamma\, \hat{\mathbf{g}} \\ \boldsymbol{\kappa}_{n+1} - \tilde{\boldsymbol{\kappa}}(\hat{\boldsymbol{\tau}}_{n+1}, \hat{\boldsymbol{\varepsilon}}^{p}_{n+1}, \Delta\gamma) \\ F(\hat{\boldsymbol{\tau}}_{n+1}, \boldsymbol{\kappa}_{n+1}) \end{array} \right\} . \tag{3.41}$$

It is quite tempting to interpret the first entry of the residual vector in Equation $(3.41)_2$ as simply a sum (or additive) decomposition of the plastic and elastic portions of the natural strain as was done for the small deformation return mapping algorithm. This, however, is not the case. Instead, $\hat{\boldsymbol{\varepsilon}}^{e,tr}_{n+1}$ is regarded as the push forward to the deformed configuration and the term $\Delta\gamma\, \hat{\mathbf{g}}$ represents the corrected plastic increment in the deformed configuration of Figure 3.1. Additional details of this transformation are provided in Truesdell and Noll (1965); Marsden and Hughes (1983). The corresponding Jacobian matrix to $\mathbf{x}$ and $\mathbf{r}(\mathbf{x})$ for finite strain measures is

$$\mathbf{J}(\mathbf{x}) = \left[\frac{\partial \mathbf{r}}{\partial \mathbf{x}} \right] = \left[\begin{array}{ccc} [\mathbb{D}^{e}_{d}] + \Delta\gamma \left[\frac{\partial^2 G}{\partial \hat{\boldsymbol{\tau}} \otimes \partial \hat{\boldsymbol{\tau}}} \right] & \Delta\gamma \left[\frac{\partial \hat{\mathbf{g}}}{\partial \boldsymbol{\kappa}} \right] & \hat{\mathbf{g}} \\ - \left[\frac{\partial \tilde{\boldsymbol{\kappa}}}{\partial \hat{\boldsymbol{\tau}}} \right]^{T} & [\mathbf{1}_{n_{\boldsymbol{\kappa}}}] & - \left\{ \frac{\partial \tilde{\boldsymbol{\kappa}}}{\partial \Delta\gamma} \right\} \\ \hat{\mathbf{f}}^{T} & \left\{ \frac{\partial F}{\partial \boldsymbol{\kappa}} \right\}^{T} & 0 \end{array} \right] , \tag{3.42}$$

where $[\mathbb{D}^{e}_{d}]$ is the portion of the elastic compliance matrix $[\mathbb{D}^{e}]$ that corresponds to the principal values.

These definitions motivate the algorithm listed in Table 3.4. This algorithm is suitable for large deformation analysis of isotropic solids. As an important side note, this algorithm relies on the fact that $\boldsymbol{\varepsilon}^{e,tr}_{n+1}$, $\boldsymbol{\varepsilon}^{e}_{n+1}$, $\boldsymbol{\tau}^{tr}_{n+1}$ and $\boldsymbol{\tau}_{n+1}$ are all coaxial for an isotropic solid, that is, the principal directions are specified by the same basis vectors $\mathbf{m}^{tr(i)} = \mathbf{n}^{tr(i)} \otimes \mathbf{n}^{tr(i)}$. This key relationship is noted in several sources, e.g., Truesdell and Noll (1965); Malvern (1969).

The return mapping algorithms for infinitesimal and finite deformations are quite similar as can be seen by comparing Tables 3.3 and 3.4. Several families of material models intended to capture a wide range of natural phenomena can be obtained by specifying the ingredients at the beginning of this section and following the procedures outlined herein. Prior to investigating specific material models a side tour is taken to discuss additional implementation considerations, notation, and key relationships.

3.3 General Considerations

An attempt has been made thus far to present the basic equations needed for the return mapping algorithms of Tables 3.3 and 3.4. In this section additional considerations that

Table 3.4: Strain-driven return mapping algorithm for finite deformation theory.

1. Compute the trial elastic left Cauchy-Green tensor: $\mathbf{b}^{e\,,tr}_{n+1} = \tilde{\mathbf{f}} \cdot \mathbf{b}^{e}_{n} \cdot \tilde{\mathbf{f}}^{T}$
2. Perform the spectral decomposition: $\mathbf{b}^{e\,,tr}_{n+1} = \sum_i^3 \; b_i^{e\,,tr}\, \mathbf{m}^{tr(i)}$
3. Compute the trial elastic Hencky strain: $\boldsymbol{\varepsilon}^{e\,,tr}_{n+1} = \sum_i^3 \; \frac{1}{2} \log b_i^{e\,,tr}\, \mathbf{m}^{tr(i)}$
4. Compute the trial stress: $\hat{\boldsymbol{\tau}}^{tr}_{n+1} = [\mathbb{C}^{e}_{d}] \cdot \hat{\boldsymbol{\varepsilon}}^{e\,,tr}_{n+1}$
5. Determine loading condition from yield function.

   If $F(\hat{\boldsymbol{\tau}}^{tr}_{n+1}, \boldsymbol{\kappa}_n) < 0$:

   Elastic response

   (a) Update Stress: $\hat{\boldsymbol{\tau}}_{n+1} = \hat{\boldsymbol{\tau}}^{tr}_{n+1}$

   (b) Update hardening variables: $\boldsymbol{\kappa}_{n+1} = \boldsymbol{\kappa}_n$

   (c) Set plastic increment: $\Delta\gamma = 0$

   Else:

   Plastic loading

   (a) Perform iteration outlined in Table 3.2 using Equations (3.41) and (3.42)

   (b) Update $\hat{\boldsymbol{\tau}}_{n+1}$, $\boldsymbol{\kappa}_{n+1}$ and $\Delta\gamma$ with the values from the converged $\mathbf{x}^k$ vector.

   (c) Compute the elastic left Cauchy-Green tensor: $\mathbf{b}^{e}_{n+1} = \sum_i^3 \; 2 \exp \varepsilon^{e}_{i,n+1}\, \mathbf{m}^{tr(i)}$

   (d) Compute the full Kirchhoff stress tensor: $\boldsymbol{\tau}_{n+1} = \sum_i^3 \; \tau_i\, \mathbf{m}^{tr(i)}$

apply to both small and finite deformation theories are discussed.

3.3.1 The 4^{th} Order Elasticity Tensor

Very little discussion has been dedicated to the specific form of the 4^{th} order elasticity tensor $\mathbb{C}^e$. In the present discussion this tensor is derived from a mass specific *strain energy function*, $\bar{\psi}$, which itself is part of a larger framework dedicated to thermodynamically consistent constitutive equations. For additional discussion regarding materials in the context of thermodynamics see Holzapfel (2000) and the references therein.

In order to obtain a definitive $\mathbb{C}^e$ it is first necessary to investigate the relationship between stress measures and the strain energy function. At a bare minimum it is sufficient to say that the Kirchhoff stress can be expressed as

$$\boldsymbol{\tau} = \rho_0 \, \frac{\partial \bar{\psi}}{\partial \boldsymbol{\varepsilon}} \tag{3.43}$$

where ρ_0 is the initial mass density of the material and $\boldsymbol{\varepsilon}$ is a general strain measure associated with the deformed configuration. The Cauchy stress is obtained in light of Equations (3.37) and (3.43) and the density relation $\rho_0 = J\,\rho$ via

$$\boldsymbol{\sigma} = \rho \, \frac{\partial \bar{\psi}}{\partial \boldsymbol{\varepsilon}} \,, \tag{3.44}$$

implying both stress measures may be obtained from the same free energy function. A very common choice for the free energy function is the following mass specific form

$$\bar{\psi} = \frac{1}{2}\left(\bar{K} - \frac{2}{3}\bar{G}\right)\mathrm{tr}(\boldsymbol{\varepsilon})^2 + \bar{G}\,\mathrm{tr}(\boldsymbol{\varepsilon}^2)\ , \tag{3.45}$$

where $\bar{K} = K/\rho_0$ is the mass specific bulk modulus and $\bar{G} = G/\rho_0$ is the mass specific shear modulus. The isotropic, linear-elastic material stiffness tensor follows as

$$\mathbb{C}^e = \frac{\partial^2 \bar{\psi}}{\partial \boldsymbol{\varepsilon} \otimes \partial \boldsymbol{\varepsilon}} = \bar{K}\,\mathbf{1} \otimes \mathbf{1} + \bar{G}\left(\mathbb{I} - \frac{1}{3}\mathbf{1} \otimes \mathbf{1}\right)\ , \tag{3.46}$$

where $\mathbf{1}$ is the second order identity tensor while $\mathbb{I}$ is the symmetric fourth order identity tensor. The compliance matrix is

$$\mathbb{C}^{e^{-1}} = \mathbb{D}^e = \frac{1}{9\bar{K}}\,\mathbf{1} \otimes \mathbf{1} + \frac{1}{2\bar{G}}\left(\mathbb{I} - \frac{1}{3}\mathbf{1} \otimes \mathbf{1}\right)\ . \tag{3.47}$$

The matrix representation for $[\mathbb{C}^e]$ and $[\mathbb{D}^e]$) is typically a compressed 6x6 square matrix that operates on the vector representation of second order tensors—e.g, see Equation (3.20). There are associated pitfalls related to such storage schemes that must be avoided in a numerical implementation. The paper by Helnwein (2001) provides clarification on this matter and identifies appropriate strain and stress-like vector representations, as well as the appropriate matrix representations for $[\mathbb{C}^e]$ and $[\mathbb{D}^e]$.

3.3.2 Special Cases

At some point it becomes necessary to introduce special cases or modifications that cannot be cast in the general framework or can make the general framework cumbersome and unnecessarily complex. Two such cases are discussed in this sub-section. The first is those cases that have no material hardening laws. The second portion is reserved for simplified material models and/or hardening laws that solve for the unknown plastic increment, $\Delta\gamma$, without the iteration procedure described in Table 3.2.

No Material Hardening

For some materials it is sufficient to prescribe only a yield function and plastic potential. The material hardening laws are not used. In such cases the response is referred to as perfectly plastic, i.e., the mechanical properties of the material in question are indifferent to continuous and excessive plastic deformations. In general this reduces the length of the unknown and residual vectors, as well as the size of the Jacobian matrices.

For small strain measures the absence of material hardening leads to a simplified unknown vector, $\mathbf{x}$, and residual vector, $\mathbf{r}(\mathbf{x})$:

$$\mathbf{x} = \left\{ \begin{array}{c} \hat{\boldsymbol{\sigma}}_{n+1} \\ \Delta\gamma \end{array} \right\} \qquad \text{and} \qquad \mathbf{r}(\mathbf{x}) = \left\{ \begin{array}{c} \hat{\boldsymbol{\epsilon}}^{e}_{n+1} - \hat{\boldsymbol{\epsilon}}^{e,tr}_{n+1} + \Delta\gamma\,\hat{\mathbf{g}} \\ F(\boldsymbol{\sigma}_{n+1}, \boldsymbol{\kappa}_{n+1}) \end{array} \right\} . \tag{3.48}$$

The corresponding Jacobian matrix is reduced to

$$\mathbf{J}(\mathbf{x}) = \left[\frac{\partial \mathbf{r}}{\partial \mathbf{x}}\right] = \left[\begin{array}{cc} [\mathbb{D}^{e}] + \Delta\gamma \left[\frac{\partial^2 G}{\partial \boldsymbol{\sigma} \otimes \partial \boldsymbol{\sigma}}\right] & \hat{\mathbf{g}} \\ \hat{\mathbf{f}}^{T} & 0 \end{array} \right] , \tag{3.49}$$

in which all rows and columns related to material hardening have been removed. The large deformation return mapping strategy follows suit and yields

$$\mathbf{x} = \left\{ \begin{array}{c} \hat{\boldsymbol{\tau}}_{n+1} \\ \Delta\gamma \end{array} \right\} \qquad \text{and} \qquad \mathbf{r}(\mathbf{x}) = \left\{ \begin{array}{c} \hat{\boldsymbol{\varepsilon}}^{e}_{n+1} - \hat{\boldsymbol{\varepsilon}}^{e,tr}_{n+1} + \Delta\gamma\,\hat{\mathbf{g}} \\ F(\hat{\boldsymbol{\tau}}_{n+1}, \boldsymbol{\kappa}_{n+1}) \end{array} \right\} . \tag{3.50}$$

for the unknown and residual vectors, $\mathbf{x}$ and $\mathbf{r}(\mathbf{x})$, respectively. For this case the Jacobian matrix reads

$$[\mathbf{J}(\mathbf{x})] = \left[\frac{\partial \mathbf{r}}{\partial \mathbf{x}}\right] = \left[\begin{array}{cc} [\mathbb{D}^{e}_{d}] + \Delta\gamma \left[\frac{\partial^2 G}{\partial \hat{\boldsymbol{\tau}} \otimes \partial \hat{\boldsymbol{\tau}}}\right] & \hat{\mathbf{g}} \\ \hat{\mathbf{f}}^{T} & 0 \end{array} \right] . \tag{3.51}$$

Using these reduced definitions the return mapping algorithm listed in Tables 3.2 or 3.4 can be used without additional modification. From a computational standpoint this smaller system can be significantly easier to work with.

Simplified Material Models

In several instances it is simply not necessary to perform the Newton-Raphson iteration described in this chapter. While the algorithm will work, it is inefficient from a computational standpoint since it is possible to solve for the plastic increment $\Delta\gamma$ by other means. This is the case for three of the models presented herein, namely the J_2 model of Section 3.5 and two of the Drucker-Prager models in Section 3.6. The alternative solution methods will be outlined as each of these models is introduced.

3.3.3 A Semi-Implicit Return Mapping Scheme

The integration algorithms presented thus far assume an implicit time integration scheme. During optimal conditions the return mapping strategy can be shown to achieve quadratic rate of asymptotic convergence with at least first order accuracy and exhibit unconditional

stability (Simo, 1998; Simo and Hughes, 1998). Unfortunately, under less than optimal circumstances hardening and evolution laws can become very complex and may include both hardening/softening as well as non-smooth functions. In these cases convergence issues can arise in the algorithm, and in particular computing the Jacobian matrix in (3.25) and (3.42) becomes problematic. This leads to poor convergence rates and outright divergence of the return mapping algorithm—particularly if a Newton-Raphson solution scheme is utilized to find the roots of the system.

In order to combat these issues a *semi-implicit* return mapping algorithm is introduced by Tu et al. (2009). The algorithm is based on the assumption that the rate of the stress-like plastic hardening variables can be frozen over each time step. The updated hardening variables $\boldsymbol{\kappa}_{n+1}$ are updated *after* a converged value for the stress tensor $\boldsymbol{\sigma}_{n+1}$ (or $\boldsymbol{\tau}_{n+1}$) and plastic increment $\Delta\gamma$ are obtained. In other words, the reduced systems of Equations (3.48)–(3.51) are used in the return mapping strategy with the hardening variables $\boldsymbol{\kappa}_n$ obtained from the previous time step. The updated values $\boldsymbol{\kappa}_{n+1}$ are determined from the converged solution of the reduced system. In this manner the hardening variables lag the stress and plastic deformation by a time step.

In the work by Tu et al. (2009) this algorithm is implemented and tested for smooth and non-smooth evolution laws. Using a series of examples and iso-error maps they show sufficiently that the proposed approach handles the evolution equations and material response both accurately and efficiently. A clear distinction is made for those models in this chapter based on that formulation.

3.4 Notation and Key Relationships

This short section addresses notation and other aspects common to all models presented in this chapter. First and foremost, the symbol $\boldsymbol{\sigma}$ will be used to represent a general stress tensor. This may be the Cauchy stress—as was previously assigned the symbol $\boldsymbol{\sigma}$—but may also represent the Kirchhoff stress previously denoted by $\boldsymbol{\tau}$. The reader is held accountable for understanding the context in which these equations are presented. Two sets of coordinates are discussed in what follows. The principal stress space is denoted by $\{\sigma_1, \sigma_2, \sigma_3\}$. Alternatively, a transformed set of coordinates $\{\xi_1, \xi_2, \xi_3\}$ is used in some figures in which ξ_3 is coaxial with the hydrostatic axis, i.e., $\sigma_1 = \sigma_2 = \sigma_3$. This coordinate transformation means the coordinates $\{\xi_1, \xi_2\}$ reside on the deviatoric plane. Both coordinate systems are shown in Figure A.1. Appendix A outlines a procedure to identify those points in principal stress space that are on the yield surface. This technique is used to generate all surface data depicted in this chapter.

Each yield function and plastic potential appearing in this chapter can be written in terms of the stress invariants, I_1, I_2, and I_3. These are defined in terms of the principal stress values as

$$I_1 = \operatorname{tr}\boldsymbol{\sigma} = \sigma_1 + \sigma_2 + \sigma_3 \ , \tag{3.52}$$

$$I_2 = \frac{1}{2}\left[(\operatorname{tr}\boldsymbol{\sigma})^2 - \operatorname{tr}(\boldsymbol{\sigma}^2)\right] = \sigma_1\,\sigma_2 + \sigma_1\,\sigma_3 + \sigma_2\,\sigma_3 \ , \qquad \text{and} \tag{3.53}$$

$$I_3 = \det\boldsymbol{\sigma} = \sigma_1\,\sigma_2\,\sigma_3 \ . \tag{3.54}$$

An additional parameter, c, is introduced for some models. This allows the yield function or plastic potential to be shifted along the hydrostatic axis. An auxiliary stress, $\bar{\boldsymbol{\sigma}} = \boldsymbol{\sigma} - c\mathbf{1}$, is defined using an overbar symbol. This is not to be confused with the mass-specific notation used previously in other chapters. The shift by c leads to a set of modified invariants $\bar{I}_1, \bar{I}_2$, and $\bar{I}_3$ that are defined in terms of their former selves and c by way of

$$\bar{I}_1 = \operatorname{tr}\bar{\boldsymbol{\sigma}} = \bar{\sigma}_1 + \bar{\sigma}_2 + \bar{\sigma}_3 = I_1 - 3\,c \ , \tag{3.55}$$

$$\bar{I}_2 = \frac{1}{2}\left[(\operatorname{tr}\bar{\boldsymbol{\sigma}})^2 - \operatorname{tr}(\bar{\boldsymbol{\sigma}}^2)\right] = \bar{\sigma}_1\,\bar{\sigma}_2 + \bar{\sigma}_1\,\bar{\sigma}_3 + \bar{\sigma}_2\,\bar{\sigma}_3 = I_2 - 2\,I_1\,c + 3\,c^2 \ , \ \text{and} \tag{3.56}$$

$$\bar{I}_3 = \det\bar{\boldsymbol{\sigma}} = \bar{\sigma}_1\,\bar{\sigma}_2\,\bar{\sigma}_3 = I_3 - I_2\,c + I_1\,c^2 - c^3 \ . \tag{3.57}$$

The deviatoric stress, $\mathbf{s}$, is used extensively in what follows. This tensor is related to the stress tensor and I_1 through

$$\mathbf{s} = \bar{\mathbf{s}} = \boldsymbol{\sigma} - \frac{I_1}{3}\mathbf{1} \ . \tag{3.58}$$

Note that the relation $\bar{\mathbf{s}} = \mathbf{s}$ holds, as the cohesion modifies only the volumetric portion of the tensor. Largely of interest in the material models is the magnitude of the deviatoric stress, $\|\mathbf{s}\|$, which is related to the other invariants by

$$\|\mathbf{s}\|^2 = \mathbf{s} : \mathbf{s} = \frac{2}{3}(I_1^2 - 3\,I_2) \ . \tag{3.59}$$

Both the plastic flow direction, $\mathbf{g}$, and yield surface normal, $\mathbf{f}$, invoke derivatives with respect to the stress tensor. However, both F and G need to be expressed in terms of the invariants—which are themselves a function of the stress tensor. The following differential relations (Wriggers, 2008) are useful in computing said derivatives:

$$dI_1 = \frac{\partial I_1}{\partial\boldsymbol{\sigma}} : d\boldsymbol{\sigma} \Longrightarrow \frac{\partial I_1}{\partial\boldsymbol{\sigma}} = \mathbf{1} \ , \tag{3.60}$$

$$dI_2 = \frac{\partial I_2}{\partial\boldsymbol{\sigma}} : d\boldsymbol{\sigma} \Longrightarrow \frac{\partial I_2}{\partial\boldsymbol{\sigma}} = I_1\,\mathbf{1} - \boldsymbol{\sigma} \ , \ \text{and} \tag{3.61}$$

$$dI_3 = \frac{\partial I_3}{\partial \boldsymbol{\sigma}} : d\boldsymbol{\sigma} \Longrightarrow \frac{\partial I_3}{\partial \boldsymbol{\sigma}} = I_3\, \boldsymbol{\sigma}^{-1} \ . \tag{3.62}$$

In light of the shifted invariant definitions of (3.55)–(3.57), as well as (3.60)–(3.62), the differential of the shifted invariants are

$$d\bar{I}_1 = \frac{\partial \bar{I}_1}{\partial \boldsymbol{\sigma}} : d\boldsymbol{\sigma} \Longrightarrow \frac{\partial \bar{I}_1}{\partial \boldsymbol{\sigma}} = \mathbf{1} \ , \tag{3.63}$$

$$d\bar{I}_2 = \frac{\partial \bar{I}_2}{\partial \boldsymbol{\sigma}} : d\boldsymbol{\sigma} \Longrightarrow \frac{\partial \bar{I}_2}{\partial \boldsymbol{\sigma}} = I_1\, \mathbf{1} - \boldsymbol{\sigma} - 2\, c\, \mathbf{1} \ , \text{ and} \tag{3.64}$$

$$d\bar{I}_3 = \frac{\partial \bar{I}_3}{\partial \boldsymbol{\sigma}} : d\boldsymbol{\sigma} \Longrightarrow \frac{\partial \bar{I}_3}{\partial \boldsymbol{\sigma}} = I_3\, \boldsymbol{\sigma}^{-1} - c\,(I_1\, \mathbf{1} - \boldsymbol{\sigma}) + c^2\, \mathbf{1} \ . \tag{3.65}$$

With respect to the deviatoric stress two useful relationships are

$$d\mathbf{s} = \frac{\partial \mathbf{s}}{\partial \boldsymbol{\sigma}} : d\boldsymbol{\sigma} \Longrightarrow \frac{\partial \mathbf{s}}{\partial \boldsymbol{\sigma}} = \mathbb{I} - \frac{1}{3}\mathbf{1} \otimes \mathbf{1} = \mathbb{I}_{dev} \ \text{ and} \tag{3.66}$$

$$d\|\mathbf{s}\| = \frac{\partial \|\mathbf{s}\|}{\partial \boldsymbol{\sigma}} : d\boldsymbol{\sigma} \Longrightarrow \frac{\partial \|\mathbf{s}\|}{\partial \boldsymbol{\sigma}} = \frac{\mathbf{s}}{\|\mathbf{s}\|} \ , \tag{3.67}$$

and finally, the derivative of the inverse stress tensor can be determined (Wriggers, 2008) as

$$\left(\frac{\partial \boldsymbol{\sigma}^{-1}}{\partial \boldsymbol{\sigma}} \right)_{iklm} = -\frac{1}{2} \left(\sigma_{il}^{-1}\, \sigma_{mk}^{-1} + \sigma_{im}^{-1}\, \sigma_{lk}^{-1} \right) \ . \tag{3.68}$$

Here index notation is used and the free indices i, k, l, and m range from 1–3. The remainder of this chapter is dedicated to the presentation of multiple material models that utilize many of the relations given in this section. These models are presented and implemented in a framework consistent with the MPM. The explicit nature of the MPM does not require/use the consistent elasto-plastic tangent operator, $\mathbb{C}^{ep}$. Therefore, the formulation of the tangent operator is omitted in the following discussions.

3.5 J_2 Material Model

The J_2 material model predicts material failure when the second invariant of the deviatoric stress tensor reaches a critical value. Of the many nonlinear material models and failure theories, the J_2 theory is perhaps the simplest from a formulation and implementation standpoint. Yet, despite the simplicity, this yield condition accurately replicates the mechanical response of a wide variety of materials.

The yield function and plastic potential are written in terms of the stress and stress-like hardening variables as

$$F(\boldsymbol{\eta}, \boldsymbol{\kappa}^{kin}, \kappa^{iso}) = G(\boldsymbol{\eta}, \boldsymbol{\kappa}^{kin}, \kappa^{iso}) = \|\boldsymbol{\eta}\| + \sigma_Y^{Eff} \tag{3.69}$$

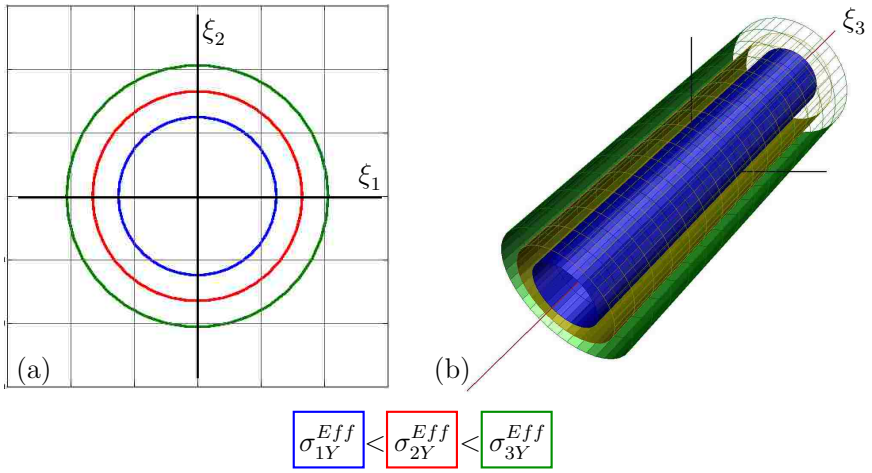

Figure 3.2: J_2 yield surface.

where

$$\boldsymbol{\eta} = \mathbf{s} + \boldsymbol{\kappa}^{kin} \qquad \text{and} \qquad \sigma_Y^{Eff} = \sqrt{\frac{2}{3}} \left(\kappa^{iso} - \sigma_Y \right) \ . \tag{3.70}$$

In the literature $\boldsymbol{\kappa}^{kin}$ is often referred to as the back stress tensor. The present formulation uses the kinematic hardening function

$$\boldsymbol{\kappa}^{kin} = \tilde{\boldsymbol{\kappa}}^{kin}(\boldsymbol{\alpha}^{kin}) = -\frac{2}{3} H \, \mathrm{dev}(\boldsymbol{\alpha}^{kin}) \tag{3.71}$$

where H is the kinematic hardening modulus and $\boldsymbol{\alpha}^{kin}$ is a strain-like kinematic hardening variable with a prescribed evolution law (more on this shortly). Listing (3.71) implies a linear relationship linking the strain-like variable $\boldsymbol{\alpha}^{kin}$ and the back stress term. This is not a requirement and more complex expressions could be derived. In the present case $\boldsymbol{\kappa}^{kin}$ and is purely deviatoric. The isotropic hardening function $\kappa^{iso} = \tilde{\kappa}^{iso}(\alpha^{iso})$ relies on the strain-like hardening variable α^{iso}. Here a linear relationship is used as

$$\kappa^{iso} = \tilde{\kappa}^{iso}(\alpha^{iso}) = -k\alpha^{iso} \ , \tag{3.72}$$

where k is the isotropic hardening modulus. Again, a linear relationship is not a requirement for this formulation.

Visually this yield condition creates a cylindrical surface in principal stress space, centered about the hydrostatic axis as depicted in Figure 3.2(b). Recall that ξ_3 is coaxial with the hydrostatic axis. The role of the hardening terms is determined by examining different cuts in either the deviatoric plane $\{\xi_1, \xi_2\}$ as seen in Figure 3.2(a). The concentric circular rings or ellipses are obtained by increasing the effective yield stress and examining cuts through the yield surface at a given ξ_3. The increase in effective yield stress may be

interpreted *either* as three separate materials, each with a larger yield stress, σ_Y, *or* a single material that accumulates isotropic hardening through plastic deformation. Either way the net result is a cylindrical surface whose radius grows perpendicular to the hydrostatic axis. The back stress, $\boldsymbol{\kappa}^{kin}$, shifts/translates the yield surface about the hydrostatic axis (not pictured).

As hinted above the strain-like terms follow from a prescribed hardening law. The updated values at time t_{n+1} are obtained by time integration of the prescribed hardening laws. Algorithmically these are expressed as

$$\boldsymbol{\alpha}^{kin}_{n+1} = \boldsymbol{\alpha}^{kin}_{n} + \Delta\gamma \left.\frac{\partial F}{\partial \boldsymbol{\kappa}^{kin}}\right|_{n+1} = \boldsymbol{\alpha}^{kin}_{n} + \Delta\gamma \left.\frac{\boldsymbol{\eta}}{\|\boldsymbol{\eta}\|}\right|_{n+1} \tag{3.73}$$

and

$$\alpha^{iso}_{n+1} = \alpha^{iso}_{n} + \Delta\gamma \left.\frac{\partial F}{\partial \alpha^{iso}}\right|_{n+1} = \alpha^{iso}_{n} + \Delta\gamma \left.\sqrt{\frac{2}{3}}\frac{\partial \tilde{\kappa}^{iso}}{\partial \alpha^{iso}}\right|_{n+1} . \tag{3.74}$$

Note that (3.73) follows from the linear kinematic hardening described by (3.71), while listing (3.74) is not yet restricted to a linear isotropic hardening function. This motivates the following definitions for the unknown and residual vectors, $\mathbf{x}$ and $\mathbf{r}(\mathbf{x})$ respectively:

$$\mathbf{x} = \left\{ \begin{array}{c} \hat{\boldsymbol{\sigma}}_{n+1} \\ \hat{\boldsymbol{\alpha}}^{kin}_{n+1} \\ \alpha^{iso}_{n+1} \\ \Delta\gamma \end{array} \right\} \qquad \text{and} \qquad \mathbf{r}(\mathbf{x}) = \left\{ \begin{array}{l} \hat{\boldsymbol{\epsilon}}^{e}_{n+1} - \hat{\boldsymbol{\epsilon}}^{e\,,tr}_{n+1} + \Delta\gamma \left.\frac{\hat{\boldsymbol{\eta}}}{\|\hat{\boldsymbol{\eta}}\|}\right|_{n+1} \\ \Delta\hat{\boldsymbol{\alpha}}^{kin} - \Delta\gamma \left.\frac{\hat{\boldsymbol{\eta}}}{\|\hat{\boldsymbol{\eta}}\|}\right|_{n+1} \\ \Delta\alpha^{iso} - \Delta\gamma \left.\sqrt{\frac{2}{3}}\frac{\partial \tilde{\kappa}^{iso}}{\partial \alpha^{iso}}\right|_{n+1} \\ F(\boldsymbol{\eta}, \boldsymbol{\kappa}^{kin}, \kappa^{iso})\big|_{n+1} \end{array} \right\} , \tag{3.75}$$

from which the corresponding terms in the Jacobian matrix of either (3.25) or (3.42) can be computed.

However, as noted in Section 3.3.2, for some material models it is possible to solve for the plastic increment $\Delta\gamma$ by other means—and that is certainly the case here. Provided the back stress is linearly related to $\boldsymbol{\alpha}^{kin}_{n}$, the relationship

$$\boldsymbol{\eta}_{n+1} = \boldsymbol{\eta}^{tr}_{n+1} - (2G + \frac{2}{3}H)\,\Delta\gamma\,\frac{\boldsymbol{\eta}_{n+1}}{\|\boldsymbol{\eta}_{n+1}\|} \tag{3.76}$$

can be established using $(3.70)_1$ and (3.71). The trial term $\boldsymbol{\eta}^{tr}_{n+1}$ follows from the definition

$$\boldsymbol{\eta}^{tr}_{n+1} = \mathbf{s}^{tr}_{n+1} + \boldsymbol{\kappa}^{kin}_{n} , \tag{3.77}$$

where the notion of a trial state is obtained by assuming the plastic flow is frozen over the time step. Equation (3.76) can be reorganized to read

$$\left[1 + \frac{(2G + \frac{2}{3}H)\,\Delta\gamma}{\|\boldsymbol{\eta}_{n+1}\|}\right]\boldsymbol{\eta}_{n+1} = \boldsymbol{\eta}^{tr}_{n+1} , \tag{3.78}$$

from which it is concluded that $\boldsymbol{\eta}_{n+1}$ is nothing more than a scaled version of $\boldsymbol{\eta}^{tr}_{n+1}$. Thus, the relationship

$$\frac{\boldsymbol{\eta}_{n+1}}{\|\boldsymbol{\eta}_{n+1}\|} = \frac{\boldsymbol{\eta}^{tr}_{n+1}}{\|\boldsymbol{\eta}^{tr}_{n+1}\|} \tag{3.79}$$

is obtained. Considering the consistency condition and the definition of a yield surface ($F = 0$), the following condition is used to solve for the plastic increment $\Delta\gamma$:

$$\begin{aligned} F(\boldsymbol{\eta}, \boldsymbol{\kappa}^{kin}, \kappa^{iso})\Big|_{n+1} &= \|\boldsymbol{\eta}_{n+1}\| + \sqrt{\frac{2}{3}}\,\kappa^{iso} - \sqrt{\frac{2}{3}}\sigma_Y \\ 0 &= \|\boldsymbol{\eta}^{tr}_{n+1}\| - (2G + \frac{2}{3}H)\,\Delta\gamma + \sqrt{\frac{2}{3}}\,\kappa^{iso} - \sqrt{\frac{2}{3}}\sigma_Y \ . \end{aligned} \tag{3.80}$$

In general Equation (3.80) is a non-linear scalar function of $\Delta\gamma$ and an iterative procedure is needed to obtain a solution. This, however, is less demanding from a computational standpoint than the iteration scheme utilizing the full $\mathbf{x}$ and $\mathbf{r}(\mathbf{x})$ vectors defined in (3.75). For the nice case of a linear isotropic hardening law

$$\kappa^{iso} = \tilde{\kappa}^{iso}(\alpha^{iso}) = -k\alpha^{iso} \Longrightarrow \frac{\partial\kappa}{\partial\alpha^{iso}} = -k \ , \tag{3.81}$$

the updated yield condition is modified to read:

$$\begin{aligned} F(\boldsymbol{\eta}, \boldsymbol{\kappa}^{kin}, \kappa^{iso})\Big|_{n+1} &= \|\boldsymbol{\eta}_{n+1}\| - \sqrt{\frac{2}{3}}\,(k\,\alpha^{iso}_{n+1} + \sigma_Y) \\ 0 &= \|\boldsymbol{\eta}^{tr}_{n+1}\| - \sqrt{\frac{2}{3}}(k\,\alpha^{iso}_{n} + \sigma_Y) - (2G + \frac{2}{3}H + \frac{2}{3}k)\,\Delta\gamma \\ 0 &= F^{tr}_{n+1} - (2G + \frac{2}{3}H + \frac{2}{3}k)\,\Delta\gamma \ . \end{aligned} \tag{3.82}$$

Equation (3.82) is easily solved for the plastic increment

$$\Delta\gamma = \frac{F^{tr}_{n+1}}{2G + \frac{2}{3}H + \frac{2}{3}k} \ . \tag{3.83}$$

It is important to note that this expression for $\Delta\gamma$ is only realizable from the linear hardening laws assumed for $\boldsymbol{\kappa}^{kin}$ and κ^{iso}. Linear expressions are not a requirement, but as shown above lead to a simple expression for the plastic increment.

The J_2 model presented in this section is well suited for capturing the material response of several materials; in particular ductile metals. Unfortunately the formulation is decoupled from the volumetric portion of the stress tensor as shown in Figure 3.2(b). This limits the applicability of the J_2 model, especially in the context of granular materials and pressure dependent media. In the next few sections alternative models are examined in which the volumetric and deviatoric components of the stress state are directly linked via the yield function.

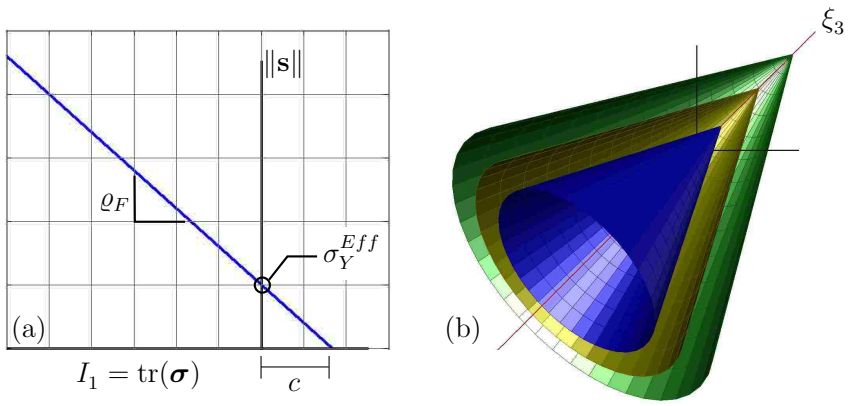

Figure 3.3: Drucker Prager yield surface.

3.6 Two Surface Drucker-Prager Material Models

The Drucker-Prager yield criterion combines the volumetric and deviatoric invariant of the stress tensor. In doing so the mechanical response of pressure-dependent aggregates, composites, and cohesive-frictional materials—such as granular media, can be accurately predicted. In this section three variants of the two surface Drucker-Prager model are presented. The first follows as the more traditional implementation—employing a flat tension cutoff surface near or at the apex of the conic yield surface. The second incorporates a smooth circular cap near the tip to avoid difficulties and numerical instabilities associated with the traditional single surface formulation. The third and final variant handles the hardening/softening response in a slightly different manner than the other two approaches. Each model is investigated in additional detail below.

3.6.1 Traditional Two Surface Drucker-Prager

The yield surface and plastic potential associated with the conic portion of the Drucker-Prager model are

$$F(\boldsymbol{\eta}, \boldsymbol{\kappa}^{kin}, \kappa^{iso}) = \|\boldsymbol{\eta}\| + \varrho_F \, I_1 + \sigma_Y^{Eff} \quad \text{and} \tag{3.84}$$

$$G(\boldsymbol{\eta}, \boldsymbol{\kappa}^{kin}, \kappa^{iso}) = \|\boldsymbol{\eta}\| + \varrho_G \, I_1 + \sigma_Y^{Eff} \ , \tag{3.85}$$

where $\boldsymbol{\eta}$ and the effective yield stress, σ_Y^{Eff}, are defined as they were for the J_2 model in Section 3.5. The terms ϱ_F and ϱ_G are the frictional parameters for the yield function and plastic potential, respectively. In the context of granular media these terms are related to the effective friction angle, ϕ_F, and plastic dilation angle, ψ_G. The volumetric portion of the

stress tensor is defined in Equation (3.52) as $I_1 = \mathrm{tr}(\boldsymbol{\sigma})$. The yield surface corresponding to Equation (3.84) is conic in nature and is depicted in Figure 3.3(b). Concentric conic surfaces are obtained by increasing the effective yield stress. This increase may be interpreted *either* as three separate materials—each with a larger yield stress σ_Y but the same friction parameter ϱ_F, *or* a single material that accumulates isotropic hardening through plastic deformation. Cuts through these surfaces at a given ξ_3 results in concentric rings similar to those depicted in Figure 3.2(a).

The relationship among the model parameters is highlighted in Figure 3.3(a). Here the yield criterion is viewed as a line in the purely deviatoric plane as a function of the stress invariant I_1. The effective slope of the line is the friction parameter ϱ_F, establishing the following relationship

$$c = \frac{\sigma_Y^{Eff}}{\varrho_F} \ . \tag{3.86}$$

The cohesion, c, is a generalized shift along the hydrostatic axis[4]. The cohesion increases without bound and ceases to be a meaningful quantity as the friction parameter tends to zero ($\varrho_F \to 0$). The Drucker-Prager criterion is equivalent to the J_2 criterion presented in Section 3.5 for the limiting case of $\varrho_F = 0$.

For $I_1 \leq c$ the material response is governed by the yield function and plastic potential defined in Equations (3.84) and (3.85). For this model it is assumed that the deviatoric back stress is obtained using the linear relation expressed in (3.71). Isotropic hardening is again described by the function $\kappa^{iso} = \tilde{\kappa}_{iso}(\alpha^{iso})$. These definitions are consistent with those used in the J_2 formulation. Here the unknown and residual vectors, $\mathbf{x}$ and $\mathbf{r}(\mathbf{x})$, follow as

$$\mathbf{x} = \left\{ \begin{array}{c} \hat{\boldsymbol{\sigma}}_{n+1} \\ \hat{\boldsymbol{\alpha}}^{kin}_{n+1} \\ \alpha^{iso}_{n+1} \\ \Delta\gamma \end{array} \right\} \qquad \text{and} \qquad \mathbf{r}(\mathbf{x}) = \left\{ \begin{array}{l} \hat{\boldsymbol{\epsilon}}^{e}_{n+1} - \hat{\boldsymbol{\epsilon}}^{e\,,tr}_{n+1} + \Delta\gamma \left(\frac{\hat{\boldsymbol{\eta}}}{\|\hat{\boldsymbol{\eta}}\|} + \varrho_G \, \mathbf{1} \right)_{n+1} \\ \Delta\hat{\boldsymbol{\alpha}}^{kin} - \Delta\gamma \left. \frac{\hat{\boldsymbol{\eta}}}{\|\hat{\boldsymbol{\eta}}\|} \right|_{n+1} \\ \Delta\alpha^{iso} - \Delta\gamma \left. \sqrt{\frac{2}{3}} \frac{\partial \tilde{\kappa}_{iso}}{\partial \alpha^{iso}} \right|_{n+1} \\ \left. F(\boldsymbol{\eta}, \boldsymbol{\kappa}^{kin}, \kappa_{iso}) \right|_{n+1} \end{array} \right\} \ . \tag{3.87}$$

The Jacobian matrix of either (3.25) or (3.42) can be formulated given these particular unknown and residual vectors. However, considering the similarity of this model to the J_2 model of the previous section, it is not surprising to learn that this formulation may also be simplified to solve for the plastic increment $\Delta\gamma$ without resorting to the full system listed in (3.87). The relationship between the purely deviatoric tensors $\boldsymbol{\eta}_{n+1}$ and $\boldsymbol{\eta}^{tr}_{n+1}$ given in (3.79) still holds, as ϱ_G affects only the volumetric portion of the plastic strain.

---

[4]Alternative formulations in the literature sometimes write this hydrostatic shift as $3\,c$—in which case the following discussion is simply modified by an appropriate factor.

The updated yield function at time t_{n+1} is expressed as

$$F(\boldsymbol{\eta}, \boldsymbol{\kappa}^{kin}, \kappa^{iso})\Big|_{n+1} = \|\boldsymbol{\eta}_{n+1}\| + \varrho_F \ \mathrm{tr}(\boldsymbol{\sigma}_{n+1}) + \sqrt{\frac{2}{3}}\ \kappa_{iso} - \sqrt{\frac{2}{3}}\sigma_Y = 0 \ , \tag{3.88}$$

which is generally a non-linear scalar equation in terms of $\Delta\gamma$. The volumetric term $\mathrm{tr}(\boldsymbol{\sigma}_{n+1})$ can be expanded to read

$$\mathrm{tr}(\boldsymbol{\sigma}_{n+1}) = \mathrm{tr}(\boldsymbol{\sigma}^{tr}_{n+1}) - 9\,K\,\varrho_G\,\Delta\gamma \ , \tag{3.89}$$

where K is the previously defined bulk modulus of the material. Employing linear kinematic and isotropic hardening, and in light of Equation (3.89), the updated yield condition is reduced to

$$F(\boldsymbol{\eta}, \boldsymbol{\kappa}^{kin}, \alpha^{iso})\Big|_{n+1} = F^{tr}_{n+1} - \left(2G + \frac{2}{3}H + \frac{2}{3}k + 9\,K\,\varrho_G\,\varrho_F\right)\ \Delta\gamma = 0 \ . \tag{3.90}$$

The trial condition F^{tr}_{n+1} is obtained as it has been for all other trial states, i.e., under the assumption that no plastic deformation accumulates over the given time step. From (3.90) the plastic increment is easily obtained as

$$\Delta\gamma = \frac{F^{tr}_{n+1}}{2G + \frac{2}{3}H + \frac{2}{3}k + 9\,K\,\varrho_G\,\varrho_F} \ . \tag{3.91}$$

The above procedure is valid for all stress states when $I_1 < c$ (assuming that $c \geq 0$). When this secondary condition is not satisfied an alternative procedure must be implemented.

Tension Cutoff

At the point $I_1 = c$ and $\|\mathbf{s}\| = 0$ in Figure 3.3 the model is numerically unstable and a definitive flow direction does not exist. A second surface perpendicular to the hydrostatic axis is defined to combat this problem. In general the second surface may be located at any I_1 along the hydrostatic axis. However, for this particular implementation it is assumed the surface coincides with the tip of the Drucker-Prager cone.

The flat tension cutoff surface is active when the trial stress state satisfies the condition $I^{tr}_1 \geq c$. A linear combination of flow directions derived from *both* active surfaces are used to map the trial state back to the tip of the Drucker-Prager envelope. The tension cutoff is described by the yield function

$$F_2(\boldsymbol{\sigma}, \kappa^{iso}_2) = I_1 - c - \kappa^{iso}_2)\,, \tag{3.92}$$

where the hardening function $\kappa_2^{iso} = \tilde{\kappa}_2^{iso}(\alpha_2^{iso})$ prescribes the evolution of this surface Petek (2006). In general this is a non-linear function in terms of the strain-like isotropic hardening parameter α_2^{iso}. The surface resides exclusively at the cone tip as stated previously thus $\kappa_2^{iso} = 0$. The yield function and plastic potential are modified to read

$$F_2(\boldsymbol{\sigma}, \kappa^{iso}) = I_1 - \frac{\sigma_Y^{Eff}}{\varrho_F} \qquad \text{and} \qquad G_2(\boldsymbol{\sigma}, \kappa^{iso}) = I_1 - \frac{\sigma_Y^{Eff}}{\varrho_G} \ . \tag{3.93}$$

In what follows the subscript $(\bullet_1)$ refers to those quantities derived from the traditional Drucker-Prager yield function and plastic potential defined in Equations (3.84) and (3.85). A subscript $(\bullet_2)$ is in reference to the current tension surface.

An updated elastic strain is obtained as

$$\begin{aligned} \boldsymbol{\epsilon}_{n+1}^{e} &= \boldsymbol{\epsilon}_{n+1}^{e\,,tr} - \Delta\gamma_1\, \mathbf{g}_1 - \Delta\gamma_2\, \mathbf{g}_2 \\ &= \boldsymbol{\epsilon}_{n+1}^{e\,,tr} - \Delta\gamma_1 \left(\frac{\boldsymbol{\eta}}{\|\boldsymbol{\eta}\|} + \varrho_G\, \mathbf{1} \right)_{n+1} - \Delta\gamma_2\, \mathbf{1} \ , \end{aligned} \tag{3.94}$$

from which the updated stress follows accordingly

$$\boldsymbol{\sigma}_{n+1} = \boldsymbol{\sigma}_{n+1}^{tr} - \Delta\gamma_1 \left(2\,G\, \frac{\boldsymbol{\eta}}{\|\boldsymbol{\eta}\|} + 3\,K\,\varrho_G\, \mathbf{1} \right)_{n+1} - 3\,K\,\Delta\gamma_2\, \mathbf{1} \ . \tag{3.95}$$

The volumetric term is expanded as

$$I_{1,n+1} = I_{1,n+1}^{tr} - 9\,K\,\varrho_G\,\Delta\gamma_1 - 9\,K\,\Delta\gamma_2 \ . \tag{3.96}$$

The updated yield conditions provide the final piece of the puzzle necessary to solve for the two increments $\Delta\gamma_1$ and $\Delta\gamma_2$, i.e.,

$$F_{1,n+1} = F_{1,n+1}^{tr} - \left(2G + \frac{2}{3}H + \frac{2}{3}k + 9\,K\,\varrho_G\,\varrho_F \right) \Delta\gamma_1 - 9\,K\,\varrho_F\,\Delta\gamma_2 = 0 \tag{3.97}$$

and

$$F_{2,n+1} = F_{2,n+1}^{tr} - 9\,K\,\varrho_G\,\Delta\gamma_1 - 9\,K\,\Delta\gamma_2 = 0 \ . \tag{3.98}$$

Equations (3.97) and (3.98) are expressed alternatively as the linear system

$$\left\{ \begin{array}{c} F_{1,n+1}^{tr} \\ F_{2,n+1}^{tr} \end{array} \right\} = \left[\begin{array}{cc} J_{11} & J_{12} \\ J_{21} & J_{22} \end{array} \right] \cdot \left\{ \begin{array}{c} \Delta\gamma_1 \\ \Delta\gamma_2 \end{array} \right\} \ , \tag{3.99}$$

with the coefficients

$$\begin{aligned} J_{11} &= 2G + \tfrac{2}{3}H + \tfrac{2}{3}k + 9\,K\,\varrho_G\,\varrho_F \qquad & J_{12} &= 9\,K\,\varrho_F \\ J_{21} &= 9\,K\,\varrho_G & J_{22} &= 9\,K \end{aligned} \tag{3.100}$$

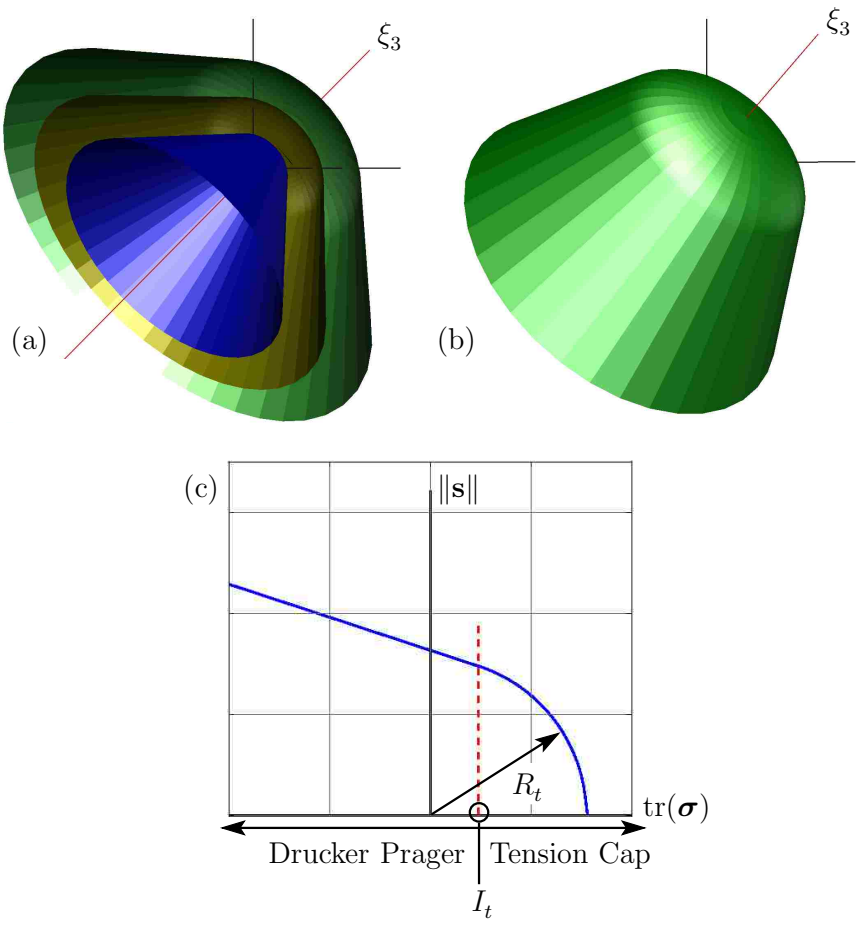

Figure 3.4: Smooth cap Drucker Prager yield surface.

The linear system in (3.99) is easily inverted to solve for $\Delta\gamma_1$ and $\Delta\gamma_2$. However, this form is very much contingent upon the assumption that the isotropic hardening laws are linear *and* the fact that the tension cutoff surface always resides at the tip of the Drucker-Prager cone. If these conditions are not satisfied, an alternative solutions method is needed to determine $\Delta\gamma_1$ and $\Delta\gamma_2$.

3.6.2 Smooth-Cap Two Surface Drucker-Prager

The two surface model presented in the previous subsection uses a conic envelope and a planar surface that is perpendicular to the hydrostatic axis. Both surfaces are active states satisfying the trial condition $I_1^{tr} > c$. This leads to a coupled linear system that must be solved for the plastic increments. An alternative approach defines a smooth, circular tension cap that intersects the linear Drucker-Prager envelope in a smooth fashion. This concept is illustrated in Figure 3.4(a), (b), and (c). The tension cap is the largest circle of radius R_t

centered about the origin that can fit within the Drucker-Prager envelope. The point at which the two surfaces intersect with the same tangent occurs at the tension transition point I_t.

The model formulation and integration algorithm is outlined in the paper by Swan and Seo (2006). Their presentation includes an additional circular compression cap that is neglected in the current implementation. Most of the formulation is omitted in this document since the details are described in the original. Here only the two yield functions are given in piecewise form:

$$F(\boldsymbol{\sigma}, R_t) = \begin{cases} F_1(\boldsymbol{\sigma}) = \|\mathbf{s}\| + \rho_F \, I_1 - \mu & \text{for} \quad I_1 \leq I_t \\ F_2(\boldsymbol{\sigma}, R_t) = R_t^2 - I_1^2 & \text{for} \quad I_1 > I_t \end{cases} , \tag{3.101}$$

where F_1 is the Drucker-Prager criterion and F_2 is the circular tension cap. The Drucker-Prager yield criterion is written in a slightly different form to grant additional flexibility. The traditional formulation is obtained by selecting $\mu = \sqrt{2/3}\,\sigma_Y$. Unlike the previous two surface formulation in which both surfaces are active for a trial state $I_1^{tr} > c$—there is only a single surface active at any given time in this formulation. Simple checks using the trial state are performed to determine which yield surface is active. This simplifies the return mapping algorithm considerably.

The only potential downside to the current implementation is the lack of hardening functions describing the evolution of the yield surface. This, however, could easily be modified for future applications.

3.6.3 Modified Two Surface Drucker-Prager

The traditional Drucker-Prager yield described by (3.84) is visualized in Figure 3.3(b). The concentric conic sections can be interpreted as a single material that accumulates hardening through plastic deformation as was stated previously. The net result is a shifting or translating of the cone through space but no variation in the cone opening. Unfortunately the simplicity of this model fails to account for more commonly observed behavior in the context of granular media—namely the evolution of the effective friction angle, ϕ_F, and plastic dilation angle, ψ_G. To this end a model is presented in which these variables evolve as a function of the plastic deformation. The current formulation focuses exclusively on the conic section of the yield surface; the tension cutoff surface outlined in Section 3.6.1 is utilized for stress states beyond the tip of the cone in the tension regime.

One possible two invariant yield function (Chen, 1994a,b) is

$$F(\boldsymbol{\sigma}, \alpha, \kappa) = \sqrt{J_2} + \alpha \, I_1 - \kappa = 0 \, , \tag{3.102}$$

where α and κ denote hardening parameters for the time being. The deviatoric invariant J_2 can be expressed in terms of I_1 and I_2 as

$$J_2 = \frac{1}{3}(I_1^2 - 3\,I_2) \ . \tag{3.103}$$

In light of the definition given in listing (3.59), it is possible to obtain the following equivelence:

$$\|\mathbf{s}\|^2 = 2\,J_2 \Longrightarrow \|\mathbf{s}\| = \sqrt{2}\,\sqrt{J_2} \ . \tag{3.104}$$

Equation (3.102) is then recast using (3.104) as

$$F(\boldsymbol{\sigma}, \alpha, \kappa) = \|\mathbf{s}\| + \sqrt{2}\,\alpha\,I_1 - \sqrt{2}\,\kappa = 0 \ . \tag{3.105}$$

The form of (3.105) allows a clear connection to be made with the yield function presented in (3.84). In particular, by identifying $\varrho_F = \sqrt{2}\,\alpha$ and $\sigma_Y^{Eff} = -\sqrt{2}\,\kappa$, a nearly equivalent form is obtained in

$$F(\boldsymbol{\sigma}, \phi_F) = \|\mathbf{s}\| + \varrho_F\,I_1 + \sigma_Y^{Eff} = 0 \ . \tag{3.106}$$

Here ϱ_F and σ_Y^{Eff} are hardening variables linked with the friction angle, ϕ_F, using the relations

$$\varrho_F = \sqrt{\frac{2}{3}}\frac{2\,\sin\phi_F}{\left(3 - \sin\phi_F\right)} \qquad \text{and} \qquad \sigma_Y^{Eff} = -\sqrt{\frac{2}{3}}\frac{6\,\sigma_Y\,\cos\phi_F}{\left(3 - \sin\phi_F\right)} \ . \tag{3.107}$$

Equations (3.107) follow from the Mohr-Coulomb criteria defined in Chen (1994a,b). Here it should be noted that these values correspond to a yield function that circumscribes the outer points of the Mohr-Coulomb criterion. Conversely, by changing the denominator to $(3 + \sin\phi_F)$ in both Eqs. (3.107), the circular cross section of the Drucker-Prager model will coincide with the inner points of the Mohr-Coulomb criteria (the relationship between the Mohr-Coulomb and Drucker-Prager criterion is later visualized in Figure 3.7).

Not surprisingly the plastic potential is defined in a similar manner, i.e.,

$$G(\boldsymbol{\sigma}, \psi_G) = \|\mathbf{s}\| + \varrho_G\,I_1 - C_G = 0 \ , \tag{3.108}$$

where C_G is a cohesion parameter that ensures the plastic potential coincides with the current stress point on the yield surface. The hardening parameter ϱ_G is obtained in terms of the plastic dilation angle, ψ_G, from

$$\varrho_G = \sqrt{\frac{2}{3}}\frac{2\,\sin\psi_G}{\left(3 - \sin\psi_G\right)} \ . \tag{3.109}$$

The denominator in (3.109) may be modified to $3 + \sin\psi_G$ to be consistent with a yield surface coincident with the inner points of the Mohr-Coulomb criteria.

This particular formulation employs the semi-implicit return mapping srategy (Tu et al., 2009) outlined in Equations (3.48)–(3.51). As such it is necessary to define the yield surface tangent, $\hat{\mathbf{f}}$, and the plastic flow direction, $\hat{\mathbf{g}}$. These quantities are derived in Appendix A.2.1 as

$$\hat{\mathbf{f}} = \frac{\mathbf{s}}{\|\mathbf{s}\|} + \varrho_F \mathbf{1} \qquad \text{and} \qquad \hat{\mathbf{g}} = \frac{\mathbf{s}}{\|\mathbf{s}\|} + \varrho_G \mathbf{1} \tag{3.110}$$

The remaining component is the second derivative of the plastic potential with respect to the stress. This value is also derived in Appendix A.2.1 and is reproduced from listing (A.17):

$$\frac{\partial^2 G}{\partial \hat{\boldsymbol{\sigma}} \otimes \partial \hat{\boldsymbol{\sigma}}} = \frac{1}{\|\mathbf{s}\|} \left(\mathbb{I} - \frac{1}{3} \mathbf{1} \otimes \mathbf{1} - \frac{\mathbf{s}}{\|\mathbf{s}\|} \otimes \frac{\mathbf{s}}{\|\mathbf{s}\|} \right) . \tag{3.111}$$

Some important observations can be made by closer examination of both (3.110) and (3.111). Two key points can be made about the plastic flow tensor $\mathbf{g}$. When examining the extents of the dilation angle, $\varrho_G = 0.8615$ and $\varrho_G = 0$ correspond to $\psi_G = 90^\circ$ and $\psi_G = 0^\circ$, respectively. Clearly a dilation angle of $\psi_G = 90^\circ$ is unobtainable from a physical perspective but nonetheless represents a valid limit. For these extrema—as well as all values in between—the norm of $\|\mathbf{g}\|$ is constant for all points on the yield surface. When the dilation angle vanishes, i.e., $\psi_G = 0^\circ$, the plastic flow is purely deviatoric and of unit length in stress space. These particular observations will be highlighted shortly and play a pivotal role in the context of granular materials.

The remaining portion of this section develops key equations for the mobilized friction and plastic dilation angles; these parameters play a crucial role in defining both the yield surface and plastic potential as shown in Equations (3.106)–(3.109). This topic is addressed in its own sub-section—as the current and subsequent models make use of the framework.

3.6.4 Evolution of Friction Angle and Plastic Dilation

The mobilized friction and plastic dilation angles are two parameters that provide the basis for capturing material hardening/softening in the context of granular media models. There are different ways of linking these two angles. This work follows the arguments outlined by many researchers, including Wood (1990); Chen (1994a,b); Andrade and Tu (2009), and links the variables using the notion of a critical state, defined as a point in which continued deformation does not accumulate additional stresses or changes in volume. This state—often dubbed a constant volume state—is widely observed in experimental behavior of granular materials and provides a benchmark in material modeling that even the basic simulations capture. To this end the effective friction angle, ϕ_F, is linked to the plastic dilation angle, ψ_G, via the critical state angle, ϕ_{cs}, and the relation

$$\tan \psi_G = \tan \phi_F - \tan \phi_{cs} \ . \tag{3.112}$$

This particular linkage follows from the phenomenological stress-dilatancy relation widely observed, e.g. Wood (2004).

The current formulation will specify a value for the friction and critical state angles. This is not the only option available for relating these parameters but it is the only option explored in this work. These state angles are defined via

$$\phi_F(\boldsymbol{\sigma}, \lambda) = a_0 + (a_1\,\lambda - a_4)\,\exp\left(a_2\,I_1 - a_3\,\lambda\right) \tag{3.113}$$

and

$$\phi_{cs}(\lambda) = a_0 - a_4\,\exp\left(-a_5\,\lambda\right)\ , \tag{3.114}$$

where a_{0-5} are prescribed constants, I_1 is the trace of the current stress tensor, and λ is a measure of the deformation. This form is consistent with existing literature, e.g. Borja et al. (2003), and allows for a pressure dependent strength and dilation as a function of plastic deformation. In the context of a return mapping strategy, the plastic deformation measure is updated according to

$$\lambda_{n+1} = \lambda_n + \Delta\lambda\ , \tag{3.115}$$

where $\Delta\lambda$ is an appropriate incremental quantity. There are several (potentially limitless) options for this term. This work has identified several practical candidates—each of which uses the plastic increment $\Delta\gamma$[5]. Three such choices are

$$\Delta\lambda\ = \|\Delta\gamma\,\mathbf{g}\|\ , \qquad \Delta\lambda\ = \|\Delta\gamma\,\mathbb{I}_{vol} : \mathbf{g}\|\ , \qquad \text{or} \qquad \Delta\lambda\ = \|\Delta\gamma\,\mathbb{I}_{dev} : \mathbf{g}\|\ . \tag{3.116}$$

Clearly some of these options will lead to the same $\Delta\lambda$. Indeed, for a Drucker-Prager like plastic potential and negligible plastic dilation angle, increments $(3.116)_{1,3}$ are identical due to the deviatoric nature of $\mathbf{g}$[6]. In general these quantities will be different and different material behavior can be achieved.

At this point two potential areas of concern should be addressed regarding the definitions given in (3.113) and (3.114). The required number of prescribed constants, six in this case, is frequently a source of contention and unrest amongst researchers. Oftentimes the values are not based on physical quantities, rather they are selected using the more subjective experience and judgment. As noted by Andrade and Tu (2009), a phenomenological hardening law is a problematic ingredient to plasticity models in the context of granular media. Regardless of these downsides, it is the approach is taken here. There are in fact

[5]This framework assumes that the mobilized friction angle will change only as a result of plastic deformations.

[6]Consider Equation $(3.110)_2$ and corresponding discussion.

Table 3.5: Sample values for constants a_{0-5}.

Constant	i.	ii.	iii.
a_0	20	20	20
a_1	7750	2000	0
a_2 [kPa]$^{-1}$	$3.33\,(10)^{-4}$	$1.67\,(10)^{-5}$	0
a_3	150	100	70
a_4	20	20	20
a_5	300	100	50

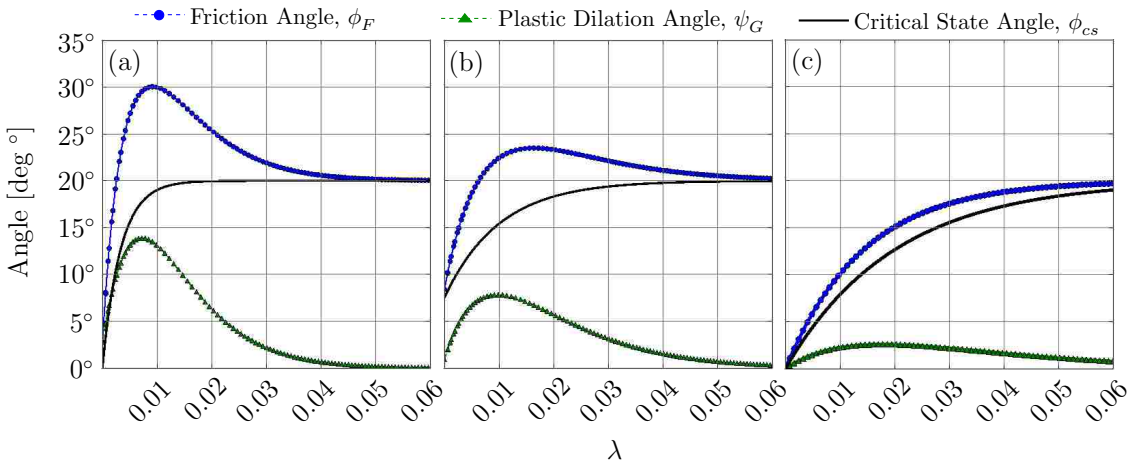

Figure 3.5: Relationship between the effective friction angle, ϕ_F, critical state angle, ϕ_{cs}, and the plastic dilation angle, ψ_G. (a), (b), and (c) are consistent with a dense, moderately dense, and loose arrangement of a granular medium (dry sand for example).

some easily identifiable physical parameters that aid in the selection of these constants. Second, some individuals may have a slight issue in mobilizing the critical state angle. And for good reason—as this lacks a direct physical meaning. Ideally the critical state angle is a single, unique value. However, if such is the case, there are situations when the relationship for dilation angle, as defined in (3.112), breaks down and erroneous values for dilation angles are computed. If used judiciously, the current definition allows for a wide variety of friction and dilation angles to be determined—provided the critical state angle approaches a constant value with excessive deformation then (3.114) is a reasonable definition.

Three sets of curves highlighting the relationship between the friction, dilation, and critical state angle are shown in Figure 3.5(a), (b), and (c). The parameters used to construct these curves are given in Table 3.5, where i., ii., and iii. correspond to curves 3.5(a), (b), and (c) respectively . Note that these a_{0-5} values define the angle in degrees (as opposed to radi-

ans). Figure 3.5(a) and (b) are representative of a granular medium with a densely packed particles. Conversely, curve 3.5(c) is more consistent with a loose arrangement. From these figures the role of the constants can be partially identified. The term a_0 represents the final value that both ϕ_F and ϕ_{cs} tend to. The difference $a_0 - a_4$ corresponds to the initial friction angle of the medium in question. The width of the friction angle curve is determined by a_2 and a_3, while the same is true for a_5 and the critical state angle. Finally, the constant a_1 determines the peak (as well as the rate to get to the peak) friction angle.

Determining the value of these constants is challenging and the notion of a single, concrete approach for identifying suitable values does not exist. Rather, the process is largely trial-and-error. The impact on the results can be extensive and is demonstrated in Chapter 7 where these models are used to simulate granular flow. A good starting point for parameter identification is to extract the quantity

$$\omega = -\frac{q}{p} \tag{3.117}$$

from experimental data, where

$$q = \sqrt{3/2}\,\|\mathbf{s}\| \qquad \text{and} \qquad p = I_1/3\ . \tag{3.118}$$

The ratio in (3.117) is linked with the effective friction angle via the relation

$$\sin\phi_F^{exp} = \frac{\omega}{(2+\omega/3)} \tag{3.119}$$

which follows from the Mohr-Coulomb failure criterionChen (1994a,b); Tu et al. (2009). In (3.119) the notation ϕ_F^{exp} is used to distinguish between a value obtained experimentally versus the curve definition of (3.113). Consistent with the definition of ϱ_F given by $(3.107)_1$, ϕ_F^{exp} assumes the yield function circumscribes the outer points of the Mohr-Coulomb criteria. The denominator may be changed to $(2-\omega/3)$ to obtain a definition consistent with a yield function that passes through the inner points of the Mohr-Coulomb criteria. The plot of ϕ_F^{exp} as a function of deformation provides a good template for constructing ϕ_F.

3.7 Two Surface Matsuoka-Nakai Material Model

The Matsuoaka-Nakai framework is built around the Mohr-Coulomb failure surface. The theory was developed in numerous works by H. Matsuoka and T. Nakai; see, e.g., Matsuoka and Nakai (1974, 1982, 1985). The isotropic, three invariant formulation has a successful track record of capturing the behavior of granular materials with differing yield strengths in tension or compression. The smooth, convex surface bypasses much of the implementation

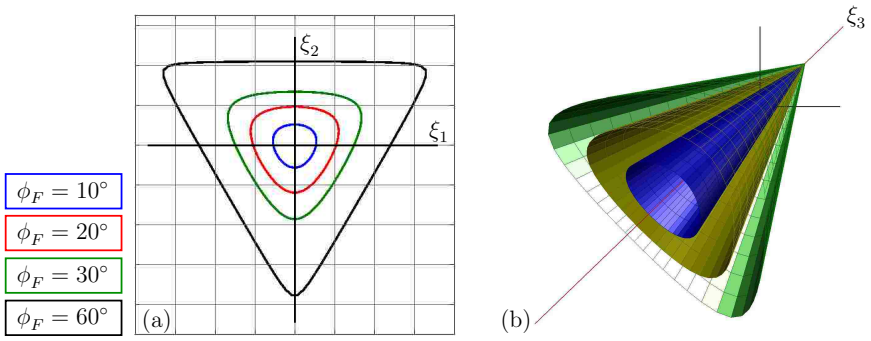

Figure 3.6: Matsuoka Nakai yield surface.

difficulties that arise in the corner regions of the traditional Mohr-Coulomb models, making the current formulation attractive in a three dimensional setting.

An overview of three invariant elasto-plastic constitutive models is given by Borja et al. (2003). Additional considerations for Matsuoka-Nakai criterion are discussed in Andrade and Tu (2009). This particular formulation differs from these presentations in two ways: a tension cutoff surface is used (see Section 3.6.1 for details) and the state angles evolve as outlined in Section 3.6.4. The Matsuoaka-Nakai yield function can be written as

$$F(\bar{\boldsymbol{\sigma}}, \kappa_F) = 6\,\bar{I}_3\,\kappa_F + 3\,\bar{I}_1\,\|\mathbf{s}\|^2 - 2\,\bar{I}_1^3\,, \tag{3.120}$$

where κ_F is a hardening parameter that is related to the friction angle via

$$\kappa_F = \frac{\sin^2\phi_F - 9.0}{\sin^2\phi_F - 1.0}\,. \tag{3.121}$$

The overbar on the invariants was introduced in Equations (3.55)–(3.57) and represents a shift along the hydrostatic axis by a distance c_F. Eliminating the shifted invariants yields

$$\begin{aligned} F(\bar{\boldsymbol{\sigma}}, \kappa_F) = {} & 6\,I_3\,\kappa_F - 6\,I_1\,I_2 + c_F\,(12\,I_1^2 + 18\,I_2 - 6\,I_2\,\kappa_F) \\ & + c_F^2\,(6\,I_1\,\kappa_F - 54\,I_1) + c_F^3\,(54 - 6\,\kappa_F)\,. \end{aligned} \tag{3.122}$$

The corresponding plastic potential is

$$\begin{aligned} G(\bar{\boldsymbol{\sigma}}, \kappa_G) = {} & 6\,I_3\,\kappa_G - 6\,I_1\,I_2 + c_G\,(12\,I_1^2 + 18\,I_2 - 6\,I_2\,\kappa_F) \\ & + c_G^2\,(6\,I_1\,\kappa_G - 54\,I_1) + c_G^3\,(54 - 6\,\kappa_G) \end{aligned} \tag{3.123}$$

where κ_G is a hardening parameter related to the plastic dilation angle ψ_G as

$$\kappa_G = \frac{\sin^2\psi_G - 9.0}{\sin^2\psi_G - 1.0}\,. \tag{3.124}$$

The term c_G is also a shift along the hydrostatic axis and is computed such that the potential surface is attached to the yield surface at the point of interest. Note that $c_G \geq c_F$ since $\phi_F \geq \psi_G$.

The yield surface and cross sections are depicted in Figure 3.6. Increasing the friction angle not only enlarges the surface but significantly alters the shape of the cross section as is observed in Figures 3.6(a) and (b). This is in stark contrast to the Drucker-Prager models considered thus far, whose cross section shape is independent of friction angle. The upper limit on the friction angle, $\phi_F = 90°$, results in a failure criterion identical to the Rankine condition, where as intermediate values correspond to a surface that circumscribes the traditional Mohr-Coulomb envelope. This latter relationship is shown in Figure 3.7.

The current implementation of the Matsuoaka-Nakai model uses the semi-implicit return mapping strategy (Tu et al., 2009) outlined in Equations (3.48)–(3.51). As such it is necessary to define the plastic flow direction $\hat{\mathbf{g}}$ as well as $d^2G/d\boldsymbol{\sigma} \otimes d\boldsymbol{\sigma}$. These quantities are derived in detail in Appendix A.2.1. The flow direction is

$$\begin{aligned}\hat{\mathbf{g}} &= 6\,\kappa_G\,I_3\,\boldsymbol{\sigma}^{-1} + 3\,\|\mathbf{s}\|^2\,\mathbf{1} - 8\,I_1^2\,\mathbf{1} + 6\,I_1\,\boldsymbol{\sigma} \\ &\quad +6\,c_G\,\left(\kappa_G\,\boldsymbol{\sigma} + 7\,I_1\,\mathbf{1} - 3\,\boldsymbol{\sigma} - \kappa_G\,I_1\,\mathbf{1}\right) \\ &\quad +6\,c_G^2\,\left(\kappa_G\,\mathbf{1} - 9\,\mathbf{1}\right)\,. \end{aligned} \tag{3.125}$$

The second derivative with respect to the stress tensor is a 4^{th} order tensor:

$$\begin{aligned}\frac{d^2G}{d\boldsymbol{\sigma} \otimes d\boldsymbol{\sigma}} &= 6\,\kappa_G\,I_3\,\left(\boldsymbol{\sigma}^{-1} \otimes \boldsymbol{\sigma}^{-1} + \frac{d\boldsymbol{\sigma}^{-1}}{d\boldsymbol{\sigma}}\right) + 6\,\left(\boldsymbol{\sigma} \otimes \mathbf{1} + \mathbf{1} \otimes \boldsymbol{\sigma}\right) - 18\,I_1\,\mathbf{1} \otimes \mathbf{1} + 6\,I_1\mathbb{I} \\ &\quad +6\,c_G\,\left(\kappa_G\,\mathbb{I} + 7\,\mathbf{1} \otimes \mathbf{1} - 3\,\mathbb{I} - \kappa_G\,\mathbf{1} \otimes \mathbf{1}\right)\,. \end{aligned} \tag{3.126}$$

These derivatives are quite cumbersome and awkward to work with, particularly so for Equation (3.126). Their complexity—not to mention physical size—is significantly reduced if working in principal stress space. Doing so reduces the first derivative to a vector and the second derivative becomes

$$\begin{aligned}\frac{d^2G}{d\sigma_I\,d\sigma_J} &= 6\,\kappa_G\,I_3\,\left(\frac{1}{\sigma_I\,\sigma_J} - \frac{\delta_{IJ}}{\sigma_I\,\sigma_J}\right) + 6\,\left(\sigma_I + \sigma_J\right) + 6\,I_1\delta_{IJ} - 18\,I_1 \\ &\quad +6\,c_G\,\left(\kappa_G - 3\right)\,\delta_{IJ} + 6\,c_G\,\left(7 - \kappa_G\right)\,. \end{aligned} \tag{3.127}$$

Here I and J are free indices ranging from 1–3 denoting the principal values. This form is advantageous because numerical difficulties associated with a zero principal stress are eliminated.

A key observation is made by taking the trace of $\hat{\mathbf{g}}$. This quantity describes how the volumetric portion of the plastic strain changes:

$$\mathrm{tr}(\hat{\mathbf{g}}) = \mathbf{1} : \hat{\mathbf{g}} = \left(6\,\kappa_G - 27\right)\,I_2 - 12\,I_1^2 + 12\,I_1\,c_G\,\left(9 - \kappa_G\right) + 6\,c_G^2\,\left(3\,\kappa_G - 27\right)\,. \tag{3.128}$$

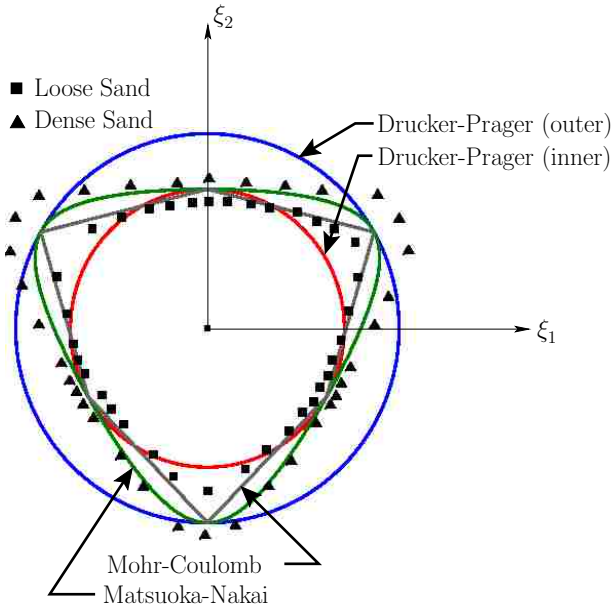

Figure 3.7: Failure points for dense and loose sand. Different yield criteria are plotted for comparison purposes only. The primed axes denote the deviatoric plane. Source: Lade (1972); Lade and Duncan (1975); Andrade and Tu (2009)

It is not possible to eliminate this term for non-zero stress states. Requiring the cohesion term to vanish, i.e., $c_G = 0$, does not do the trick, nor does the limit $\psi_G = 0°$. For this latter scenario $\kappa_G = 9.0$ and the volumetric portion is reduced to

$$\mathrm{tr}(\hat{\mathbf{g}}) = \mathbf{1} : \hat{\mathbf{g}} = 27\, I_2 - 12\, I_1^2. \tag{3.129}$$

This finding suggests that regardless of the deformed state, volumetric deformation will be incurred for non-zero stress states, violating the definition of a critical (or constant volume) state. This is indeed the case and is demonstrated in Section 3.8. Therefore, it can be concluded that without further modification the plastic potential defined in Equation (3.123) is problematic for reproducing key observed phenomenon in granular materials.

Here only the derivatives related to the plastic potential have been presented. The derivatives with respect the yield function can easily be obtained by substituting $\kappa_G \to \kappa_G$ and $c_G \to c_F$.

3.8 Model Verification

The primary motivation for developing these material models is the ability to simulate a granular medium. As such, this verification section has a relatively narrow focus and

considers only the Modified Drucker-Prager model from Section 3.6.3 and the Matsuoaka-Nakai model from Section 3.7. These two criteria are verified only in the context of a dry sand. Such a narrow focus is not sufficient to declare these models satisfactory in a general sense; it is, however, sufficient for the purpose of this work and the applications considered in this dissertation. The focus here is on demonstrating the ability of these models to capture experimentally observable phenomenon—such as a critical state. The focus is not on calibration. To properly calibrate these models for specific sand, soil, or gravel requires extensive comparison to experimental observations. This can be done but is beyond the current scope.

Figure 3.7 highlights the shape of the yield surface for both dense and loose Monterey No. 0 sand specimens Lade (1972); Lade and Duncan (1975); Andrade and Tu (2009). These values are superimposed on three yield separate yield criterion, namely the Drucker-Prager, Matsuoaka-Nakai, and the Mohr-Coulomb. Two Drucker-Prager surfaces are considered: the first circumscribes the outer vertices of the Mohr-Coulomb criteria while the second passes through the inner points. It is apparent that these three surfaces perform reasonably well in capturing these data. In particular, the Matsuoka-Nakai does an excellent job in defining the failure strength without the cumbersome corner effects associated with the Mohr-Coulomb model. Unfortunately—as noted in Section 3.7—the unmodified Matsuoka-Nakai plastic potential results in a plastic flow direction that is inconsistent with the notion of a critical state. To demonstrate this effect and highlight the capabilities of the current implementation, the following three non-associative material variations are considered further:

1. DP – Modified Drucker-Prager formulation. This is the model outlined in Section 3.6.3

2. MN with DP plastic potential. This formulation combines the Matsuoka-Nakai yield surface, Equation (3.120), with the Drucker-Prager plastic potential, Equation (3.108).

3. MN – Matsuoka-Nakai formulation. This is the model outlined in Section 3.7

The remainder of this section examines the response of these formulations to a prescribed set of loading conditions. This is done with the help of the mixed-control material driver as presented by Alawaji et al. (1992). Two tests are performed: a simple shear test and a biaxial compression test. The elastic material parameters used in the analysis are $E = 75,000$ [kPa] and $\nu = 0.33$ for the modulus of elasticity and Poisson's ratio, respectively. The corresponding values for the bulk modulus and shear modulus are $K = 73,530$ [kPa] and $G = 28,195$ [kPa]. All specimens are subjected to a hydrostatic stress state of $p_0 = -150$ [kPa] unless noted otherwise. The constants used to define the friction angle and

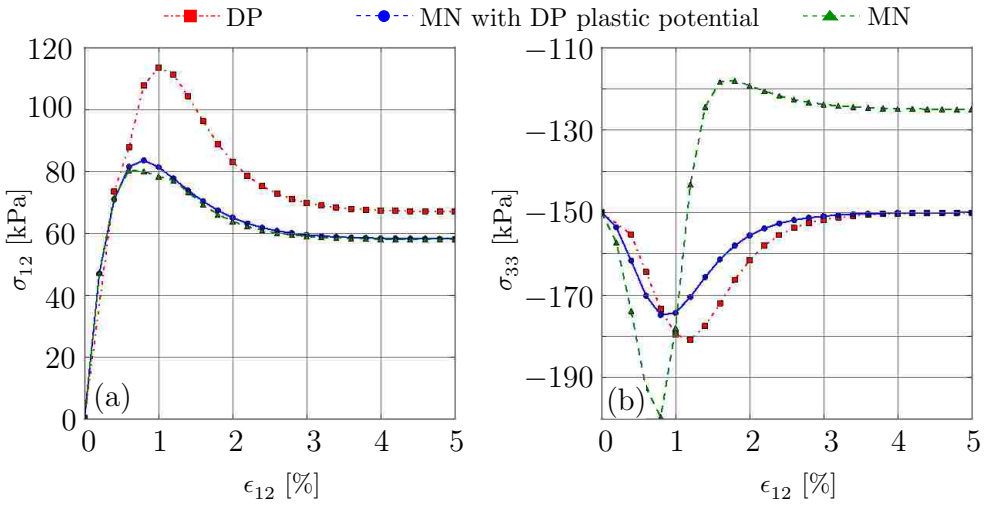

Figure 3.8: Simple shear results. (a) Shear stress σ_{12} and (b) normal stress σ_{33} as a function of shear deformation.

critical state angle are identified in the first column of Table 3.5. This set of constants creates a yield surface that is initially indistinguishable from the hydrostatic axis; any deformation instantly incurs irreversible plastic strains.

3.8.1 Simple Shear Tests

In this test a shear strain $\gamma_{12} = 2\epsilon_{12}$ is applied from the initial hydrostatic condition. A plane strain state is achieved by requiring $\epsilon_{33} = 0$ throughout the analysis. The normal stresses σ_{11} and σ_{22} are held constant at $p_0 = -150$ [kPa]. The return mapping algorithms compute the normal strains ϵ_{11} and ϵ_{22}, as well as the out of plane stress σ_{33}, due to the applied shear deformation. The results for the shear stress σ_{12} and normal stress σ_{33} are shown in Figure 3.8 as a function of ϵ_{12}. The shear stresses initially increase as the mobilized friction angle reaches a peak value. Post peak softening reduces these quantities and eventually each model yields a constant value with continued deformation. For this loading condition it is apparent that the choice of plastic potential has a negligible impact on the shear stresses; both Matsuoka-Nakai variants yield similar values—each of which is smaller in magnitude than the Drucker-Prager model. A different trend is observed, however, for the normal stresses σ_{33}. Each normal stress increases initially in magnitude as the shear deformation is applied. The behavior of the models begins to diverge near the peak of the hardening and the use of different plastic potentials has obvious ramifications on the stress states. The two models that employ the Drucker-Prager plastic potential exhibit post peak softening and return to their initial value. Both remain constant with continued shear deformation.

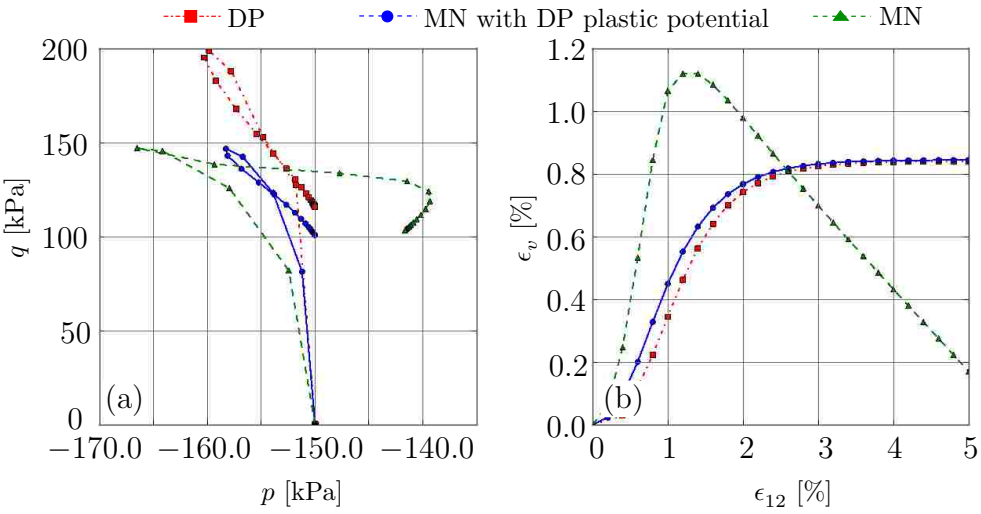

Figure 3.9: Simple shear results. (a) Relationship between pressure, p, and shear measure q. (b) Volumetric strain as a function of shear deformation.

The Matsuoka-Nakai plastic potential leads to additional reduction in stress before settling in at a reduced constant value. From these figures alone there is no apparent advantage to any one of the models.

Additional insight into the model behavior is obtained by examining the volumetric and deviatoric-like terms of the stress and strain tensors as the shear deformation is applied. In Figure 3.9 two such measures are investigated. The first plot depicts the relationship between the pressure, p, and shear stress measure, q. These two quantities are defined in Equation (3.118). The pressures initially increase in magnitude with continued deformation. Both the models that employ the Drucker-Prager plastic potential eventually return to the original pressure and remain at this value—albeit with an additional shear stress. The Matsuoaka-Nakai plastic potential leads to a constant stress state, as evidenced by the successive number of plot points in close proximity, but at a slightly lower in magnitude pressure. Figure 3.9(b) plots the change in volume—relative to the hydrostatic state—as a function of the shear deformation. Here the previous discussion regarding the accumulation of volumetric strains when using the Matuoska-Nakai plastic potential is highlighted. From this figure it is apparent that continued shear deformation leads to plastic changes in volume for the model using the plastic potential given in Equation (3.123). This occurs at a rate proportional to I_1 and I_2 as noted in Equation (3.129). This observation is inconsistent with experimental findings of shear tests performed on dry granular samples. From this it can be concluded that this model is incapable of reproducing a critical state response. On the other hand, both models using the Drucker-Prager plastic potential defined in (3.108)

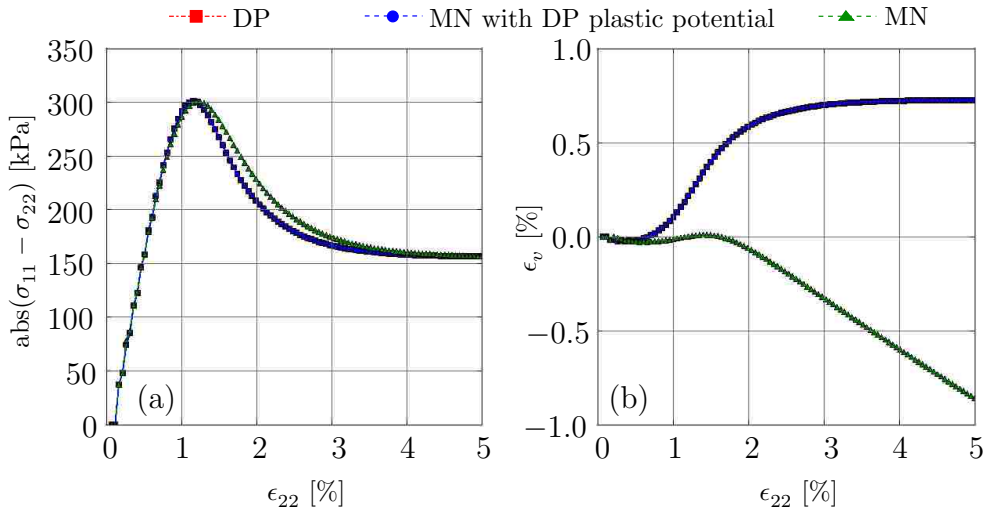

Figure 3.10: Biaxial compression results. (a) q. (b) Volumetric strain.

exhibit ideal critical state behavior: continued deformation does not accumulate additional stresses or changes in volume.

3.8.2 Biaxial Compression Tests

A compression test is also used for additional verification of the three model variants. For this series of tests an axial deformation is applied to ϵ_{22} from the hydrostatic state. Both σ_{11} and σ_{33} are held constant at $p_0 = -150$ [kPa]. The return mapping algorithm computes the normal stress σ_{22} as well as the normal strains ϵ_{11} and ϵ_{33}. Figure 3.10 highlights both q and volumetric strain, ϵ_v, as a function of the axial deformation ϵ_{22}. This loading condition is unique in that differences observed in the model behavior are attributed solely to the choice of plastic potential. This statement follows from the fact the both the Drucker-Prager and Matusoka-Nakai yield surfaces coincide in biaxial compression, cf. Figure 3.7. Not surprisingly both models that use the Drucker-Prager plastic potential yield the same plot points in both Figures 3.10(a) and (b). The third model begins to deviate only as extensive plastic deformations are incurred. The departure coincides with the accumulation of volumetric strains, already identified as problematic for proper representation of granular materials. In Figure 3.10(b) it is observed that both models employing the Drucker-Prager plastic potential initially contract and then expand before arriving at a constant volume state. Such behavior is widely observed in dense arraignments of granular matter.

Additional tests have been conducted to get a sense of the model convergence as well as the accuracy of the semi-implicit integration algorithm. Although the model driver is

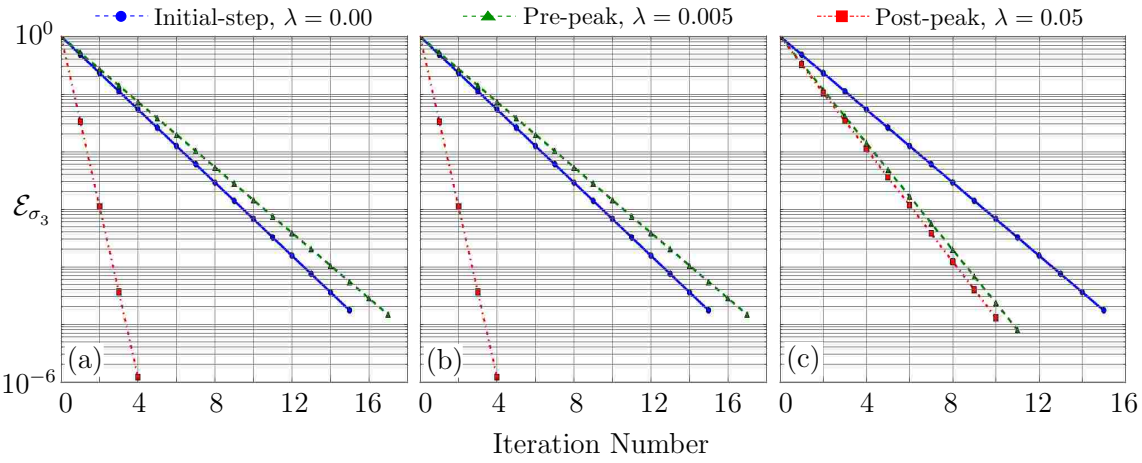

Figure 3.11: Error norm of the biaxial confining stress σ_3. (a) Modified Drucker-Prager model as presented in Section 3.6.3. (b) Matsuoka-Nakai yield surface, Eq. (3.120), coupled with the two invariant plastic potential, Eq. (3.108). (c) Matsuoka-Nakai model as presented in Section 3.7.

mixed—meaning both strain and stresses may be prescribed—the formulation relies on a purely strain driven algorithm with iteration to correct the appropriate stress components. Thus, it is possible to monitor the stresses as they converge to the prescribed value. The error norm for the principal planar stress σ_3 is defined as

$$\mathcal{E}_{\sigma_3} = \frac{|\sigma_3^* - \sigma_3|}{|\sigma_3^* - \sigma_3^0|} \,, \tag{3.130}$$

where σ_3^* is the prescribed value and the denominator $|\sigma_3^* - \sigma_3^0|$ is the initial residual at the first step of the stress iteration. The term σ_3 is the planar stress corresponding to the current strain state at a given iteration. A tolerance of 10^{-6} is used in the algorithm.

Figure 3.11(a)–(c) show the error norm for the three models under consideration thus far. Each figure examines the norm at three different points in the loading cycle. The points are determined by the net plastic deformation measure, λ, defined in Equation (3.115). The first point, $\lambda = 0$, represents the onset of plastic loading[7]. The second point, $\lambda = 005$, captures the error norm just before the peak strength, while the third and final point, $\lambda = 05$, examines the behavior under excessive plastic deformation when the strength is constant.

The convergence rate for $\lambda = 0$ is similar for each model variant. Those models employing the Drucker-Prager plastic potential converge slightly faster. The behavior changes near the peak strength; the pure Matsuoka-Nakai model enjoys the highest convergence rate

[7]Recall that plastic deformation is incurred instantaneously with any loading for the particular set of constants used to define the friction and dilation angles.

as indicated by Figure 3.11(c). As the critical state friction angle is approached, the two variations sharing the Drucker-Prager plastic potential converge the fastest. However, these plots need to be interpreted with caution and the convergence rate is not necessarily the best measure to judge their performance. The stress iteration is performed with $\mathbb{C}^e$ as defined in Equation (3.46) assuming a unit density. This value is not the consistent elastic tangent at each time step[8]. Nonetheless, these findings verify the semi-implicit algorithm's ability to converge under the conditions defined thus far in this chapter.

3.9 Summary

This chapter presented several components necessary for building a MPM-oriented constitutive framework. This included the basic concepts from computational inelasticity, small and large deformation theory, and the development of specific material models capable of simulating several kinds of materials. Particular attention was paid to developing a framework that can accommodate extremely large deformations while remaining computationally efficient and numerically stable in the context of granular media. The next two chapters present key enhancements that aid in the simulation of landslides.

[8]This is not really a point of concern in the context of this dissertation; the MPM as defined in this document enjoys a purely strain driven and explicit existence—in which case the consistent tangent plays no role.

Chapter 4

ANTI-LOCKING STRATEGY

A vast majority of the theoretical framework presented in this chapter follows (verbatim in some instances) from the paper *Mitigating kinematic locking in the Material Point Method* by Mast, Mackenzie-Helnwein, Arduino, Miller, and Shin (2012). The author is indebted to Peter Mackenzie-Helnwein, Pedro Arduino, and Greg Miller for their contributions in writing and publishing this paper.

This chapter contains the theoretical development of anti-locking routines designed to mitigate the accumulation of fictitious strains when linear shape functions are used in conjunction with the standard MPM algorithm. Multiple approaches are discussed, including various control volumes defined using a regular grid. As will be shown in later chapters, the anti-locking routines provided here are essential for modeling quality flow dynamics and obtaining reasonable stress fields.

4.1 Introduction and Background

It is common to use standard linear shape functions defined on a regular, rectangular grid in most implementations of the MPM. This is not, however, a limitation or requirement of the technique. Researchers have demonstrated the benefits of using an irregular grid consisting of either triangular or quadrilateral cells, e.g., Wieckowski (2004a); Wang et al. (2005). Others have investigated the use of higher-order shape functions—2^{nd} and 3^{rd} order B-splines, Andersen and Andersen (2010a); Steffen et al. (2008a), standard quadratic shape functions, Andersen and Andersen (2010a), as well as a Radial Basis Function, Htike et al. (2011),—in lieu of linear shape functions. In these cases the use of a higher order shape function eliminates many of the non-physical results associated with traditional implementations. However, the use of the non-linear functions can result in an increase in computational cost, potentially limiting the effectiveness of such approaches. Given the simplicity of low-order elements/cells, they remain a popular choice in FEM and MPM applications. To date, linear interpolation functions are the most common choice found in the MPM literature.

The use of linear shape functions does not come without shortcomings. These include volumetric locking due to the insufficient representation of an isochoric displacement/velocity field, Belytschko et al. (2000), as well as shear locking due to non-physical coupling

of normal strains and shear strains, Andelfinger and Ramm (1993). In addition to locking, the discontinuous gradient leads to cell-crossing errors which are attributed to the sudden jump in strain rate as a particle moves from one cell to another. A potential solution to the cell-crossing error is to counteract the discontinuity of the gradient at the interface between adjacent cells by introducing an enhanced gradient, Zhang et al. (2011). Alternatively, the particle can be represented using a finite domain, effectively smoothing out the discontinuity. This idea was first developed in the Generalized Interpolation Material Point (GIMP) method, Bardenhagen and Kober (2004) and has since been applied to wide variety of engineering problems, e.g., Daphalapurkar et al. (2007); Ma et al. (2006a,b,c); Wallstedt and Guilkey (2008). A similar variant of the MPM, the Convected Particle Domain Interpolation (CPDI) technique by Sadeghirad et al. (2011b), effectively combats the discontinuous gradient issue by introducing a parallelogram-shaped particle domain that is consistently updated using the deformation gradient at the particle. These approaches effectively combat the cell crossing problem with varying success depending on the application. Unfortunately these approaches fail to address or alleviate kinematic locking.

In fact, until very recently the topic has not been reported in the literature, Andersen and Andersen (2010a); Arduino et al. (2011); Mackenzie-Helnwein et al. (2011); Shin (2009). The closest references are the works Andersen and Andersen (2010a); Htike et al. (2011); Steffen et al. (2008a), which have found that representation and integration errors are reduced significantly by introducing higher order shape functions on the background grid. This is in agreement with related observations in the Finite Element Method (FEM), where increasing the interpolation order not only improves accuracy but also reduces locking phenomena. The approach presented in this chapter significantly improves both the kinematics and the stress field—all the while supporting traditional linear shape functions. The remaining sections introduce the anti-locking methodology and outline the implementation procedure for application in the MPM. The effectiveness of the algorithm is highlighted throughout Chapters 6 and 7 in both the elastic and inelastic material domain.

4.2 Theoretical Overview

Alleviating kinematic locking within the context of the FEM is not a new concept and there is extensive literature on the topic, e.g, Bathe (1996); Belytschko et al. (2000); Wriggers (2008); Zienkiewicz et al. (2005c,b). Many of the existing FEM strategies make use of multi-field variational principles, and this work follows suit, applying similar concepts to the MPM. More specifically, this work employs the well known Hu-Washizu multi-field variational principle Washizu (1982). Traditional weak form equations are structured such

that the solution yields an approximation of the displacement field (or its time derivatives, namely the velocity and/or the acceleration). The Hu-Washizu formulation is different in that it seeks a weak form approximation not only to the displacement, but also to the corresponding strain and stress fields as well. Such a formulation is developed from a variational standpoint by first considering the total potential energy stored in a body with mass $m_{\mathcal{B}}$. Subjecting the body to a general displacement field, $\mathbf{u}(\mathbf{x},t)$, the potential for an isothermal problem is written as

$$\Pi(\mathbf{u}) := \int_{m_{\mathcal{B}}} \bar{\psi}(\tilde{\boldsymbol{\varepsilon}}(\mathbf{u}))\, dm - \int_{m_{\mathcal{B}}} \bar{\mathbf{b}} \cdot \mathbf{u}\, dm - \int_{\Gamma_{\mathcal{B}}} \tilde{\mathbf{t}} \cdot \mathbf{u}\, d\Gamma\,. \tag{4.1}$$

where $\bar{\mathbf{b}}(\mathbf{x},t)$ is the mass specific body force at position $\mathbf{x}$ and time t, $\tilde{\mathbf{t}}(\mathbf{x},t)$ is the prescribed external traction acting on the body's surface, $\Gamma_{\mathcal{B}}$, and $\bar{\psi}(\tilde{\boldsymbol{\varepsilon}}(\mathbf{u}))$ is the mass specific Helmholtz free energy function. The strain, $\boldsymbol{\varepsilon}$, derived from a displacement field, $\mathbf{u}$, is given by a strain function $\tilde{\boldsymbol{\varepsilon}}(\mathbf{u})$. For small deformations $\tilde{\boldsymbol{\varepsilon}}(\mathbf{u}) := \boldsymbol{\nabla}^s\mathbf{u}$ (note that small deformation theory is *not* a requirement of the MPM, rather, it is done to simplify the explanation of the current approach from a variational standpoint). The free energy is typically a function of several variables needed to define the material state. For derivation purposes this function is expressed only in terms of the strain (i.e., $\bar{\psi} := \bar{\psi}(\boldsymbol{\varepsilon})$) and thus applies to elastic materials. However, this can easily be rewritten to allow for more general material behavior, and imposes no restriction on the subsequent treatment of locking. In general, $(\bar{\bullet})$ indicates a mass specific form of a volume specific quantity, i.e., $(\bullet) = \rho(\bar{\bullet})$ where $\rho(\mathbf{x},t)$ is mass density.

Replacing the strain function, $\tilde{\boldsymbol{\varepsilon}}(\mathbf{u})$, with an independent strain field, $\boldsymbol{\varepsilon}(\mathbf{x},t)$, and expressing the kinematic relation through a constraint equation using a mass-specific Lagrange multiplier field, $\bar{\boldsymbol{\sigma}}$, yields the Hu-Washizu style three-field functional

$$\Pi^*(\bar{\boldsymbol{\sigma}},\boldsymbol{\varepsilon},\mathbf{u}) := \int_{m_{\mathcal{B}}} \bar{\psi}(\boldsymbol{\varepsilon})\, dm - \int_{m_{\mathcal{B}}} \bar{\boldsymbol{\sigma}} : [\boldsymbol{\varepsilon} - \tilde{\boldsymbol{\varepsilon}}(\mathbf{u})]\; dm - \int_{m_{\mathcal{B}}} \bar{\mathbf{b}} \cdot \mathbf{u}\, dm - \int_{\Gamma_{\mathcal{B}}} \tilde{\mathbf{t}} \cdot \mathbf{u}\, d\Gamma\,. \tag{4.2}$$

A weak form solution is found as a stationary point of $\Pi^*(\bar{\boldsymbol{\sigma}},\boldsymbol{\varepsilon},\mathbf{u})$, yielding the governing system of weak-form equations as

$$\int_{m_{\mathcal{B}}} \delta\bar{\boldsymbol{\sigma}} : [\boldsymbol{\varepsilon} - \tilde{\boldsymbol{\varepsilon}}(\mathbf{u})]\; dm = 0\;, \tag{4.3}$$

$$\int_{m_{\mathcal{B}}} \delta\boldsymbol{\varepsilon} : \left[\bar{\boldsymbol{\sigma}} - \frac{\partial\bar{\psi}(\boldsymbol{\varepsilon})}{\partial\boldsymbol{\varepsilon}}\right] dm = 0\;, \qquad \text{and} \tag{4.4}$$

$$-\int_{m_{\mathcal{B}}} \nabla^s\delta\mathbf{u} : \bar{\boldsymbol{\sigma}}\, dm + \int_{m_{\mathcal{B}}} \delta\mathbf{u} \cdot \bar{\mathbf{b}}\, dm + \int_{\Gamma_{\mathcal{B}}} \delta\mathbf{u} \cdot \tilde{\mathbf{t}}\, d\Gamma = 0\;, \tag{4.5}$$

in which $\delta\bar{\boldsymbol{\sigma}}, \delta\boldsymbol{\varepsilon}$ and $\delta\mathbf{u}$ are arbitrary independent variations of the three independent fields $\bar{\boldsymbol{\sigma}}, \boldsymbol{\varepsilon}$, and $\mathbf{u}$, respectively. From Equation (4.4) the independent tensor field $\bar{\boldsymbol{\sigma}}(\mathbf{x},t)$ is

identified as the mass-specific Cauchy stress tensor (Washizu, 1982). The standard formulation of the MPM solves the dynamic version of the weak form equilibrium equation (4.5) and yields an approximation to the acceleration field over the body domain. This procedure is outlined in Chapter 2 and is well documented in the literature. Equations (4.3) and (4.4) provide additional constraints that are used to build approximations for the strain and stress fields, respectively.

Constructing an appropriate approximation field is composed of two steps for 2^{nd} order tensors. The first step isolates the portions of the field to be constructed, e.g., the volumetric and/or the deviatoric portions of the tensor field in question. This is accomplished using a filter matrix, $\mathbf{M}$, and a reconstruction matrix, $\mathbf{M}^*$. In the second step, the shape of the desired approximation is specified by defining a shape matrix, $\mathbf{S}(\mathbf{x})$, that effectively interpolates the generalized degrees of freedom used to represent the strain and stress fields, respectively. Bearing these two steps in mind, the grid-based approximation (denoted by a superscript h) is constructed for the strain and stress using

$$\boldsymbol{\varepsilon}(\mathbf{x},t) \approx \boldsymbol{\varepsilon}^h(\mathbf{x},t) := \mathbf{M}^* \cdot \mathbf{S}(\mathbf{x}) \cdot \boldsymbol{\alpha}(t) + \mathbb{P} : \tilde{\boldsymbol{\varepsilon}} \tag{4.6}$$

and

$$\bar{\boldsymbol{\sigma}}(\mathbf{x},t) \approx \bar{\boldsymbol{\sigma}}^h(\mathbf{x},t) := \mathbf{M}^* \cdot \mathbf{S}(\mathbf{x}) \cdot \boldsymbol{\beta}(t) + \mathbb{P} : \tilde{\bar{\boldsymbol{\sigma}}}\,. \tag{4.7}$$

The generalized degrees of freedom $\boldsymbol{\alpha}(t)$ and $\boldsymbol{\beta}(t)$ are the unknown vectors to be solved for. Note that specification of $\mathbf{M}$ and $\mathbf{M}^*$ drives the dimensionality of $\mathbf{S}$, and hence, the unknown function spaces $\boldsymbol{\alpha}$ and $\boldsymbol{\beta}$. The term $\mathbb{P}$ is a projection operator, defined as

$$\mathbb{P} := \mathbb{I} - \mathbf{M}^* \cdot \mathbf{M} \tag{4.8}$$

with $\mathbb{I}$ as the 4^{th} order identity tensor. The strain function, $\tilde{\boldsymbol{\varepsilon}} = \tilde{\boldsymbol{\varepsilon}}(\mathbf{u}^h)$, is the strain derived from the displacement field approximation. The mass specific stress is obtained from the general constitutive relation $\tilde{\bar{\boldsymbol{\sigma}}} = \partial\bar{\psi}/\partial\boldsymbol{\varepsilon}$. Equations (4.6) and (4.7) reiterate the two-step nature of the approximation: the shape matrix $\mathbf{S}(\mathbf{x})$ provides a spatial interpolation of the generalized unknowns collected in $\boldsymbol{\alpha}$ (or $\boldsymbol{\beta}$). The matrix $\mathbf{M}^*$ is used to reconstruct a symmetric second-order tensor resulting from the interpolated components and is combined with the unaltered complementary portion $\mathbb{P} : \tilde{\boldsymbol{\varepsilon}}$ (or $\mathbb{P} : \tilde{\bar{\boldsymbol{\sigma}}}$) of the original tensor field.

Consistent with Equations (4.6) and (4.7) and sufficient for Equations (4.3)–(4.5), a general set of admissible variations is constructed as

$$\delta\boldsymbol{\varepsilon}(\mathbf{x}) := \delta\boldsymbol{\alpha} \cdot \mathbf{S}(\mathbf{x})^T \cdot \mathbf{M} \quad \text{and} \quad \delta\bar{\boldsymbol{\sigma}}(\mathbf{x}) := \delta\boldsymbol{\beta} \cdot \mathbf{S}(\mathbf{x})^T \cdot \mathbf{M}\,. \tag{4.9}$$

Substituting Equations (4.6), (4.7), and (4.9) into constraints (4.3) and (4.4) yields

$$\int_{m_{\mathcal{B}}} \delta\boldsymbol{\beta} \cdot \mathbf{S}^T \cdot \mathbf{M} : [\mathbf{M}^* \cdot \mathbf{S} \cdot \boldsymbol{\alpha} - \mathbf{M}^* \cdot \mathbf{M} : \tilde{\boldsymbol{\varepsilon}}] \; dm = 0 \tag{4.10}$$

and

$$\int_{m_{\mathcal{B}}} \delta\boldsymbol{\alpha} \cdot \mathbf{S}^T \cdot \mathbf{M} : [\mathbf{M}^* \cdot \mathbf{S} \cdot \boldsymbol{\beta} - \mathbf{M}^* \cdot \mathbf{M} : \tilde{\tilde{\boldsymbol{\sigma}}}] \; dm = 0 \,. \tag{4.11}$$

At first glance little has been gained by making this substitution. However, by requiring $\mathbf{M} : \mathbf{M}^* = \mathbf{1}$—where $\mathbf{1}$ is the unity operator of appropriate dimension—both Equations (4.10) and (4.11) are simplified. $\boldsymbol{\alpha}$, $\boldsymbol{\beta}$, $\delta\boldsymbol{\alpha}$ and $\delta\boldsymbol{\beta}$ can be taken outside the integrals, as these terms are independent of the spatial domain. For arbitrary variations $\delta\boldsymbol{\alpha}$ and $\delta\boldsymbol{\beta}$ two systems of equations are obtained:

$$\boldsymbol{\alpha} = \mathbf{H}^{-1} \cdot \int_{m_{\mathcal{B}}} \mathbf{S}^T \cdot \mathbf{M} : \tilde{\boldsymbol{\varepsilon}} \, dm \qquad \text{and} \qquad \boldsymbol{\beta} = \mathbf{H}^{-1} \cdot \int_{m_{\mathcal{B}}} \mathbf{S}^T \cdot \mathbf{M} : \tilde{\tilde{\boldsymbol{\sigma}}} \, dm \;, \tag{4.12}$$

with

$$\mathbf{H} = \int_{m_{\mathcal{B}}} \mathbf{S}^T \cdot \mathbf{S} \, dm \;. \tag{4.13}$$

4.3 Anti-Locking Approaches

The type of anti-locking employed depends on the filter/reconstruction operators; indeed there are multiple choices possible for the tensors $\mathbf{M}$ and $\mathbf{M}^*$. The standard decomposition of stress and strain into volumetric and deviatoric parts leads to two natural choices for $\mathbf{M}$ and $\mathbf{M}^*$. Clearly these are not the only feasible choices, but they are the only two considered here.

4.3.1 Volumetric Approach

This technique constructs a constant approximation for *only* the volumetric portions of the stress and strain fields over the desired control volume. The deviatoric fields remain unmodified. This idea was first investigated in the work by Shin (2009). The volumetric component of a tensor can be represented with a single scalar value, thus motivating the following filter matrix definitions:

$$[\mathbf{M}] = [\mathbf{M}_{vol}] := [\; 1 \;\; 1 \;\; 1 \;\; 0 \;\; 0 \;\; 0 \;] \text{ and } [\mathbf{M}^*] = [\mathbf{M}^*_{vol}] := [\; 1/3 \;\; 1/3 \;\; 1/3 \;\; 0 \;\; 0 \;\; 0 \;]^T \;, \tag{4.14}$$

with $\mathbf{M}^* \cdot \mathbf{M} = 1/3\,\mathbf{1} \otimes \mathbf{1}$ being the volumetric operator and its complementary filter, $\mathbb{P}$, becomes the deviatoric operator $\mathbb{I}^{dev} = \mathbb{I} - 1/3\,\mathbf{1} \otimes \mathbf{1}$. For this approximation scheme the

shape matrix contains a single entry: $[\mathbf{S}] = [\,1\,]$. The unknown parameters $\boldsymbol{\alpha}$ and $\boldsymbol{\beta}$ (as well as their variations) assume the following form

$$\{\boldsymbol{\alpha}\} = \{\,\alpha_1\,\}\,, \quad \{\delta\boldsymbol{\alpha}\} = \{\,\delta\alpha_1\,\}, \quad \{\boldsymbol{\beta}\} := \{\,\beta_1\,\}, \quad \text{and} \quad \{\delta\boldsymbol{\beta}\} = \{\,\delta\beta_1\,\}\,. \tag{4.15}$$

This approximation leads to

$$\alpha_1 = \operatorname{tr}\boldsymbol{\varepsilon}^h = \hat{\theta} \quad \text{and} \quad \beta_1 = \operatorname{tr}\bar{\boldsymbol{\sigma}}^h = 3\,\hat{\bar{p}}\,, \tag{4.16}$$

where $\hat{\theta}$ is the dilation and $\hat{\bar{p}}$ the mass specific isotropic stress, assumed constant throughout the selected control volume. This approach will mitigate volumetric locking and, as will be shown in the following chapters, is beneficial for all simulation types.

4.3.2 Volumetric-Deviatoric Approach

This anti-locking strategy builds approximations for both the volumetric and deviatoric portions of the strain and stress tensor fields. This technique provides finer grained control, as each portion is constructed independently. The following definitions are used for the filter matrices

$$[\mathbf{M}] := \begin{bmatrix} 1 & 1 & 1 & 0 & 0 & 0 \\ 2/3 & -1/3 & -1/3 & 0 & 0 & 0 \\ -1/3 & 2/3 & -1/3 & 0 & 0 & 0 \\ 0 & 0 & 0 & 1 & 0 & 0 \\ 0 & 0 & 0 & 0 & 1 & 0 \\ 0 & 0 & 0 & 0 & 0 & 1 \end{bmatrix} \quad [\mathbf{M}^*] := \begin{bmatrix} 1/3 & 1 & 0 & 0 & 0 & 0 \\ 1/3 & 0 & 1 & 0 & 0 & 0 \\ 1/3 & -1 & -1 & 0 & 0 & 0 \\ 0 & 0 & 0 & 1 & 0 & 0 \\ 0 & 0 & 0 & 0 & 1 & 0 \\ 0 & 0 & 0 & 0 & 0 & 1 \end{bmatrix}, \tag{4.17}$$

leading to $\mathbf{M}^* \cdot \mathbf{M} = \mathbb{I}$. Thus, the projection operator, $\mathbb{P}$, is reduced to the 4^{th} order zero tensor, $\mathbb{O}$. The shape matrix is

$$[\mathbf{S}] := \begin{bmatrix} 1 & 0 & 0 & 0 & 0 & 0 & \xi & \eta & \zeta & 0 & 0 & 0 & 0 & 0 & 0 \\ 0 & 1 & 0 & 0 & 0 & 0 & 0 & 0 & 0 & \xi & \eta & \zeta & 0 & 0 & 0 \\ 0 & 0 & 1 & 0 & 0 & 0 & 0 & 0 & 0 & 0 & 0 & 0 & \xi & \eta & \zeta \\ 0 & 0 & 0 & 1 & 0 & 0 & 0 & 0 & 0 & 0 & 0 & 0 & 0 & 0 & 0 \\ 0 & 0 & 0 & 0 & 1 & 0 & 0 & 0 & 0 & 0 & 0 & 0 & 0 & 0 & 0 \\ 0 & 0 & 0 & 0 & 0 & 1 & 0 & 0 & 0 & 0 & 0 & 0 & 0 & 0 & 0 \end{bmatrix}, \tag{4.18}$$

where the local coordinates ξ, η, and ζ are parallel to global x, y, and z with the origin shifted to the *centroid of the control volume.* Defining $\mathbf{S}$ in this way decouples the shear terms from the the normal terms. In addition, the shear terms are assumed constant throughout the

control volume. These selections for $\mathbf{M}$, $\mathbf{M}^*$, and $\mathbf{S}$ imply the following structure for $\boldsymbol{\alpha}$ and $\boldsymbol{\beta}$ (as well as their variations):

$$\{\boldsymbol{\alpha}\} = \{\alpha_1\ \alpha_2\ \alpha_3\ ...\ \alpha_{15}\}^T \quad \text{and} \quad \{\delta\boldsymbol{\alpha}\} = \{\delta\alpha_1\ \delta\alpha_2\ \delta\alpha_3\ ...\ \delta\alpha_{15}\}^T\ , \tag{4.19}$$

$$\{\boldsymbol{\beta}\} = \{\beta_1\ \beta_2\ \beta_3\ ...\ \beta_{15}\}^T \quad \text{and} \quad \{\delta\boldsymbol{\beta}\} = \{\delta\beta_1\ \delta\beta_2\ \delta\beta_3\ ...\ \delta\beta_{15}\}^T\ . \tag{4.20}$$

This formulation accounts for a full trilinear variation in both the volumetric and deviatoric portions of the stress and strain approximations. The volumetric portion of the strain and stress approximations are

$$\operatorname{tr}\boldsymbol{\varepsilon}^h = \alpha_1 + \alpha_7\,\xi + \alpha_8\,\eta + \alpha_9\,\zeta \quad \text{and} \quad \operatorname{tr}\bar{\boldsymbol{\sigma}}^h = \beta_1 + \beta_7\,\xi + \beta_8\,\eta + \beta_9\,\zeta \tag{4.21}$$

In a similar fashion, the trilinear variation of the deviatoric strain components, e_{11} and e_{22}, are constructed using $\alpha_{2,10-12}$ and $\alpha_{3,13-15}$, respectively. The deviatoric stress components $\bar{s}_{11}$ and $\bar{s}_{22}$, are built from $\beta_{2,10-12}$ and $\beta_{3,13-15}$, respectively. The deviatoric components e_{33} and $\bar{s}_{33}$ are well defined implicitly through $\operatorname{tr}(\operatorname{dev}\bar{\boldsymbol{\sigma}}) = \operatorname{tr}\bar{\mathbf{s}} = 0$ and $\operatorname{tr}(\operatorname{dev}\boldsymbol{\varepsilon}) = \operatorname{tr}\mathbf{e} = 0$, i.e.,

$$e_{33} = -e_{11} - e_{22} \qquad \text{and} \qquad s_{33} = -s_{11} - s_{22}\ . \tag{4.22}$$

This approximation will mitigate shear locking and lead to constant shear stress terms throughout the control volume. In addition, by enforcing

$$\alpha_7 = \alpha_8 = \alpha_9 = 0 \quad \text{and} \quad \beta_7 = \beta_8 = \beta_9 = 0\,, \tag{4.23}$$

the volumetric portion becomes constant, mitigating volumetric locking as well. This final modification addresses both volumetric and shear locking.

4.4 Numeric Implementation

The formulation of constraints (4.10) and (4.11) is presented in terms of a mass integral. This representation is more common in particle based methods than traditional FEM formulations. To reiterate a key formulation detail from Chapter 2, mass integrals in the MPM are evaluated by summation over particles, that is

$$\int_{m_{\mathcal{B}}} (\bullet)\ dm \approx \sum_p (\bullet)\ m_p\,, \tag{4.24}$$

where $(\bullet)$ is any quantity of interest, m_p is the mass of a particle and $\sum_p$ represents a sum over all particles that comprise the body. The subscript p refers to a particle quantity. The integrals in (4.12) and (4.13) are evaluated over control volumes that, collectively, envelop the body being analyzed. The MPM has two natural choices for control volumes, the first being a single grid cell while the second is the support of a node. These two options, along with a third variant that effectively combines the two, are explored in detail in this section.

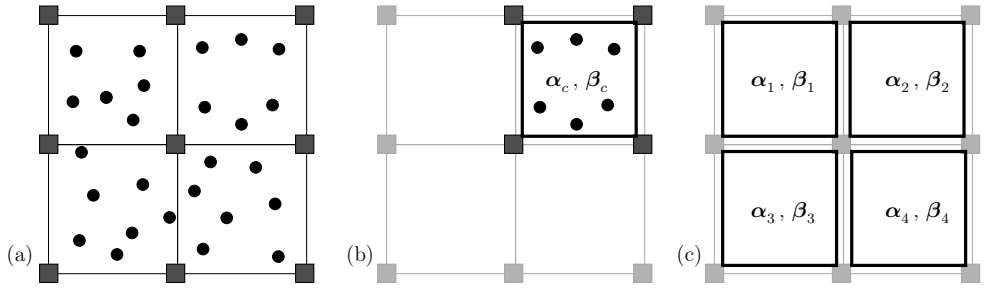

Figure 4.1: Cell-Based approach for determining unknown parameters $\boldsymbol{\alpha}$ and $\boldsymbol{\beta}$. (a) Example particle configuration. (b) Particles within each cell are used to determine a cell-based $\boldsymbol{\alpha}_c$ and $\boldsymbol{\beta}_c$. (c) Each cell containing particles has unique values for $\boldsymbol{\alpha}$ and $\boldsymbol{\beta}$.

4.4.1 Cell-Based Approach

This approach uses a single grid cell as the control volume. This is advantageous because the union of cells spans the volume of the body, and cells are non-overlapping. The resulting approximation defines local values for both $\boldsymbol{\alpha} \to \boldsymbol{\alpha}_c$ and $\boldsymbol{\beta} \to \boldsymbol{\beta}_c$ for each cell c, as illustrated in Figure 4.1. Using Equation (4.12) and the integration approximation outlined by (4.24), the unknown cell parameters are obtained from the linear systems

$$\boldsymbol{\alpha}_c = \mathbf{H}_c^{-1} \cdot \sum_{p \,\in\, c} \mathbf{S}_p^T \cdot \mathbf{M} : \tilde{\boldsymbol{\varepsilon}}_p \, m_p \qquad \text{and} \qquad \boldsymbol{\beta}_c = \mathbf{H}_c^{-1} \cdot \sum_{p \,\in\, c} \mathbf{S}_p^T \cdot \mathbf{M} : \tilde{\bar{\boldsymbol{\sigma}}}_p \, m_p \,, \tag{4.25}$$

with $\mathbf{H}_c$ following from (4.13) as

$$\mathbf{H}_c = \sum_{p \,\in\, c} \mathbf{S}_p^T \cdot \mathbf{S}_p \, m_p \;. \tag{4.26}$$

Calculating $\boldsymbol{\alpha}_c$ and $\boldsymbol{\beta}_c$ cannot occur simultaneously, contrary to what listing (4.25) may imply. Rather, $\boldsymbol{\alpha}_c$ must be computed first using Equation $(4.25)_1$ as well as the particle strain, $\tilde{\boldsymbol{\varepsilon}}_p$. Note that the strain term $\tilde{\boldsymbol{\varepsilon}}_p$ is computed a priori by numerically integrating the velocity field approximation. Once the vector $\boldsymbol{\alpha}_c$ is determined, the strain approximation *within each cell* is built using

$$\boldsymbol{\varepsilon}_p^h = \mathbf{M}^* \cdot \mathbf{S}_p \cdot \boldsymbol{\alpha}_c + \mathbb{P} : \tilde{\boldsymbol{\varepsilon}}_p \,, \tag{4.27}$$

where $\mathbf{S}_p = \mathbf{S}(\mathbf{x}_p)$. The specific particle stress is computed from the strain approximation, i.e., $\tilde{\bar{\boldsymbol{\sigma}}}_p = \partial\psi(\boldsymbol{\varepsilon}_p^h)/\partial\boldsymbol{\varepsilon}_p^h$. The cell-wise $\boldsymbol{\beta}_c$ vector is determined using Equation $(4.25)_2$ and the stress approximation follows as

$$\bar{\boldsymbol{\sigma}}_p^h = \mathbf{M}^* \cdot \mathbf{S}_p \cdot \boldsymbol{\beta}_c + \mathbb{P} : \tilde{\bar{\boldsymbol{\sigma}}}_p \,. \tag{4.28}$$

In this manner the strain and stress approximations are built in each cell of the computational domain.

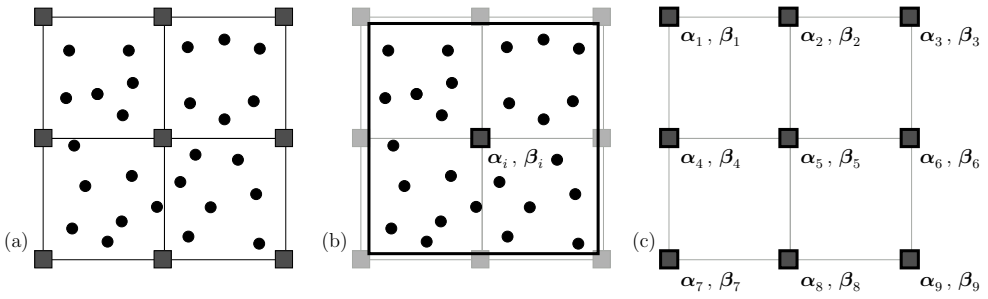

Figure 4.2: Node-Based approach for determining unknown parameters $\boldsymbol{\alpha}$ and $\boldsymbol{\beta}$. (a) Example particle configuration. (b) Particles within the support of each node are used to determine a node-based $\boldsymbol{\alpha}_i$ and $\boldsymbol{\beta}_i$ (shown support for center node assumes linear shape functions). (c) Each node containing particles within its support has unique values for $\boldsymbol{\alpha}$ and $\boldsymbol{\beta}$.

4.4.2 Node-Based Approach

This strategy uses the nodal support for node i, defined by the shape function $N_i(\mathbf{x}) \neq 0$, as a control volume for evaluating the integrals in Equations (4.12) and (4.13). The resulting approximation constructs both $\boldsymbol{\alpha} \to \boldsymbol{\alpha}_i$ and $\boldsymbol{\beta} \to \boldsymbol{\beta}_i$ at each node i in the domain as shown in Figure 4.2. The unknown nodal values are determined from

$$\boldsymbol{\alpha}_i = \mathbf{H}_i^{-1} \cdot \sum_{p\,\in\,i} \mathbf{S}_p^T \cdot \mathbf{M} : \tilde{\boldsymbol{\varepsilon}}_p \, N_{ip} \, m_p \quad \text{and} \quad \boldsymbol{\beta}_i = \mathbf{H}_i^{-1} \cdot \sum_{p\,\in\,i} \mathbf{S}_p^T \cdot \mathbf{M} : \tilde{\tilde{\boldsymbol{\sigma}}}_p \, N_{ip} \, m_p \ , \tag{4.29}$$

with $N_{ip} = N_i(\mathbf{x}_p)$ and $\mathbf{H}_i$ given by

$$\mathbf{H}_i = \sum_{p\,\in\,i} \mathbf{S}_p^T \cdot \mathbf{S}_p \, N_{ip} \, m_p \ . \tag{4.30}$$

This approach has overlapping control volumes. Thus, when compared to its cell-based counterpart, the node-based approach requires additional steps to compute the desired fields. Both the strain and and stress approximations are constructed at all nodes using $\boldsymbol{\alpha}_i$, $\boldsymbol{\beta}_i$, and the shape matrix $\mathbf{S}(\boldsymbol{\xi}_i)$:

$$\hat{\boldsymbol{\varepsilon}}_i = \mathbf{S}(\boldsymbol{\xi}_i) \cdot \boldsymbol{\alpha}_i \qquad \text{and} \qquad \hat{\tilde{\boldsymbol{\sigma}}}_i = \mathbf{S}(\boldsymbol{\xi}_i) \cdot \boldsymbol{\beta}_i \, . \tag{4.31}$$

The vector $\boldsymbol{\xi}_i$ is the location of the node i relative to the mass centroid of the particles within the support of that node. These nodal approximations are then mapped back to the particle using

$$\boldsymbol{\varepsilon}_p^h = \mathbf{M}^* \cdot \sum_i N_{ip} \, \hat{\boldsymbol{\varepsilon}}_i + \mathbb{P} : \tilde{\boldsymbol{\varepsilon}}_p \qquad \text{and} \qquad \bar{\boldsymbol{\sigma}}_p^h = \mathbf{M}^* \cdot \sum_i N_{ip} \, \hat{\tilde{\boldsymbol{\sigma}}}_i + \mathbb{P} : \tilde{\tilde{\boldsymbol{\sigma}}}_p \ . \tag{4.32}$$

As with the cell-based approach the strain and stress fields cannot be constructed simultaneously. All strain related values must be computed first, and then the stress approximation can follow. Careful testing of the node based approach shows improved performance for pressure-dominant problems. However, dissipation of the deviatoric components of stress and strain leads to poor results when applied to solids with finite shear stiffness. There are two remedies that help mitigate this problem. The first modifies the node-based philosophy and simply treats the nodal support as if it were a large cell. Doing so removes the shape function dependence in Equations (4.29) and (4.30). Particle values are still interpolated from the nodes as indicated in Equation (4.32) using a weight specific to each node. The traditional option for a nodal weight (and what is presented in Equation (4.32)) is the shape function value evaluated at the particle location. However, preliminary in-house studies suggest that just the simplistic algebraic average of all nodes a particle is in the support of can significantly reduces the shear dissipation. The second alternative is dubbed the hybrid approach and introduced next.

4.4.3 Hybrid Approach

The hybrid approximation utilizes the volumetric portion computed using the node-based control volume, and combines this with the deviatoric portion computed using the cell-based approach. The appropriate portion of the nodal tensors given in Equation (4.31) are extracted and reconstructed with $\mathbf{M} = \mathbf{M}_{vol}$, $\mathbf{M}^* = \mathbf{M}^*_{vol}$ defined in (4.14). The deviatoric portion is isolated using the cell-based approximations (4.27) and (4.28) with

$$[\mathbf{M}_{dev}] := \begin{bmatrix} 2/3 & -1/3 & -1/3 & 0 & 0 & 0 \\ -1/3 & 2/3 & -1/3 & 0 & 0 & 0 \\ 0 & 0 & 0 & 1 & 0 & 0 \\ 0 & 0 & 0 & 0 & 1 & 0 \\ 0 & 0 & 0 & 0 & 0 & 1 \end{bmatrix} \quad [\mathbf{M}^*_{dev}] := \begin{bmatrix} 1 & 0 & 0 & 0 & 0 \\ 0 & 1 & 0 & 0 & 0 \\ -1 & -1 & 0 & 0 & 0 \\ 0 & 0 & 1 & 0 & 0 \\ 0 & 0 & 0 & 1 & 0 \\ 0 & 0 & 0 & 0 & 1 \end{bmatrix} . \tag{4.33}$$

The complementary projection reduces to $\mathbb{P} = \mathbb{O}$ and the final particle strain and stress approximations are

$$\boldsymbol{\varepsilon}^h_p = \operatorname{vol} \boldsymbol{\varepsilon}^h_p + \operatorname{dev} \boldsymbol{\varepsilon}^h_p = \mathbf{M}^*_{vol} \cdot \sum_i N_{ip}\, \hat{\boldsymbol{\varepsilon}}_i + \mathbf{M}^*_{dev} \cdot \mathbf{S}_p \cdot \boldsymbol{\alpha}_c \tag{4.34}$$

and

$$\bar{\boldsymbol{\sigma}}^h_p = \operatorname{vol} \bar{\boldsymbol{\sigma}}^h_p + \operatorname{dev} \bar{\boldsymbol{\sigma}}^h_p = \mathbf{M}^*_{vol} \cdot \sum_i N_{ip}\, \hat{\bar{\boldsymbol{\sigma}}}_i + \mathbf{M}^*_{dev} \cdot \mathbf{S}_p \cdot \boldsymbol{\beta}_c \; . \tag{4.35}$$

4.4.4 Generalization for finite deformations

The presentation thus far has assumed small deformation kinematics, i.e., $\tilde{\boldsymbol{\varepsilon}}(\mathbf{u}) = \nabla^s \mathbf{u}$. Extension to finite strains does not affect the weak form Equations (4.3)–(4.5), though their derivation is somewhat more involved. The key difference is the need for a finite deformation strain function, where the resulting strain tensor must reside in the deformed configuration. A popular and convenient strain measure is Hencky-strain, also known as logarithmic strain, and defined by the strain function

$$\tilde{\boldsymbol{\varepsilon}}(\mathbf{u}) = \tilde{\tilde{\boldsymbol{\varepsilon}}}(\tilde{\mathbf{b}}) := \frac{1}{2} \log \tilde{\mathbf{b}} \,, \tag{4.36}$$

where $\tilde{\mathbf{b}} = \mathbf{F} \cdot \mathbf{F}^T$ is the left Cauchy-Green deformation tensor, and $\mathbf{F}$ is the deformation gradient. Given a particle strain $\tilde{\mathbf{b}}_{p,n}$ at time t_n, its value is updated using the incremental deformation tensor

$$\mathbf{f}_p = \mathbf{f}(\mathbf{x}_p) \approx \mathbf{1} + \Delta t \, \boldsymbol{\nabla} \mathbf{v}^h_{p,n+1} \tag{4.37}$$

as

$$\tilde{\mathbf{b}}_{p,n+1} = \mathbf{f}_p \cdot \tilde{\mathbf{b}}_{p,n} \cdot \mathbf{f}_p^T \,. \tag{4.38}$$

Since the velocity gradient $\boldsymbol{\nabla} \mathbf{v}^h_{p,n+1}$ is computed from the interpolated velocity field, $\mathbf{f}_p$ and $\tilde{\mathbf{b}}_{p,n+1}$ are subject to kinematic locking. Hence, additional steps must be taken to alleviate the accumulation of fictitious strains. The solution lies in the fact that the anti-locking algorithms are directly applied to the particle strain

$$\tilde{\boldsymbol{\varepsilon}}_{p,n+1} = \tilde{\tilde{\boldsymbol{\varepsilon}}}(\tilde{\mathbf{b}}_{p,n+1}) \,, \tag{4.39}$$

and, thus, the strain $\boldsymbol{\varepsilon}^h_{p,n+1}$ approximation does not require any modifications to the small-strain algorithm. However, using $\tilde{\mathbf{b}}_p$ as the internal particle strain measure requires inversion of $\tilde{\tilde{\boldsymbol{\varepsilon}}}(\mathbf{b})$ to obtain the modified left Cauchy-Green deformation tensor as

$$\mathbf{b}_{p,n+1} := \exp\left(2\boldsymbol{\varepsilon}^h_{p,n+1}\right) \,. \tag{4.40}$$

This value is then set $\mathbf{b}_{p,n+1} \to \tilde{\mathbf{b}}_{p,n}$ in preparation for the next time step.

4.4.5 Extension to elastoplastic materials

The MPM is a tool best used for history dependent materials in large deformation applications. The presentation thus far does not take into account material nonlinearity and this topic needs to be addressed. The fact that no distinction has been made between elastic and inelastic materials is not a restriction of the anti-locking formulation, rather, elastic

properties were assumed for presentation purposes. This subsection expands the framework to include elastoplastic materials and identifies two potential approaches.

The constraint given by Equation (4.3) is used to build an approximation for the strain field. For an elastic material this is the end of the story. The same cannot be said for an inelastic material. Careful distinction must be made between the total, elastic, and plastic deformation as outlined in Chapter 3. This immediately poses the question: which strain measure should be approximated? Two possible options are the elastic strain *or* the total strain (presumably both measures could be approximated but this is not really necessary). Aspects of each option are discussed below. This presentation is limited to elastoplastic isotropic materials in an isothermal setting. Materials that do not satisfy this description are not implemented in this framework and are beyond the primary scope of this work.

The first scheme is to approximate the elastic strain measure. This is arguably the most logical choice. This statement is based on a couple considerations. The only deformation measure that contributes directly to the mechanical stress is the elastic strain. Providing an elastic strain measure that is free of kinematic locking is one way to help ensure the stress measure will follow suit. Second, from a formulation standpoint, both the MPM and the general return mapping algorithms presented in Chapter 3 need *only* the incremental strain measure each time step. This value is tacked onto a previously known state. The material models assume the increment is elastic (recall the notion of a trial state) and modify the plastic variables as required should the yield condition be violated. Thus, a suitable elastic deformation measure—be it a trial or actual—is all that is actually needed (assuming the initial state of the material is given).

Extending this concept to the anti-locking strategy is straight forward. It is not possible to approximate the actual elastic strain field without computing the updated stress values. This would be a waste computationally since the stress is going to be re-computed using an approximated strain measure. However, what can be determined with minimal effort is the updated elastic *trial* at the particle level: $\tilde{\boldsymbol{\varepsilon}}_p^{e,tr}$. It is this trial value that replaces $\tilde{\boldsymbol{\varepsilon}}_p$ in the anti-locking discussion thus far. Note that large deformation analyses must first compute a trial left Cauchy-Green deformation tensor, $\tilde{\mathbf{b}}_p^{e,tr}$, before computing the corresponding logarithmic strain measure. Substituting $\tilde{\boldsymbol{\varepsilon}}_p^{e,tr}$ for $\tilde{\boldsymbol{\varepsilon}}_p$ builds a suitable approximation to the trial elastic strain field. As noted in several publications (e.g., Alawaji et al. (1992); Borja et al. (2003); Simo (1998)) the principle directions of the trial elastic strain and converged elastic strain coincide— thus ensuring the final shape of the elastic strain field is locking free. Once the trial elastic strain field is known, $\boldsymbol{\varepsilon}_p^{h,\ e,tr}$, the appropriate portion of the particle strain is overwritten and the stress approximation proceeds unchanged. This approach does

not change or impact the accumulation of plastic strains and internal state variables.

The second alternative seeks an approximation to the total strain field within a given control volume. From a formulation standpoint this approach is appealing; the variational formulation presented in this chapter works directly with a strain function, presumably derived from a displacement function. However, this approach does not consider how to handle plastic variables. This is a concern because approximating the total strain field can impart very large deformations on particles/points whose actual deformation history may be very small. There is no way to properly capture this history unless the state variables are modified as well. While this additional modification is possible, it presents a rabbit hole scenario where the realized benefits are significantly diminished by the overhead required to make it happen.

At one point or another both the elastic strain and the total strain approaches have been implemented. From an algorithmic standpoint the two are nearly indistinguishable but the findings are drastically different. Approximating the total strain is very problematic and is best captured by a single word: chaos! Simulations blow up and are of no value. On the other hand, approximating the elastic trial strain continues to provided favorable results. For this reason it is the preferred method for incorporating material nonlinearity into the anti-locking algorithm and is currently the only method implemented in the coding framework.

4.4.6 Computational Considerations

Problems arise when particles reside exclusively on or close to a single plane (3D simulations) or on a line (2D simulations), respectively. Under these conditions, $\mathbf{H}_c$ and/or $\mathbf{H}_i$ becomes singular or sufficiently ill-conditioned such that no solution for the weak form Equations (4.3) and (4.4) can be found. Typically, this happens if a body enters a new cell with just a few particles. Only the constant volumetric stress/strain approach is immune to this condition. Hence, if a singular matrix $\mathbf{H}$ is encountered for any given control volume (cell or nodal support), a fall-back to the volumetric smoothing is used for that time step.

4.5 Algorithmic Overview

Incorporation of the anti-locking strategy requires minor changes to the standard algorithm. Table 4.1 outlines the specific modifications to the standard algorithm for the cell-based, node-based, and hybrid approaches. Large deformation analyses and/or elastoplastic materials require additional modifications as outlined in Sections 4.4.4 and 4.4.5. The anti-locking

Table 4.1: Algorithmic implementation of anti-locking strategy

1. Map particles to nodes. Update nodes from t_n to t_{n+1} as outlined in Chapter 2.
2. Compute the velocity gradient and update the strain at the particle level. This is $\tilde{\boldsymbol{\varepsilon}}_p$.
3. (a) *IF* Cell-Based Approach:
   Compute $\boldsymbol{\alpha}_c$ from Equation $(4.25)_1$
   Compute $\boldsymbol{\varepsilon}_p^h$ from Equation (4.27)
   (b) *IF* Node-Based Approach:
   Compute $\boldsymbol{\alpha}_i$ from Equation $(4.29)_1$
   Compute $\hat{\boldsymbol{\varepsilon}}_i$ from $(4.31)_1$
   Compute $\boldsymbol{\varepsilon}_p^h$ from Equation $(4.32)_1$
   (c) *IF* Hybrid-Based Approach:
   Perform Steps 3a AND 3b
   Compute $\boldsymbol{\varepsilon}_p^h$ from Equation (4.34)
4. Overwrite $\tilde{\boldsymbol{\varepsilon}}_p$ from Step 2 with the strain approximation, $\boldsymbol{\varepsilon}_p^h$, computed in Step 3.
5. Compute $\tilde{\tilde{\boldsymbol{\sigma}}}_p$ corresponding to $\boldsymbol{\varepsilon}_p^h$ (and particle state variables if applicable).
6. (a) *IF* Cell-Based Approach:
   Compute $\boldsymbol{\beta}_c$ from Equation $(4.25)_2$
   Compute $\bar{\boldsymbol{\sigma}}_p^h$ from Equation (4.28)
   (b) *IF* Node-Based Approach:
   Compute $\boldsymbol{\beta}_i$ from Equation $(4.29)_2$
   Compute $\hat{\boldsymbol{\sigma}}_i$ from $(4.31)_2$
   Compute $\bar{\boldsymbol{\sigma}}_p^h$ from Equation $(4.32)_2$
   (c) *IF* Hybrid-Based Approach:
   Perform steps 6a AND 6b
   Compute $\bar{\boldsymbol{\sigma}}_p^h$ from Equation (4.35)
7. Overwrite $\tilde{\tilde{\boldsymbol{\sigma}}}_p$ from Step 5 with the stress approximation, $\bar{\boldsymbol{\sigma}}_p^h$, computed in Step 6
8. Update particle velocity and position as outlined in Chapter 2.

algorithm is highlighted through a series of example simulations in Chapters 6 and 7, where both elastic and inelastic materials are considered for fluid and solid mechanics applications.

4.6 Summary

In this chapter the theoretical framework of different anti-locking strategies was presented. Both cell- and node-based control volumes were identified, from which three anti-locking approaches emerged. In addition to multiple control volumes, different techniques for approximating the volumetric and deviatoric portions of the strain and stress field were discussed. In Chapters 6 and 7 the effectiveness of the anti-locking routines is highlighted.

Chapter 5

A VOLUME CONSTRAINT APPROACH AND OTHER CONSIDERATIONS

The pointwise nature of the traditional MPM assumes the mass associated with a given integration point is confined to a single location. When describing this field in a mathematical sense the only option is the traditional Dirac delta function. This fundamental treatment is argued here to be among the most basic premises upon which the Material Point Method is built—and implies that each particle has an assumed, or implicit, volume definition obtainable from the point-wise mass and current density. The particle volume definition can lead to scenarios in which the implied volume is not consistent with the amount of space available. Of course, the available space itself must be defined in terms of some global, all encompassing frame of reference whereby the notion of an under- or over-filled volume is physically meaningful. In the context of the MPM a natural choice for this frame of reference is the Eulerian computational grid. Physically this entity represents the global domain the body lives in. The volume constraint presented in this chapter provides assurance that the spatial volume occupied by the body throughout the simulation remains consistent with the amount of space available as defined by the computational grid.

Before delving into the formulation it is necessary to identify the most basic goal of this particular volume constraint. This is just one of many possible volume-based constraints. The current constraint was initially conceived to prevent volume overloading of a region. From a physical perspective this notion is very appealing: the amount of matter in a global or reference space cannot exceed 100% of said space. This qualitative argument bred the idea that a unique, compressive pressure must develop to prevent the overloading scenario from occurring. Over time this idea has evolved to a general framework in which the goal is to compute a constraint pressure that ensures the amount of space occupied by the matter is consistent with the available space. The pressure can be compressive (negative) or expansive (positive). In this context, the term *consistent* implies the volume occupied by matter in a given region is unchanging, that is, if the reference volume is initially 100% full, then the reference volume will remain 100% full at all times. The same is true for any initial volume. For example, if the reference volume is initially 1.63254% full, then the reference volume will remain 1.63254% full at all times. Thus, the analyst assumes some

responsibility for ensuring an appropriate spatial definition at the outset of a simulation. In actuality this responsibility is no different than the traditional MPM—where the analyst must ensure reasonable particle mass values that are consistent with the amount of space occupied by the body.

An important point to keep in mind is the following: the entire premise of this work is based on the singular, qualitative notion that a pressure must develop to ensure the matter occupies a user prescribed percentage of the reference volume. This logic presupposes that the volume constraint and corresponding pressure are *the physical phenomena responsible for obtaining desired behavior*. If in fact the underlying physical phenomenon governing the desirable response is something different, e.g., an alternative momentum exchange process, then this entire framework is subject to scrutiny and the relative importance of the volume constraint diminishes considerably. Indeed this was found to be the case, and this work has shown the volume constraint is not capable of providing the unifying behavior the constraint was originally thought to provide. Considerations supporting this viewpoint are presented in Section 5.4, where discussions outlining the limitations imposed by the constraint far exceed the capabilities in the context of the MPM.

The volume constraint formulation is presented from a mulitphase viewpoint, and in particular, a saturated or fully saturated porous media viewpoint. This is not strictly necessary and is not a limitation of the constraint framework. Such an approach is taken here because it provides a natural environment for which the constraint can be applied. That being the case, several tidbits of notation and theory are pulled from existing multiphase frameworks cast specifically in a geotechnical engineering context—including those by Zienkiewicz and Shiomi (1984), Diebels and Ehlers (1996), and Lewis and Schrefler (1998). This chapter does not provide a theoretical treatise on the background and development of the governing equations of multiphase mechanics. Nor does this formulation address other momentum exchange processes that occur between phases, including drag or permeability related forces, buoyancy forces, thermo-coupling forces, or the transformation of matter via phase change. These are topics that exist *independently* of the volume constraint and unnecessarily complicate the process of obtaining a pressure consistent with the amount of material in a given space. Readers interested in alternative momentum exchange processes can consult the large number of textbooks and papers available on the subject. Here the emphasis is placed on presenting the general governing equations in a format immediately applicable to the Material Point Method framework.

This chapter employs the following notation:

$$(\bullet)^{\alpha} = \theta^{\alpha} (\bullet)_{\alpha} \ , \tag{5.1}$$

where $(\bullet)$ is a general quantity of interest, a superscript character denotes a *bulk*, or *partial*, quantity of the phase indicator (α in the present case). A subscript indicates a *constituent*[1] quantity. The term θ^α is the current volume ratio of the constituent volume to reference volume—also known as the volume fraction.

5.1 Building an Appropriate Weak Formulation

The volume constraint itself has very little to do with the weak form of the momentum balance equations. However, examining these equations in a multiphase context serves two purposes. First, key relationships between constituent and bulk properties are identified that are not readily observable from the weak form presentation in Chapter 2. For example, this presentation will show the stress-like terms must be mass specific with respect to the constituent density when the weak form is cast in terms of mass integrals. Second, this discussion provides a road map (for lack of a better term) as to what portions of the standard MPM algorithm are modified due the inclusion of a constraint pressure.

Since the end desire is to implement this formulation in the MPM only those equations necessary to do so are presented in this chapter. The approach taken here assumes that each phase will be modeled using a distinct motion. Individual phase equations are the initial focus (as opposed to those commonly employed in mixture theories, such as momentum balance of the mixture or other mixture balance equations). In the presence of more than one phase, the balance of linear momentum of each constituent requires

$$\rho^\alpha \, \dot{\mathbf{v}}^\alpha = \operatorname{div} \boldsymbol{\sigma}^\alpha + \mathbf{b}^\alpha + \hat{\mathbf{p}}^\alpha \ , \tag{5.2}$$

where ρ^α is the bulk density, $\boldsymbol{\sigma}^\alpha$ is the bulk Cauchy stress tensor, $\mathbf{b}^\alpha$ is the phase specific body force per volume, following from $\rho^\alpha \, \bar{\mathbf{b}}$, in which $\bar{\mathbf{b}}$ is the previously defined mass-specific body force acting on *all phases*, and $\hat{\mathbf{p}}^\alpha$ is an additional volume-specific momentum producing term that accounts for forces arising from the interaction of phase α with the other phases present, Diebels and Ehlers (1996). This term is arguably the single most important term in a multiphase formulation, as it is responsible for linking the phases that are present in a given domain. Generally speaking this additional force term can take many forms. In a multiphase setting this term can be used to capture, among other things, the drag force interaction (and consequently permeability-related interactions) and/or buoyancy forces

[1] In the literature constituent values have been referred to as *real* or *particle* quantities. The latter grammatical choice creates confusion in the context of the MPM. To disambiguate, the term *particle* is reserved for computational particles used in an analysis. The term *constituent* as used here describes a material's components and is applicable beyond the context of a specific numerical method.

between phases. Closer examination identifies this term as the only thing distinguishing Equation (5.2) from the traditional, single phase momentum balance equation presented in Chapter 2. That is, if only a single phase is present, then the interaction term is reduced to zero and the traditional momentum balance is obtained. Though this comment is quite obvious, it is nonetheless a valid statement and serves as a reminder that, at any point in time, the current multiphase formulation must reduce to the traditional formulation if only a single phase is present and $\theta^\alpha = 1.0$ holds.

The weak form follows as

$$\int_V (\rho^\alpha \dot{\mathbf{v}}^\alpha - \operatorname{div} \boldsymbol{\sigma}^\alpha - \mathbf{b}^\alpha - \hat{\mathbf{p}}^\alpha) \cdot \boldsymbol{\eta} \, dV = 0 \ , \tag{5.3}$$

where $\boldsymbol{\eta}$ is an admissible weight function. The integration domain is the total spatial volume V occupied by the mixture and is not the individual phase volume V_α. Expanding this equation yields

$$\int_V \rho^\alpha \dot{\mathbf{v}}^\alpha \cdot \boldsymbol{\eta} \, dV - \int_V \operatorname{div} \boldsymbol{\sigma}^\alpha \cdot \boldsymbol{\eta} \, dV - \int_V \mathbf{b}^\alpha \cdot \boldsymbol{\eta} \, dV - \int_V \hat{\mathbf{p}}^\alpha \cdot \boldsymbol{\eta} \, dV = 0 \ . \tag{5.4}$$

Again, the final term in the weak form listing (5.4) is due to the interaction of phases. Common practice in alternative mixture theories is to cast this interaction in terms of the void ratio (and thus volume fraction), the relative phase velocity, and a material constant, effectively linking the permeability of the solid phase with other phases present in the analysis, e.g., Diebels and Ehlers (1996). Such an approach, however, requires the use of a porous skeleton as the reference frame which conflicts with the desire to model each phase as a distinct motion. Again, the goal here is to asses the effects of a confining pressure resulting from a volume constraint—not to use existing mixture theory equations in the MPM. That being the case, this term is omitted from the remainder of this presentation, as it has no direct bearing on the volume constraint formulation. See the work by Mackenzie-Helnwein et al. (2010) for one possible treatment of this term in a multiphase context.

The following transformation follows from the chain rule of differentiation

$$-\int_V \operatorname{div} \boldsymbol{\sigma}^\alpha \cdot \boldsymbol{\eta} \, dV = -\int_V \operatorname{div} (\boldsymbol{\sigma}^\alpha \cdot \boldsymbol{\eta}) \, dV + \int_V \boldsymbol{\sigma}^\alpha : \boldsymbol{\nabla} \boldsymbol{\eta} \, dV \ , \tag{5.5}$$

from which the term

$$\int_V \operatorname{div} (\boldsymbol{\sigma}^\alpha \cdot \boldsymbol{\eta}) \, dV = \int_{\mathcal{S}} \boldsymbol{\sigma}^\alpha \cdot \mathbf{n} \cdot \boldsymbol{\eta} \, d\mathcal{S} = 0 \tag{5.6}$$

is altered using the divergence theorem to reflect an integral over the body surface, $\mathcal{S}$. Here $\mathbf{n}$ is the unit normal to said surface. Equation (5.6) may only be eliminated if the following

two conditions are met: $\boldsymbol{\eta}$ vanishes where geometric boundary conditions are prescribed *and* there are no applied exterior loads. The latter requirement is not a limitation of this framework (or the MPM in general); rather, is done here to reduce clutter as this has no immediate impact on computing the constraint pressure. Collecting the remaining terms gives

$$\int_V \rho^\alpha \, \dot{\mathbf{v}}^\alpha \cdot \boldsymbol{\eta} \, dV + \int_V \boldsymbol{\sigma}^\alpha : \boldsymbol{\nabla}\boldsymbol{\eta} \, dV - \int_V \mathbf{b}^\alpha \cdot \boldsymbol{\eta} \, dV = 0 \; . \tag{5.7}$$

The weak form in (5.7) provides a starting point for establishing a volume constraint algorithm in the context of the MPM. To reach this end goal additional modifications are necessary. Attention is first delegated to the bulk stress tensor, $\boldsymbol{\sigma}^\alpha$. Per notation consistent with Diebels and Ehlers (1996), the bulk stress is decomposed as

$$\boldsymbol{\sigma}^\alpha = \boldsymbol{\sigma}^\alpha_E - \theta^\alpha \, p \, \mathbf{1} \; , \tag{5.8}$$

where $\boldsymbol{\sigma}^\alpha_E$ is the stress obtained by the prescribed constitutive relationship and p is the additional constraint pressure this entire formulation seeks to obtain. Note that this definition assumes p carries the correct sign, that is a compressive value is negative and an expansive pressure is positive. Strictly speaking, the definition given in (5.8) is legitimate as it stands. From a geotechnical engineering perspective, the literature often gives alternate labels to these stress like variables. The $\boldsymbol{\sigma}^\alpha_E$ is cast as the effective stress and p is the pressure in the voids or pores, and hence is the pore pressure. Writing $\boldsymbol{\sigma}^\alpha_E$ as

$$\boldsymbol{\sigma}^\alpha_E = \frac{\partial \psi^\alpha \left(\boldsymbol{\varepsilon}^\alpha, K^\alpha, G^\alpha \right)}{\partial \boldsymbol{\varepsilon}^\alpha} \; = \frac{\partial \psi^\alpha}{\partial \boldsymbol{\varepsilon}^\alpha} \tag{5.9}$$

will provide additional insight shortly. For the time being, the free energy is written as a function of the bulk quantities; including the bulk volumetric stiffness, K^α, and bulk shear stiffness G^α. The free energy may also be a function of additional state variables but for presentation purposes this functional dependence is omitted.

In light of (5.8), (5.9) and (5.1) applied to the bulk density, the weak form in (5.7) becomes

$$\int_V \dot{\mathbf{v}}^\alpha \cdot \boldsymbol{\eta} \, \theta^\alpha \, \rho_\alpha \, dV + \int_V \left(\frac{\partial \psi^\alpha}{\partial \boldsymbol{\varepsilon}^\alpha} - \theta^\alpha \, p \, \mathbf{1} \right) : \boldsymbol{\nabla}\boldsymbol{\eta} \, dV - \int_V \bar{\mathbf{b}} \cdot \boldsymbol{\eta} \; \theta^\alpha \, \rho_\alpha \, dV = 0 \; , \tag{5.10}$$

where the volume element, dV, is the entire space occupied by the mixture. There are alternative integration domains, including the phase volume, dV_α, as well as the mass element dm_α. The latter proves beneficial for the MPM. The relationship between these domains is laid out as

$$dm_\alpha = \rho_{\,\alpha} \, dV_\alpha = \rho_{\,\alpha} \, \theta^\alpha \, dV \Longrightarrow dV = \frac{dm_\alpha}{\theta^\alpha \rho_{\,\alpha}} \; , \tag{5.11}$$

which provides a framework from which a mass-based formulation can be isolated:

$$\int_{m_\alpha} \dot{\mathbf{v}}^\alpha \cdot \boldsymbol{\eta}\, \theta^\alpha\, \rho_\alpha\, \frac{dm_\alpha}{\theta^\alpha \rho_{\,\alpha}} + \int_{m_\alpha} \left(\frac{\partial \psi^\alpha}{\partial \boldsymbol{\varepsilon}^\alpha} - \theta^\alpha\, p\, \mathbf{1} \right) : \boldsymbol{\nabla}\boldsymbol{\eta}\, \frac{dm_\alpha}{\theta^\alpha \rho_{\,\alpha}} - \int_{m_\alpha} \bar{\mathbf{b}} \cdot \boldsymbol{\eta}\; \theta^\alpha\, \rho_\alpha\, \frac{dm_\alpha}{\theta^\alpha \rho_{\,\alpha}} = 0 \; . \tag{5.12}$$

This is reorganized to yield

$$\int_{m_\alpha} \dot{\mathbf{v}}^\alpha \cdot \boldsymbol{\eta}\, dm_\alpha + \int_{m_\alpha} \bar{\boldsymbol{\sigma}}_\alpha : \boldsymbol{\nabla}\boldsymbol{\eta}\, dm_\alpha - \int_{m_\alpha} \bar{\mathbf{b}} \cdot \boldsymbol{\eta}\; dm_\alpha = 0 \; , \tag{5.13}$$

where

$$\bar{\boldsymbol{\sigma}}_\alpha = \frac{1}{\theta^\alpha} \left(\frac{\partial \bar{\psi}^\alpha}{\partial \boldsymbol{\varepsilon}^\alpha} \right) - \bar{p}\, \mathbf{1} \; . \tag{5.14}$$

This format leads to the critical observation that stress related measures must be *mass specific with respect to constituent density* for a mass-based weak form. Again, comparing (5.13) to the traditional form in Chapter 2 shows the standard form is easily realized for a single phase with $\theta^\alpha = 1.0$ and no constraint pressure[2]. This similarity quickly identifies how the standard algorithm is augmented by the inclusion of a constraint pressure. This topic is briefly explored in the next section where the volume constraint algorithm is presented.

5.2 Incorporating the Volume Constraint in the MPM

In the Material Point Method the unknown acceleration field, $\dot{\mathbf{v}}^\alpha$, and arbitrary weight function, $\boldsymbol{\eta}$, are constructed and solved at the nodes that make up the computational grid. Nodal values are projected into the domain via shape functions. The current implementation builds upon the multigrid framework developed by numerous MPM authors: each phase or separate body is assigned a separate grid and the motion is tracked individually. The interested reader can explore mulit-grid concepts in a contact or multiphase setting in several works, including Bardenhagen et al. (2000, 2001); Hu and Chen (2003); Pan et al. (2008); Zhang et al. (2008); Mackenzie-Helnwein et al. (2010). In these formulations there are $m+1$ grids corresponding to m phases or bodies and a single common grid that contains the contribution from all phases or bodies. This type of multigrid framework implies each individual grid represents the physical space a phase or body lives in; for multiphase simulations this treatment establishes node-based quantities on each individual grid as *partial* or *bulk* values associated with a given phase α. The *mixture* quantities and properties, should

[2]Strictly speaking a single phase formulation does not require the volume fraction to be unity nor does the pressure need to vanish. This framework can be shown to be very effective in MPM simulations for a single phase with any non-zero volume fraction.

these values be desired[3], then correspond to the common grid containing all phases. From this perspective the relationship

$$(\bullet)_i^\alpha = \hat{\theta}_i^\alpha \, (\bullet)_{p,\alpha} \ , \tag{5.15}$$

is defined which provides a physical interpretation of the link between MPM computational particles and node i values on each grid. Here a hat ($\hat{\bullet}$) is introduced to signify a volume fraction relative to the space defined by the computational grid, thus establishing $\theta^\alpha \to \hat{\theta}_i^\alpha$ as the volume fraction evaluated at a node. In this context, $(\bullet)_p$ is intended to be read as the particle *contribution*, e.g., a sum of applicable particles in a cell, or nodal support, etc., and is not intended as a strong relation between a single particle and a nodal value. The striking similarity between relation (5.15) and (5.1) leads to the important conclusion that MPM computational particles represent constituent quantities for this formulation. This statement is *not* to be interpreted as material points suddenly representing discrete grains, or physical particles. Rather, in this setting the constituent matter is represented as a continuum occupying a portion or all of the physical space defined by grid.

The system of governing equations is constructed in the same manner as outlined in Chapter 2. This includes the solution of linear momentum balance as

$$\sum_j m_{ij}^\alpha \, \dot{\mathbf{v}}_j^\alpha = \mathbf{f}_{i,\,int}^\alpha + \mathbf{f}_{i,\,ext}^\alpha \ , \tag{5.16}$$

where the force terms follow as

$$\mathbf{f}_{i,\,int}^\alpha = -\sum_{p_\alpha} \bar{\boldsymbol{\sigma}}_{p,\,\alpha} \cdot \boldsymbol{\nabla} N_{ip_\alpha} \, m_{p_\alpha} \qquad \text{and} \qquad \mathbf{f}_{i,\,ext}^\alpha = \sum_{p_\alpha} \bar{\mathbf{b}}_p \, N_{ip_\alpha} \, m_{p_\alpha} \ . \tag{5.17}$$

The particle stress term—accounting for the constraint pressure, $\bar{p}_p$—is

$$\bar{\boldsymbol{\sigma}}_{p,\,\alpha} = \frac{1}{\hat{\theta}^\alpha} \left(\frac{\partial \bar{\psi}^\alpha}{\partial \boldsymbol{\varepsilon}^\alpha} \right) \Bigg|_{p_\alpha} - \bar{p}_p \, \mathbf{1} \ , \tag{5.18}$$

where it is noted again that ($\bar{\bullet}$) denotes a quantity that is mass specific with respect to constituent density.

The remainder of this section emphasizes obtaining the time dependent constraint pressure $\bar{p}_p(t)$. Ultimately this value is obtained from the nodes using

$$\bar{p}_p = \sum_i N_{ip_\alpha} \, \bar{p}_{i,\alpha} \qquad \text{with} \qquad p_i = \rho_\alpha \, \bar{p}_{i,\alpha} \ . \tag{5.19}$$

---

[3]Common grid values are used extensively in the multigrid contact algorithms. In the present multiphase treatment the common grid is essentially ignored—as each phase is tracked with its own motion. The most glaring of the limitations of the current volume constraint as outlined in Section 5.4 could be eliminated by dropping the notion that individual phases must be tracked by individual grids.

The point mass nature of the MPM can create sceneries in which the presumed volume occupied by the particles exceeds the amount of available space (an equivalent argument can be made for under-filling space as well). The nodal pressure, $p_i(t)$, combats this shortcoming by ensuring the space occupied by matter at a node remains constant over any given time step. This statement manifests itself in terms of volume fractions as

$$\sum_{j=1}^{m} \hat{\theta}^j_{i,n} = \sum_{j=1}^{m} \hat{\theta}^j_{i,n+1} \tag{5.20}$$

for the m phases present at a node i. Such a treatment was first explored in the work by Zhang et al. (2008) and this work follows suit, establishing a framework that is very similar to theirs.

At any and all nodes the mass is conserved over a time step, $\Delta t = t_{n+1} - t_n$. This means that the bulk density at a node satisfies the relationship

$$\rho^\alpha_{n+1} = \frac{J^\alpha_n}{J^\alpha_{n+1}} \rho^\alpha_n = \frac{\rho^\alpha_n}{j^\alpha} \qquad \text{with} \qquad j^\alpha = \det \mathbf{f}^\alpha = \frac{J^\alpha_{n+1}}{J^\alpha_n} \ . \tag{5.21}$$

The scalar J^α is the volume ratio, or Jacobian determinate (Holzapfel, 2000), at t_{n+1} and t_n. The incremental volume ratio, j^α, follows from the incremental deformation gradient. Note that (5.21) describes the action at a node. Unfortunately, the MPM formulation computes the deformation gradient at the particles[4]. Thus, the current form of Equation (5.21) needs to capture deformation related measures that occur at the body/phase (a.k.a. particle) level, at the node location (which does not actually represent the body/phases). Invoking the notion that computational particles represent constituent quantities and applying the definition in (5.15), the constituent-based form of the mass conservation reads

$$\rho^\alpha_{n+1} = \frac{\rho^\alpha_n}{j^\alpha} \Longrightarrow \hat{\theta}^\alpha_{i,n+1}\, \rho_{\alpha,n+1} = \frac{\hat{\theta}^\alpha_{i,n}}{j^\alpha}\, \rho_{\alpha,n} \ , \tag{5.22}$$

from which the updated volume fraction is isolated to form the crux of this entire formulation:

$$\hat{\theta}^\alpha_{i,n+1} = \underbrace{\frac{\hat{\theta}^\alpha_{i,n}}{j^\alpha}}_{\text{spatial change}} \quad \underbrace{\frac{\rho_{\alpha,n}\,(p_n)}{\rho_{\alpha,n+1}(p_{n+1})}}_{\text{volume change}} \ . \tag{5.23}$$

Equation (5.23) is the root of this volume constraint formulation. This value is computed at a node but is based solely on constituent values in the nodal support or control volume.

[4]Node-centered deformation gradients are computed in purely Eulerian formulations. This is a potential avenue that could be pursued in later research.

Since subscript space comes at an unprecedented premium price in this formulation, the nodal subscript i is dropped and the context is understood by the reader. Each of the two labeled sub-components require attention and are discussed individually below.

The volume change fraction on the right side of (5.23) is considered first. This term describes a ratio of the constituent densities present at the node level and is written as a function of pressure to emphasize the role that the nodal pressure terms p_n and p_{n+1} play in the algorithm. Physically this term represents the change in volume fraction due to the compression or extension of the constituents themselves, hence the name *volume change*. The quantity p_n must be specified at the outset of a time step. Typically this is the value of p_{n+1} from the previous time step—although in some cases (such as when a new node is instantiated) this is not true. The end goal is to determine p_{n+1} such that Equation (5.20) is satisfied. To this end expressions for the numerator and denominator are developed in additional detail.

At the beginning of each time step the constituent mass and volume, $m_{\alpha,n}$ and $V_{\alpha,n}(p_n)$, are known for each phase α. This information is used to establish the basic node-based relationship

$$\rho_{\alpha,n} = \frac{m_{\alpha,n}}{V_{\alpha,n}} \tag{5.24}$$

The volumetric deformation is defined as

$$e_{\alpha,n} = \tilde{e}_{\alpha,n}\left(p_n, K_\alpha^{eff}\right) = \frac{\Delta V_n}{V_0} \tag{5.25}$$

where $\tilde{e}_{\alpha,n}$ is a general function[5] relating volumetric deformation to applied pressure and an effective constituent stiffness, K_α^{eff}. Ostensibly $\tilde{e}$ could depend on additional state variables, but that is beyond the scope of the current discussion. ΔV_n is the current total change in volume and V_0 is the original volume. The current volume can be as

$$V_{\alpha,n} = V_0 + \Delta V_n = V_0 + V_0\, e_{\alpha,n} = V_0\, \left(1 + \tilde{e}_{\alpha,n}\right)\ . \tag{5.26}$$

As constituent mass is constant, the original volume is expressed in terms of initial density, $\rho_{\alpha,0}$. This leads to the final expression for the current volume as

$$V_{\alpha,n} = \frac{m_{\alpha,n}}{\rho_{\alpha,0}}\, \left(1 + \tilde{e}_{\alpha,n}\right)\ . \tag{5.27}$$

In light of Equation (5.24), the final expression for the constituent density at t_n is

$$\rho_{\alpha,n} = \frac{\rho_{\alpha,0}}{1 + \tilde{e}_{\alpha,n}} \tag{5.28}$$

[5]The final form of the equations is specialized for a linear relationship between e_α, K_α, and p. This, however, is not a requirement of the current formulation.

The same argument can be spelled out for the density at t_{n+1}. The volumetric deformation is modified to reflect the updated pressure, i.e.,

$$e_{\alpha,n+1} = \tilde{e}_{\alpha,n+1}\left(p_{n+1}, K_\alpha^{eff}\right) \ , \tag{5.29}$$

in which the updated pressure must be obtained according to

$$p_{n+1} = p_n + \Delta p \ . \tag{5.30}$$

This leads to an updated density expression

$$\rho_{\alpha,n+1} = \frac{\rho_{\alpha,0}}{1 + \tilde{e}_{\alpha,n+1}} \ . \tag{5.31}$$

Equations (5.28) and (5.31) provide the needed ingredients to build the density ratio expression on the right side of (5.23). This ratio is expressed in general form as

$$\frac{\rho_{\alpha,n}}{\rho_{\alpha,n+1}} = \frac{1 + \tilde{e}_\alpha\left(p_n + \Delta p, K_\alpha^{eff}\right)}{1 + \tilde{e}_\alpha\left(p_n, K_\alpha^{eff}\right)} \ , \tag{5.32}$$

where the only unknown value appearing in (5.32) is the pressure increment, Δp. This format facilitates a general expression relating the pressure to volumetric deformation. A compact expression is obtained for the density ratio assuming a linear relationship between volumetric deformation and applied pressure, e.g., $p = K_\alpha\, e_\alpha$:

$$\frac{\rho_{\alpha,n}}{\rho_{\alpha,n+1}} = \frac{1 + {}^{(p_n + \Delta p)}/_{K_\alpha}}{1 + {}^{p_n}/_{K_\alpha}} \ . \tag{5.33}$$

This fraction can be computed for any Δp. If there is no change in pressure, i.e., $\Delta p = 0.0$, then the density ratio remains unity. If the constituent is incompressible, $K_\alpha \to \infty$, and again there is no change in constituent density over the time step. Note that a density ratio of 1.0 does not imply the volume fraction of a phase is constant over a time step. This formulation assumes that p and Δp carry the correct sign: $p < 0.0$ is compressive.

With the volume change portion taken care of the focus shifts to the *spatial change* term in (5.23). Physically this term represents the change in the volume fraction due to motion and/or reorganization of the body/constituents. In other words, this term captures the change in volume fraction as the constituents get closer together or farther apart. The current formulation computes this value at a node from the particles within a given node's support via

$$\frac{\hat{\theta}_{i,n}^\alpha}{j^\alpha} = \frac{\sum_{p_\alpha} \Theta_{p_\alpha,n}\, m_{p_\alpha}\, N_{p_\alpha}}{\sum_{p_\alpha} m_{p_\alpha}\, N_{p_\alpha}} \qquad \text{with} \qquad \Theta_{p_\alpha,n} = \frac{\hat{\theta}_{p,n}^\alpha}{j_p^\alpha} \tag{5.34}$$

where $\sum_{p_\alpha}$ is a sum over all particles of phase α in the nodal support and $\hat{\theta}^{\alpha}_{p,n}$ is the node-based volume fraction evaluated at the particle location. The incremental volumetric ratio follows from the incremental particle deformation as

$$j^{\alpha}_{p} = \det\left(\mathbf{f}^{\alpha}_{p}\right) = \det\left(\mathbf{1} + \Delta t \nabla \mathbf{v}^{\alpha}_{p}\right) \ . \tag{5.35}$$

Equation (5.34) is consistent with the mass-weighted particle-to-node mapping scheme used for all variables in the MPM. Armed with both the spatial and volume change contributions, the total updated volume fraction described by (5.23) can be computed for each phase with an appropriate Δp such that the constraint in (5.20) is satisfied.

5.3 Algorithmic Overview

The volume constraint does not affect the anti-locking routine presented in Chapter 4. Those techniques modify the bulk deformation field as well as the stress obtained via the constitutive relation, or $\boldsymbol{\sigma}^{\alpha}_{E}$ in the notation of this chapter. The only point of overlap is the computation of j^{α}_{p}, thus, the constraint algorithm should be performed after the approximation of the strain field to ensure a locking-free incremental deformation. The volume constraint algorithm is detailed in Table 5.1 (undefined values in Table 5.1 are explained in the next paragraph) and is applied at each node in the domain each time step. The support volumes listed in Step 1 refer to 1D, 2D, and 3D simulations.

There are available options or variations regarding the implementation. The version presented in Table 5.1 has proven to be the most reliable. The alterations include:

- Normalization of the volume fraction. This modification ensures the volume fractions sum to 1.0 at all times. This tool functions as an aid for edge and corner nodes whose supports are never full due to the boundary conditions. This option is referred to as VfracNorm. This option is problematic[6] and not necessary for achieving reasonable results.
- Extrapolating the volume fraction from the nodes to the particles in Step 3 at t_n is not entirely necessary. The volume fraction from the previous time step can be used here. However, the previous value is based on the previous particle position and thus is inconsistent with the current particle location. If this step is inserted

[6]Such a normalization scheme is especially troublesome at the interface between phases or at the edge of a body where a free surface condition is intended to exist. Simple thought experiments show why normalizing the volume fraction is inconsistent with the material description and this normalization is not physically realizable. Thus it is not recommended.

Table 5.1: Volume Constraint Algorithm.

1. Compute the true volume fraction for each phase present:

$$\hat{\theta}^{\alpha}_{i,n} = \frac{\sum_{p_\alpha} v_{p_\alpha,n}\, N_{ip_\alpha}}{V_s} \qquad \text{with} \qquad v_{p_\alpha,n} = \frac{m_{p_\alpha}}{\rho_{p_\alpha,n}}$$

   with the nodal support volume $V_s = \ h_x \mid h_x\, h_y \mid h_x\, h_y\, h_z$

2. Compute volume fraction sum and modified volume fraction for each phase:

$$\tilde{\theta}_{i,n} = \sum_{j=1}^{m} \hat{\theta}^{j}_{i,n} \qquad \text{IF VfracNorm:} \qquad \hat{\theta}^{\alpha}_{i,n} = \frac{\hat{\theta}^{\alpha}_{i,n}}{\tilde{\theta}_{i,n}}$$

3. Evaluate the volume fraction at the particle location at t_n:

$$\hat{\theta}^{\alpha}_{p,n} = \sum_{i} \hat{\theta}^{\alpha}_{i,n}\, N_{ip_\alpha}$$

4. Compute the spatial change in the trial updated volume fraction:

$$\hat{\theta}^{tr}_{i,\alpha,n} = \frac{\hat{\theta}^{\alpha}_{i,n}}{j^{\alpha}} = \frac{\sum_{p_\alpha} \Theta_{p_\alpha,n}\, m_{p_\alpha}\, N_{ip_\alpha}}{\sum_{p_\alpha} m_{p_\alpha}\, N_{ip_\alpha}} \qquad \text{with} \qquad \Theta_{p_\alpha,n} = \frac{\hat{\theta}^{\alpha}_{p,n}}{j^{\alpha}_{p}}$$

5. IF a node is new the pressure needs to be established:

$$p_{i,n} = \frac{\sum_{p} \rho_{p,n}\, \bar{p}_{p,n}\, m_p\, N_{ip}}{\sum_{p} m_p\, N_{ip}}$$

6. Compute updated volume fraction by changing Δp in the updated pressure definition $p_{n+1} = p_n + \Delta p$ subject to the constraint :

$$\sum_{j=1}^{m} \hat{\theta}^{j}_{i,n+1} - \sum_{j=1}^{m} \hat{\theta}^{j}_{i,n} \leq \text{TOL} \Longrightarrow \sum_{j=1}^{m} \hat{\theta}^{tr}_{i,\alpha,n} \frac{1 + {}^{p_{n+1}}/_{K_\alpha}}{1 + {}^{p_n}/_{K_\alpha}} - \tilde{\theta}_{i,n} \leq \text{TOL}$$

7. Prepare node for next time step:

$$p_{n+1} \rightarrow p_n$$

8. Update particle values
   - Volume fraction:
$$\hat{\theta}^{\alpha}_{p,n+1} = \sum_{i} \hat{\theta}^{\alpha}_{i,n+1}\, N_{ip_\alpha}$$
   - Density:
$$\rho_{p_\alpha,n+1} = \frac{\hat{\theta}^{\alpha}_{p,n}}{j^{\alpha}_{p}} \frac{\rho_{p_\alpha,n}}{\hat{\theta}^{\alpha}_{p,n+1}}$$
   - Pressure:
$$\bar{p}_{p_\alpha,n+1} = \sum_{i} \frac{p_{n+1}}{\rho_{p_\alpha,0}}\, N_{ip_\alpha}$$

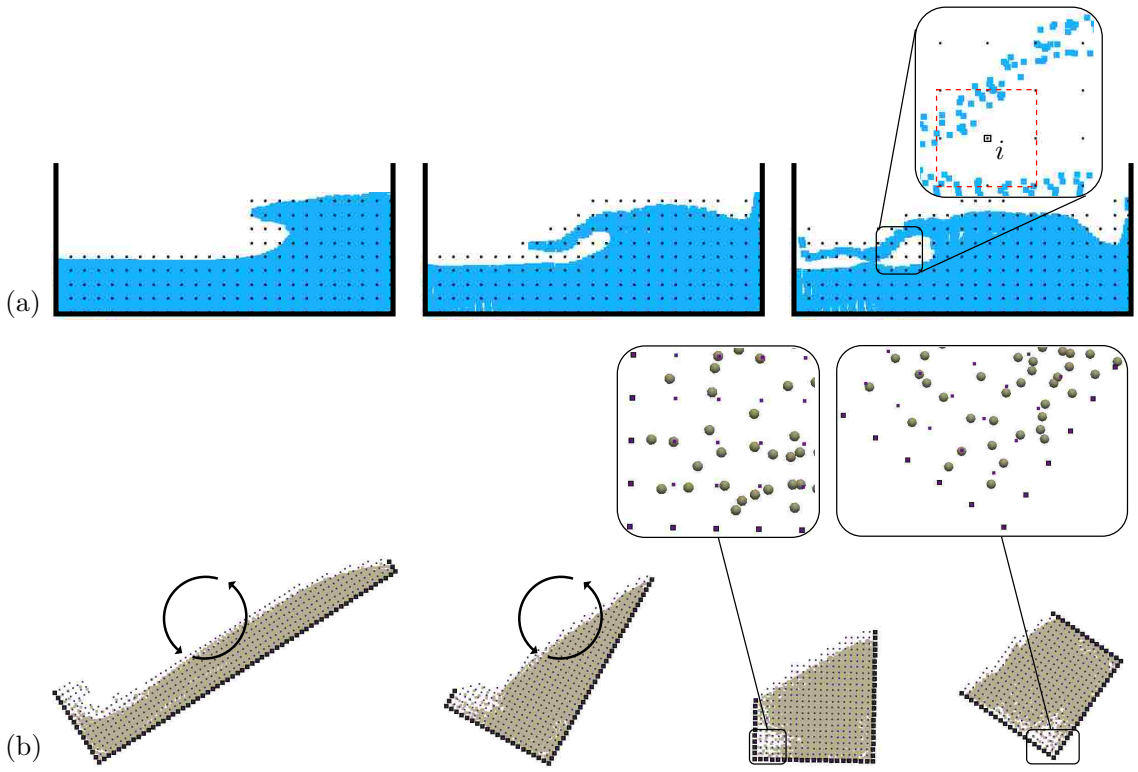

Figure 5.1: Fundamental explanation of force transfer in the context of the MPM. (a) Wave crashing in fluid simulation and (b) Accumulation of sand in the corners of a rotating box.

appropriately in the global algorithm then the suggested mapping from the nodes incurs little additional computational cost.

- The spatial change in volume fraction outlined in Step 4 can be modified if Step 3 is not performed. Since $\hat{\theta}^{\alpha}_{i,n}$ is known at the nodes, the contraction or expansion $1/j^{\alpha}_{p}$ can be interpolated from the particles (as opposed to $\hat{\theta}^{\alpha}_{p,n}/j^{\alpha}_{p}$). This too can be argued as inconsistent but does not incapacitate the constraint calculation.

- Step 6 is iterative in nature. The current tolerance is set to TOL$= 1.0\,(10)^{-9}$

Some very basic simulations employing the algorithm in Table 5.1 are presented in Chapter 6. The limited number of examples relative to the total number of simulations presented in this dissertation reflects the fact that the volume constraint itself provides very little benefit beyond the scalar quantity, p. The next section examines this singular capability and presents the fundamental limitations of this constraint in a multigrid environment.

5.4 Limitations of the Volume Constraint

The presentation thus far has not restricted the problem type or phase distribution within the domain. However, the only analyses the current formulation can handle effectively are small-deformation and small displacement, linear elastic material simulations in which all phases present span the entire domain at all times. The current formulation is unable to handle phase boundaries or phase transitions in a physically reasonable fashion. This section aims to identify why these restrictions exist and identify weaknesses with the current formulation.

The volume constraint as presented in this chapter yields a single pressure. This pressure ensures the total particle volume contribution maintains a user prescribed value at a given node. Beyond this singular function the constraint serves no other purpose. Consider the progression of images in the upper row of Figure 5.1(a) . A mass of water has rebounded off the wall at right and the wave is about to experience a collapse. As the wave rolls over it appears to ride, or hover, just above the flat free surface. The finger-like protrusion shuffles along until the mass crashes into the left wall. This undesirable behavior is a fundamental limitation of the MPM. The particles that make up the crashing wave interact with the free surface as soon as they get into the support of a node containing both the wave and the flat surface. One such node is labeled i in the close up image. Node i has no knowledge of the underlying particle structure or arrangement. This node knows only a mass, force, and velocity, and is not concerned with how these values came to be, the node is only concerned with what these values are. The solution of the governing equation of motion proceeds independently of the number of particles or the arrangement of these integration points in the support of a node. Adding a pressure in the form of a volume constraint does not impart knowledge of the underlying particle structure to node i, and it cannot mitigate the type of behavior observed in this scenario. Nor will adding an additional phase in the form of air solve this problem, as this too will suffer from the same shortcomings described above.

Another related example is shown in Figure 5.1(b). Here a drum is rotating about the center point as indicated by the circular arrows. The sandy contents flops around as the canister spins in a counter-clockwise direction. After the contents has been sufficiently jumbled situations arise in the corners like those shown in the close-up images of Figure 5.1(b). Here the sand appears to not fill the spatial region. Again, this is a fundamental limitation of the MPM that cannot be eliminated by adding a pressure to the simulation. The force interaction of the sand and the surface begins to occur before the material reaches the actual surface. In a sense this is merely an extension of the observation identified in the previous paragraph and is consistent with observations documented in several MPM papers

and writings, as well as the work by Mast (2008), who investigated the intrinsic behavior of computational particles near boundaries.

Initially there was hope that the volume constraint could provide the ability to model mixing and separation, the idea being that the interaction of multiples phases can be properly captured by assigning each phase its own motion—thus establishing an individual grid for each phase—and adding momentum exchange terms in a piecewise manner to achieve an entire multiphase picture. Certain aspects of this paradigm are effective, such as modeling the drag interaction in Mackenzie-Helnwein et al. (2010). However, the idea that the volume constraint can provide additional puzzle pieces in this regard has proven problematic. Consider the series of two-phase examples shown in Figure 5.2(a). There is no restriction on the types of phases in this algorithm, thus, it is reasonable to assume phase α is the same material as phase β. By selecting a pressure dominant material, such as water, these simple examples provide an ideal setting to test the current volume constraint's capabilities. Ideal behavior in this case is rather straightforward: the analysis should remain static and a hydrostatic pressure distribution should develop due to the volume constraint.

Figure 5.2(b) helps explain why ideal behavior cannot be achieved with the current formulation. Here the multiphase, multigrid framework is broken down grid-by-grid and the force distributions, $\mathbf{f}_{int}^{\alpha}$ and $\mathbf{f}_{int}^{\beta}$, are shown for each phase. Note that this force develops as a result of the pressure term supplied by the volume constraint as indicated in Equation 5.17_1. The portion of the force distributions occurring along the container boundaries will be offset perfectly by the reaction force that develops in these locations. That is, the reaction force will ensure that the net force along the edges is zero and no net acceleration perpendicular to the bounding surfaces is observed. The same cannot be said along the centerline of nodes for the individual grids housing phase α and β. In Figure 5.2(c) basic equilibrium is applied to centerline nodes and it is apparent that a net acceleration will occur on both Grid α and Grid β. This in turn generates motion and the desired static response is not achieved.

The important point to take away from this discussion is the following: the desired behavior for examples like those shown in Figure 5.2(a), or the ability to model mixing and separation of multiple phases, or the ability to simulate the mechanical response of partially/fully saturated porous media can be achieved using the MPM, but the mechanism responsible for ensuring satisfactory behavior is not the volume constraint presented here.

One potential solution is to use the common grid values, as this grid takes into account forces and motion from all phases. Starting from this mixture, begin dissecting the components of existing mixture theory equations and identify which components of the individual phase motions need to be modified to achieve this result. A second possible solution is to

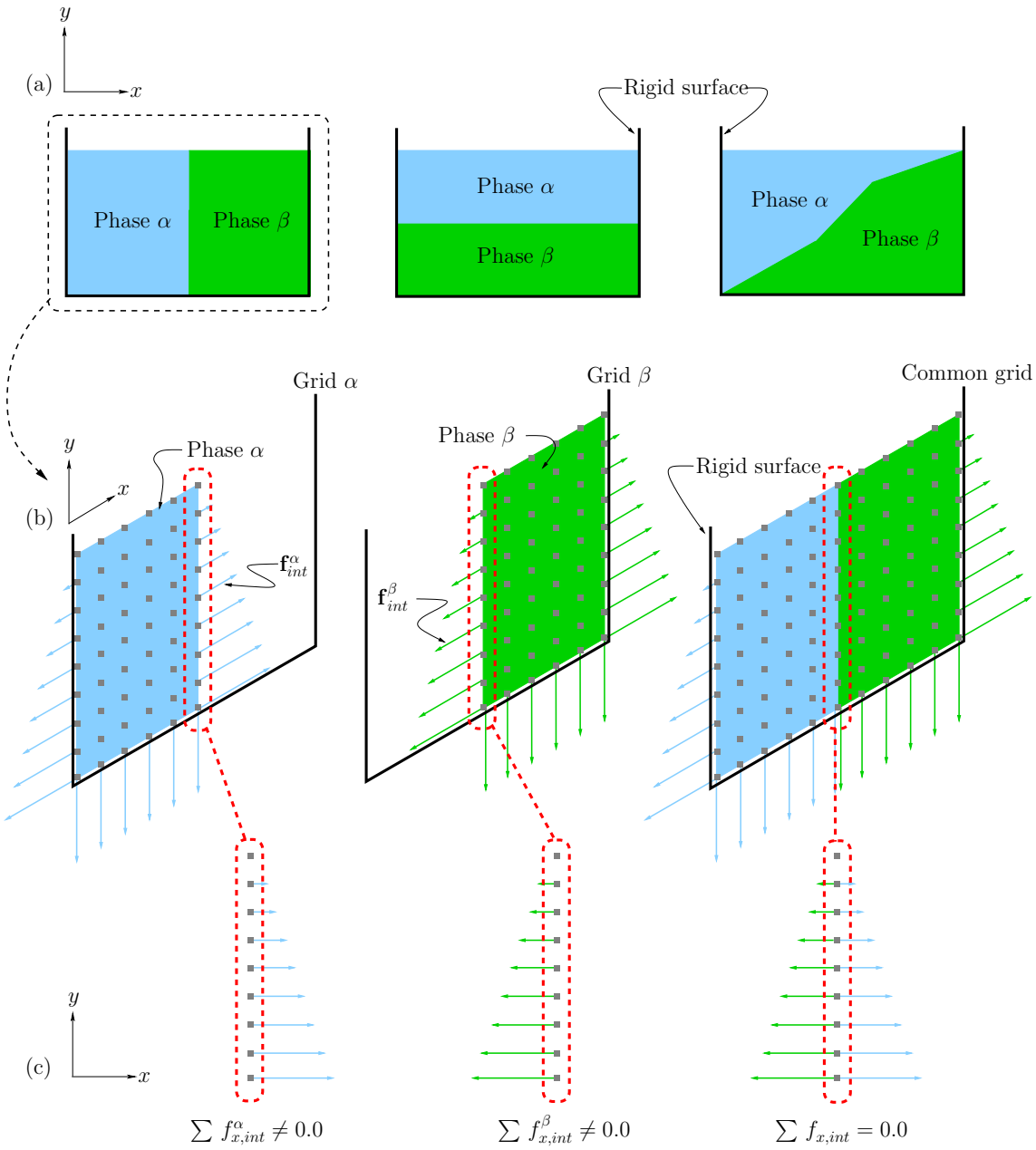

Figure 5.2: Force balance and phase interaction. (a) Three multiphase scenarios, (b) Grid decomposition for first multiphase scenario, and (c) Force equilibrium.

use one of the several multigrid contact algorithms already designed and implemented in the MPM, including those by Bardenhagen et al. (2000, 2001); Hu and Chen (2003); Pan et al. (2008). These frameworks build an environment identical to that depicted in Figure 5.2(b), but borrow (for lack of a better term) extra force from the common grid to balance each individual grid. In this manner the force contribution from other bodies/phases present in the analysis is explicitly accounted for. The disadvantage of this proposed solutions lies in the inherent inability to model overlap and phase penetration in the current algorithms. This, however, could potentially be overcome by using the relative volume fraction of each body/phase on each individual grid, and borrowing a volume fraction corrected amount of force from the common grid to replicate the desired behavior.

5.5 Conclusions

This chapter presents a volume constraint for use in the Material Point Method. The overview includes a discussion of weak form equations in a multiphase context, and represents an extension to the traditional framework. The algorithmic details and possible implementation alternatives are identified in Table 5.1 and corresponding discussion. In Chapter 6 three example problem outlining some of the capabilities of the constraint are presented. These examples represent the only types of problems the current formulation can handle, namely small-deformation, linear elastic material simulations in which all phases present span the entire domain. The current formulation is simply unable to handle phase boundaries or phase transitions in a physically reasonable fashion for the reasons discussed in Section 5.4.

Chapter 6

EXAMPLE PROBLEMS 1: LINEAR ELASTIC SIMULATIONS

Several examples presented in this chapter follow (verbatim in some instances) from the paper *Mitigating kinematic locking in the Material Point Method* by Mast, Mackenzie-Helnwein, Arduino, Miller, and Shin (2012). The author is indebted to Peter Mackenzie-Helnwein, Pedro Arduino, and Greg Miller for their contributions in writing and publishing said paper.

The primary focus of this chapter is to discuss a series of MPM simulations from fluid and solid mechanics. The different examples show the effectiveness of the anti-locking approach (see Chapter 4) applied to a wide variety of problem types. In particular, large deformation, nearly incompressible flow simulations are examined in order to validate the anti-locking strategy from a kinematic viewpoint. The ensuing pressure field and interaction between fluid and bounding surface are examined. On the solid mechanics end of the spectrum, a cantilever beam with prescribed velocity is analyzed and compared to small deformation beam theory. The normal and shear stresses are examined throughout the beam and the beam deformation is analyzed in detail. The final sections model saturated soil specimens, validating the certain aspects of the volume constraint algorithm highlighted in Chapter 5. This chapter contains only simulations of materials with linear elastic properties.

6.1 Applications to Fluid Dynamics

The constitutive equation for isotropic elasticity can be formulated in such a way that it represents compressible and incompressible materials Hughes (1987). In the present case, the constitutive relationship for a nearly incompressible fluid can be written as

$$\boldsymbol{\sigma} = \rho\,\bar{k}\,\hat{\theta}\,\mathbf{1} + 2\,\mu\,\mathbf{d}\,, \tag{6.1}$$

where ρ is the mass density, $\bar{k} = k/\rho_0$ with k as the bulk modulus, $\hat{\theta}$ is the volumetric dilation, μ is the dynamic viscosity, and $\mathbf{d}$ is the rate of deformation tensor calculated from the velocity field, $\mathbf{v}$, as

$$\mathbf{d} = \frac{1}{2}(\boldsymbol{\nabla}\mathbf{v} + \boldsymbol{\nabla}\mathbf{v}^T)\,. \tag{6.2}$$

All fluid simulations appearing in this section are large deformation, plane strain analyses. Gravity is the driving force and is applied in the vertical direction, i.e., $\mathbf{g} = -9.81\mathbf{j}$ m/s^2.

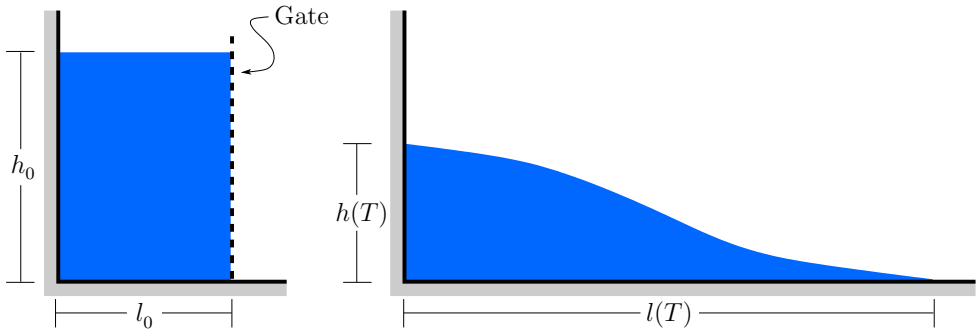

Figure 6.1: Dam break simulation: (a) Initial configuration, and (b) Configuration at normalized time T.

The material parameters are: $\rho_0 = 997.5$ kg/m^3, $k = 2.0$ GPa, and $\mu = 0.001$ Pa-s. All nodes representing a surface satisfy $\mathbf{v}_i \cdot \mathbf{n} = 0$ and $\dot{\mathbf{v}}_i \cdot \mathbf{n} = 0$ for the nodal velocity and acceleration, respectively. The unit normal, $\mathbf{n}$, is defined perpendicular to the surface.

6.1.1 Dam Break

A simplified dam break simulation is shown in Figure 6.1. This idealized model is frequently used for kinematic verification of numerical algorithms—due in part to the availability of experimental data, e.g., Martin and Moyce (1952). A water column of initial height, h_0, and length, l_0, is initially constrained horizontally and rests on a smooth, flat surface. At an arbitrary starting time, say $t = 0$, the gate on the right-hand side is removed and the water is allowed to flow freely under the force of gravity. The following parameters describe the free surface runout:

$$T = t\sqrt{\frac{h_0\, g}{l_0^2}}\,, \qquad L(T) = \frac{l(T)}{l_0}\,, \qquad \text{and} \qquad H(T) = \frac{h(T)}{h_0} \tag{6.3}$$

where T, $L(T)$, and $H(T)$ are the dimensionless time, length, and height ratios, respectively. The parameters $l(T)$ and $h(T)$ are shown on the right side of Figure 6.1 and represent the length and height extents of the water column at a given time, T. The term $g = |\mathbf{g}| = 9.81$ m/s^2.

The MPM paramaters used for this analysis are listed in Table 6.1. Two different aspect ratios are examined, namely $h_0/l_0 = 1.0$ and $h_0/l_0 = 2.0$. The MPM data is compared to the benchmark experiments of Martin and Moyce (1952). Values for $L(T)$ and $H(T)$ are shown in Figure 6.2 for both aspect ratios. The experimental values are shown as bullets, and are plotted against three different MPM variants: the standard MPM, a cell-based anti-locking strategy, and a hybrid anti-locking strategy. The anti-locking algorithms use

Table 6.1: Input parameters for dam break simulations

	Variable	$h_0/l_0 = 1.0$	$h_0/l_0 = 2.0$	*w/Barrier*
Water Column Description				
Initial Dimensions [m]	$l_0,\ h_0$	0.057, 0.057	0.057, 0.114	4.0, 2.0
Domain Description				
Barrier location [m]	b_x	n/a	n/a	6.0
Analysis Parameters				
Cell size [m]	$h_x = h_y$	0.00875	0.00875	0.25
Time Step [s]	Δt	$5.0\,(10)^{-7}$	$5.0\,(10)^{-7}$	$1.0\,(10)^{-5}$
Number of Particles in x, y	$P_x,\ P_y$	35, 35	35, 70	40, 80

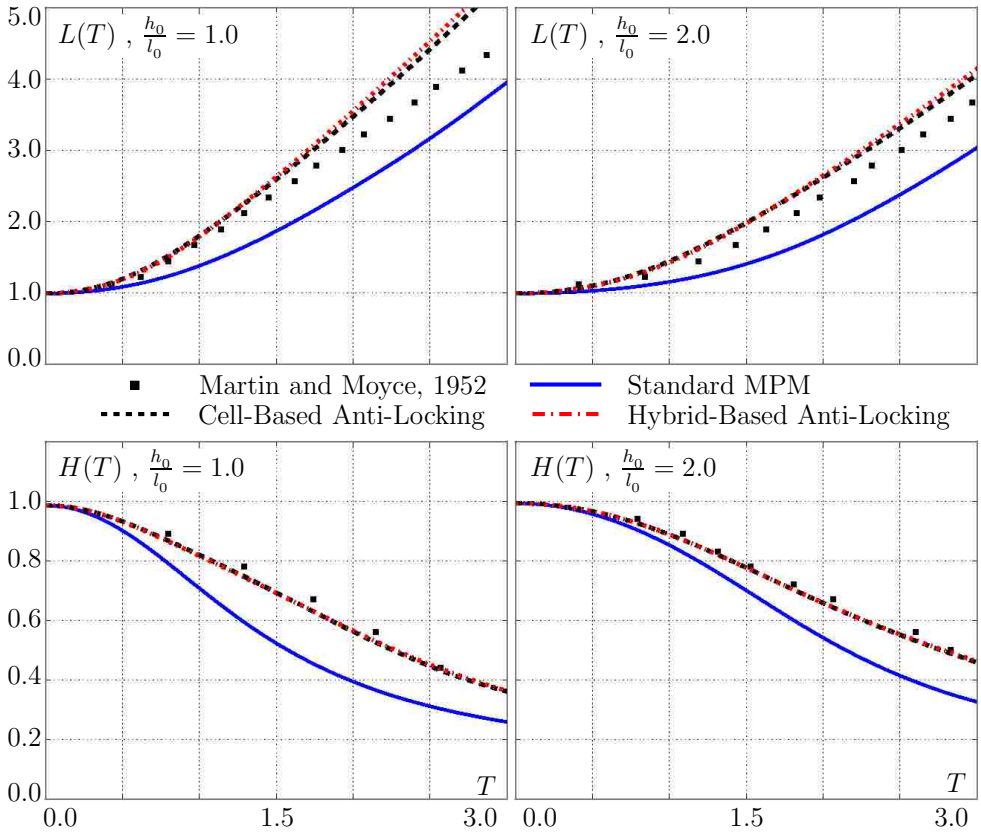

Figure 6.2: Comparison between MPM simulations and experimental data for dam break analyses. The upper row compares the run out length, while the lower row compares the run out height. Experimental data is from Martin and Moyce Martin and Moyce (1952).

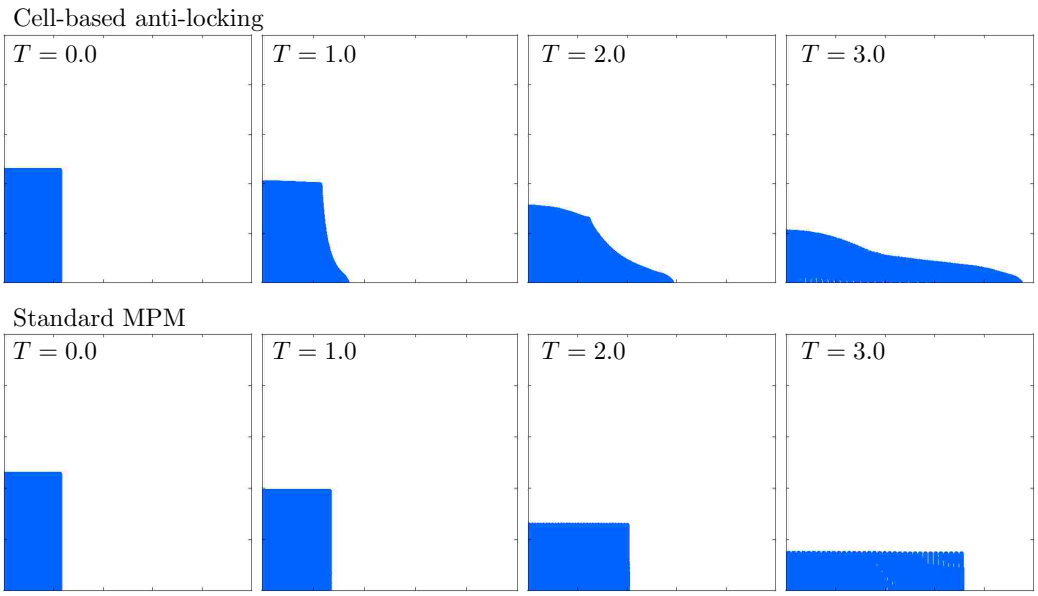

Figure 6.3: Dam break sequence for MPM simulations with $h_0/l_0 = 2.0$.

the volumetric approximation outlined in Section 4.3.1.

Both the cell-based and hybrid implementations perform very well. From a kinematic standpoint the two strategies produce nearly identical results. The runout length, $L(T)$, is slightly longer than the experimental findings while the runout height, $H(T)$, is slightly shorter for both aspect ratios. This implies that both locking-free MPM variants are flowing slightly faster than observed in the lab. The data from the standard MPM algorithm conflicts with ideal notions of fluid flow. Considering the runout length, it is apparent that the standard method under-predicts the length, implying a flow that is moving slower. Contrary to this finding, the height is shorter than the experimental values—implying a flow that is moving faster. This suggests the standard algorithm is producing non-physical kinematics.

The fluid motions are observed by examining a sequence of particle positions throughout the analysis. In Figure 6.3 a cell-based scheme is shown against the standard algorithm and a striking difference is observed. The free surface definition for the cell-based approach is very good, while the standard MPM exhibits non-physical flow patterns due to volumetric locking and in no way resembles a flowing fluid. This observation is consistent with Figure 6.2.

These findings clearly demonstrate the improved kinematics when using the proposed anti-locking variants. A slightly more realistic dam break simulation is examined next in an effort to further validate the kinematics and examine the pressure field. This second analysis increases the scale of the problem and adds a layer of kinematic complexity by

introducing a barrier for the surging water to interact with.

6.1.2 Dam Break with Barrier

A water column with dimensions $l_0 = 4.0$ m, $h_0 = 2.0$ m is constrained in the horizontal directions and rests on a smooth surface. The particles are in a hydrostatic state to begin the analysis. At the start of the simulation, the gate is removed and the water allowed to flow under the force of gravity towards a vertical, rigid barrier placed at $b_x = 6.0$ meters. Additional analysis parameters are listed in Table 6.1.

The ensuing flow (or lack thereof) is highlighted in Figure 6.4, in which a sequence of snapshots from multiple analyses are depicted. The left column shows particle pressure obtained using the standard MPM algorithm. The center column is for a cell-based anti-locking strategy, while the right column is for the hybrid scheme. From this montage it is apparent that severe volumetric locking significantly retards the flow when using the standard implementation, and nearly no resemblance to a free flowing fluid is obtained. The mixed formulations—both of which enforce a constant volumetric field for both the stress and strain—exhibit ideal behavior both in the splash that occurs on the far wall as well as the rebounding wave. Throughout the analysis the free surface of the water is well represented.

Pressure profiles (shown as colored contours) for both anti-locking strategies demonstrate the expected behavior. This is particularly so for the hybrid cell-based/node-based implementation—a smooth pressure distribution coincident with hydrostatic principles is well represented at each snapshot in time, despite the fact that this is a dynamic analysis. For example, at time $t = 0.40$ s the hybrid approach pressure distribution along the left wall nearly resembles the initial hydrostatic state. The pressure magnitude begins to decrease continuously traversing lengthwise along the water column until the free surface is reached. Near the end of the analysis (i.e., at $t = 2.0$ s), the water depth on the right-hand side is nearly as deep as the initial state, and again, a smooth pressure distribution in agreement with hydrostatics is observed.

The cell-based approximation also maintains an expected pressure distribution (albeit not continuous) for those regions not experiencing a high velocity gradient. The cell-wise discontinuous pressure oscillations are a side effect of—among other things—linear shape functions and are commonly referred to as 'checkerboard' modes. Belytschko et al. (2000); Hughes (1987); Zienkiewicz et al. (2005b). Interestingly, despite the sometimes excessive oscillations observed in the cell-based approximation, the kinematics between the hybrid- and cell-based approaches are nearly identical. Furthermore, it is common practice in the

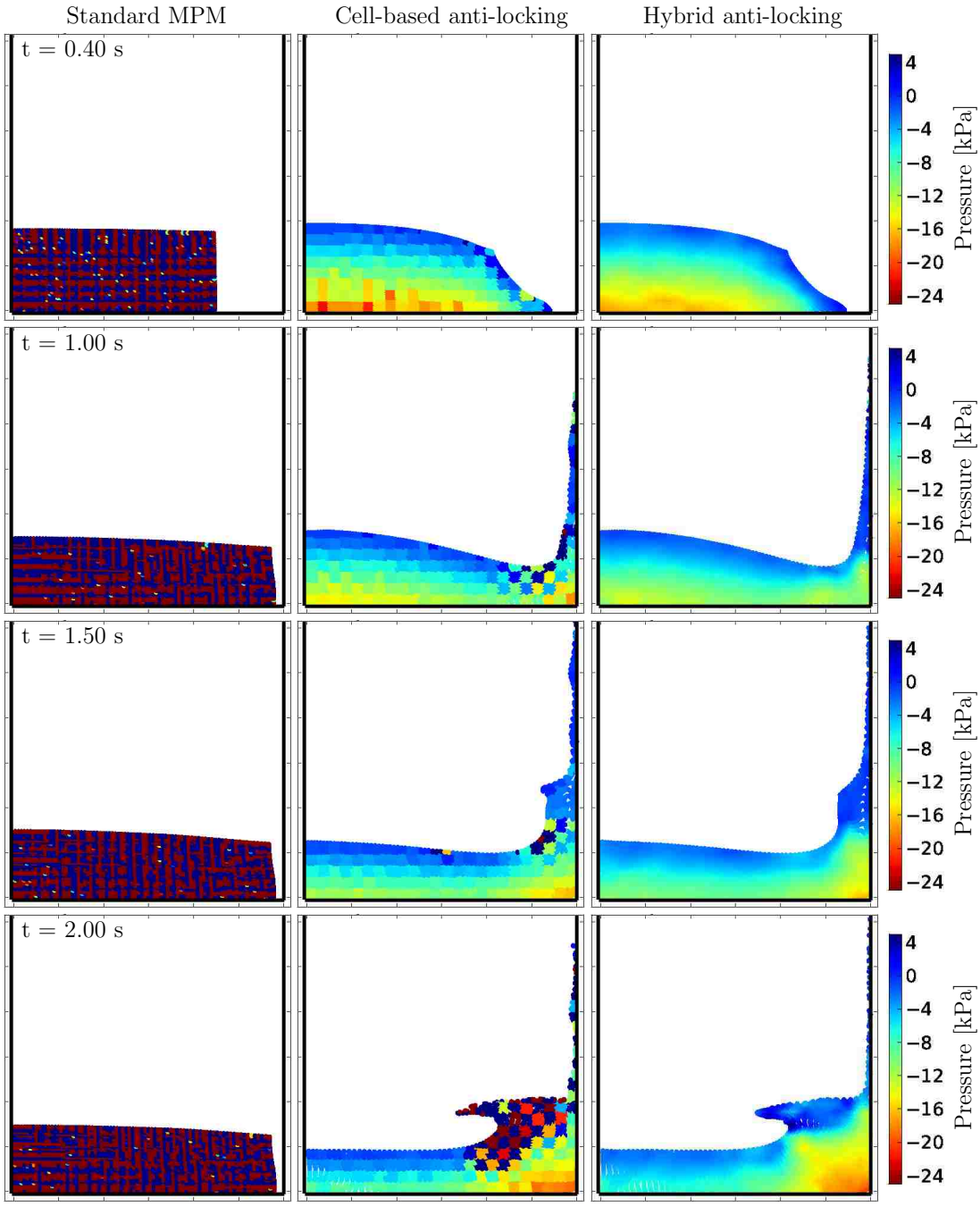

Figure 6.4: Time evolution for the dam break with barrier.

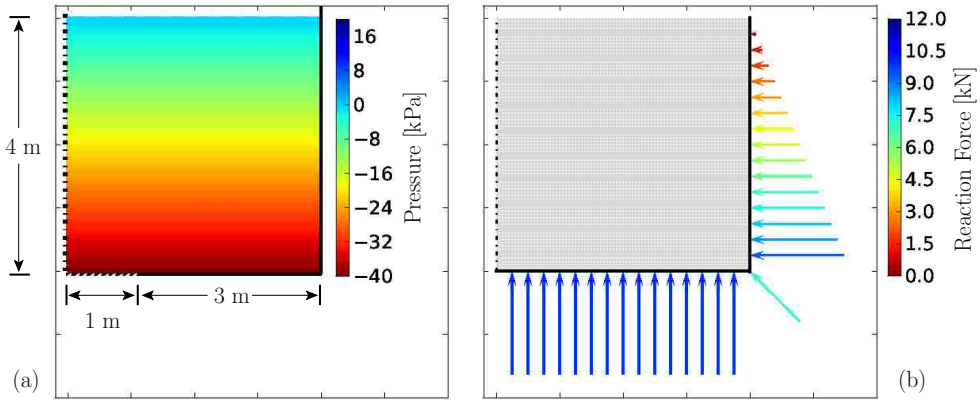

Figure 6.5: Initial state for the tank drain analysis. (a) The particle pressure. (b) The reaction force, $\mathbf{f}_{ir}$.

FEM to use a stress smoothing/averaging technique for plotting and interpretation purposes. Hughes (1987); Zienkiewicz et al. (2005b). The pressure field for the cell-based approach would appear very similar to that of the hybrid technique if such a procedure were to be implemented here.

The dam break simulations show the proposed anti-locking strategies significantly improve the pressure field, and ultimately, are key for obtaining an ideal free surface definition for the runout simulation, as well as the splash and rebounding wave due to the interaction between the water and the barrier. The latter simulation with barrier suggests the MPM with appropriate anti-locking extension is a valid tool for recovering or assessing the magnitude of the reaction force/traction between two media, e.g., a fluid-like material interacting with a structure. This idea is explored in the following example.

6.1.3 Tank Drain

A rectangular water tank with a narrow drain located in the center is used as the model for this series of simulations. Only half of the domain needs to be analyzed due to symmetry, and the initial state is shown in Figure 6.5. Here, a hydrostatic stress state is shown alongside the reaction force that develops in response to the fluid pressure exerting an outward force on the tank surface. The edge of the computational domain is used to represent the rigid exterior surface. The reaction force is calculated as $\mathbf{f}_{ir} = -\mathbf{f}_i \cdot \mathbf{n}$, where $\mathbf{f}_i$ is the nodal force at a node representing the boundary. All other analysis parameters are listed in Table 6.2.

The nodal reaction force and velocity fields are shown in Figures 6.6 and 6.7. Particle positions are shown only for reference purposes. Each figure consists of three columns; the leftmost is for the standard MPM algorithm, the center is for a cell-based anti-locking

Table 6.2: Input parameters for tank drain

	Variable	*Value*
Water Column Description		
Initial Dimensions [m]	$l_0,\ h_0$	4.0, 4.0
Domain Description		
Drain diameter [m]	d_d	1.0
Analysis Parameters		
Cell size [m]	$h_x = h_y$	0.25
Time Step [s]	Δt	$1.0\,(10)^{-5}$
Number of Particles in x, y	$P_x,\ P_y$	80, 80

algorithm, while the far right column is for a hybrid implementation. The tank drain is opened at time $t = 0.0$ seconds and three sequential images are shown. Since the primary region of interest is the tank itself as well as the flow in the immediate vicinity of the drain, particles venturing more than 2.0 meters from the exit spout are eliminated from the numerical algorithm. Such an elimination has an insignificant effect on the simulation itself and substantially decreases the associated computational time.

With respect to the reaction force in Figure 6.6, it is apparent that the erroneous pressure field that develops using standard MPM leads to an incorrect and inconsistent reaction force on the tank surface. The force distribution that started out triangular on the right side very quickly becomes chaotic and varies both in direction and magnitude for each time step of the analysis. Both the cell-based and hybrid methods maintain a quality force distribution at each sequential point in time. In both cases, the reaction force is triangular in shape along the right wall and has an appropriate magnitude with respect to basic hydrostatics. The bottom of the tank is subjected to a constant force for regions where the fluid pressure is relatively uniform.

The benefits of the proposed anti-locking approach are further highlighted by examining the nodal velocity. The velocity vector at each node is shown in Figure 6.7. As has been the case throughout, the standard MPM velocity field is distorted and non-physical. The particles appear to slide off in layers over the drain, leaving only a rectangular fluid mass with poor free surface definition. This observation is confirmed by examining the velocity field along the line of symmetry. At each point in time these values increase in magnitude and are oriented downward. The velocity fields for the anti-locking approaches are very good from a qualitative viewpoint. The resulting streamlines (not pictured) are consistent with the boundary conditions and represent a physically realistic flow—particularly when considering the symmetry condition and free surface description observed here.

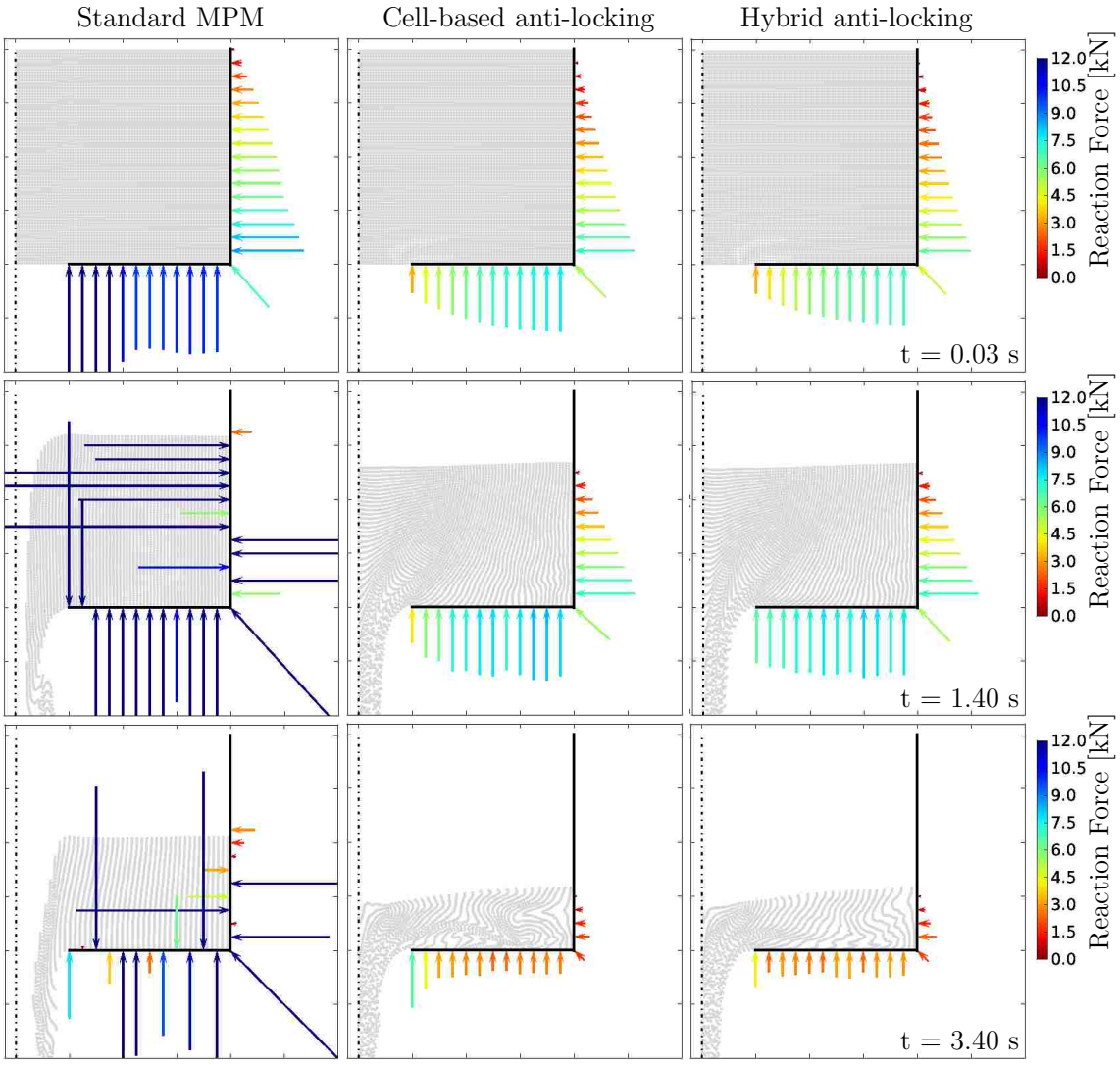

Figure 6.6: Reaction force along tank surface for the tank drain analysis.

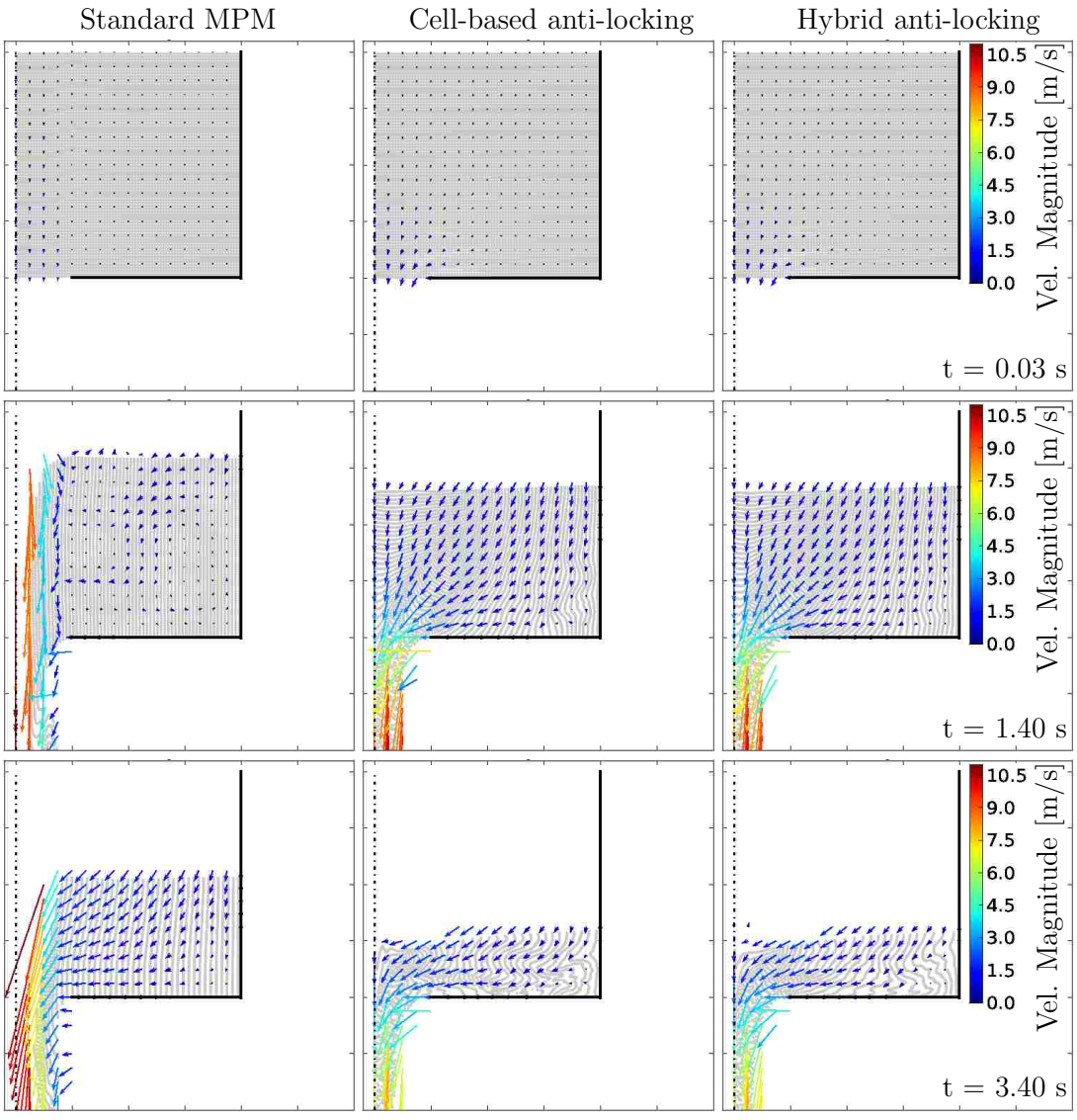

Figure 6.7: Nodal velocity for the tank drain analysis.

It is apparent from this section that an anti-locking strategy is indispensable for modeling nearly incompressible flow. Failure to alleviate the fictitious stress and strains that accumulate in the standard implementation leads to nonphysical and unusable results. The anti-locking algorithms employed in this section successfully eliminate the volumetric locking and lead to improved findings with respect to all field variables, including the particle pressure and nodal/particle velocity. In addition, it is shown that the MPM with appropriate anti-locking extension is a valid tool for recovering or assessing the magnitude of the reaction force/traction between a body and a rigid surface.

6.1.4 Conclusion

The nearly incompressible flow simulations presented in this section demonstrate volumetric locking within the context of the MPM. The anti-locking formulation presented in Chapter 4 not only eliminates volumetric locking but also leads to significantly improved results for all field variables, including the particle pressure and nodal/particle velocity. The fluid kinematics are verified by comparison to experimental data. In addition, the finding suggests that the MPM can be used as a valid tool for recovering or assessing the magnitude of the reaction force/traction between a body and a rigid surface.

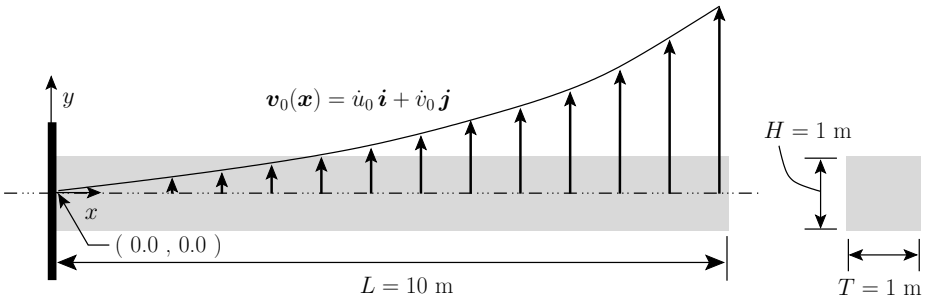

Figure 6.8: Cantilever beam with applied initial velocity field.

6.2 Application to Solid Mechanics: Vibrating Cantilever Beam

The MPM with suitable anti-locking extension is capable of modeling nearly incompressible flow as was outlined in the previous section. The flow problem is, however, a pressure driven problem that has nearly no influence from deviatoric terms. A problem with shear stiffness needs to be analyzed in order to exam the effectiveness of the proposed implementation on the deviatoric portion of the stress and strain field. This is accomplished by examining the

Table 6.3: Input parameters for plane stress beam study

	Var.	*#1*	*#2*	*#3*	*#4*	*#5*
Analysis Parameters						
Cell size [m]	$h_x = h_y$	1.0	0.5	0.25	0.125	0.0625
Time Step [s]	Δt	$2.0\,(10)^{-5}$	$1.0\,(10)^{-5}$	$5.0\,(10)^{-6}$	$2.5\,(10)^{-6}$	$1.25\,(10)^{-6}$
Number of Particles in x, y	P_x, P_y	$20, 2$	$40, 4$	$80, 8$	$160, 16$	$320, 32$

cantilever beam, a benchmark problem from solid mechanics. The model with schematic loading is shown in Figure 6.8.

The velocity field, $\mathbf{v}_0(\mathbf{x}) = \dot{u}_0\,\mathbf{i} + \dot{v}_0\,\mathbf{j}$, is applied to the particles as an initial condition and is consistent with the first mode of vibration. All displacement degrees of freedom are fixed along the vertical plane at $x = 0$. Material parameters for the linear elastic, plane stress analyses are as follows: $\rho_0 = 2710.0$ kg/m^3, $k = 70.28$ GPa, and $G = 26.23$ GPa. Additional analysis parameters are listed in Table 6.3.

The cell-based approximations appearing in this section have two variants: the first uses the volumetric-deviatoric anti-locking approach outlined in Section 4.3.2. This approach is referred to as variant AL. The second also uses the volumetric-deviatoric approach—but with a constant volumetric portion, that is, the modification listed in Equation (4.23) for the parameters $\boldsymbol{\alpha}_c$ and $\boldsymbol{\beta}_c$. This approach is referred to as ALCV, where the CV extension signifies a 'Constant Volumetric' approximation.

The displacement response of the beam is periodic with constant amplitude in the absence of viscous damping. Attention is fixed to the point in time at which the first peak displacement occurs in order to evaluate the performance of the standard MPM as well as the proposed anti-locking algorithms. Normal and shear stress contours are shown in Figure 6.9 for the analysis parameters listed in Column #5 of Table 6.3. All particle stress values have been normalized to the maximum normal or shear stress value from the beam theory solution.

From Figure 6.9(a) it is easy to see that both the standard MPM algorithm and the cell-based anti-locking (variant AL) do a reasonable job in representing the normal stress field. The shear stress contours, depicted in Figure 6.9(b), show a different story. The standard MPM algorithm with rectangular cells ($h_x = 4\,h_y$) suffers from a wildly varying stress field. At first glance the situation is dramatically improved by using square cells. However, the fluctuations still exist—as indicated by closer inspection of the beam segment. These findings are in contrast to those obtained using a cell-based anti-locking approach (variant AL). For this case the resulting shear distribution is of much higher quality when compared

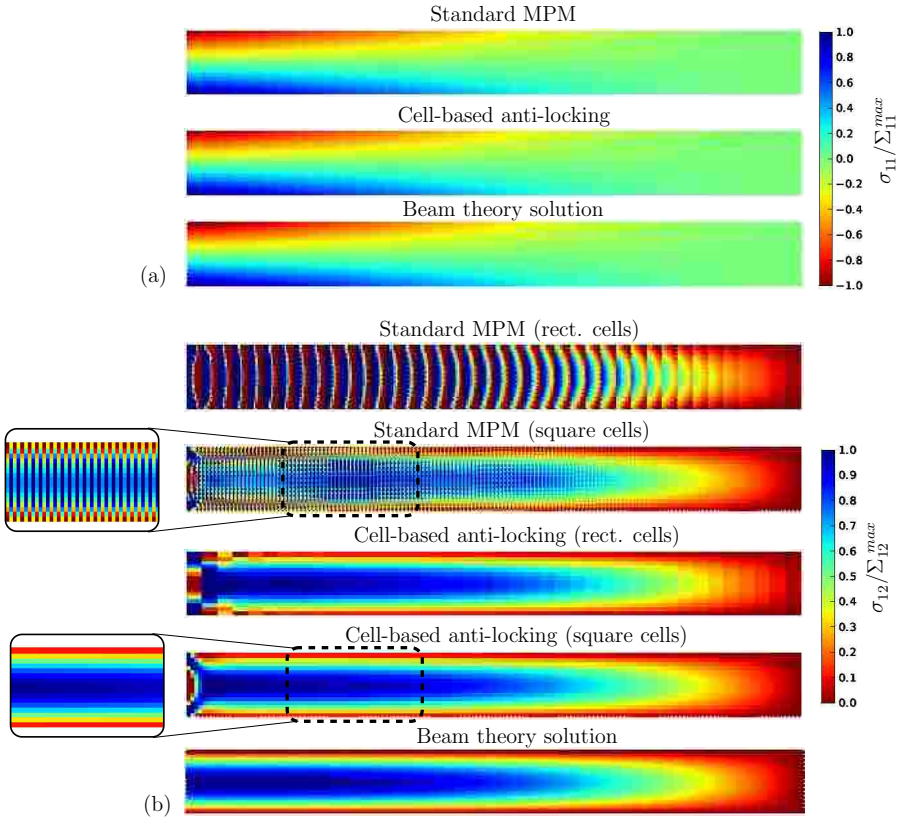

Figure 6.9: Normalized stress distribution in cantilever beam. (a) Normal stress. (b) Shear stress. All stress values are normalized to the maximum value predicted by small deformation beam theory, denoted by Σ_{11}^{max} and Σ_{12}^{max} for the normal and shear components, respectively.

to the beam theory solution, regardless of rectangular or square cells.

A quantitative comparison between the standard algorithm and the proposed approaches is obtained by examining the energy norm for continuous refinements of the body, both in space and time. Spatial and body discretization (the total number of computational nodes and particles, respectively) are sequentially doubled for five consecutive analyses. Correspondingly, the time step is reduced by a factor of 50% for each sequential analysis. These values are reflected in Table 6.3. The norm,

$$\mathcal{E} = \int_{t_i}^{t_f} \mathcal{E}(t)\, dt \quad \text{where} \quad \mathcal{E}(t) = \int_{V_{\mathcal{B}}} (\boldsymbol{\sigma}_{MPM} - \boldsymbol{\sigma}_{BT}) : \mathbb{D} : (\boldsymbol{\sigma}_{MPM} - \boldsymbol{\sigma}_{BT})\, dV\,, \tag{6.4}$$

is calculated for a duration equal to one period of motion ($t_f - t_i = 2\pi/w_1$). The stresses $\boldsymbol{\sigma}_{MPM}(\mathbf{x}, t)$ and $\boldsymbol{\sigma}_{BT}(\mathbf{x}, t)$ are the stress tensors from the MPM analysis and the beam theory solution, respectively. The linear elastic plane stress compliance tensor is denoted by $\mathbb{D}$.

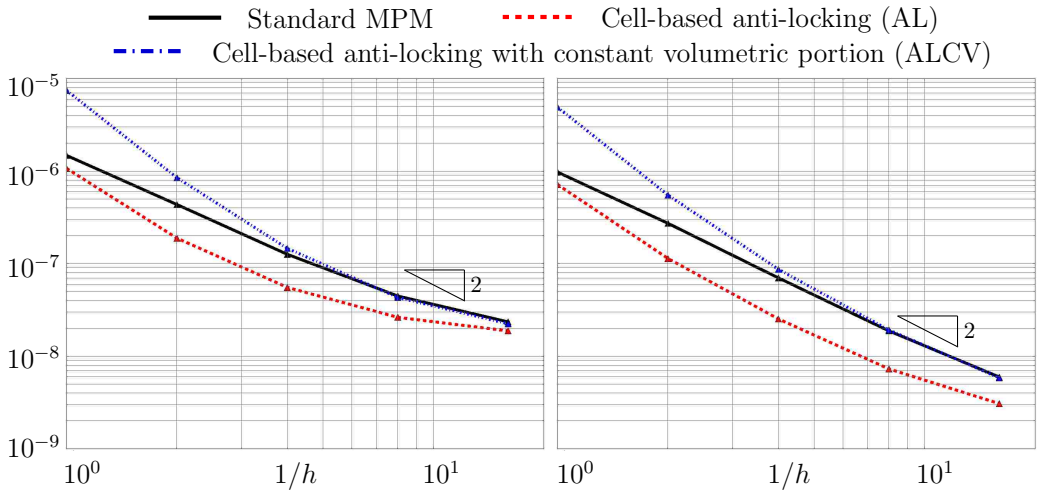

Figure 6.10: Energy norm convergence for cantilever beam. The left side considers all particles when calculating $\mathcal{E}$, while the right side considers only those particles whose horizontal position is greater than one beam depth away from the support.

The volume integral in (6.4) is performed in accordance with the MPM, i.e., as a sum over particles with $\mathbf{x} \to \mathbf{x}_p$.

The energy norm is plotted against the cell size, h, in Figure 6.10 for the standard MPM and the two cell-based variants. The left plot evaluates the integral in Equation $(6.4)_2$ as a sum over all the particles that make up the beam. All three methods exhibit convergence as the model parameters are refined. However, the error becomes saturated for successively refined cases. This is due in part to the finite error incurred from the boundary conditions, as the numerical model is unable to resolve both the displacement and stress condition at the fixed end. This error can be observed in Figure 6.9(b) for the MPM simulations, particularly for the cell-based approach. The boundary effects are approximately resolved a distance H (the beam depth) away from the support. Thus, there is merit in considering only those particles whose horizontal position is greater than one beam depth away from the support when computing the error norm. This modified energy norm appears on the right side of Figure 6.10. The net result is a more accurate approximation with a nearly identical convergence rate for each approach. The AL approach serves as the best approximation for all levels of refinement. For more coarse representations, the ALCV is not able to resolve the stress field as well as the other two approaches. Ultimately both the AL and ALCV surpass the standard MPM algorithm in the quality of the approximation.

Table 6.4: Input parameters for plane strain beam study

	Var.	$\nu = 0.0$	$\nu = 0.15$	$\nu = 0.30$	$\nu = 0.40$	$\nu = 0.45$	$\nu = 0.49$
Material Properties							
Bulk modulus [GPa]	k	23.33	33.33	58.30	117.11	233.00	1170.00
Shear modulus [GPa]	G	35.00	30.04	26.90	25.00	24.10	23.50

6.2.1 Incompressible Limit

Numerical simulations of materials with Poisson's ratio in the realm of $\nu \approx 0.0$ - 0.4 will predominately experience shear locking if a set of incompatible shape functions are used to represent the approximation space. However, as Poisson's ratio approaches the incompressible limit of 0.5, volumetric locking will dominate the response if care is not taken to mitigate the accumulation of fictitious strains. Thus, an alternative plane strain beam study examines the effectiveness of the proposed approach in the context of solid mechanics as the material approaches the incompressible limit. This is accomplished by varying the bulk modulus, k, and shear modulus, G, such that the product $EI/(1-\nu^2)$ stays constant through the allowable physical range of Poisson's ratio, ν. These modified material parameters are listed in Table 6.4. The beam geometry is consistent with Figure 6.8 and the following analysis parameters are used for the cell size: $h_x = h_y = 0.125\,,\, 0.125$ m, the time step: $\Delta t = 5.0\,(10)^{-6}$ s, and the number of particles in the x- and y-directions: $P_x\,,\, P_y = 160\,,\, 16$.

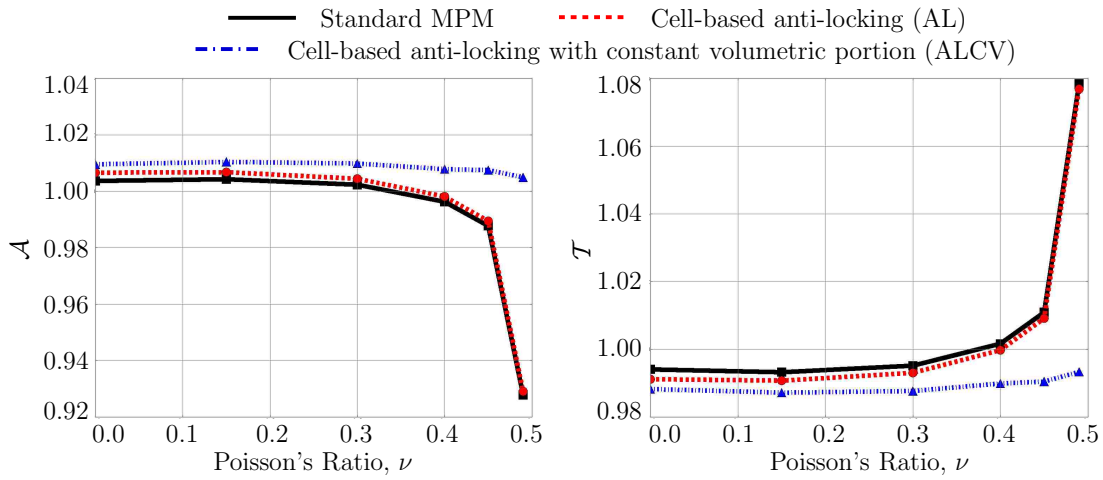

Figure 6.11: Amplitude ratio, $\mathcal{A}$, and period ratio, $\mathcal{T}$, as a function of Poisson's ratio.

Considering a single point on the beam, the displacement function takes the form:

$$u(t) = A\,\sin(\omega t)\,, \tag{6.5}$$

where A represents the amplitude (and thus displacement) and ω the effective frequency. A non-linear least squares fit of the data allows A_{MPM} and ω_{MPM} to be determined for each value of ν. These are compared to the beam theory solutions (denoted by the subscript BT) and the ratios

$$\mathcal{A} = \frac{A_{MPM}}{A_{BT}} \quad \text{and} \quad \mathcal{T} = \frac{T_{MPM}}{T_{BT}} \tag{6.6}$$

are used to assess the quality for the maximum displacement and period of the center line at the free end of the beam. The periods T_{MPM} and T_{BT} are derived from the relations $T = 2\pi/\omega_{MPM}$ or $T = 2\pi/\omega_{BT}$, respectively. The target ratio is 1.0 for both $\mathcal{A}$ and $\mathcal{T}$.

The least squares fit is computed for one period of motion. The findings for the ratios defined in (6.6) are plotted in Figure 6.11. Both the standard MPM and cell-based variant AL exhibit volumetric locking as Poisson's ratio approaches the incompressible limit. In both cases the magnitude of the free end displacement is decreasing as the period of motion increases. This observation indicates an artificial increase in beam stiffness due solely to the locking phenomenon. The ALCV variant, however, does not experience this problem as indicated by its consistent performance with respect to the amplitude and period ratio for increasing values of ν. Thus, the ALCV is an ideal candidate for eliminating both shear and volumetric locking in MPM simulations, regardless of Poisson's ratio or material type (fluid or solid).

6.2.2 Conclusion

MPM's ability to capture a linear elastic response for a material with finite shear stiffness is investigated in the form of free vibration. In particular, the effectiveness of the anti-locking approach presented in Chapter 4 is instrumental to mitigating shear locking for a cantilever beam subjected to a prescribed velocity field. Both normal and shear stresses are successfully recovered, and represent a significant improvement over the standard MPM algorithm. The example also shows that the proposed anti-locking technique exhibits ideal convergence behavior. Volumetric locking in the context of solid mechanics is addressed by examining the algorithmic performance when approaching the incompressible material limit. A single anti-locking variant (ALCV) is identified that is capable of mitigating both shear and volumetric locking, making it an ideal candidate for both fluid and solid mechanics simulations.

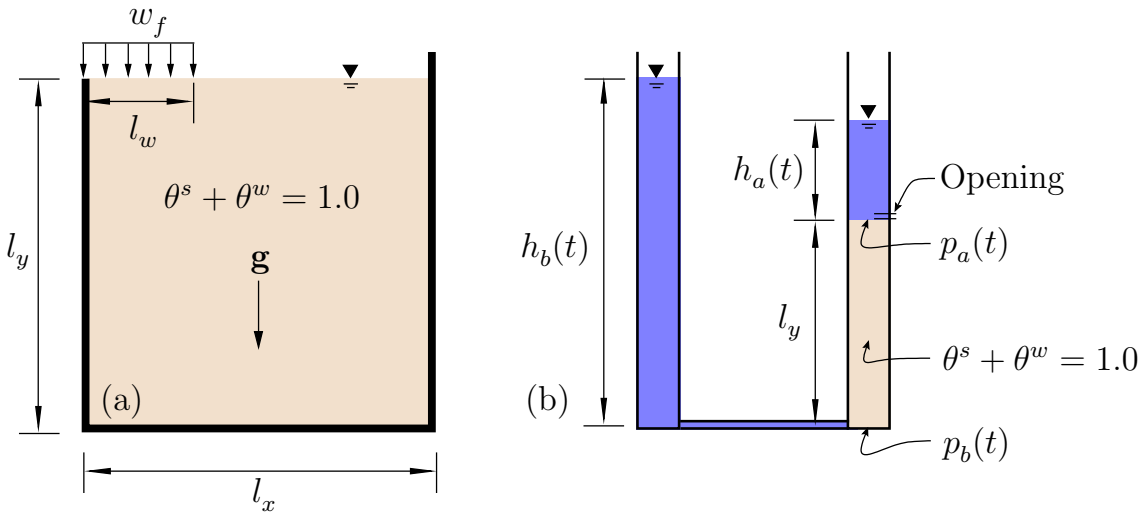

Figure 6.12: Geometric description for volume constraint validation. (a) Saturated soil with foundation loading and (b) pressure drawdown schematic.

6.3 Volume Constraint Validation

This section presents three example problems used to test and validate the volume constraint algorithm presented in Chapter 5. This is done in a multiphase setting, using solid and fluid phases to emulate a saturated soil. These simulations include a simple, 1-dimensional (1D) hydrostatic analysis of a saturated soil panel, a pressure head drawdown examining the effects of prescribed boundary conditions, and a 2-dimensional (2D) foundation analysis. The schematic for these analysis is depicted in Figure 6.12. Though straightforward in scope, these examples provide a setting for evaluation of the volume constraint and highlight the various capabilities of the implementation. Where possible the volume constraint findings are compared to theoretical solutions and/or other implementations from the MPM literature and FEM community.

6.3.1 Hydrostatic Conditions

Perhaps the most basic multiphase examples is the hydrostatic analysis of a saturated, 1D soil panel under the action of gravity. This multiphase setting assumes that the voids contained in a solid, porous medium are filled in their entirety by a water phase throughout the domain in question. This example evaluates the critical components the volume constraint algorithm presented in Chapter 5, including obtaining and interpreting different stress measures, such as the pore pressure and vertical stress. The study also investigates the panel displacement and provides a comparison to a closed form solution.

Table 6.5: Hydrostatic analysis geometry, material description, and MPM parameters.

Domain Parameters	Symbol	Value(s)
Height, [m]	l_y	2.0
Length, [m]	l_x	0.125
Load length, [m]	l_w	0.0
Load magnitude, [Pa]	w_{fnd}	0.0
Gravity magnitude, [m/s^2]	$\|\mathbf{g}\|$	10.0
Solid Phase	–	–
Initial volume fraction	θ^s	0.9 , 0.8 , 0.7 , 0.6 , 0.5
Microscopic density, [kg/m^3]	ρ_s	2600.0
Microscopic bulk modulus, [Pa]	K_s	$1.0\,(10)^{16}$
Macroscopic bulk modulus, [Pa]	K^s	Eqn. (6.7)
Macroscopic shear modulus, [Pa]	G^s	Eqn. (6.8)
Macroscopic Poisson's ratio	ν^s	0.0
Water Phase	–	–
Initial volume fraction	θ^w	0.1 , 0.2 , 0.3 , 0.4 , 0.5
Microscopic density, [kg/m^3]	ρ_w	997.5
Microscopic bulk modulus, [Pa]	K_w	$2.0\,(10)^6$
Macroscopic bulk modulus, [Pa]	K^w	0.0
Macroscopic shear modulus, [Pa]	G^w	0.0
Macroscopic Poisson's ratio	ν^w	0.0
MPM Parameters	–	–
Time step, [s]	Δt	$5.00\,(10)^{-6}$
Duration, [s]	t_f	2.0
Cell size, [m]	$h_x = h_y = h_z$	0.125
Particles per cell	PPC	9

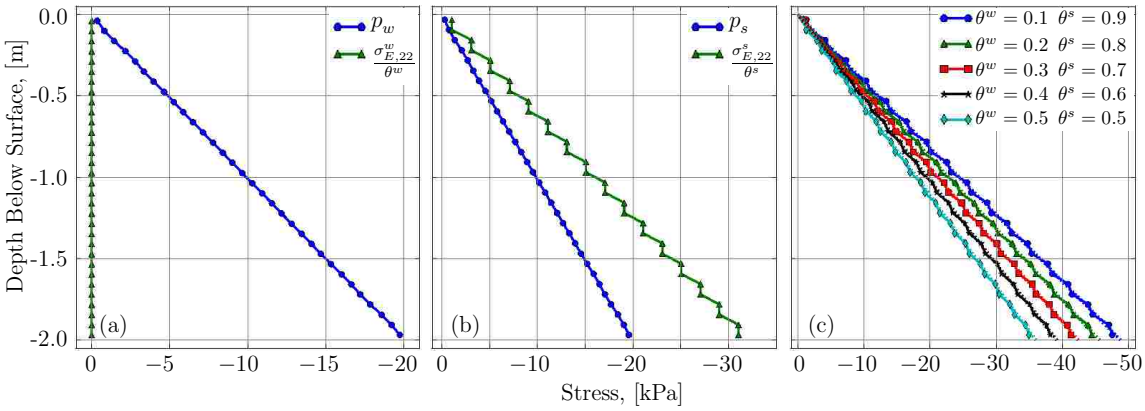

Figure 6.13: Pore pressure and vertical stress distribution at t_f with increasing depth. (a) Water phase ($\theta^w = 0.1$ shown), (b) solid phase ($\theta^s = 0.9$ shown), and (c) mixture vertical stress, σ_{22}^{mix}, for all mix combinations.

The solid and fluid properties, as well as the MPM parameters used in this study, are listed in Table 6.5. These geometric conditions and material properties effectively convert this simulation into a 1D analysis. A multigrid framework is used to describe the motion of both the solid and fluid phase throughout the analysis. Under this formulation the solid phase assumes the role of a soil skeleton. As such, the solid phase is a assigned a mixture, or bulk stiffness, while the fluid phase has no such contribution. The mixture bulk modulus is obtained via

$$K^{\mathrm{m}} = \frac{1}{\theta^s/K_s + \theta^w/K_w} \ , \tag{6.7}$$

where K_s and K_w are the constituent volumetric stiffnesses of the solid and water phases, respectively. For this and the other saturated soil analyses appearing in this chapter, the solid constituents are assumed incompressible, and hence have $K_s \approx 10^{16}$. The mixture shear modulus follows suit as

$$G^{\mathrm{m}} = \frac{3\,(1-2\,\nu^{\mathrm{m}})}{2\,(1+\nu^{\mathrm{m}})}\,K^{\mathrm{m}} \tag{6.8}$$

with ν^{m} as Poisson's ratio (0.0 for the 1D analysis). Using these definitions it is easy to show that the mechanical properties of a single phase are obtained when either $\theta^s = 1.0$ and $\theta^w = 0.0$, or $\theta^s = 0.0$ and $\theta^w = 1.0$.

In Figure 6.13 a series of plots examines the pore pressure and effective vertical stress from several perspectives. The plots in 6.13(a) and 6.13(b) are for the case $\theta^w = 0.10$ and $\theta^s = 0.90$, and are constituent-based values for the fluid and solid phases, respectively. Equations (5.8) and (5.14) identify what these quantities physically represent. In the case of the water, the term $\sigma^w_{E,22}$ is zero because the water phase has no bulk stiffness. On the

other hand, the pressure term $p_w = p_s$ is present in both phases. The solid phase has a nominal effective stress value as indicated in Figure 6.13(b). These plots represent what the computational MPM particles carry and *output* as stress quantities.

In this formulation the vertical component of the mixture stress is obtained according to

$$\sigma_{22}^m = \sigma^s + \sigma^w = \sigma_{E,22}^s - \theta^s\, p_s + \sigma_{E,22}^w - \theta^w\; p_w = \sigma_{E,22}^s - p\ , \tag{6.9}$$

where $p = p_w = p_s$ and $\theta^s + \theta^w = 1.0$. Keep in mind this is the vertical stress of the saturated medium *as a whole* or as a *single* body. Figure 6.13(c) compares the vertical stress components extracted from the MPM simulations to the stress distribution

$$\sigma_{22} = -\rho^m\, g\, d = -\left(\theta^w\, \rho_w + \theta^s\, \rho_s\right)\; g\, d\ , \tag{6.10}$$

where g is the magnitude of gravity and d is the depth below the free surface. The quantities obtained using (6.10) appear as dashed lines in the figure. Clearly the MPM simulations are building a stress field consistent with these values for all volume fraction pairs considered.

This example illustrates that mixture or total values must be obtained as part of post-processing [1] , due exclusively to the fact that each phase is analyzed using its own motion (and own grid in the context of this MPM implementation). This point will be revisited again shortly, but for now the seed of a question is planted: in a multiphase setting whose formulation and solution reflects the ideology that phases are tracked by way of their own motion, what is the global behavior of interest—the individual phases or the mixture as a whole single body? The answer cannot be both in the current multigrid, mulitphase MPM formulation. Seeking both the individual phase behavior as well as a single, total mixture response poses a fundamental contradiction.

Stress values alone do not tell the whole story and it is necessary to also exam the displacement terms, as these values are also critical in validating an approach. In Figure 6.14 the displacement of the solid phase is examined in detail. In 6.14(a) the raw displacement values are shown for a particle representing the surface of the solid phase. Even with damping significant oscillations are observed. However, the surface displacement is moving about the analytical solution depicted by the dashed line. This is better observed by applying a smoothing filter to the raw data. In 6.14(b) a simple moving average is applied and the

[1] This statement is not entirely true. The code could be modified to output any mixture value. However, obtaining the mixture values is an additional exercise that must be performed, as individual phases do not have direct knowledge of other phases in the analysis. That is, each phase knows only of a constraint pressure and forces arising due to momentum exchange processes, such as drag forces. How these forces came to be is irrelevant to an individual phase from an algorithmic perspective.

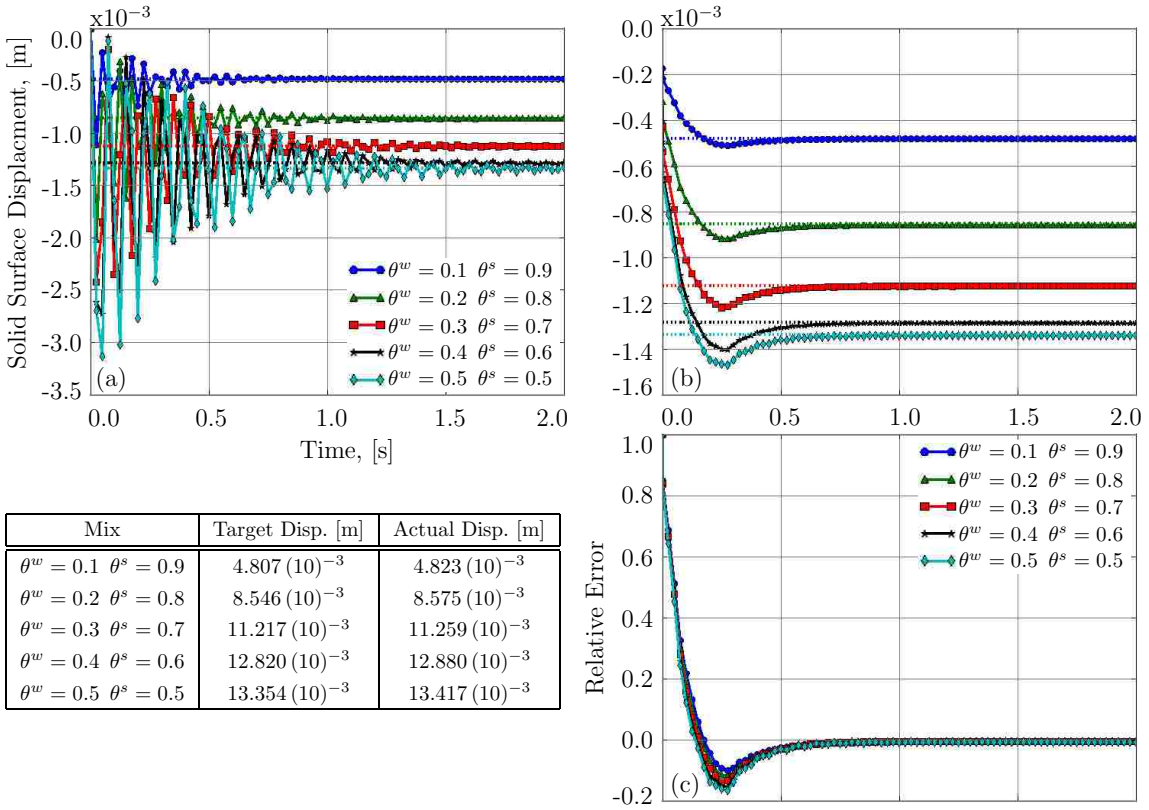

Mix	Target Disp. [m]	Actual Disp. [m]
$\theta^w = 0.1\ \theta^s = 0.9$	$4.807\,(10)^{-3}$	$4.823\,(10)^{-3}$
$\theta^w = 0.2\ \theta^s = 0.8$	$8.546\,(10)^{-3}$	$8.575\,(10)^{-3}$
$\theta^w = 0.3\ \theta^s = 0.7$	$11.217\,(10)^{-3}$	$11.259\,(10)^{-3}$
$\theta^w = 0.4\ \theta^s = 0.6$	$12.820\,(10)^{-3}$	$12.880\,(10)^{-3}$
$\theta^w = 0.5\ \theta^s = 0.5$	$13.354\,(10)^{-3}$	$13.417\,(10)^{-3}$

Figure 6.14: Vertical displacement history of the surface for the solid phase. (a) Raw data, (b) Simple moving average of data, and (c) relative error in the vertical displacement of the MPM hydrostatic simulations.

surface motion is seen to approach the theoretical values. Each volume fraction pair is compared by introducing the relative displacement error as

$$u_{\text{Rel. Error}} = \frac{u^h - u_e}{u_0^h - u_e} \ , \tag{6.11}$$

where u^h and u_0^h are the current and initial displacements from the MPM simulation and u_e is the analytical solution. These calculations are displayed in the table next to Figure 6.14(b), where the similarity in displacement profiles is shown.

The target displacement of the solid phase is obtained by integrating the vertical strain of the soil skeleton. For this particular 1D analysis this amounts to evaluating the integral

$$\delta_{y,s} = \int_0^{l_y} \varepsilon_{y,s}\, dy = \int_0^{l_y} \frac{\sigma'_{y,s}}{E^{\text{m}}}\, dy \Longrightarrow \frac{\gamma'_s\, l_y^2}{2\, E^{\text{m}}} \ , \tag{6.12}$$

where $\delta_{y,s} > 0.0$ indicates a downward displacement and E^{m} is the mixture elastic modulus. The prime super script $(\bullet')$ indicates an effective quantity. The effective weight term follows

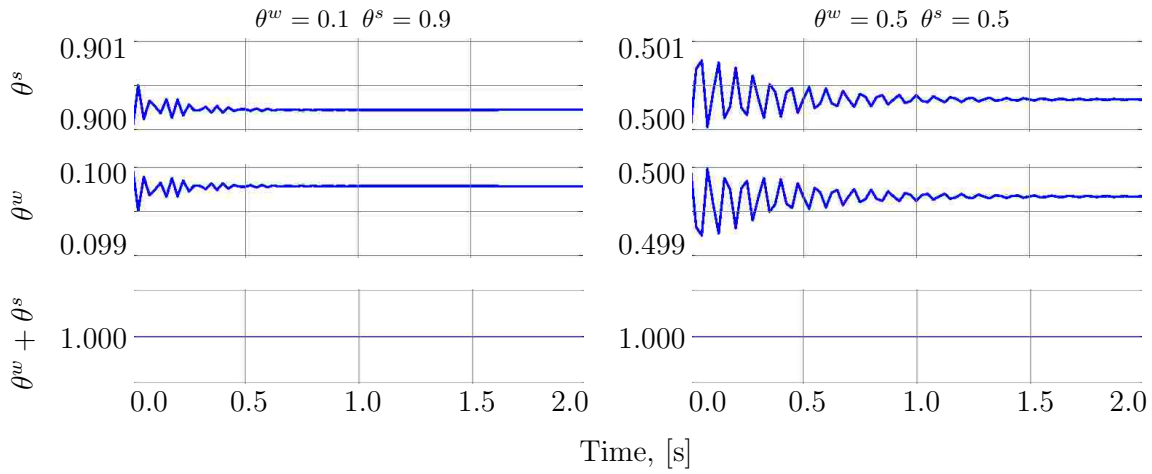

Figure 6.15: Volume fraction history for two mixtures. (a) $\theta^w = 0.1\,,\, \theta^s = 0.9$ and (b) $\theta^w = 0.5\,,\, \theta^s = 0.5$.

from

$$\gamma_s^{'} = \gamma_{\text{sat}} - \gamma_w \tag{6.13}$$

with the saturated unit weight as

$$\gamma_{\text{sat}} = \frac{\gamma_w \left(\rho_s/\rho_w + e\right)}{1+e}\ . \tag{6.14}$$

The void ratio is determined from the porosity, n (or θ^w in this example), by way of the ratio

$$e = \frac{n}{1-n}\ . \tag{6.15}$$

The volume constraint algorithm is based on the notion that the volume occupied by all phases relative to some control, or reference volume, meets a prescribed value for each time step. In the present example the matter initially occupies 100% of the physical space. That being the case, the amount of matter should always occupy this prescribed value of 100%. This process can be monitored by tracking the volume fraction of each phase at a specific location. This is shown in Figure 6.15 for two simulations, namely $\theta^w = 0.1\,,\, \theta^s = 0.9$ and $\theta^w = 0.5\,,\, \theta^s = 0.5$. Here the the volume fraction is evaluated at the particle representing the base, or bottom, of the saturated soil column. Strictly speaking this is not correct to compare the volume fraction at these particles, as their positions do not coincide precisely. In this case, however, the phase positions differ by very small amounts and the volume fraction analysis is shown to meet the stated goals: at each point in time the total volume occupied sums to 100% of the available space. In these plots the solid phase is observed to contract, i.e., θ^s increases due to the action of gravity, as indicated by the downward

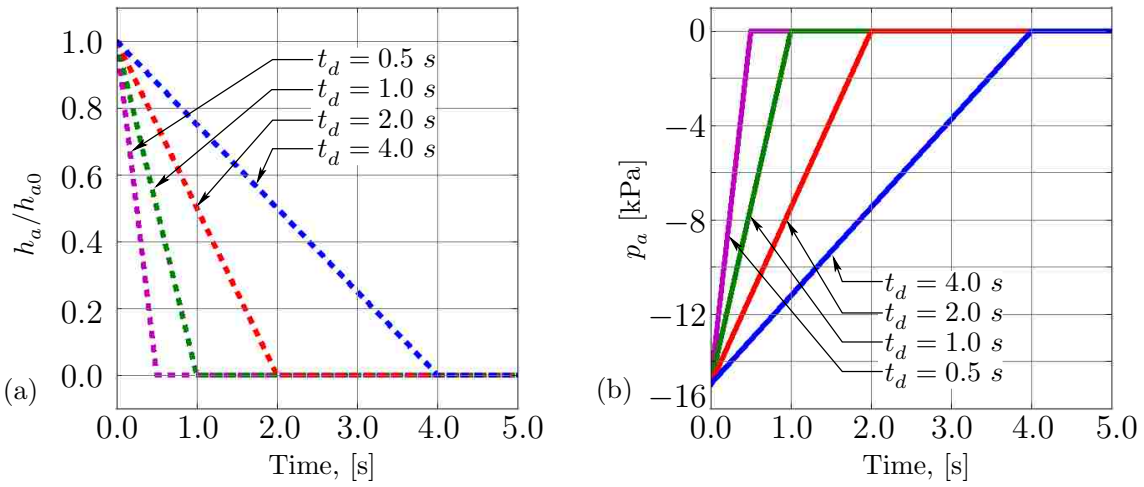

Figure 6.16: Prescribed conditions at top of chamber. (a) Variation of water height h_a as a function of time. (b) Prescribed pressure p_a as a function of time.

displacement shown in Figure 6.14. To compensate for this change the water phase volume fraction decreases proportionately. The size of the relative oscillations in the volume fraction are a function of the water to soil ratio. Not surprisingly, the higher θ^s the faster the medium achieves balance in the volume fraction. For these cases the mixture bulk modulus—the driving quantity behind the volume constraint algorithm—is significantly higher and results in smaller volume changes of each phase during each time step.

6.3.2 Pressure Head Drawdown

The setup for this numerical study is shown in Figure 6.12(b). A saturated soil column is subjected to a prescribed pressure at both the top and bottom, p_a and p_b, resulting from the fluid columns of height h_a and h_b, respectively. These two pressures can vary in time. Here, however, it is assumed that the lower value, p_b, is constant as h_b is fixed in time. The upper pressure is controlled by prescribing the opening size just above the saturated soil mass. Under the action of gravity the upper water column will drain, continuously decreasing the pressure magnitude at the surface of the saturated soil column. This in concert with the constant pore pressure at the bottom induces a pressure gradient over the height of the column.

This study has practical significance and can potentially help simulate the liquefaction process in saturated sands. For example, in the Master's research work by Heller (2003), a physical specimen replicating the setup shown in Figure 6.12(b) is constructed in order to examine the diffusion coefficient in sands, with the end goal of predicting beach scour

Table 6.6: Pressure head drawdown analysis geometry, material description, and MPM parameters.

Domain Parameters	Symbol	Value(s)
Chamber height, [m]	l_y	1.0
Initial water height a, [m]	h_{a0}	1.5
Initial water height b, [m]	h_{b0}	2.5
Initial pressure a, [kPa]	p_{a0}	-14.97
Initial pressure b, [kPa]	p_{b0}	-24.94
Gravity magnitude, [m/s^2]	$\|\mathbf{g}\|$	10.0
Drag interaction coefficient, [N-s/m^4]	μ	$1.0\,(10)^0 - 1.0\,(10)^8$
Solid Phase	–	–
Initial volume fraction	θ^s	0.67
Microscopic density, [kg/m^3]	ρ_s	2600.0
Microscopic bulk modulus, [Pa]	K_s	$1.0\,(10)^{16}$
Macroscopic bulk modulus, [Pa]	K^s	$1.0\,(10)^9$
Macroscopic shear modulus, [Pa]	G^s	$1.5\,(10)^9$
Macroscopic Poisson's ratio	ν^s	0.0
Water Phase	–	–
Initial volume fraction	θ^w	0.33
Microscopic density, [kg/m^3]	ρ_w	997.5
Microscopic bulk modulus, [Pa]	K_w	$2.0\,(10)^9$
Macroscopic bulk modulus, [Pa]	K^w	0.0
Macroscopic shear modulus, [Pa]	G^w	0.0
Macroscopic Poisson's ratio	ν^w	0.0
MPM Parameters	–	–
Time step, [s]	$\Delta\, t$	$2.50\,(10)^{-6}$
Drawdown time, [s]	t_d	0.5 , 1.0 , 2.0 , 4.0
Duration, [s]	t_f	5.0
Cell size, [m]	$h_x = h_y = h_z$	0.0625
Particles per cell	PPC	4

from tsunamis. By studying how the pressure profile varies in both time and space, it is possible to isolate the transition in the effective stress tensor that is responsible for inducing liquefaction. This study takes a similar approach and focuses on the pore pressure distribution at select locations in the soil column.

The goals of this study are two fold in nature. The first goal is to examine the effects of prescribed boundary conditions when using the volume constraint algorithm. This is accomplished by specifying multiple drawdown times of the water height h_a. The second goal identifies which component(s), in addition to the volume constraint, are necessary for capturing a realistic response of the saturated soil column in this setting. As will be shown shortly, it is important to add a time dependent momentum dissipating force to the system. This study does not attempt to validate or calibrate the existing material models, nor is there an attempt to match results to from various physical experiments. The material properties and MPM parameters used for in this simulation are listed in Table 6.6.

The water height h_a is decreased according to the plots shown in Figure 6.16(a). These linear profiles are best characterized by the drawdown time, t_d, which represents the time elapsed for the upper water portion to drain completely. An increasing drawdown time corresponds to a decreasing orifice opening. If the goal is to emulate a gravity driven drawdown then these profiles should be parabolic in shape. However, preliminary studies indicate a linear decay is sufficient to capture the physical behavior and eliminates unnecessary complexity. The prescribed pressure profiles for the various drawdown times are shown in Figure 6.16(b), assuming $h_{a0} = 1.5$ [m] as indicated by Table 6.6. Each prescribed value starts around -15 [kPa] and is ultimately reduced to 0.0 [kPa][2]

The volume constraint alone is not sufficient for obtaining realistic results. As noted previously, the constraint provides only a single pressure, and is not capable of capturing other momentum exchange processes including the time-dependent permeability force which links the velocity field and pressure gradient. To account for this an additional drag force is added consistent with the approach described in the paper by Mackenzie-Helnwein et al. (2010), where a time dependent term proportional to the relative phase velocity and an interaction coefficient, μ, is added to the governing equation of motion for each phase. In the current example this additional force can be interpreted as an alternative form of Darcy's Law, which quantifies the force exchange resulting from the flow of a fluid through a porous medium; Lewis and Schrefler (1998). However, the general nature of the presentation in Mackenzie-Helnwein et al. (2010) does not easily yield a direct comparison of the interaction coefficient, μ, to the terms contained in Darcy's Law, such as k, the permeability

[2]These are gauge pressures, thus zero referenced relative to atmospheric pressure.

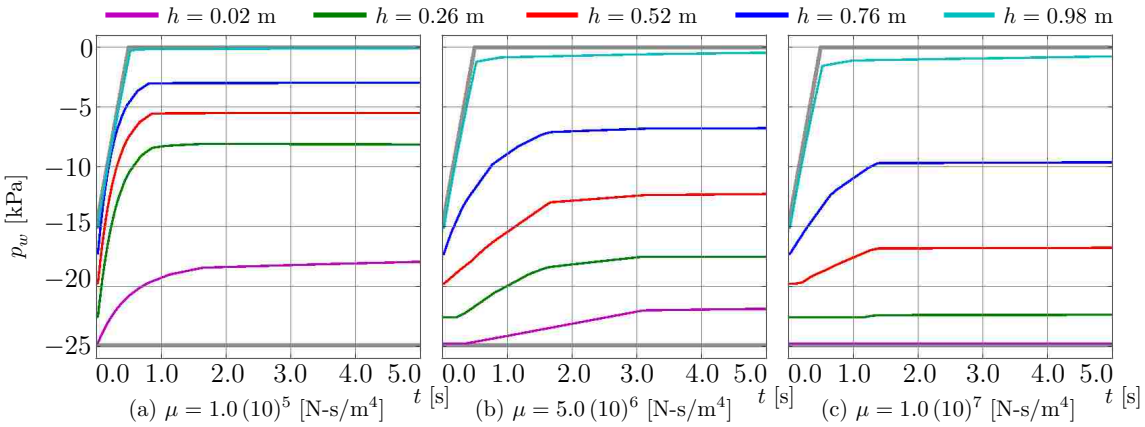

Figure 6.17: Pore pressure history at various heights, h, for a pressure drawdown time of $t_d = 0.5\ s$. Three different time-dependent permeabilities coefficients are considered: (a) $\mu = 1.0\,(10)^5$ [N-s/m^4], (b) $\mu = 5.0\,(10)^6$ [N-s/m^4], and (c) $\mu = 1.0\,(10)^7$ [N-s/m^4].

of the medium. It is possible to establish a direct comparison, but it will be case-specific and does not affect current investigation. Instead, this study employs μ in the interval $(10)^0 - (10)^8$ [N-s/m^4], which, when coupled with the volume constraint algorithm, proves sufficient in capturing all aspects of the mechanical response.

The pressure history at various heights is shown in Figure 6.17(a)–(c). The readings correspond to particle values, hence the slight irregularity in physical spacing of the readings. The prescribed nodal pressures at the bottom and top of the soil column are shown by the thicker line and indicate these figures are for $t_d = 0.5\ s$. Three different interaction coefficients are shown: $\mu = 1.0\,(10)^5$, $5.0\,(10)^6$ and $1.0\,(10)^7$ [N-s/m^4]. The impact of this term on the analysis is quite profound. For $\mu \lesssim 1.0\,(10)^5$ there is essentially no contribution from the additional force term. This is a result of the extremely small relative velocity between the solid and water phases. For these simulations reducing the upper pressure has an immediate impact through the entire soil column as seen in Figure 6.17(a). That is, all pressure readings immediately increase and attempt to go to the hydrostatic state. The particles located in the bottom cell, such as the one at $h = 0.02$ [m], are restricted from increasing as much as their counterparts simply because of the prescribed pressure p_b at the adjacent nodes representing the base of the saturated column. This response is not reasonable and hints that the volume constraint acting alone is not capable of capturing all desired behavior.

Reasonable results begin to emerge as the drag interaction coefficient is increased. Two examples are shown in Figures 6.17(b) and 6.17(c). In both cases the pressure response in the saturated soil is delayed based on the vertical location. The bottom particle located at

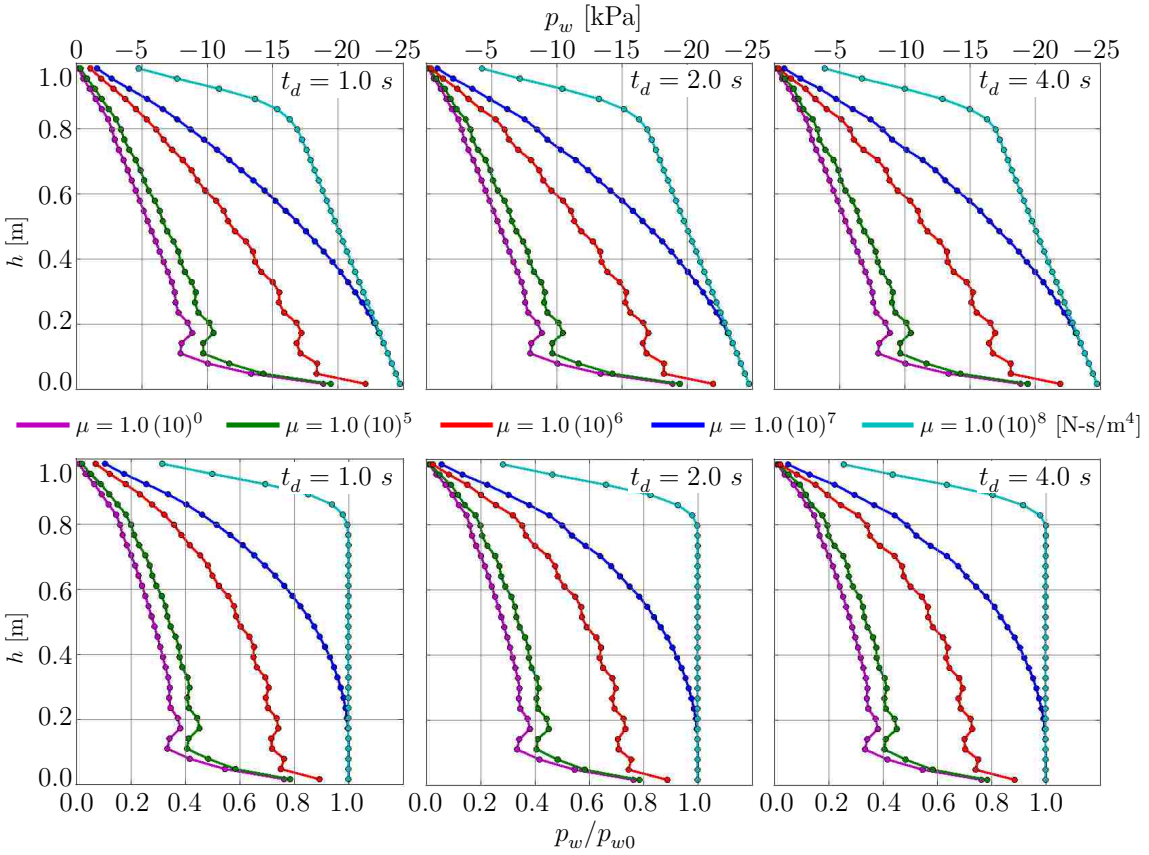

Figure 6.18: Vertical pore pressure distribution in the chamber at $t = 5.0\ s$. The particle locations are shown as circular points. The upper row is the actual value and the lower row is normalized to the initial pressure, p_{w0}. Each column represents a different drawdown time, t_d.

$h = 0.02$ [m] exhibits no change for over half a second for $\mu = 1.0\,(10)^6$. The final pressure distribution appears to be nearly linear with height. When the interaction coefficient is increased to $\mu = 1.0\,(10)^7$ the lower particle experiences no change in pressure throughout the duration of the analysis. The end result is a pressure distribution that is quadratic over the height of the column.

Figure 6.17 provides a great example of the pressure history for a given drawdown time. But what about the spatial variation of the pressure? In Figure 6.18 the spatial distribution is examined at $t = 5.0\ s$ for three different drawdown times: $t_d = 1.0$, 2.0 and 4.0 s. The particle values are plotted for several drag interaction values. The upper row of plots shows the actual pressure while the lower row depicts the final pressure value normalized to the initial pressure, p_{w0}. The first observation made from this figure is that drawdown time is

irrelevant provided the time examined ($t = 5.0\ s$ in this case) is significantly larger than the drawdown time itself. Of course these plots would look quite different if the spatial profile at, say, $t = 2.32\ s$ were shown. The second observation is the role the prescribed boundary conditions play as well as the drag interaction coefficient. For those particles at the bottom of the column the impact of the prescribed pressure condition can be dramatic, particularly if the drag coefficient is on the smaller end of the scale considered. For example, those analysis with $\mu \lesssim 1.0\,(10)^5$ the distribution is tending to the linear profile consistent with the action of gravity. However, the prescribed condition at the bottom is altering the profile and generating a non-physical spatial distribution. These problems are again eliminated by increasing the drag coefficient. As shown by these figures it is possible to select a high enough drag coefficient such that almost no change in pressure occurs throughout the column, save of course at the top where the prescribed value is changing. This scenario is exemplified by the $\mu = 1.0\,(10)^8$ case. The actual response observed in the field could be simulated here by selecting μ in the range of $(10)^6 - (10)^8$ [N-s/m^4], and suggests that with proper calibration this model could be matched to any experimental results. These findings again support the notion that although the volume constraint is capable of providing a pressure, by itself it is not capable of capturing desired behavior in a multiphase, geotechnical engineering context. In fact, this example suggests that individual pressure is of little importance compared to the effects of the drag force in achieving desirable results.

In the interest of space some results have been omitted from this discussion. These include the effective stress plots of the solid phase. As noted at the outset of this section, liquefaction is induced when the effective stress of the soil skeleton attempts to transition into the tension regime. In the present case this transition was observed but proceeded without loss of strength because a linear elastic material model was employed. Of course a cohesionless, elastoplastic model could be used for simulations like this and the plastic effects associated with the prescribed pressure field could be documented. This is largely beyond the scope of this validation example but provides a potential avenue of study for future simulations.

6.3.3 Foundation Loading Analysis

A benchmark example often presented for these types of formulations is the plane strain loading condition shown in Figure 6.12(a). A saturated 2D soil panel is loaded over a small region as would be the case for a spread footing or strip foundation. Analysis parameters are listed in Table 6.7. For this example the loading is increased linearly from $w_{fnd} = 0.0$ [Pa] to 100 [Pa] over a duration of 1.0 s. Dissipative mechanisms are not considered in this study.

Table 6.7: Planar foundation analysis geometry, material description, and MPM parameters for use with the volume constraint algorithm in Chapter 5 and the $u-p$ CMPM formulation by Zhang et al. (2008).

Domain Parameters	Symbol	Value(s)
Height, [m]	l_y	30.0
Length, [m]	l_x	30.0
Load length, [m]	l_w	3.0
Load magnitude, [Pa]	w_{fnd}	100.0
Gravity magnitude, [m/s^2]	$\|\mathbf{g}\|$	0.0
Solid Phase	–	–
Initial volume fraction	θ^s	0.7
Microscopic density, [kg/m^3]	ρ_s	2670.0
Microscopic bulk modulus, [Pa]	K_s	$1.0\,(10)^{16}$
Macroscopic bulk modulus, [Pa]	K^s	$2.08\,(10)^7$
Macroscopic shear modulus, [Pa]	G^s	$9.62\,(10)^6$
Water Phase	–	–
Initial volume fraction	θ^w	0.3
Microscopic density, [kg/m^3]	ρ_w	997.5
Microscopic bulk modulus, [Pa]	K_w	$2.0\,(10)^9$
Macroscopic bulk modulus, [Pa]	K^w	0.0
Macroscopic shear modulus, [Pa]	G^w	0.0
$u-p$ CMPM	–	–
Mixture density, [kg/m^3]	ρ^m	2168.25
Mixture bulk modulus, [Pa]	K^m	$2.08\,(10)^7$
Mixture shear modulus, [Pa]	G^m	$9.62\,(10)^6$
Biot's constant	α	1.0
Fluid permeability, [m/s]	k	0.0
MPM Parameters	–	–
Time step, [s]	Δt	$1.25\,(10)^{-4}$
Duration, [s]	t_f	5.0
Cell size, [m]	$h_x = h_y = h_z$	1.5
Particles per cell	PPC	4

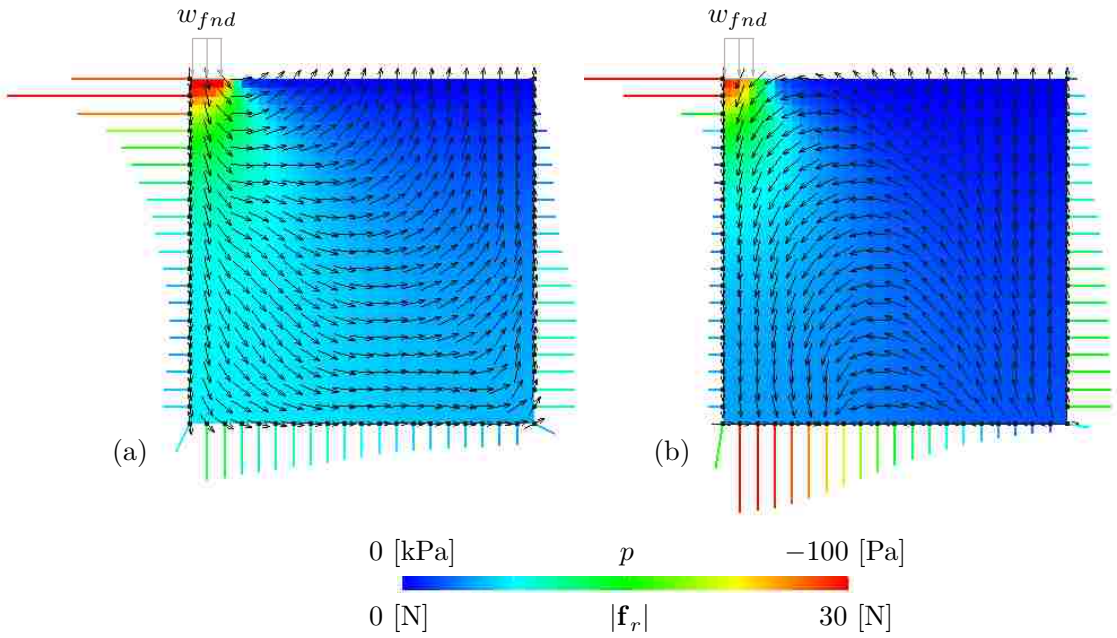

Figure 6.19: Pore pressure, reaction force, and velocity distribution. (a) Using the volume constraint outlined in Chapter 5. The nodal vector field shows the relative velocity between the solid and fluid phases. (b) The $u-p$ CMPM formulation by Zhang et al. (2008). The velocity field is for the mixture.

Nodes representing the surface that are directly under the loading assume the prescribed pore pressure $p = w_{fnd}$ [Pa]. The remaining free surface nodes assume a prescribed value of $p = 0.0$ [Pa]. Findings obtained using the volume constraint algorithm of Chapter 5 are compared to the $u-p$ CMPM, a multiphase MPM formulation described in the paper by Zhang et al. (2008), where researchers build a $u-p$ form of the governing equations of saturated porous media for use in the MPM. Both MPM simulations are presented alongside results obtained by McGann et al. (2012) using the OpenSEES FEM framework.

The loaded soil panels from the MPM simulations are shown in Figure 6.19. These correspond to $t = 1.0$, when the loading reaches the peak magnitude. The particle colormap highlights the pore pressure distribution where both the volume constraint and $u-p$ CMPM yield similar pressures. Under the foundation the pressure tend to the applied value and are distributed reasonably throughout the domain. The small vectors overlaying the particles in 6.19(a) represent the flow direction of the relative phase velocity between the fluid and solid phase. Since only a single particle phase is used in the $u-p$ CMPM, the small vectors show the velocity field of the mixture in 6.19(b). Note that these vectors indicate only the flow direction and are not plotted by magnitude. The reaction force is plotted around

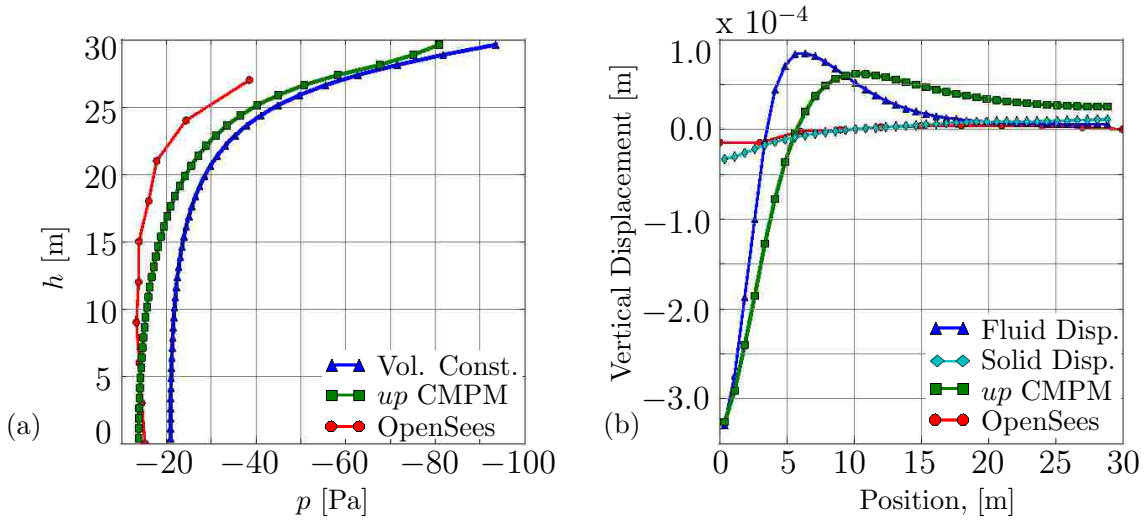

Figure 6.20: Comparison of pore pressure and displacement between the volume constraint outlined in Chapter 5, $u-p$ CMPM formulation by Zhang et al. (2008), and a FEM $u-p$ formulation from McGann et al. (2012). (a) Vertical pressure distribution under load at $t = 1.00\ s$. (b) surface displacement profile at $t = 1.00\ s$.

the perimeter of each figure. In the case of the volume constraint formulation, the plotted force represents the sum of the two phases present in the analysis, or the value from the common grid. The shape of these profiles compare favorably with slight discrepancies in the magnitude.

The pressure profile under the load and free surface displacements are shown in Figure 6.20. For comparison purposes values from the OpenSEES FEM framework as prepared by McGann et al. (2012) are shown. The FEM framework employs a mixed $u-p$ element suitable for dynamic analysis of saturated media. A word of caution in comparing the MPM findings to the OpenSEES simulation: the FEM examples assume a finite soil permeability, and that the pressure under the loading is fixed at 0.0 [Pa]. The end result is a profile that is slightly shifted towards 0.0 in Figure 6.20(a) and the upper point of $h = 30.0$ [m], $p = 0.0$ [Pa] has been omitted from the current figure. The boundary conditions are also slightly different for the FEM model, as the right side of the saturated panel is fixed for the OpenSEES analysis. With respect to pore pressures each simulation gives comparable results with similar shapes. Both the CMPM and FEM models tend to approximately -10 [Pa] at the base. For all heights the volume constraint formulation yields a slightly smaller pressure.

The surface displacement for each simulation is shown in Figure 6.20(b). For the volume constraint algorithm there is not a definitive surface definition for the saturated medium

since each phases is modeled on separate grids. Thus, the surface of both the water and soil phase is plotted. This rehashes an observation from Section 6.3.1 where the question was asked what is the behavior of interest: the individual phases or the mixture as a whole single body? In the current example it arguably makes more sense to claim the mixture of the whole saturated mass is the behavior of interest, yet this contradicts the premise of the multiphase formulation in a multigrid context. Certainly if a foundation was placed on this panel the global displacement of the saturated medium as a whole is the target value. The common grid cannot be used to settle this argument, as the particle motion (acceleration, velocity, and position) are all determined using their unique motions, thus rendering common grid kinematics obsolete. Comparing to the other methods yields mixed results. For this example the water phase closely resembles the $u - p$ CMPM in Figure 6.20(b), whose particles represent the mixture as a whole. However, despite the difference in boundary conditions for the OpenSEES model, the solid phase surface tends to agree with the FEM approach. These comparisons are at at best inconclusive and highlight some of the pitfalls associated with a multigrid treatment of different phases when the goal is in fact to model a single mixture quantity.

6.3.4 Conclusion

This section presented three examples highlighting the capabilities of the volume constraint algorithm. The saturated soil simulations were performed in a multigrid, multiphase framework consistent with the approach presented in Mackenzie-Helnwein et al. (2010) and Chapter 5. Analyses were limited to the linear elastic material regime. The 1D hydrostatic test cases produced accurate distributions of the constituent, bulk, and mixture stresses. Solid phase displacements were shown to converge to an analytical solution. The pressure head drawdown simulations showed how prescribed conditions could potentially be used to capture the liquefaction process. The drawdown examples emphasized the need for alternative momentum exchange mechanisms in addition to the pressure obtained from the volume constraint, as it was shown that these alternative exchange processes are largely more important in a saturated soil context. The final example considered a 2D saturated panel subject to a distributed foundation loading. Pore pressure distribution and surface displacements were compared to the $u - p$ CMPM formulation by Zhang et al. (2008) and an FEM implementation using stabilized elements created by McGann et al. (2012). All results compared favorably with respect to pore pressure. Surface displacement plots illuminated some of the pitfalls associated with a multigrid treatment of different phases when the goal is in fact to model a single mixture quantity.

Chapter 7

EXAMPLE PROBLEMS 2: FINITE DEFORMATION ELASTOPLASTIC SIMULATIONS

The examples presented in the previous chapter established the Material Point Method as a valuable tool for modeling both solids and fluids within a single framework. Those examples were, however, limited to the elastic material domain. This chapter extends the focus and incorporates material nonlinearity into the fold.

The following studies highlight the many capabilities of the MPM when coupled with the nonlinear material models developed and presented in Chapter 3. Specific applications include a large-deformation ductile impact simulation, planar sand flow, snow and avalanche diversion, as well as debris flow interaction with protective structures. Many of the investigations are parametric in nature and attempt to identify key relationships between analysis parameters and values of interest.

7.1 Taylor Bar Impact

Establishing the effectiveness of the anti-locking framework in the nonlinear material regime is among the first orders of business in this chapter. The general anti-locking strategy is outlined in Chapter 4, while specific details regarding the extension of the framework to nonlinear materials are presented in Section 4.4.5. The current section investigates the different anti-locking approaches and evaluates their performance in simulating the hyper-velocity impact of a ductile projectile with a rigid surface.

The analysis configuration is shown in Figure 7.1. The ductile mass is flung with an initial velocity v_0 into a rigid surface. The geometry is cylindrical in nature and is described by the initial height and radius, H_0 and R_0, respectively. The parameters H_f and R_f describe the final configuration after motion has ceased and are shown Figure 7.1(b) and 7.1(c). This class of problem is commonly referred to as a *Taylor Bar* impact—a historical homage to Geoffrey Taylor and his work in quantifying the yield strength of solids in dynamic applications, Taylor (1948).

This impact problem has been targeted in the past by researches utilizing the MPM. Specifically, the pioneering works of Sulsky et al. (1994, 1995) and the MPM-SPH comparative work by Ma et al. (2009). In these previous applications the emphasis is primarily

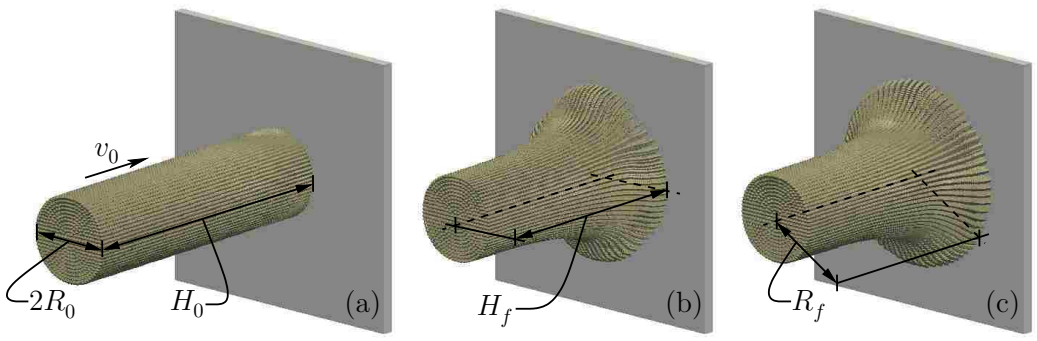

Figure 7.1: Taylor bar geometric description. (a) Initial configuration. (b) Final configuration for Standard MPM. (c) Final configuration using an anti-locking strategy.

Table 7.1: Analysis geometry, material description, and MPM parameters.

Description	Symbol	Value(s)
Initial height, [cm]	H_0	28.0
Initial radius, [cm]	R_0	4.0
Initial velocity, [m/s]	v_0	150
Macroscopic density, [kg/m^3]	ρ_0	2710
Bulk modulus, [MPa]	K	68,600
Shear modulus, [MPa]	G	23,300
Yield stress, [MPa]	σ_Y	61
Isotropic hardening slope	k	0.2
Time step, [s]	Δt	$5.00\,(10)^{-8}$
Duration, [s]	t_f	0.001
Cell size, [cm]	$h_x = h_y = h_z$	1
Particles per cell	PPC	27

on final geometry with little or no focus on the mechanical fields, such as the stress[1]. Here the goal is to identify the benefits and limitations of the proposed anti-locking strategies. This is accomplished by examining the geometry as well as the stress field throughout the simulation for the various anti-locking approaches. As a benchmark for reasonable behavior, the MPM findings are compared to those obtained using MSC Software's Marc, a nonlinear FEM package. That being said, this impact study is not meant to serve as an extensive error analysis comparing MPM to FEM; nor is the goal geared towards model calibration and comparison with experimental findings or existing MPM results.

[1]The work Sulsky et al. (1995) examines the net plastic deformation.

Table 7.1 specifies geometry, material, and MPM parameters. The J2 model described in Section 3.5 is used for these simulations. Four anti-locking strategies are considered:

- *Cell-based volumetric approximation* (CB-VA): The volumetric portion of the strain and stress tensor are approximated using the filter and shape matrices presented in Section 4.3.1 and the cell-based approach described in Section 4.4.1.
- *Cell-based full approximation* (CB-FA): The volumetric and deviatoric portions of the strain and stress tensor are approximated using the filter and shape matrices presented in Section 4.3.2 and the cell-based approach described in Section 4.4.1.
- *Node-based volumetric approximation* (NB-VA): The volumetric portion of the strain and stress tensor are approximated using the filter and shape matrices presented in Section 4.3.1 and the node-based approach described in Section 4.4.2.
- *Hybrid-based full approximation* (HB-FA): The volumetric and deviatoric portions of the strain and stress tensor are approximated using the filter and shape matrices presented in Sections 4.3.1 and 4.3.2. The approximations are combined using the hybrid technique outlined in Section 4.4.3.

The performance of each approach is measured against the standard MPM (STD).

7.1.1 Kinematic Description

The configuration of the cylindrical bar is described in terms of the current height, H, and radius, R, at any time, t. These values are used to construct the normalized variables

$$\bar{H}(t) = \frac{H(t)}{H_0} , \qquad \bar{R}(t) = \frac{R(t)}{R_0} , \qquad \text{and} \qquad T = \frac{t}{t_f} , \tag{7.1}$$

where H_0, R_0, and t_f are given in Table 7.1. The time t_f is the net duration and the same for all cases presented. Here it is assumed that the reference time $t = 0.0\ s$ corresponds to instant impact occurs. The final configuration is represented using

$$H_f = H(t)|_{t=t_f} \qquad \text{and} \qquad R_f = R(t)|_{t=t_f} . \tag{7.2}$$

Due to symmetry only one quarter of the bar is actually modeled. The height of the bar is determined simply by tracking the upper edge of the cylinder. Determining a precise value for the radius can be challenging considering the point-wise body definition in the MPM. Tracking individual particle locations is not necessarily indicative of the position of the body as a whole and proves to be problematic for a radial measure. In order to eliminate this ambiguity, the radius is determined from the center of mass values $\bar{x}$ or $\bar{y}$ computed using

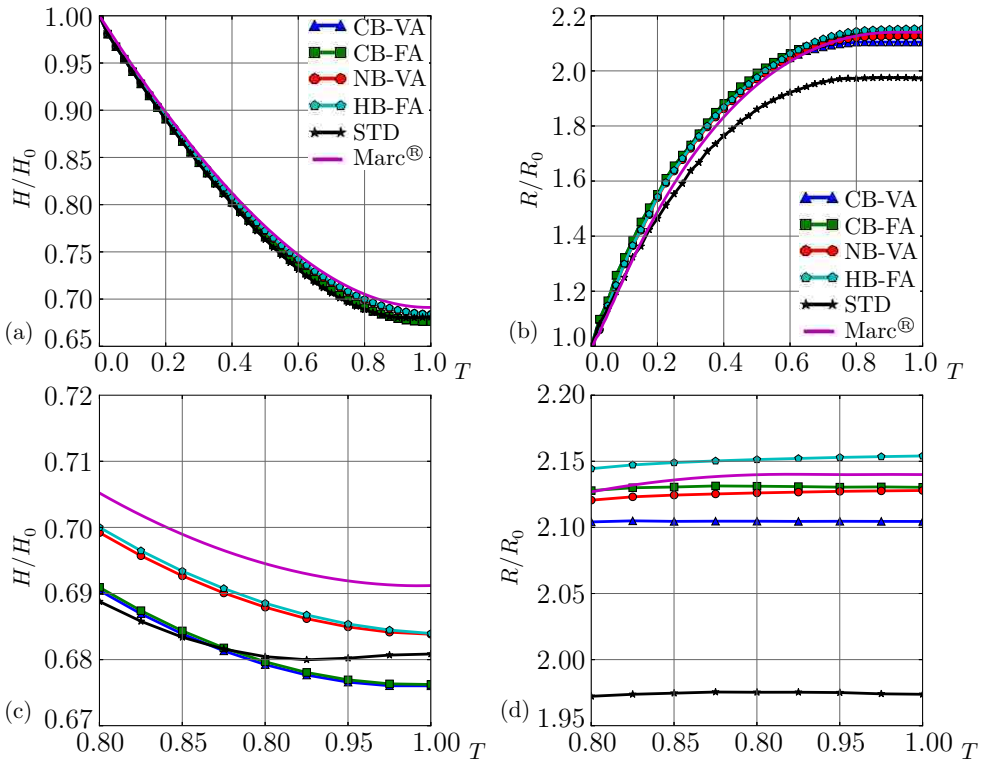

Figure 7.2: Comparison of various anti-locking strategies to the standard MPM. (a) Normalized height as a function of normalized time. (b) Normalized radius as a function of normalized time. (c) and (d) are zoomed in of (a) and (b), respectively.

those particles in contact with the rigid surface[2]. This is a two step procedure. First, the center of mass values are computed as

$$\bar{x}(t) = \frac{\sum_{p_b} x_p(t)\, m_p}{\sum_{p_b} m_p} \qquad \text{and} \qquad \bar{y}(t) = \frac{\sum_{p_b} y_p(t)\, m_p}{\sum_{p_b} m_p}\,, \tag{7.3}$$

where $x_p(t)$ and $x_p(t)$ are the x and y coordinates of each particle. The term p_b indicates a sum over those particles in contact with the rigid surface. The radius is then determined by invoking planar area properties of the quarter circle:

$$\bar{x} = \bar{y} = \frac{4R}{3\pi} \tag{7.4}$$

In this manner a consistent radius is determine throughout the deformation of the solid.

[2]Provided the initial configuration is a quarter circle and the symmetry boundary conditions are applied correctly, then the two quantities $\bar{x}$ and $\bar{y}$ will always be the same (the height or length of the bar is described by the z-coordinate direction).

The normalized values are plotted in Figure 7.2 for the standard MPM and each anti-locking strategy considered. For comparative purposes the same quantities are plotted for the Marc FEM model [3] . The left column depicts the current height while the right displays the radius. The upper row tracks the global geometry and the lower row provides a modified scale so minute differences can be observed.

With respect to the height parameter, the anti-locking techniques provide very little benefit over the standard algorithm. All the MPM lines collapse to essentially the same curve. The FE model height is, as a whole, taller than the MPM simulations. However, this difference is minimal and differs by at most 2.0%. The benefits of the anti-locking approaches are highlighted when examining the normalized radial measure, $\bar{R}(t)$. During the early stages of the analysis there is little difference between all MPM solutions and the FEM results. The lines begin to diverge around $T = 0.25$. The anti-locking techniques and the FE model etch out a nearly identical path in space—suggesting the bar is more spread out than the standard MPM simulation. The lower right corner of Figure 7.2 highlights the magnitude of this difference and illuminates the consistency of the anti-locking techniques. What the parameter $\bar{R}$ fails to capture is the overall shape of the final cylinder since this value is computed in an average sense. Close examination of Figure 7.1 (or a quick sneak preview ahead to Figure 7.5) show that the standard MPM leads to a slightly disfigured cylinder. That is, the cylinder is not entirely circular where excessive deformation has occurred. The difference is not that prominent and if an irregular grid that catered to radial expansion could be employed in the current MPM framework these effects would likely be eliminated. Nonetheless, the other approaches do not see this type of disfigurement and further promotes the anti-locking strategies.

7.1.2 Stress Field

From a geometric standpoint the the anti-locking approaches provide an improvement to the standard algorithm. But what about the stress measures? This question is investigated here by delving into two stress measurements and comparing the findings. The first stress measure is the norm of the deviatoric stress tensor, $\|\mathbf{s}\|$. This value is plotted in Figure 7.3

[3]This analysis proved to be quite challenging using Marc. Initially an effort was made to use similar element size, time step, solution scheme, etc. However, this proved unsuccessful and the large deformation, linear elements were simply unable to converge due to excessive mesh distortion. This was the case even with the kitchen sink thrown at the linear elements in terms of technology (enhanced assumed strain, reduced integration, isochoric modifications, etc.). The 27-node quadratic element suffered the same fate for both explicit and implicit dynamic solution schemes. The mesh distortion problem was finally mitigated enough to complete the simulation using a 20-node quadratic element with an implicit Newmark-Beta solution method.

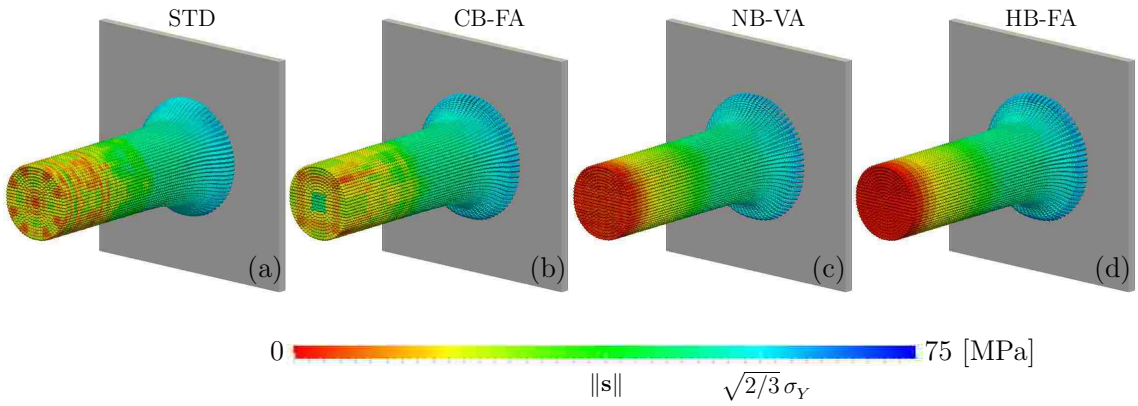

Figure 7.3: $\|\mathbf{s}\|$ at $T = 0.25$ for different MPM strategies. (a) The standard MPM [STD] (b) Cell-based full approximation [CB-FA] (c) Node-based volumetric approximation [NB-VA] and (d) Hybrid-based full approximation [HB-FA].

for select MPM techniques. As a whole the results are quite favorable. The STD model adequately captures material yielding and leads to reasonable distribution of the shear-related measure. Comparing the STD to CB-FA, it is apparent that little is gained by approximating the full tensor with respect to $\|\mathbf{s}\|$. An explanation for this is as follows: if the material model can be decomposed into a volumetric and deviatoric component, and the yielding of a material affects only the deviatoric stress, then the STD algorithm will recover a constant shear stress for those regions that have yielded. This is equivalent to what the deviatoric approximation constructs in the anti-locking techniques. Thus, for this type of problem, the affects of locking are kept in check due to material yielding. The distribution of $\|\mathbf{s}\|$ for NB-VA and HB-FA represent a decided improvement over both the CB-FA, CB-VA (not pictured), and STD. The transition from a yielded region at the cylinder base to the free end is smooth with no discernible jumps in the field quantity.

The normal stress component, σ_{33}, is shown in Figure 7.4 (any $(\bullet)_{33}$ tensor component is aligned with the z-axis and the initial velocity direction). Here the issues due to locking are illustrated. The σ_{33} component of the stress field is riddled with inconsistencies and sharp fluctuations in sign for the STD model. This is in stark contrast to the anti-locking approaches—whose field values are reasonable and distributed in a less jarring manner. The cell-based approach experiences some checkerboarding, but this is largely inconsequential and does not disparage the results compared to the node-based findings.

Select results from the Marc model are shown in Figure 7.5. These images correspond to $T = 0.90$. An attempt was made to select a colormap that is as close as possible to those used to present the MPM findings. Unfortunately, there is still a large disparity and

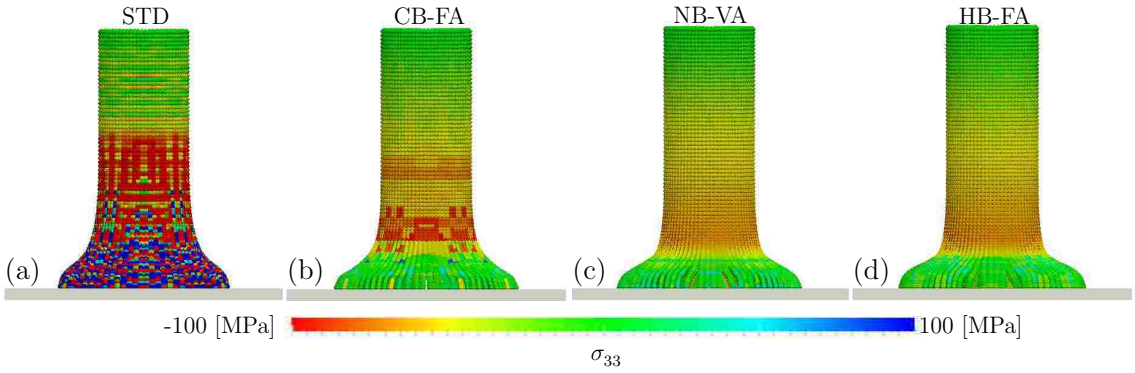

Figure 7.4: Normal stress component σ_{33} at $T = 1.0$ for different MPM strategies. (a) The standard MPM [STD] (b) Cell-based full approximation [CB-FA] (c) Node-based volumetric approximation [NB-VA] and (d) Hybrid-based full approximation [HB-FA].

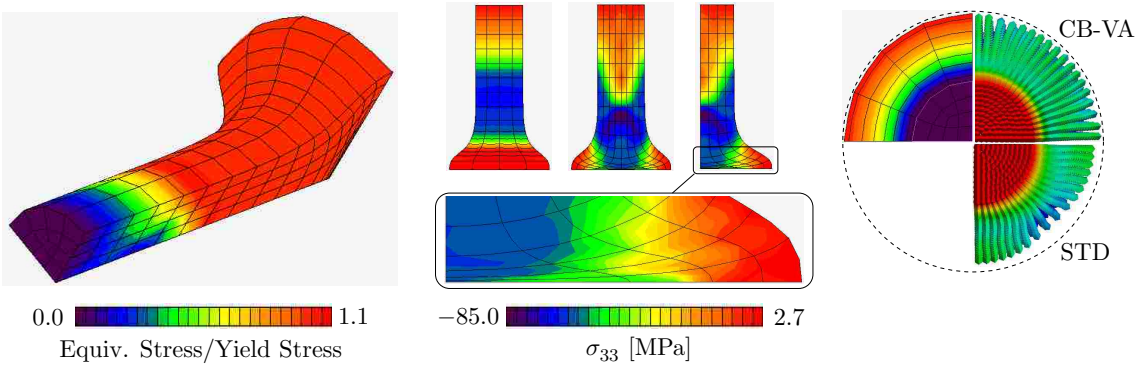

Figure 7.5: Marc nonlinear FEM results from $T = 0.95$. Isometric view of equivalent stress to yield stress, normal stress component σ_{33}, and top view comparing to the Material Point Method.

this makes a true visual comparison challenging. The left side of Figure 7.5 depicts the equivalent stress/yield stress and indicates significant yielding over most of the height. This pattern is consistent with the NB-VA and HB-FA anti-locking stress distributions shown in Figure 7.3. The center images of Figure 7.5 show the σ_{33} stress component at various viewing angles. In terms of values, the FE model is significantly more compressive in regions near the center of the cylinder. The true extent of the mesh distortion is appreciated by examining the element close-up. At this stage in the analysis these unfortunate entities are rather crunched and verging on a singular inversion. The far right series of superimposed images in Figure 7.5 show a plan view of the deformed cylinder. The FEM and locking free variants of the MPM provide a very reasonable deformed shape. The standard MPM not only has a smaller radius, but is also slightly deformed.

An important note to consider is the stress-related fields pictured in both Figures 7.3

and 7.4 are raw and unfiltered. Common practice in the FEM is to visualize smoothed stress values; as a result, intra-element stress variations are largely eliminated and the field appears much better than the raw data would. If such a practice were applied here to the MPM results even the chaos depicted in Figure 7.4 for the STD algorithm would be dramatically improved. So much so in fact, that there may be little observable difference between the standard algorithm and the anti-locking techniques. Thus, the benefits of the anti-locking techniques need be interpreted with caution depending on presentation format and in concert with the improved geometric description afforded by such enhancements.

7.1.3 Efficiency of Anti-Locking Algorithms

The benefits of the anti-locking techniques are easily realized by examining kinematic quantities and mechanical fields. However, increasing the quality requires effort and typically arrives with an additional cost. In this context, the anti-locking strategies add computational effort and increase the CPU time. The algorithm presented in Chapter 4 augments the standard algorithm and there is no way to make this enhancement more efficient than the original form. To help quantify this expense, the computational time for 10 different simulations is averaged for the standard MPM and the four anti-locking strategies investigated here. The timing from the standard algorithm provides a baseline reference; the relative increase in computation time is shown in the center table column of Figure 7.6 for each approach. Note that overall inefficiencies within the current framework are projected to all approaches, thus, the relative figures provide an accurate estimate of the isolated cost incurred by the anti-locking routines listed in Table 4.1. The minimum cost of employing the anti-locking routine is a 27% increase in computational time. The additional time varies from there up to nearly 3 times as long for a hybrid, full tensor averaging scheme.

The right table column presents the computational times in terms of a global time index. This quantity is referred to as the Relative Strength and measures how a particular analysis time stacks up relative to it counterparts. These values comprise the pie-chart shown on the right side of Figure 7.6. From this alternative vantage point, the true costs of using a node-based volumetric approximation are realized.

7.1.4 Conclusions

The anti-locking algorithms yield higher quality results with respect to geometric parameters than the original algorithm with linear shape functions. Each anti-locking technique yields very similar values that are consistent with the Marc model. This latter point should not be taken lightly; the FE model employs higher order shape functions that are not subject

Algorithm	Relative to STD	Relative Strength
STD	— %	9.0%
CB-VA	27%	11.0%
CB-FA	41%	13.0%
NB-VA	268%	32.0%
HB-FA	294%	35.0%

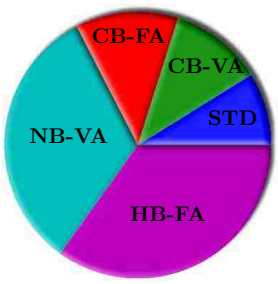

Figure 7.6: Average relative performance comparison. The table lists the algorithmic performance relative to the standard MPM as well as the relative time strength of each algorithm. The pie-chart provides an overview of the time strength for each method.

to locking. Thus, the anti-locking approach provided in Chapter 4 with the appropriate nonlinear material extension outlined in Section 4.4.5 is doing its job in eliminating the undesirable side effects of linear shape functions. Examining the stress values leads to the same conclusion. The node-based volumetric approaches NB-VA and HB-FA produced exceptional quality results with respect to both the deviatoric measure $\|\mathbf{s}\|$ and the normal stress component σ_{33}.

The standard algorithm with linear shape functions provides provides a more efficient framework compared to the anti-locking enhancements. The locking free variants result in a net time increase on the order of 27%–294%. Additional studies into this matter indicate these percentages are highly correlated with particles per cell, and are independent of other grid parameters. This observation is reasonable considering the anti-locking approaches construct approximations over particles in a given control volume—i.e., the particles in a cell or nodal support. Thus, increasing the amount of particles obviously increases the computational overhead and might do so in a nonlinear fashion with the anti-locking approaches.

Comparing all aspects of the findings—geometric, mechanical fields, efficiency, etc.—a picture begins to emerge that suggests the use of a full-tensor averaging technique is superfluous in a nonlinear material context. The volumetric averaging scheme, be it cell- or node-based, provides the same benefits at a reduction in cost when compared to the cell- or node-based full tensor schemes. This observation is not limited to the Taylor Bar impact problem analyzed in this section. A moderate amount of time is always invested in selecting appropriate simulation parameters and this statement holds true for most of the simulations appearing in this document. Preliminary investigations identify appropriate domain and body geometry, material properties, time step, and test different anti-locking routines. Initial studies continue to indicate time and again that a full-tensor averaging technique

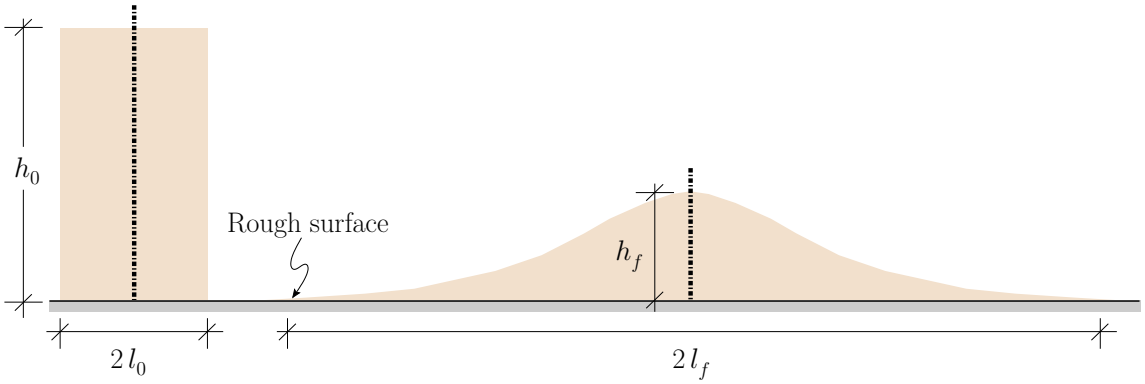

Figure 7.7: Planar sand column description. The initial and final geometry is described by the height, h, and length parameter, l.

yields no discernible improvement over the volumetric counterpart for large deformation, history-dependent analyses. Typically these full approximations take longer to provide an indistinguishable result. For this reason only the CB-VA and NB-VA approaches are used in the analyses that follow. And of these studies, CB-VA is the predominant choice—as this avenue provides a large time benefit over the NB-VA. There are situations, however, where the increased cost associated with a node-based approach is worth it, as it can dramatically improve—among other things—stress fields and reaction force distributions.

7.2 Planar Sand Column Collapse

One of the primary goals of this work is to develop a framework capable of modeling granular materials and, in particular, the flow of said medium under the action of gravity. As a starting point a two-dimensional, plane strain sand column collapse is simulated using the MPM.

Past researchers have examined the spreading of sand and other granular materials on a flat surface in both experimental and computational settings. On the experimental side, the most notable and extensively documented cases are the works by Lajeunesse et al. (2004) and Lube et al. (2004). These works investigate the collapse of cylindrical columns on a rough, horizontal substrate (sand paper). The materials tested include glass beads, sand, salt, couscous, rice, and sugar. The motion is captured via photographs and key relationships linking the initial aspect ratio to the final geometry are developed. A series of two-dimensional tests are reported in the work by Lube et al. (2005) as an alternative to the cylindrical experiments. For this series of analyses the researchers photographed both fine

and course grained sand, sugar, and rice as the medium spread in a confined channel. Their experiments investigate, among other things, the effects of symmetrical boundary conditions on the planar flow. A series of quasi two-dimensional experiments are reported by Balmforth and Kerswell (2005). Additional experimental results for both two- and three-dimensional configurations are documented in the paper by Thompson and Herbert (2007). On the computational side, the work by Staron and Hinch (2005) examines planar collapse using a numerical technique they have dubbed Contact Dynamics—more commonly referred to as the Discrete Element Method. The DEM simulations do a reasonable job in reproducing the dynamics observed in a laboratory setting.

The goal of the MPM analyses presented here is *not* to reproduce the experimental results with a high degree of accuracy; nor is it to match the DEM simulations down to the last point. Rather, the goal is to demonstrate that the MPM is a valid tool for capturing the complex dynamics associated with granular flow—provided an appropriate material model is combined with realistic mechanical parameters. The experimental results can be thought of as a benchmark for ideal behavior, but beyond that there is little direct numerical comparison. This seemingly simplified approach is taken only because little or no mechanical material properties are presented in the published work. Without these values and without extensive material model calibration there is little point in a thorough numerical comparison.

7.2.1 Parameter Identification and Analysis Description

A schematic of the sand column analyzed here is shown in Figure 7.7. The initial height and length are described by the parameters h_0 and l_0. A natural way to link these two values is the aspect ratio, a, defined as

$$a = \frac{h_0}{l_0} \ . \tag{7.5}$$

The experimental evidence shows this fundamental ratio is the driving parameter linking the final height, h_f, and final length, l_f, to the initial geometry.

As previously stated the primary goal of these analyses is to demonstrate that the MPM is a valid tool for replicating the dynamics associated with granular flow—provided an appropriate material model is combined with realistic mechanical parameters. The choice of material model is arguably the most important element in achieving this goal. This aspect poses a challenge, especially considering the wide variety of models available in the literature for granular flow. Ostensibly one could use or conceive a model that is endlessly complex, with the hope of capturing observed behavior down to the last detail. The focus

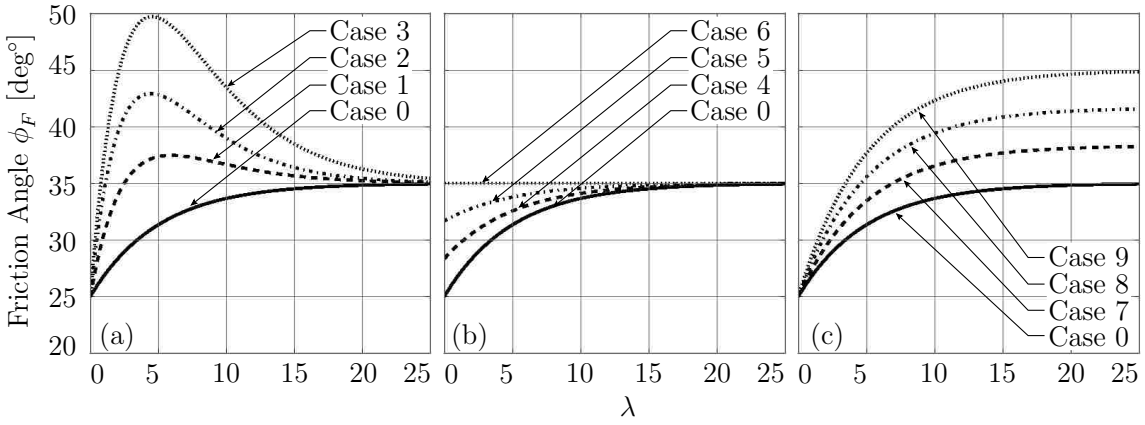

Figure 7.8: Mobilized friction angle, ϕ_F. (a) Analysis A: peak strength (b) Analysis B: initial strength (c) Analysis C: residual strength

here, however, is quite the opposite. Rather, emphasis is placed on utilizing comparatively simple models that are capable of reproducing key observed phenomena, such as the notion of a critical state.

The sand column collapse simulations use the pressure dependent models developed in Chapter 3. In particular, two model variants are considered here:

1. Modified Drucker-Prager formulation (DP). This is the model outlined in Section 3.6.3

2. Matsuoka-Nakai yield surface with the Drucker-Prager plastic potential formulation (MN with DP G) – This approach combines Matsuoka-Nakai yield surface, Equation (3.120), with the Drucker-Prager plastic potential, Equation (3.108).

These models are referred to throughout by the name given above in parenthesis. The validation of these models in the context of a granular medium is discussed in Section 3.8.

Both model variants rely heavily on the definition of the mobilized friction angle, ϕ_F, and the plastic dilation angel, ψ_G. The definition of these parameters is discussed in Section 3.6.4. Preliminary studies of the collapse indicate that the evolution of the friction angle plays a dominant role in determining the final geometry of the collapsed state. As such, this study presents the effects of changing the mobilized friction angle. Ten total friction angle curves are investigated. These curves fall into three analysis types. Each analysis type is designed to target a different effect. The first class of curves examines the role of peak strength. The second looks at how the initial strength impacts the final results, and the third class evaluates the residual strength, or long term behavior under excessive deformations. The curves are shown in Figure 7.8. Each curve is constructed using the

Table 7.2: Constant definitions for a_{0-4} for defining the friction angle curves in Figure 7.8.

Case:	0	1	2	3	4	5	6	7	8	9
a_0	35.00	35.00	35.00	35.00	35.00	35.00	35.00	38.33	41.67	45.00
a_1	0.00	4.00	9.00	13.00	0.00	0.00	0.00	0.00	0.00	0.00
a_2	0.00	0.00	0.00	0.00	0.00	0.00	0.00	0.00	0.00	0.00
a_3	0.20	0.29	0.30	0.27	0.20	0.20	0.20	0.20	0.20	0.20
a_4	10.00	10.00	10.00	10.00	6.67	3.33	0.00	13.33	16.67	20.00

definition given in Equation (3.113) and collectively represent a wide variety of sand types, i.e., loose, moderately dense, dense, etc. The corresponding constants used to define the curves are tabulated in Table 7.2. Each Figure 7.8(a)–(c) contains Case 0, which serves as a reference or baseline curve that provides a standard for visual comparison between the three families.

Given these ten curves, the two material model variants, and the nine aspect ratios examined—these are discussed shortly, a grand total of 180 simulations have been performed. This work assumes the plastic dilation angle is linked to the friction and critical state angles via Equation (3.112). This potentially leaves the door open for an infinite number of dilation curves that could be correlated to the friction angle curves in Figure 7.8. In an attempt to keep some uniformity between the experiments it is assumed the dilation angle is zero, i.e., $\psi_G = 0°$. Note that this violates the definition given by Equation (3.112). However, for excessive deformations this is acceptable and allows the sole effect of friction angle to be isolated.

The aspect ratios in this study vary according to

$$a = 0.25,\ 0.50,\ 1.00,\ 1.50,\ 2.00,\ 4.00,\ 6.00,\ 8.00,\ 10.00\ , \tag{7.6}$$

where the higher frequency for smaller aspect ratios is used in an attempt to capture the observed transition in behavior for short, stubby columns compared to taller, slender columns. The initial length of each column fixed at $l_0 = 0.05$ [m] for all aspect ratios. The initial height of each column is obtained using the ratio defined in (7.5). The macroscopic material properties assigned to the sand particles are $K = 29.5$ [MPa] and $G = 13.6$ [MPa] for the bulk and shear modulus, respectively. The initial density is taken to be $\rho_0 = 2,200$ [kg/m^3]. These properties are consistent with a moderately dense, cohesionless sand (Holtz and Kovacs, 1981; EPR, 1990). Gravity is aligned with the vertical direction and has a magnitude of $|\mathbf{g}| = 9.81$ [m/s^2].

The grid and MPM parameters are constant for each analysis. Square cells are used with

dimension $h_x = h_y = 0.005$ [m]. The time step is fixed at $\Delta t = 5.0\,(10)^{-5}$ [s]. The initial particle geometry is a uniform arrangement of 16 particles per cell (PPC). The cohesion parameter, c, for both models is set to 0.0 [kPa]. Due to the symmetry, only the right half is modeled and a frictionless planar boundary condition inhibiting motion in the x-direction is imposed along the left side of the sand. Along the horizontal surface a Coulomb friction model is coupled with the planar boundary condition that restricts motion in the vertical direction. In doing so a tangential reaction force develops that is a function of the normal reaction force and the friction parameter, $\mu_{fr} = \tan\theta_{fr}$, where θ_{fr} is the effective static friction angle of the surface. Often times this value is linked to the angle of repose in a granular material. This is not done here—as the experiments employed a sand paper surface of unknown roughness. This series of simulations assumes a surface friction angle of 65°. This value was chosen somewhat arbitrarily but ensures that motion occurs due to material failure which is consistent with the observations reported by Lube et al. (2004). Clearly the surface roughness will affect the results. This topic is, however, beyond the current scope of this study and is not addressed further.

7.2.2 Kinematic Description

The column is released from rest at a reference time $t = 0.0$ [s] and spreads out over the flat surface. The evolution of the motion is described using the normalized variables

$$H\,(t) = \frac{h(t)}{l_0}\ , \qquad L\,(t) = \frac{l(t) - l_0}{l_0}\ , \qquad \text{and} \qquad T = \frac{t}{t_f}\ , \tag{7.7}$$

where $H\,(t)$ and $L\,(t)$ are the dimensionless height and length of the sand column. In this case initial length is used as characteristic quantity. The quantity t_f is the duration of time for motion to cease (when $l\,(t)$ fails to change by more than 0.01% in successive time steps). Determining precise values for $h(t)$ and $l(t)$ can be challenging considering the point-wise body definition in the MPM. Simply tracking the extents of the particle location, i.e. minimum and maximum values, is not necessarily indicative of the position of the body as a whole. Thus, in order to eliminate this ambiguity in body definition, the parameters $h(t)$ and $l(t)$ are determined using a weighted average of those particles in contact with the vertical and horizontal boundaries. More formally this statement translates to

$$h(t) = 2\,\frac{\sum_{p_{vb}} y_p(t)\,m_p}{\sum_{p_{vb}} m_p} \qquad \text{and} \qquad l(t) = 2\,\frac{\sum_{p_{hb}} x_p(t)\,m_p}{\sum_{p_{hb}} m_p}\ , \tag{7.8}$$

where $y_p(t)$ and $x_p(t)$ are the vertical and horizontal positions of each particle. The terms p_{vb} and p_{hb} are those particles in contact with the vertical and horizontal boundaries, respectively. This technique assumes a rectangular distribution of the body over the portion

in contact with each surface. This is consistent with the rectangular grid definition used for these analyses, which, as far as the nodes and governing equations are concerned, is the shape of the body. Moreover, this definition helps reinforce the notion that the body is a continuum in the MPM, an idea that is often times overlooked/forgotten in the context of a particle discretization.

Of particular interest here are L_f and H_f, the normalized variables describing the final runout length and height, respectively. These values are obtained as

$$L_f = L(t)|_{t=t_f} \qquad \text{and} \qquad H_f = H(t)|_{t=t_f} \ . \tag{7.9}$$

In Figure 7.9 the length parameter is plotted as a function of the aspect ratio for the 10 different friction angles curves defined in Table 7.2. Each subfigure contains four plots, two of which correspond to the DP model and the other two to the MN with DP G model. For each material type the baseline friction angle, Case 0, is plotted and serves as a reference to provide continuity amongst the figures. Several key observations can be made in examining these plots. Each row in Figure 7.9 corresponds to a different analysis type. The upper row employs those curves that are designed to target peak strength. Conversely, the center row investigates the role the initial strength plays and the lower row depicts the influence of the residual strength. The mobilized friction angles corresponding to the top, middle, and lower row in Figures 7.8(a), (b), and (c), respectively.

Clearly the evolution of ϕ_F impacts the final length. Rather surprisingly the largest influencing factor appears to be the peak strength as opposed to the residual strength for large aspect ratios. This is unexpected because the friction angle curves have been designed such that a vast majority of the particles experience a value for λ, the plastic deformation measure given in Equation (3.115), significantly larger than 5—the approximate value for which the strength is at a peak. In fact, of the three analysis types, the residual strength cases have the smallest deviation from the reference Case 0. These findings suggest that the final deposit geometry is influenced largely by what happens early on in the collapse, long before the final state is reached. Additional findings supporting this claim are presented shortly.

From Figure 7.9 it is also apparent that the yield surface plays a role in determining the final length. This finding is, perhaps, not a surprise but nonetheless worth noting—especially considering the similarity between the two yield surfaces in the deviatoric plane. For smaller aspect ratios ($a \lesssim 1.0$) the difference between the models is less obvious; however, as the aspect ratio is increased the difference becomes much more discernible. In general, using the Matsuoak-Nakai yield surface leads to a collapse that is more spread out. The final deposit length is larger than the corresponding collapse modeled using the Drucker-Prager

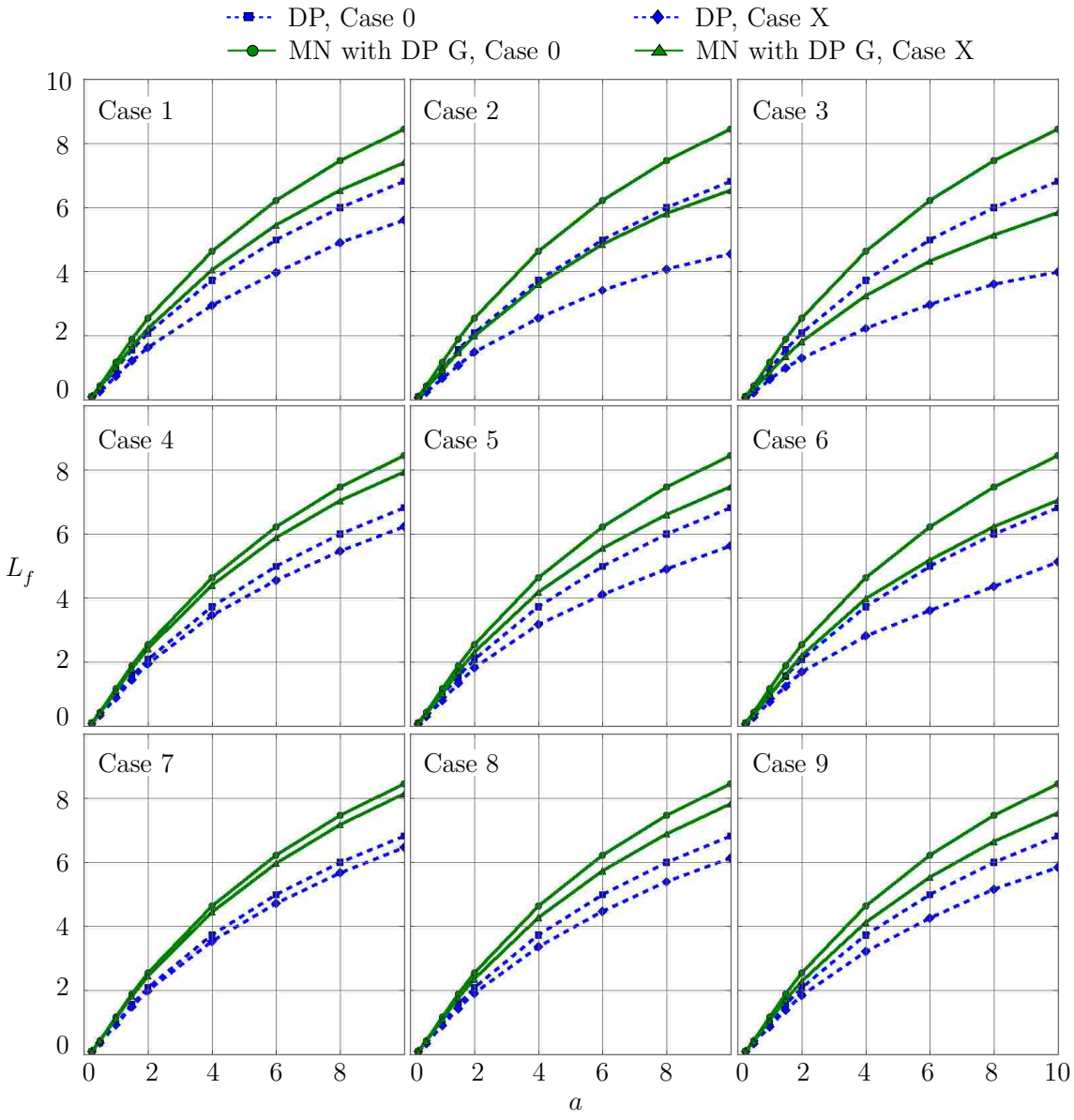

Figure 7.9: L_f for Cases 0–9. Case 0 is plotted in each figure for comparison purposes.

surface. What is not directly apparent from Figure 7.9 is the shape of the collapse profile. The Matsuoka-Nakai framework generates a final shape that is parabolic in nature and more closely resembles the experimental. This observation is in contrast to the Drucker-Prager simulations, which yield a nearly triangular profile with constant slope.

In addition to the length of the profile it is also of value to consider the dimensionless final height, H_f. This parameter is plotted in Figure 7.10. Here the same organization scheme is used as in Figure 7.9; each subfigure contains four plots, two of which correspond to the DP model and the other two to the MN with DP G model. For each material type the baseline friction angle, Case 0, is plotted and serves as a reference to provide continuity amongst the figures. Similar trends are observed for the final height of the columns as were for the length. The largest influencing factor is the peak friction angle. Higher peak strength results in columns that remain taller when the mass comes to rest. The residual strength plays an even smaller role in determining the final height. Again, this supports the claim that the final geometry is influenced largely by what happens during the early stages of collapse. In general the Matsuoka-Nakai yield surface leads to collapse profiles that are shorter than the simulations employing Drucker-Prager surface. This is consistent with the previous observation regarding the length and suggests that a larger degree of spreading is occurring for the Matusoka-Nakai simulations.

Figure 7.10 shows a distinct transition point between smaller aspect ratios and the larger aspect ratios. Quite clearly for $a \lesssim 1.0$ there is little change in the height of the column during the collapse, as the spreading occurs only in the length direction. For these cases the vertical motion of the top of the column does not contribute to the overall kinetic energy of the system. The presence of such a transition begins to hint at the existence of a static region of particles. As will be shown in subsequent figures this phenomenon is not restricted to smaller aspect ratios. A no-flow conic volume (or triangular area for planar problems) is observed in the experiments and is replicated here in the planar MPM analyses for all aspect ratios. In the case of these shorter aspect ratios the no-flow area extends above the original height, and thus there is no observable change in the column height.

The experimental studies have identified scaling laws that allow both the final length and height to be determined via the original aspect ratio, a. There is a general consensus among the research community that both the final dimensionless length and height is best described by a power law relation of the form

$$L_f = A\, a^B \qquad \text{and} \qquad H_f = C\, a^D \ , \tag{7.10}$$

where A, B, C, and D are constants determined from the data. In general it is necessary to provide a piecewise law based on the aspect ratio a, as both Figures 7.9 and 7.10 show

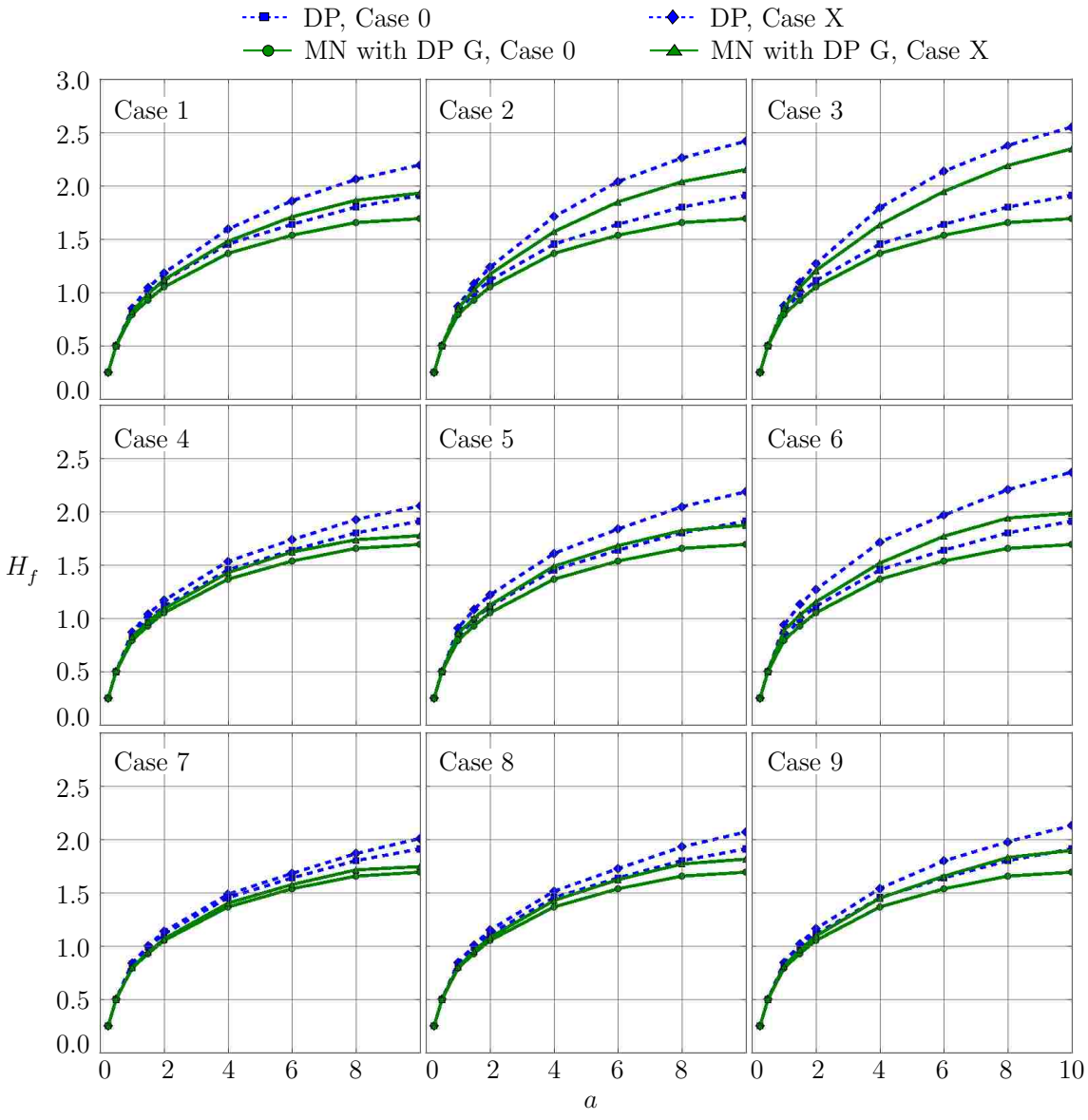

Figure 7.10: H_f for Cases 0–9. Case 0 is plotted in each figure for comparison purposes.

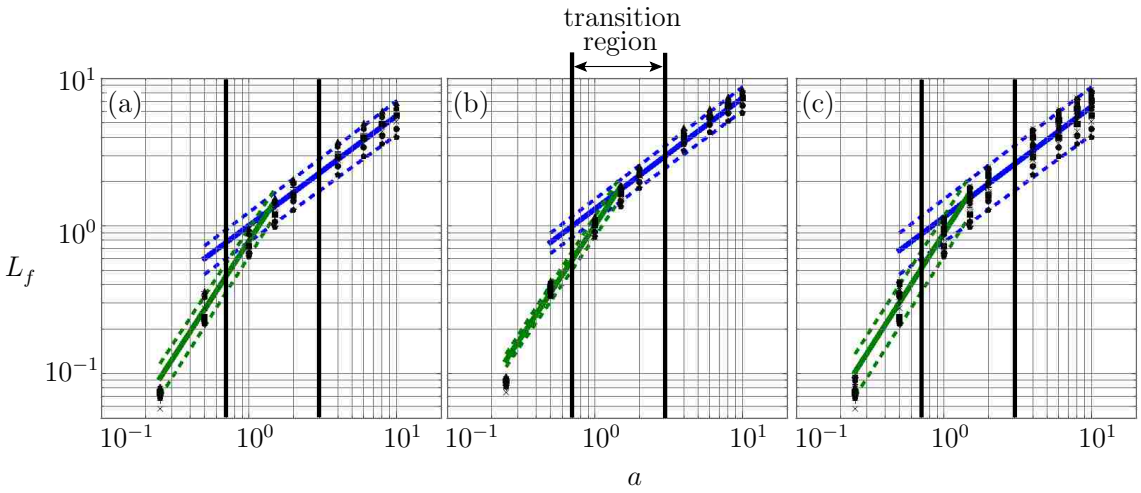

Figure 7.11: Log-Log plot of L_f as a function of a for Cases 0–9. (a) DP model (b) MN with DP G model and (c) All data points.

Table 7.3: Best fit constants for determining $L_f(a)$ via a power law.

	Material Model		
	DP	MN with DP G.	All Models
$a \lesssim 1.5$	$0.791\, a^{\,1.542}$	$1.007\, a^{\,1.516}$	$0.893\, a^{\,1.560}$
$a \gtrsim 1.5$	$1.007\, a^{\,0.744}$	$1.304\, a^{\,0.753}$	$1.148\, a^{\,0.745}$

a distinct transition region based on this ratio.

A least squares fit of the data in log-log space is performed to determine the unknown power law constants. Figure 7.11 examines the final length data for both models, as well as all the data points combined. Each sub-figure contains multiple lines: a solid line corresponding to the best fit of the points, and dashed lines representing the lower and upper bound of the data points. This approach is taken in an effort to provide a reasonable range for the constants used to define the power law. From these figures it is apparent that a single line cannot represent all cases; a transition region is introduced to describe the flow. Based on the MPM analyses, a reasonable region is between $0.75 \lesssim a \lesssim 2.0$ for L_f. This is a relatively wide region and suggests that caution be used in comparing these findings too closely to experimental results—as the log-log space is friendly to the researcher and can lead to a subjective comparison. Nonetheless, an attempt is made to correlate these results to the experimental findings.

In Table 7.3 the power law is given for the final length L_f. These are determined using all the data points for a given model (or all the data for both models) and represent the

Table 7.4: Lower and upper bound constants for determining $L_f(a)$ via a power law.

	Material Model					
	DP		MN with DP G.		All Models	
	LB	*UB*	*LB*	*UB*	*LB*	*UB*
$a \lesssim 1.5$	$0.621\,a^{1.578}$	$0.960\,a^{1.520}$	$0.851\,a^{1.471}$	$1.165\,a^{1.551}$	$0.621\,a^{1.578}$	$1.165\,a^{1.551}$
$a \gtrsim 1.5$	$0.778\,a^{0.725}$	$1.235\,a^{0.754}$	$1.089\,a^{0.742}$	$1.518\,a^{0.760}$	$0.778\,a^{0.725}$	$1.518\,a^{0.760}$

best fit line. The best fit values are bracket by upper and lower bound values displayed in Table 7.4. In this format the exponent gives the slope of the line in log-log space. The planar collapse experiments by Lube et al. (2005) identify an exponent value of 1.000 and 0.667 for short and tall columns, respectively. Their findings identify the transition in behavior between $1.9 \lesssim a \lesssim 2.8$. These authors claim that the runout is independent of the material friction angle—which may be a misleading claim since the range of materials tested had internal friction angles between 29.5°–32.0°. The work by Balmforth and Kerswell (2005) concluded differently, namely that the exponent is somewhere between 0.65–0.9 with an error of ± 0.1. They surmise the actual value is dependent on domain geometry (these researchers conclude the pre-factor, A in the present case, is very dependent on material properties). The DEM simulations by Staron and Hinch (2005) report an exponent of 1.0 for short columns and 0.705 ± 0.022 for tall columns, with the transition between the two occurring at $a \approx 2$.

Clearly there is a lot of variation in the reported findings. The MPM study presented here has found, in general, a larger exponent for the final length than the experiments. This implies longer runout. There could be a multitude of reasons for this. One contributing factor is surface roughness. Preliminary studies indicate a moderate dependence on this parameter. Alternatively, body discretization and grid dimensions could change the final length profiles. As discussed previously, determining precise values for $h(t)$ and $l(t)$ can be challenging considering the point-wise body definition in the MPM. This study uses the definitions given by Equations (7.8). This too may be affecting the geometry. However, regardless of the exact source of the difference, the MPM is producing findings that are consistent with the experimental results. It is conceivable to select appropriate data points from the MPM simulations that will yield a near exact fit to any of the experimental data published. This however, is not consistent with the stated goal of these analyses, namely to demonstrate that the MPM is a valid tool for capturing the complex dynamics associated with granular flow.

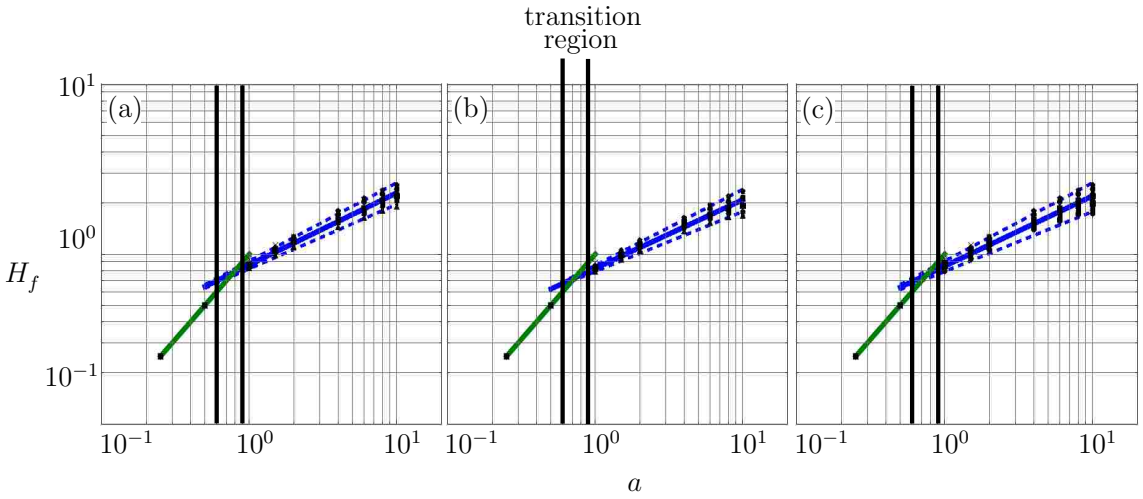

Figure 7.12: Log-Log plot of H_f as a function of a for Cases 0–9. (a) DP model (b) MN with DP G model and (c) All data points.

Table 7.5: Best fit constants for determining $H_f(a)$ via a power law.

	Material Model		
	DP	MN with DP G.	All Models
$a \lesssim 1.0$	$1.000\, a^{\,1.000}$	$1.000\, a^{\,1.000}$	$1.000\, a^{\,1.000}$
$a \gtrsim 1.0$	$0.865\, a^{\,0.425}$	$0.825\, a^{\,0.404}$	$0.850\, a^{\,0.414}$

The same exercise can be repeated for the final height of the columns. In Figure 7.12 the log-log plots of the height parameter defined in Equation $(7.9)_2$ are shown as a function of the aspect ratio. Here the transition region is much smaller than compared to its length counterpart and occurs between $0.75 \lesssim a \lesssim 1.0$. The upper and lower bounds collapse to a single best fit line describing the final height for shorter columns. As the aspect ratio is increased beyond 1.0 the disparity between the upper and lower bound lines grows.

The values for the power law constants are given in Table 7.3 for the final height. The expressions for the upper and lower bound are given in Table 7.4. For this parameter the MPM findings compares quite favorably to the experimental results. All experimental evidence and DEM simulations point to an exponent of 1.0 for $a \lesssim 1.0$. For taller columns, an exponent of 0.4 was reported by Lube et al. (2005) based on their analysis of sand, sugar, and rice. Interestingly enough there is very little deviation in behavior reported for the height profile of these different materials—suggesting that the influence of gravity and inertial forces are more dominant in determining the final height profiles than mechanical

Table 7.6: Lower and upper bound constants for determining $H_f(a)$ via a power law.

	Material Model					
	DP		MN with DP G.		All Models	
	LB	*UB*	*LB*	*UB*	*LB*	*UB*
$a \lesssim 1.0$	$1.000\,a^{\,1.000}$	$1.000\,a^{\,1.000}$	$1.000\,a^{\,1.000}$	$1.000\,a^{\,1.000}$	$1.000\,a^{\,1.000}$	$1.000\,a^{\,1.000}$
$a \gtrsim 1.0$	$0.820\,a^{\,0.381}$	$0.911\,a^{\,0.461}$	$0.741\,a^{\,0.353}$	$0.860\,a^{\,0.450}$	$0.791\,a^{\,0.353}$	$0.911\,a^{\,0.461}$

properties[4]. On the simulation side of things—Staron and Hinch (2005) determined using the Discrete Element Method that the exponent should be 0.35. However, this conclusion is reached based on a single set of results with essentially no discussion of how the internal friction mechanism is implemented. Nor did this work mention the impact other material parameters have on the results.

There is no doubt that Figures 7.9–7.12 provide an adequate description of the final geometry of the planar sand column collapse. When compared to the experimental results and other published simulations it is reasonable to conclude that the MPM is a valid tool for modeling granular flow. What the discussion has lacked thus far and these figures fail to show is a description of how the final geometry came to be; that is, what are the dynamics of the flow throughout collapse and what qualitative information can be obtained from the simulations.

As a springboard into this discussion two additional length and height parameters are defined as follows:

$$\bar{H} = \frac{h_0 - h(t)}{h_0 - h_f} \qquad \text{and} \qquad \bar{L} = \frac{l(t) - l_0}{l_f - l_0}\ . \tag{7.11}$$

These dimensionless values provide a normalized metric for easy comparison between aspect ratios. In Figure 7.13 both $\bar{L}$ and $\bar{H}$ are plotted against the normalized time, T. Note that this time is defined in $(7.7)_3$ and is linked to t_f, the time duration for all motion to cease for a given simulation. It is apparent that, regardless of aspect ratio, all analyses can more or less be categorized by a single master curve. Much insight can be gained by examining these curves. The upper row shows the evolution of $\bar{L}$ for the two material models considered in this study. Three distinct model independent flow regimes are observed. Initially the length profile is concave up—indicative of a net positive acceleration outward. This brief acceleration is followed by the second stage of motion in which the length of column expands

[4]This statement is only valid for reasonable mechanical properties in the context considered here. Obviously the mechanical properties of a given medium can be selected such that little no or flow occurs; such materials are, however, not the granular materials this study focuses on.

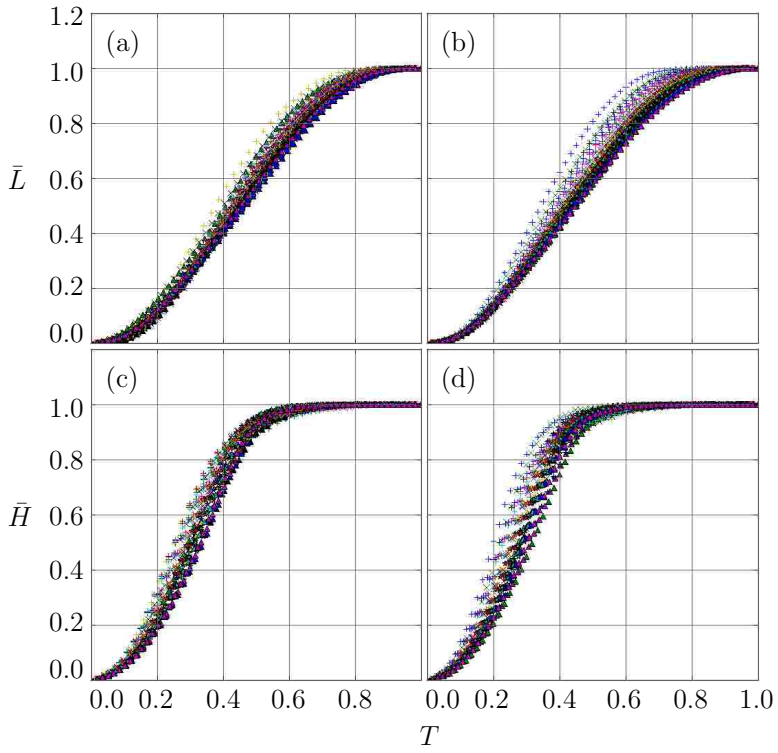

Figure 7.13: Evolution of sand column geometry with respect to normalized time. Plots contain all cases with $a > 2.0$. The upper row is the normalized variable $\bar{L}$ while the lower row is $\bar{H}$. Subplots (a) and (c) follow from the DP model while subplots (b) and (d) follow from the MN with DP G. material model.

linearly at a constant rate. Finally the column decelerates and comes to rest. Of these three regimes, the constant expansion stage accounts for roughly 50% of the total duration.

The lower row in Figure 7.13 plots the evolution of $\bar{H}$. Here it is immediately obvious that vertical motion of the column ceases prior to the radial motion. This is evidenced by the quick ascent of $\bar{H}$ to a value of 1.0. In fact, the height of the profile has reached the final value around $T \approx 0.5$ for both material models. Only two distinct flow regimes are observed. Namely, an acceleration downward followed by an immediate deceleration. This transition is perhaps better viewed in Figure 7.14, where the profiles for larger aspect ratios are plotted alongside the curve representing gravitational free fall. The line representing the free fall profile is plotted only from the time data for the $a = 10.0$ case and leads to the following conclusion: when downward acceleration of the height is occurring, the upper portion is experiencing a motion indistinguishable from a free fall. Flow in this regime is dominated by inertial forces and the relative importance of mechanical properties is vanquished. This observation has fairly wide ranging consequences. First, comparing the upper row and lower

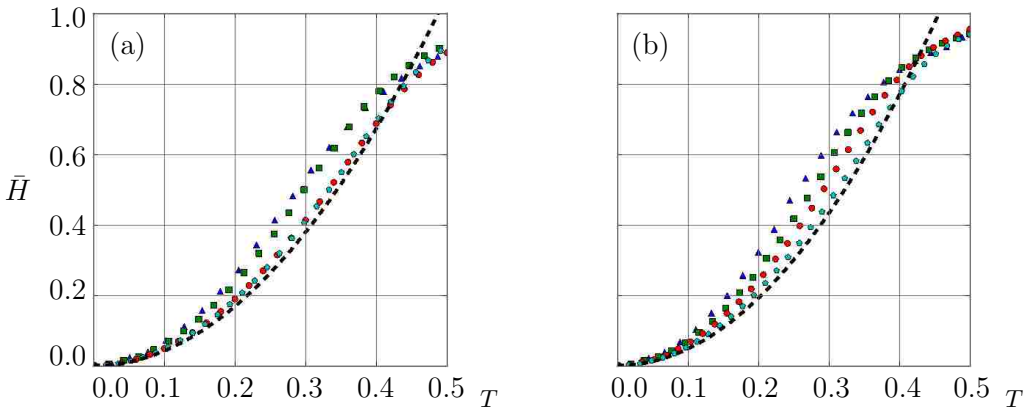

Figure 7.14: Case 2 $\bar{H}$ compared to free fall in a gravitational field. The free fall is denoted by the dashed line. Plots contain all cases with $a > 2.0$. Subplot (a) follows from the DP model data while subplot (b) follows from the MN with DP G. data.

row of Figure 7.13, the duration of gravitational acceleration corresponds directly to the radial acceleration. In other words, when the height is accelerating downward the length is accelerating outward. Second, it was previously noted that the peak friction angle has the largest impact on the final geometry. This was surprising because the peak strength occurs early on in the analysis. From this observation it is postulated that the early stages of collapse play the largest role in determining the final geometry. A potential explanation for this is given here—the material state at peak acceleration is the dominant factor in determining final geometry.

The nodal velocity fields provide an alternative way to visualize the different flow regimes. This is shown Figures 7.15–7.17, where the three aspect ratios $a = 2.0,\ 4.0,$ and 8.0 are shown. Each figure contains four sequential snapshots of the flow configuration. This data follows from the MN with DP G material model and the mobilized friction angle defined as Case 2 in Table 7.2. A different velocity scale is used for each aspect ratio considered. While each snapshot has a common color scale for the velocity field, the geometry is plotted at different scales. Comparisons regarding the shape of the profile at the different snapshots in time are ill advised and misleading, as these figures have been created to examine the velocity profile.

During the early stages of the collapse ($T \lesssim 0.10$) the upper portion of all columns falls in a strictly vertical manner for the three aspect ratios shown. As the analysis proceeds the the difference in behavior becomes apparent. At time $T = 0.30$ the purely vertical motion has ceased for $a = 2.0$ and lateral spreading is underway. Figure 7.16 shows the upper region near the center line is still moving downward but outward effects are becoming

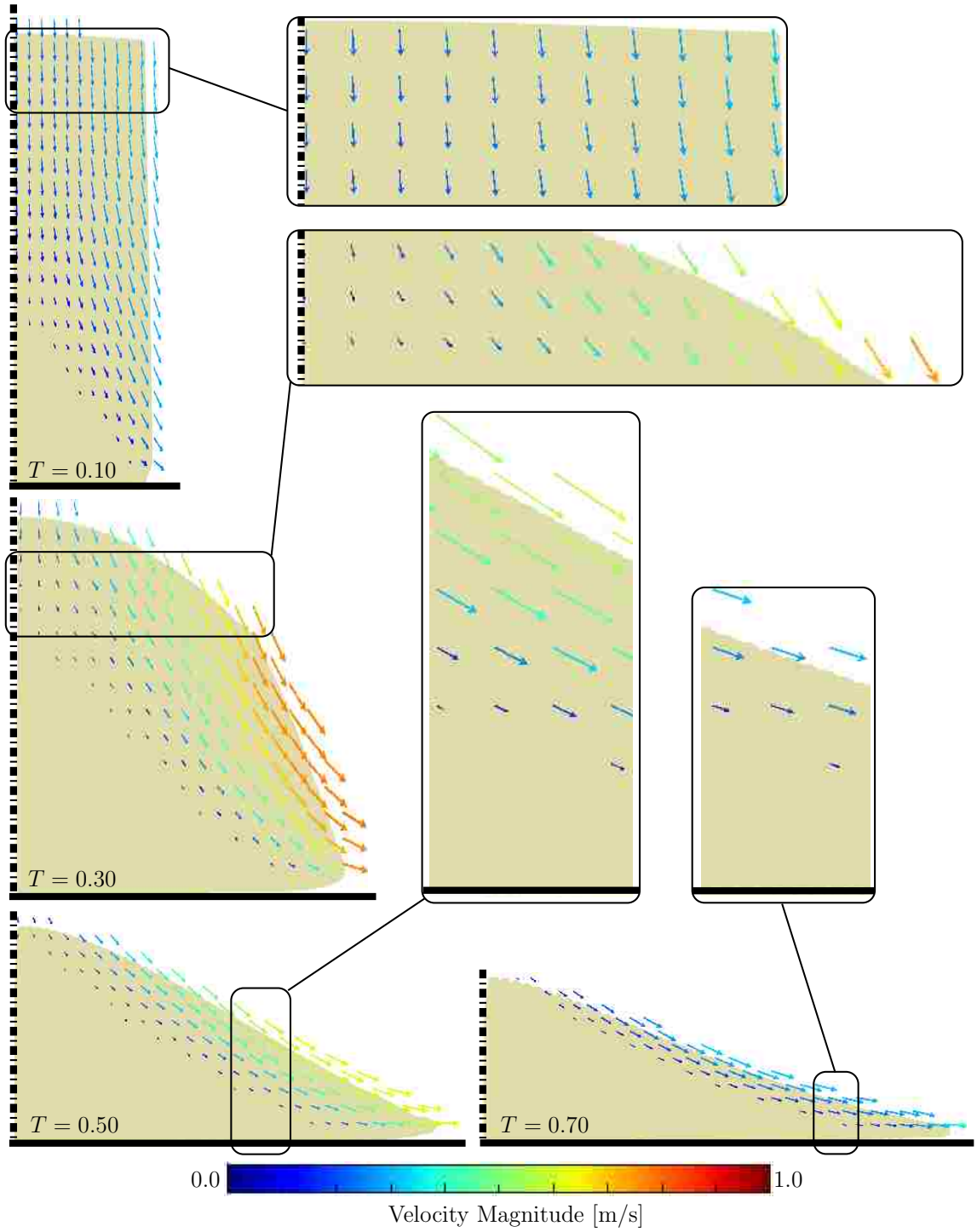

Figure 7.15: Evolution of the velocity field for $a = 2.0$, Case 2, and the MN with DP G material model. The velocity vectors are generated from nodal data and plotted alongside the particles.

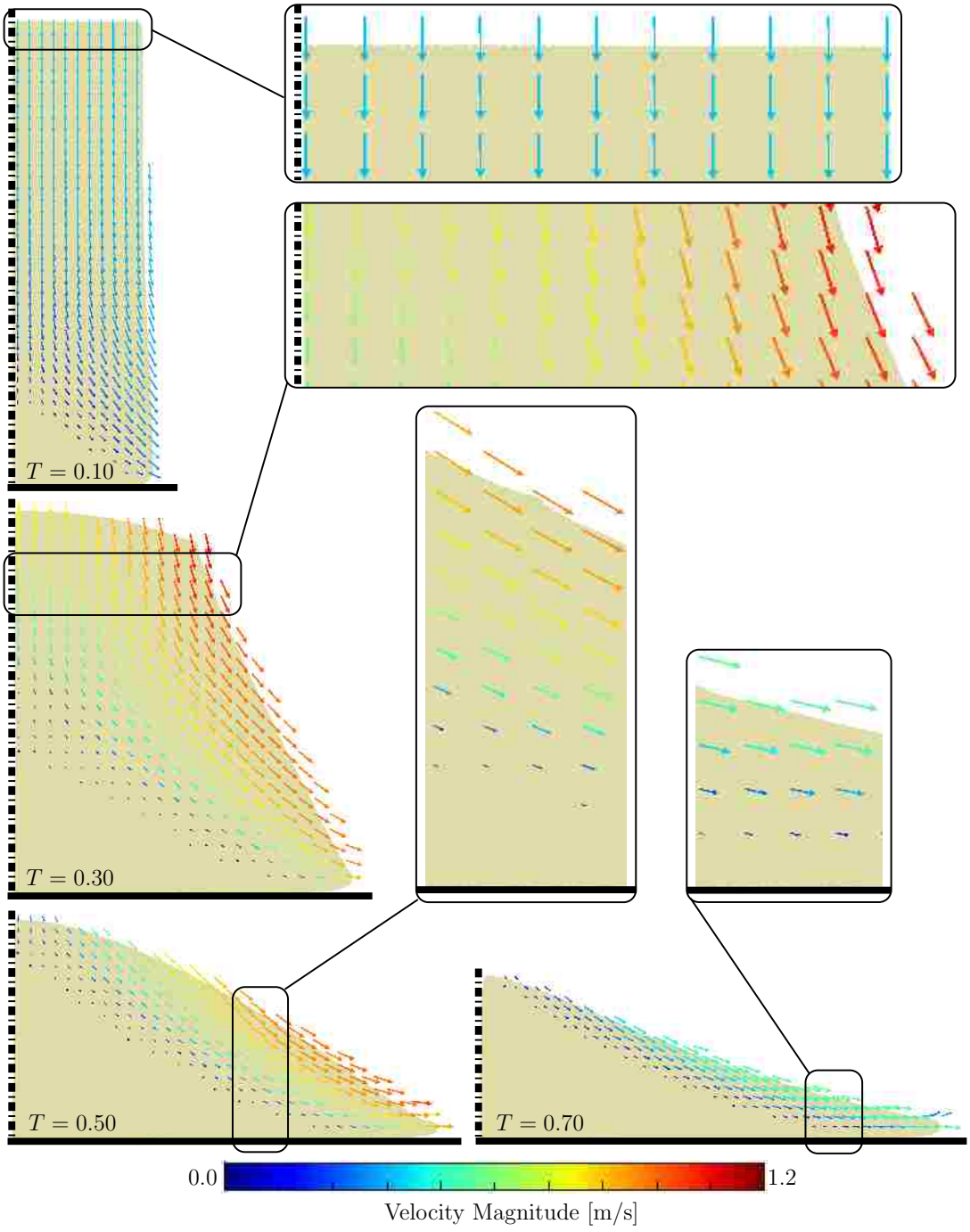

Figure 7.16: Evolution of the velocity field for $a = 4.0$, Case 2, and the MN with DP G material model. The velocity vectors are generated from nodal data and plotted alongside the particles.

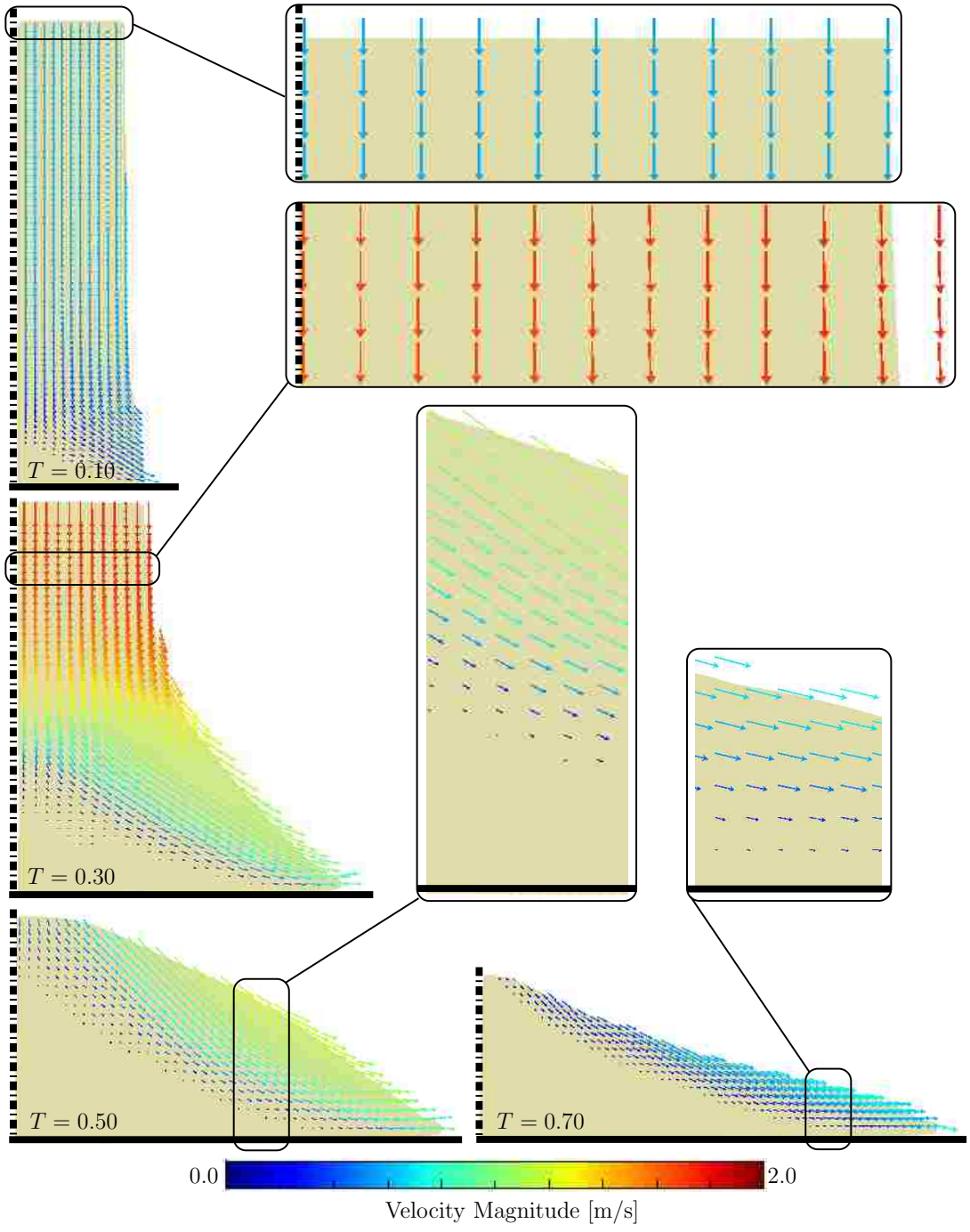

Figure 7.17: Evolution of the velocity field for $a = 8.0$, Case 2, and the MN with DP G material model. The velocity vectors are generated from nodal data and plotted alongside the particles.

visible. This is in contrast to the $a = 8.0$ ratio, where a vast majority of the column is still experiencing a net vertical motion at $T = 0.30$. By the time $T = 0.50$, all columns are moving predominantly in a horizontal direction. At this instant an interesting observation can be made in Figures 7.15–7.17: the velocity profile is parabolic though vertical slices of the sand. This effect is particularly noticeable for $a \gtrsim 4.0$, and is the mechanism that leads to the final parabolic shape of the sand profile. As time proceeds the motion is confined to the upper region of the flow as indicated by the $T = 0.70$ snapshots. This final observation is consistent with the observations first reported by Lube et al. (2004), that is, that motion or flow of granular material occurs as grains pass over their static counterparts.

A key phenomenon observed in the experiments and replicated by the simulations is the existence of a static cone or triangular region in which the material does not move. Such a region is observed regardless of aspect ratio, and can be seen in the lower left corner of the snapshots of Figures 7.15–7.17. Preliminary investigations of the static cone angle, i.e., the cone's slope, indicate that there is a link between this angle and the internal friction angle of the material. It is postulated here that the static angle exhibits a stronger correlation with the material properties than the final slope, or the final angle of repose. These simulations have indicated the final geometry is dominated by inertial forces—particularly so for large aspect ratios. Thus, attempting to establish an exclusive link between the final angle of repose and material properties should not be done. Loosely speaking, this situation is analogous to the role of the Reynolds number in fluid mechanics. This quantify relates the relative importance of inertial forces to the internal forces that follow from material properties. An extensive comparison between the static cone angle, the final angle of repose, and material parameters is largely beyond the scope of interest here, but could prove to be an area of focus for future simulations.

An interesting observation is made by tracking material in the vertical direction for different aspect ratios. In Figure 7.18 three aspect ratios are shown, beginning with $a = 2.0$ and doubling twice to $a = 8.0$. Material points whose position corresponds initially are plotted with the same color at each snapshot in time. The normalized time, T, corresponds to $a = 8.0$ data. While there is some variation between each figure, it is safe to conclude that, regardless of aspect ratio, material that starts in the same spot will end in the same spot.

The discussion thus far has largely been geometry oriented. Numerous plots and figures describing the shape of the runout have been presented with no discussion of body stresses or forces. One of the key enhancements of the MPM highlighted throughout this dissertation is the improved stress and corresponding force field that follows from the anti-locking

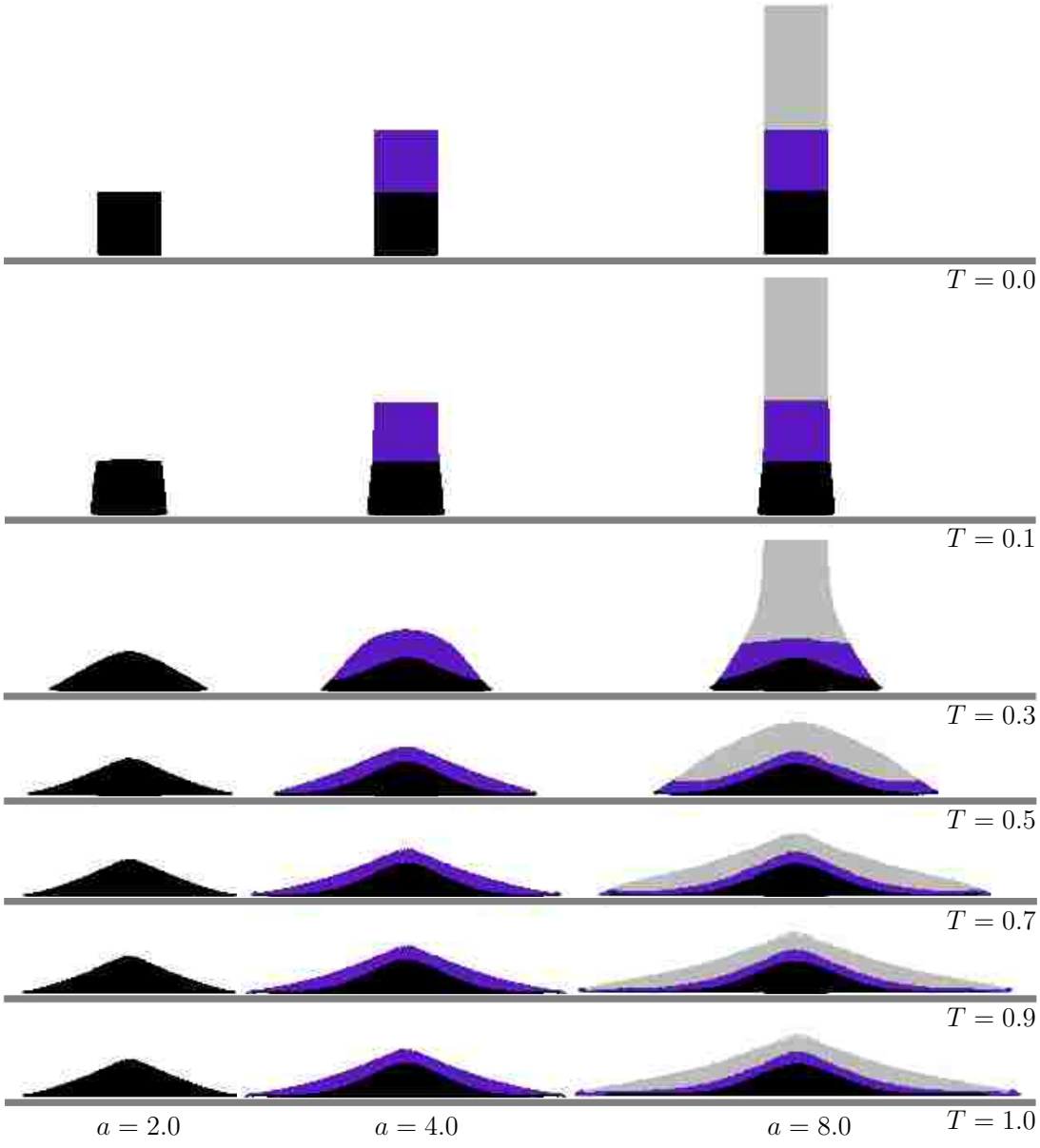

Figure 7.18: Spatial comparison of particle locations for $a = 2.0$, $a = 4.0$, and $a = 8.0$. Particles whose positions correspond initially are plotted with the same color at each snapshot in time. The normalized time, T, corresponds to $a = 8.0$ data.

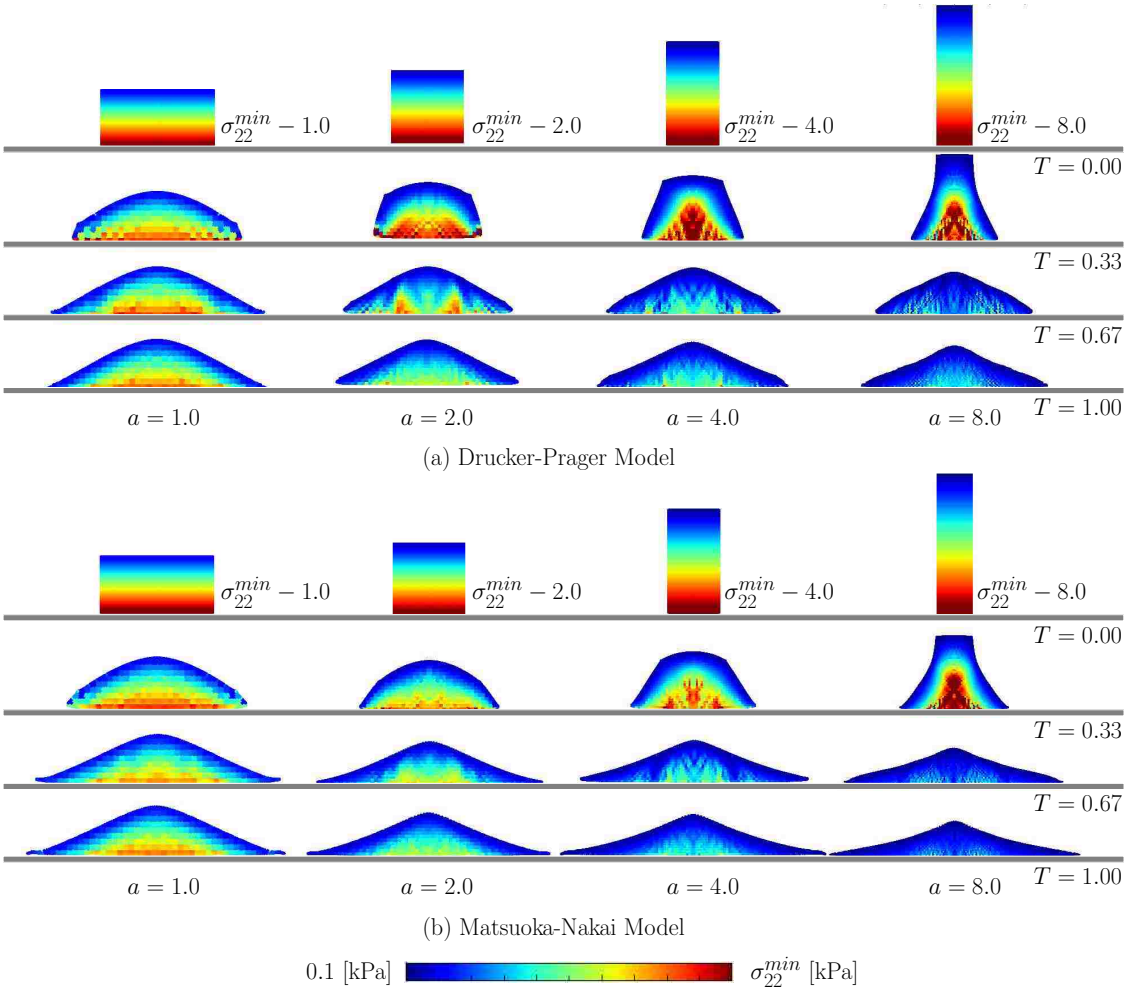

Figure 7.19: Evolution of the vertical stress, σ_{22}, for Case 2.

framework presented in Chapter 4. The remainder of this discussion evaluates these fields and links these values to key geometric observations.

7.2.3 Internal Stresses

In Figure 7.19 the evolution of the vertical stress, σ_{22}, is presented for both material models. The figure depicts the columns at several stages throughout the analysis, including the initial and final states. The initial stress distribution is consistent with a confined column subjected to gravity. As the analysis proceeds the vertical stress field behaves as expected for shorter aspect ratios ($a \lesssim 2.0$): the initial triangular distribution is more or less maintained throughout. In these cases the overall height of the column is not changing drastically. For taller columns an interesting stress field emerges. For $a \gtrsim 4.0$ there is a wedge shaped

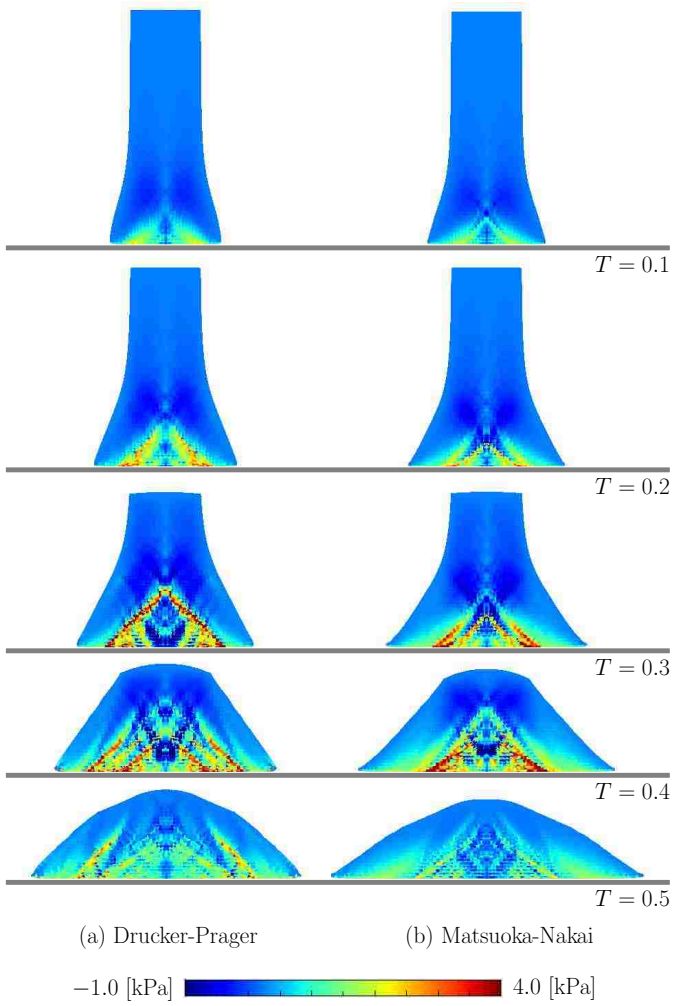

Figure 7.20: Evolution of the shear stress, σ_{12}, for Case 2.

increase in vertical stress. The shape of this wedge is consistent with the static cone previously discussed. The abrupt change in vertical stress is present until the columns stop their outward acceleration and come to rest. Although not visible in Figure 7.19 due to the stress color scale, the final deposit for the taller ratios does in fact exhibit a triangular stress distribution consistent with the final height.

Figure 7.19 also provides an excellent comparison between the final deposit shape for the two material models considered here. All simulations using the MN with DP G model yield a final shape that is parabolic, whereas the DP model tends to triangular profiles. This feature is less prominent for the shorter columns, but a difference is observed nonetheless. The final parabolic profile is more accurate when comparing to the experimental findings. All published photographs depict a surface that cannot be categorized by a single repose

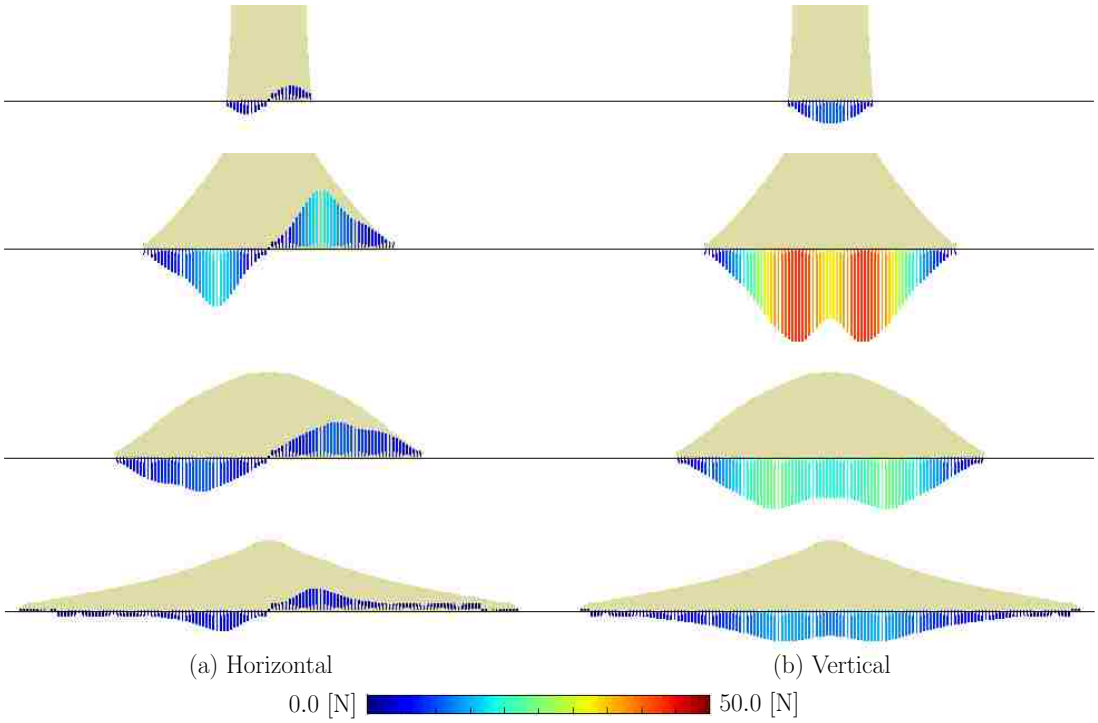

Figure 7.21: Reaction force profiles for Case 2 and the MN with DP G material model. The aspect ratio is $a = 8.0$. (a) Horizontal/shear component and (b) vertical component.

angle. The difference in shape profiles can be attributed to the shape of the Matsuoka-Nakai yield surface when there are shear stresses present. Figure 3.7 shows the Drucker-Prager surface is independent of the loading direction, while the Matsuoka-Nakai is very much influence by the load path. This key difference accumulates over time and ultimately affects the final shape.

In Figure 7.20 the shear stresses are shown for both models with the aspect ratio $a = 8.0$. The formation of distinct shear bands is visible. The material is failing along these paths and these regions are responsible for driving the outward motion. Again, the formation of a static wedge is observed.

7.2.4 External Surface Forces

The reaction force between the body and boundary surface can be visualized as a vector field. This was originally demonstrated in Chapter 6 in the context of a draining water tank. In the present case the dynamics are more complex and the resulting profile more interesting. In Figure 7.21 the reaction forces are plotted for the aspect ratio $a = 8.0$ and the MN with DP G material model. Two separate profiles can be plotted since the bottom

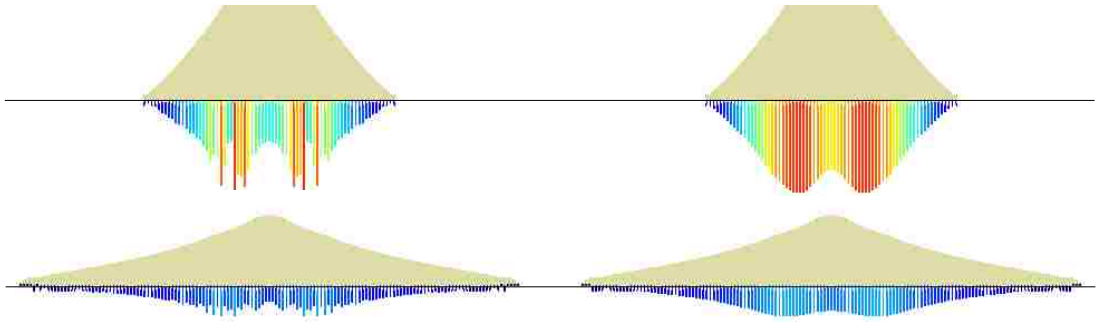

(a) Raw Profile (b) Filtered Profile

Figure 7.22: Comparison of reaction force profiles. (a) raw data profile and (b) filtered profile.

surface is non-smooth: the shear force that develops due to friction and the normal force preventing penetration into the boundary. The left side of Figure 7.21 examines the shear profile. At all times the shear force is directed towards the center line of the column, leading to a skew-symmetric distribution. The largest magnitude values occur when the vertical velocity of the column is at its highest value. Local maximums for each snapshot occur at the location where the shear stress band reaches the surface, as seen by comparing the shear force profile to the shear stress from Figure 7.20.

The normal force perpendicular to the surface is plotted in Figure 7.21(b). This distribution begins as a single parabolic shape. The profile grows and eventually reaches a global peak when the vertical downward momentum is at its largest—that is, when the vertical velocity is at its maximum value. Following said peak, the motion begins to move radially; two distinct parabolic regions are observed, each with a local maximum propagating outward. These local maxima coincide with the shear profile maxima. The final profile is shown in the bottom layer of Figure 7.21. Again the dual parabolic distribution is observed. Here it is noted that the final shape of this profile is slightly counterintuitive: from static principles one could argue for the existence of a force profile that mirrors the final geometric profile of the collapse. Clearly that is not occurring, and can be explained by the internal strength of the medium—diagonal stress bands emanating from the static cone leads to the observed distribution

For aesthetic purposes the final reaction profiles have been smoothed over. Stress wave propagation and checkerboard modes cause profile fluctuations in time. The filtering is done as follows: the plot value for any given node is obtained by computing the average of itself

and its neighbors [5] . The resulting profile is smoothed—but the maximum and minimum values of the original profile have been compromised. Since the value of interest is typically the largest magnitude force, the smooth profile is normalized by the largest smoothed magnitude, and then multiplied by the largest magnitude value from the original non-smooth profile. Doing so maintains the absolute value of the local maximums of the force profile. This technique is not the only option and alternative smoothing techniques could be employed. One alternative is to normalize with respect to the impulse at a given snapshot in time. This would ensure that momentum is conserved. However, since the smoothing is being done for plotting purposes only and has no bearing on the actual dynamics of the body, conserving momentum for the sake of a nice looking plot is unnecessary. The aforementioned technique is used here and provides a valid reaction force distribution. A comparison of the raw and filtered data is shown in Figure 7.22. The maximum values from the raw data are maintained, but as a side effect the minimum values are embellished—particularly where the gradient of the profile changes rapidly.

7.2.5 Conclusions

This section has demonstrated the Material Point method is a viable tool for modeling granular flow when coupled with an appropriate material model. Using a planar sand column collapse as a proving ground, the MPM simulations reproduced key geometric observations from published experiments. The analyses identified the peak material strength as being the most influential factor in determining the final shape of the collapse. In addition to the geometric aspects, it was shown that the MPM can be used to visualize other field variables of interest; the velocity and stress fields were shown here but many other options exist. The reaction force between the planar surface and the body of sand was investigated. Parabolicesque profiles were obtained for both. Future studies could investigate the influence of surface roughness on the final geometry. Alternatively, the work could be expanded to 3-d in an attempt to identify a link between planar behavior and the antisymmetric column collapse.

7.3 Avalanche Control: Energy Dissipation Using Earthen Embankments

Mountainous areas are notorious breeding grounds for avalanches of various mediums, including rocks, soil, trees and vegetation, and the most common culprit, snow. As a force of nature these powerful occurrences are awe inspiring and truly a force to be reckoned with.

---

[5] in this case a centered, five node window width is used.

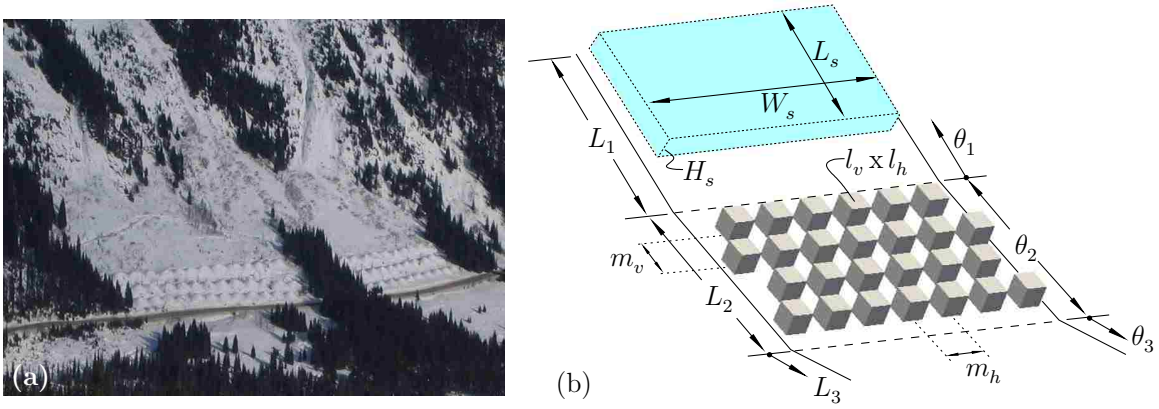

Figure 7.23: Earthen embankments are used to protect infrastructure in the event of an avalanche. (a) Road protection in alpine setting. (b) Simulation schematic.

Aside from the obvious danger and threat to human life, these slides pose a serious problem to civil infrastructure and the annual costs are estimated in the billions (Highland, 2006). Having the ability to model these events and evaluate energy dissipation mechanisms is paramount in mitigating their disastrous effects. This section shows the MPM is capable of such feats and has the potential to be an indispensable tool for testing and developing energy dissipation structures.

Oftentimes the location where an avalanche will occur is easy to discern, as these events can take place cyclically along well defined flow paths. Natural ravines develop and effectively serve as funnels—concentrating slides to relatively small regions. While trees, vegetation, and hillside geometry can help abate the snow mass, there are regions in which slides travel relatively unimpeded for large distances—gaining significant momentum and ultimately delivering a crippling blow to anything in their path. The predictable flow channels has led engineers to construct energy dissipation devices to protect roadways and buildings in such instances. This includes earthen embankments at regular intervals as shown in Figure 7.23(a)[6]. In this image three distinct regions of the mountainside are observed. The steep, upper portion with ravines that channel the flow event, an intermediate sloped area where the mounds are constructed, and a flat region containing a road, happily winding its way through the countryside. The mounds are built for an obvious purpose: to slow avalanches and reduce the flow onto the road. Replicating and modeling this scenario is the focus for the remainder of this section.

[6]This photograph was obtained and is utilized without explicit permission on 1/30/2013 from the URL: http://www.avalancheservices.ca/gallery.html

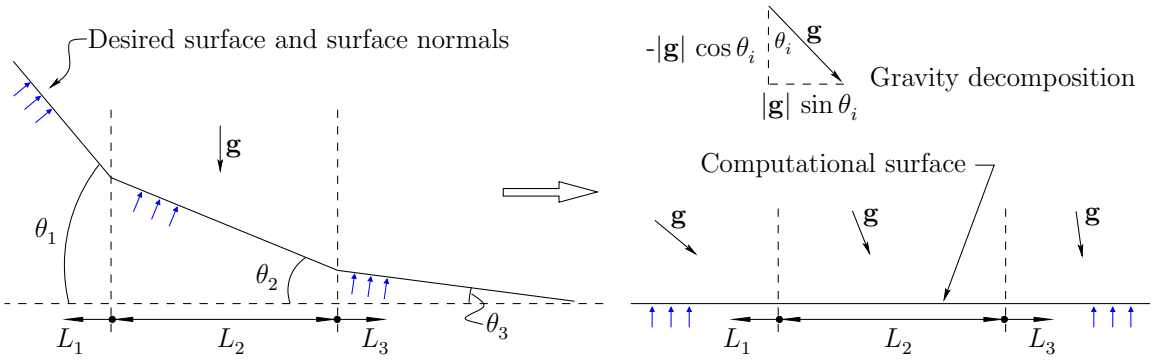

Figure 7.24: Representation of a sloped domain in a regular grid space. The desired environment is shown on the left while the computational representation is depicted at right.

7.3.1 Model Representation and Other Considerations

The geometric schematic used in this study is shown in Figure 7.23(b). Several key parameters are identified in this figure, including the snow mass length, width, and height, the mound length, width, and height, as well as the mound spacing. For the purpose or this study it is assumed that cubic structures will suffice. This is due primarily to the restrictions imposed by the regular grid in the current MPM implementation. Obviously this is not perfect but will prove to be acceptable for the purposes of this study. Also defined are the slope angles and the relative length of each region, using the variables θ_1 , θ_2 , θ_3 and L_1 , L_2 , L_3, respectively. The slope angle is defined relative to the horizontal.

This study provides an opportunity to test and implement a powerful feature for use in any numerical framework when a regular grid restricts the domain geometry. Square or rectangular cells are incapable of providing a sloped region as required for this analysis. However, a slope may be emulated by altering the direction that gravity acts as a function of spatial position. This modification can be taken to an even higher level of abstraction by varying the bounding surface normals. These vectors can also vary as a function of global position to create circular and curved domains within the confines of a square or rectangular grid framework. If done appropriately the general surface is represented using a spatial map linking the flat computational space to the general desired geometry. For the present study a complicated map is not required, nor is it necessary to modify the surface normal direction. Only the gravity vector is altered using the original magnitude, g, as

$$\mathbf{g} = 0\ \mathbf{i} - g\ \cos\theta_i\ \mathbf{j} + g\ \sin\theta_i\ \mathbf{k}\ , \tag{7.12}$$

where $\mathbf{i}$, $\mathbf{j}$ and $\mathbf{k}$ are the standard unit base vectors and θ_i is the current slope angle corresponding to a global position. Clearly the vector $\mathbf{g}$ is dependent on the users coordinate

Table 7.7: Initial avalanche geometry and tri-planar domain description.

Description	Symbol	Value
Avalanche length, [m]	L_s	36.0
Avalanche width, [m]	W_s	72.0
Avalanche eepth, [m]	H_s	6.0
Slope angle 1 [deg °]	θ_1	25.0
Slope angle 2 [deg °]	θ_2	20.0
Slope angle 3 [deg °]	θ_3	0.0
Slope length 1 [m]	L_1	48.0
Slope length 2 [m]	L_2	54.0
Slope length 3 [m]	L_3	1000.0
Horizontal mound length [m]	l_h	6.0
Vertical mound length [m]	l_v	6.0
Horizontal mound spacing [m]	m_h	12.0
Vertical mound spacing [m]	m_v	12.0

definition. This modification is applied at the particle level, as the particles themselves represent the snow. In the flat computational space, a rough planar boundary whose normal is coaxial with the **j** direction, is applied throughout the domain. This concept is visualized in Figure 7.24.

The analysis itself has little knowledge of the domain shape and is carried out in a regular manner when using the technique described in the previous paragraph. The user is responsible for appropriately visualizing the results. This, however, is a post-processing exercise and has no bearing on the computational algorithm. The end result can be quite appealing and is shown in this and other examples in this dissertation. This modification is applicable to any numerical method. In the present case the feature expands the capabilities of the MPM coding framework.

The specific geometric values employed in this study are listed in Table 7.7. Identifying an appropriate material model to capture the mechanical behavior of snow is a challenge. The extreme dependence on temperature is usually the limiting factor for any single constitutive framework, and quickly glancing at works like Petrovic (2003) can show the inherent fluctuations of the mechanical properties with temperature. The literature varies significantly both in the nature and complexity of these models. Past treatment has included elastic and history *independent* nonlinear viscoelastic constitutive equations, all the way to thermodynamically consistent, strength and history *dependent* failure criteria. An overview

Table 7.8: Material and MPM parameters for avalanche simulation.

Description	Symbol	Value(s)
Density, [kg/m^3]	ρ_0	500.0
Bulk modulus, [Pa]	K	$5.55\,(10)^6$
Shear modulus, [Pa]	G	$4.17\,(10)^6$
Friction angle, [deg°]	ϕ_F	20°
Yield stress, [Pa]	μ	500
Associativity	ϱ_G/ϱ_F	0.0
Time step, [s]	Δt	$1.00\,(10)^{-3}$
Duration, [s]	t_f	25.0
Cell size, [m]	$h_x = h_y = h_z$	1.0
Particles per cell	PPC	8

of models is obtainable in several works, e.g., Brown et al. (1973); Salm (1982) and the references therein. Ultimately the choice boils down to balancing the intricacies of a given formulation with the realizable benefit. The level of detail employed must be linked to the nature of the application. In the current context the role of temperature variation, for example, is not relevant and is beyond the scope of the goals governing the study. Properties are selected for a given temperature and it is assumed that these apply throughout the avalanche. In a similar manner, entire classes of models may be eliminated based on the current goals of the study. The current example relies on a pressure dependent conic failure surface similar to the approach applied by Nicot (2004). In doing so the snow is treated as a cohesive granular material which allows the relatively simple models defined in Chapter 3 to be used with no modification. In particular, the bi-surface smooth tension cap model of Section 3.6.2 is used with a constant friction angle. The model parameters are identified in Table 7.8.

7.3.2 Flow Description

The snow mass is released from rest and proceeds down the slope and into the earthen mounds as shown in Figure 7.25. The first snapshot shows the snow shortly after reaching the first row of mounds at $t = 6.25\ s$. The front line of barriers is engulfed by the flow, as the snow accumulates behind the obstruction and serves as a ramp for the tailing portion of the slide. As time proceeds the avalanche works its way through the remaining barriers, with each successive row seeing less and less snow. By the time $t = 25.00\ s$, the slide has ceased moving and it appears that the mounds have served their purpose: only a small

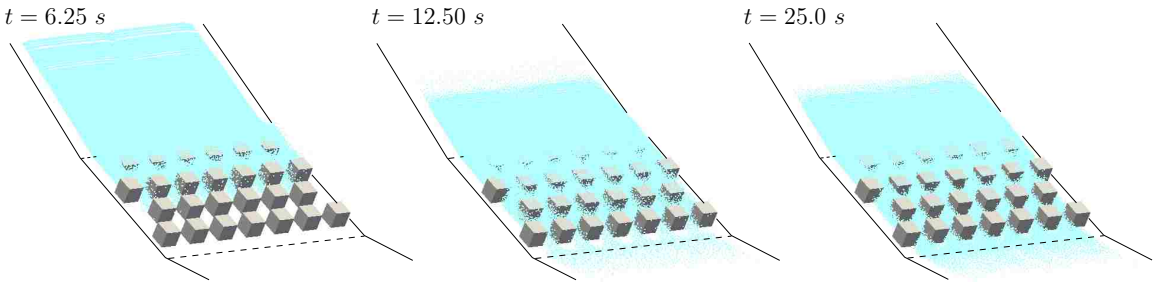

Figure 7.25: Evolution of avalanche flow from initiation to static state. The embankments prevent a majority of the flow from proceeding onto the level ground.

portion of snow has infiltrated the lower flat regions of the domain.

The true service of the mounds is better appreciated by examining a plan view depicting the snow velocity magnitude. In Figure 7.26 simulations with and without the mounds are shown in the upper and lower row, respectively. The mound location is shown in the lower row only as a point of reference. Shortly after contact at $t = 3.75\ s$, the leading edge of the avalanche is slowed and a reduction in velocity is observed propagating up the slope. Eventually this upward moving front reaches the tailing end of the slide and the entire mass comes to rest as indicated in the upper row of Figure 7.26 at $t = 15.00\ s$. The same cannot be said for the simulation without mounds, as even at $t = 15.00\ s$ a considerable portion of the avalanche is still accelerating down the mountain. This figure shows the earthen structures significantly dissipate the kinetic energy of the flow.

An alternative vantage point comparing the two simulations is shown in Figure 7.27. Here a side view captures the interaction at a higher frequency, offering additional insight into the nature of the interaction. From this perspective a large plume of snow emanating upward is seen as the flow front impacts the leading row of mounds. In a strictly fluids sense this might be called a splash, but such a moniker ceases to be an effective verb in the context of a pseudo-solid mass. Each successive row of embankments slows the mass until an interspersed, static state exists. The most striking observation this figure provides is a comparison of the final deposit. Here the total runout is reduced by several factors, and the potential underlying benefits associated with the use of earthen mounds to protect civil infrastructure are easily realized.

7.3.3 Force Interaction

Among other things, the current coding framework enables the analyst to easily extract the force reaction between the particle-based body definition and the node-based bounding surface. For the current study this is depicted in Figure 7.28, where the force vectors

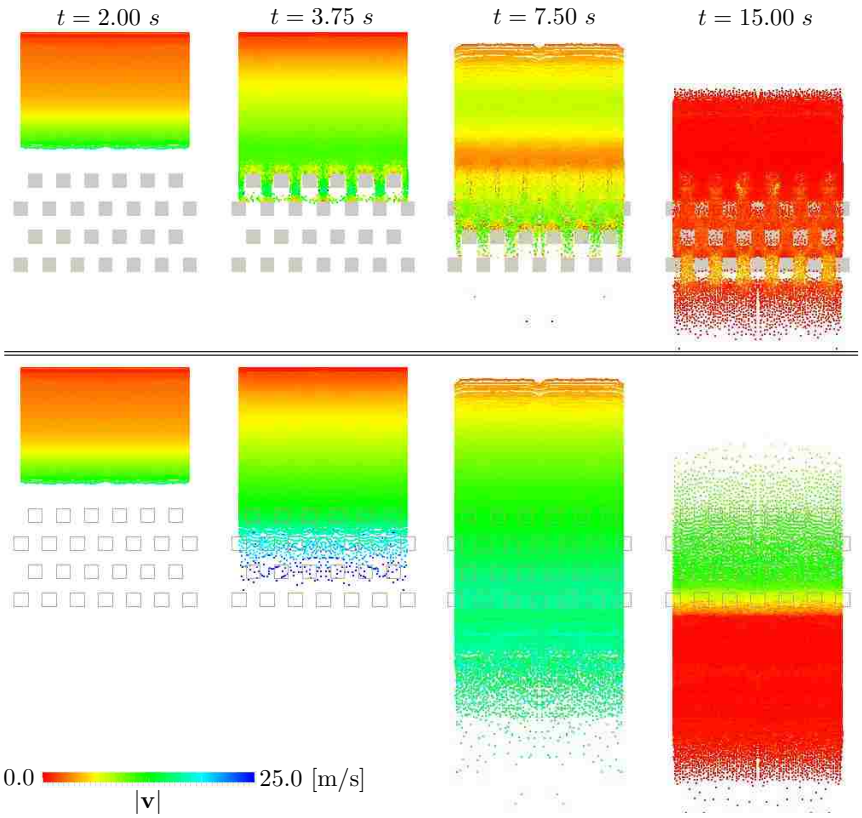

Figure 7.26: Plan view comparing velocity magnitudes. The upper row is inhibited by the earthen mounds. The lower row is a simulation without the embankments (the mound outline is shown for reference purposes only).

emanating from the nodes of select mounds are shown. The force distribution is initially triangular as the avalanche strikes the leading row at $t = 3.75\ s$. As the flow accumulates the reaction forces become uniform and steady, and each successive row has a reduced net force magnitude. These observations are consistent with intuitive notions regarding the force interaction between the avalanche and the earthen structures, and this framework establishes a means of quantifying the magnitude of said interaction.

The node-based forces are, of course, subject to the limitations imparted by the MPM itself. These include a rigid and continuous reaction, independent of underlying force-displacement relations that would undoubtedly exist between the real structure and encroaching flow. Nor does this framework have the ability to capture other process, such as mound erosion and breakup. Nonetheless, these forces provide an accurate estimate from which mound design could proceed for practical implementation in the field.

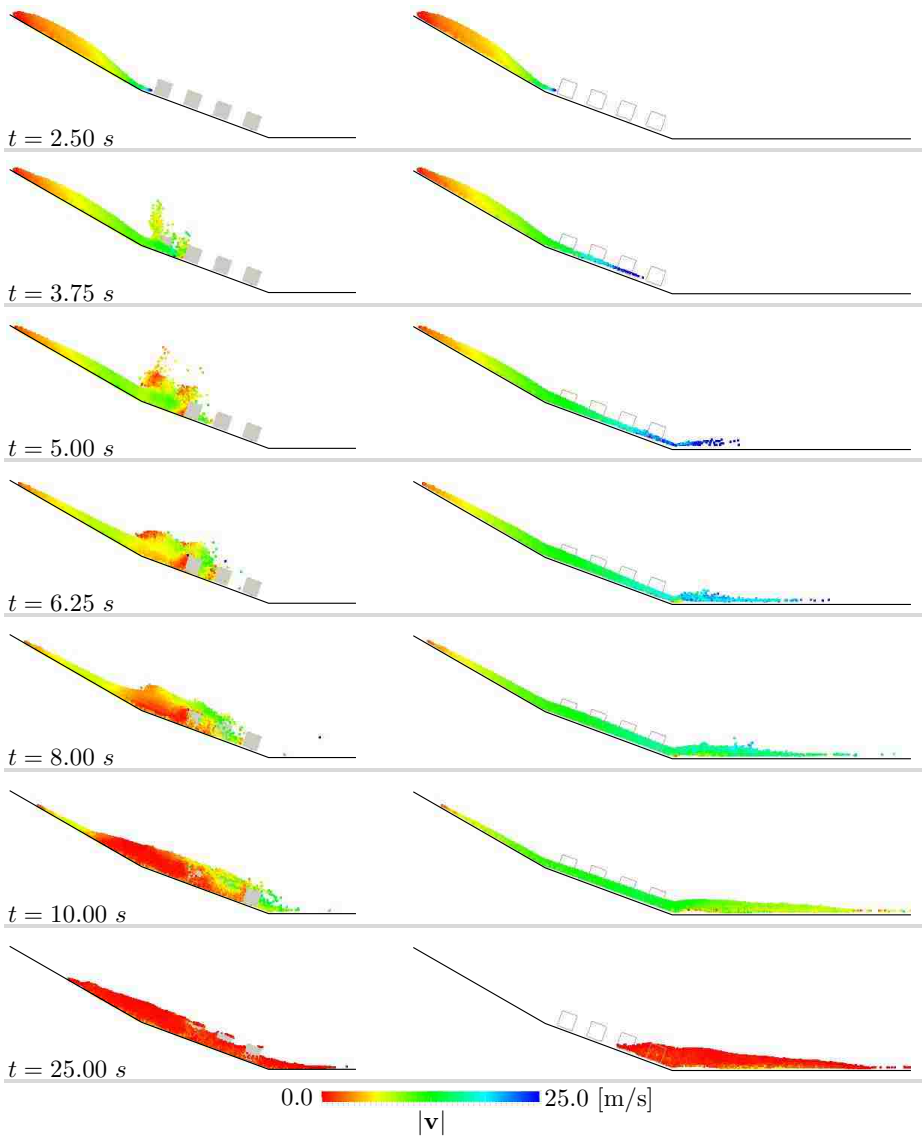

Figure 7.27: Side view comparing velocity magnitudes. The left column is inhibited by the earthen mounds. The right column is a simulation without the embankments (the mound outline is shown for reference purposes only).

7.3.4 Conclusions

This study has shown the MPM is an appropriate tool for capturing snow avalanches and quantifying the interaction between the slide and the energy dissipating mounds. This study provides an example of the MPM's capabilities in this regard and opens the door for several quantitative parametric studies. One such future study could seek to establish the link between the kinetic energy of the avalanche and the mound geometry. This includes not

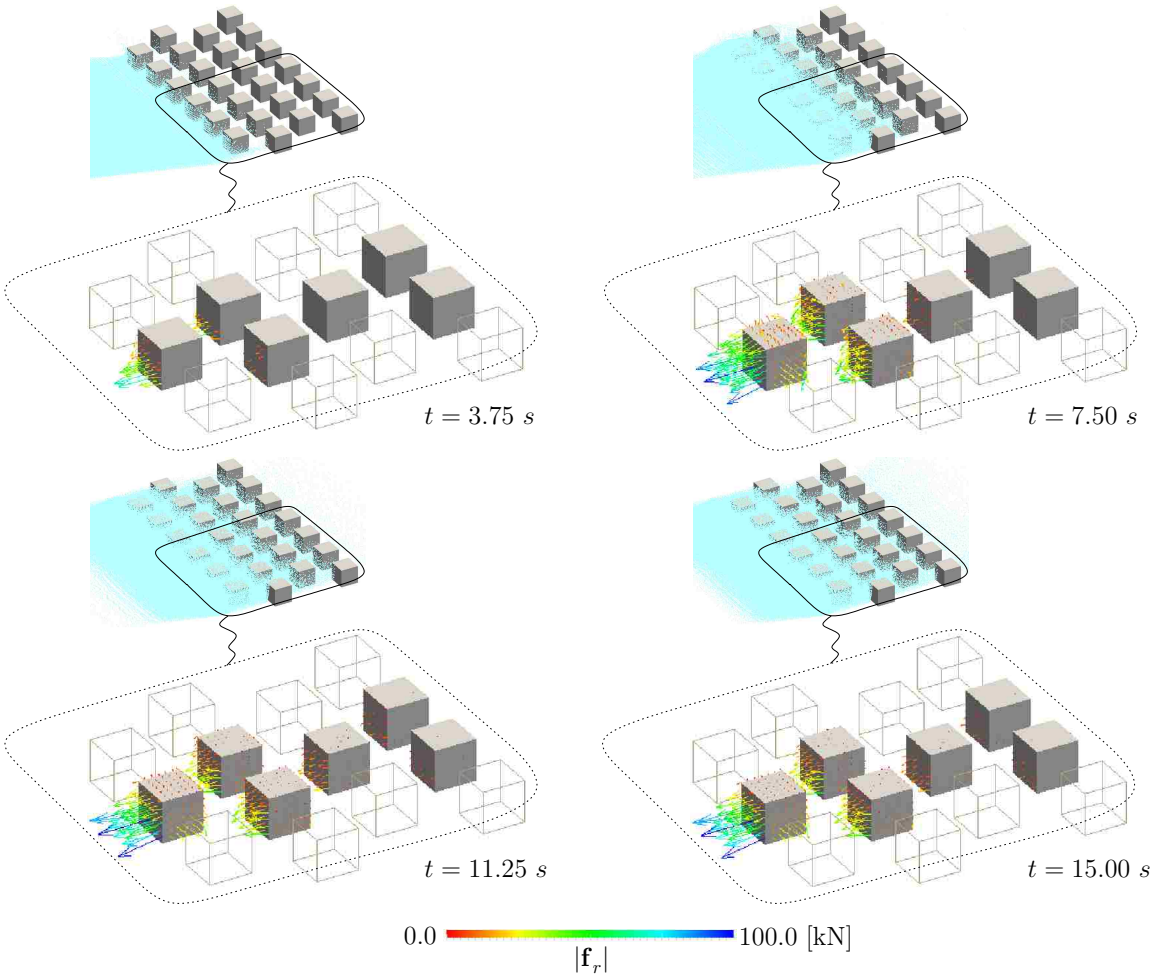

Figure 7.28: Reaction force exerted by mounds to ensure no flow penetration.

only the length, width and height of the mounds themselves, but more importantly their spacing and number of rows required to dissipate the flow momentum. There is undoubtedly a dependence on slope angle as well as surface roughness, and these additional parameters are worth investigating. It is postulated here that very well defined curves exist linking the avalanche energy to these geometric properties. Alternative mound definitions could also be explored. This includes employing one of the many multi-grid contact algorithms in the literature, e.g., Bardenhagen et al. (2000, 2001); Hu and Chen (2003); Pan et al. (2008) and using a particle-based mound definition as opposed to the grid-based bounding surface. Even without specific contact algorithms, a particle-based embankment was modeled successfully, including breakup and erosion induced by the passing debris flow, in the work by Shin (2009).

The repetitive structure of the mounds has motivated a quantitative study identifying

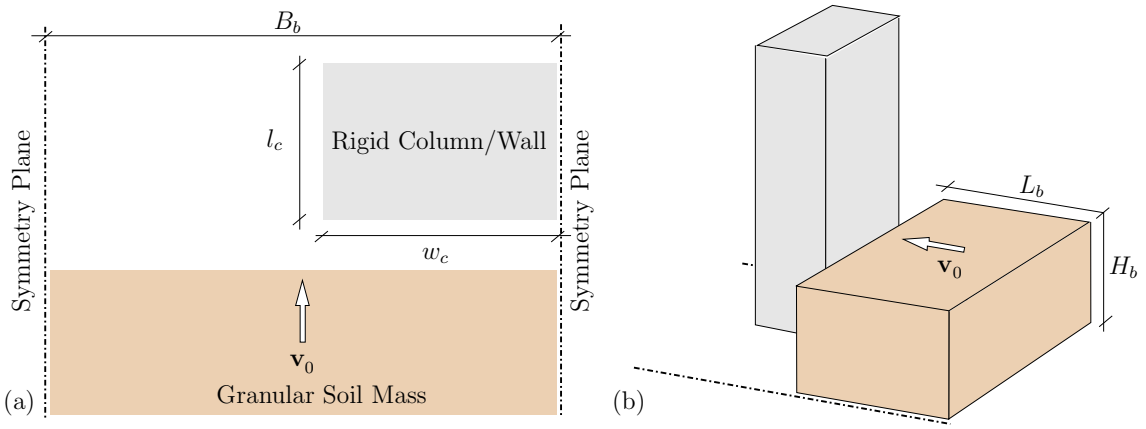

Figure 7.29: Initial configuration for granular flow around column. (a) Plan view and (b) isometric view.

the underlying link between reaction force magnitude and geometric, material, and analysis parameters. The study is undertaken in the next section and while the medium has changed from snow to a general granular material, the results remain applicable to this study and could easily be tailored to this context.

7.4 Soil-Column Impact: Granular Flow into a Single Column/Wall

A natural starting point for quantifying the force interaction between a debris flows and a rigid object is to simulate the relatively straight forward scheme shown in Figure 7.29. The left hand side depicts the plan view of a granular, cohesionless soil mass approaching a rigid structure with applied velocity $\mathbf{v}_0$. An isometric view is shown in Figure 7.29(b). The symmetry boundary conditions imply a repeating column structure and multiple interpretations exist as to what this schematic represents physically. One option, albeit a bit of a stretch, is a series repeating bridge/overpass supports in a flat ravine. Alternatively, the side conditions could be interpreted as a smooth ravine or channel directing the flow into an impact barrier. Or finally, such a setup could represent the avalanche mounds presented in the previous section.

The column geometry is described by parameters l_c and w_c for the length and width, respectively. The soil body exists across the entire channel as described by B_b; the corresponding height and length parameters, H_b and L_b, complete the geometric description of the body. All bounding surfaces are smooth, save the ravine/channel bed whose surface roughness is significantly higher than the internal friction angle of the granular medium (see Section 7.2 for an additional discussion regarding surface roughness in the context of MPM

Table 7.9: Column and soil mass geometry.

Description	Symbol	Value(s)
Column length, [m]	l_c	2.0
Column width, [m]	w_c	1.0, 2.0, 3.0, 4.0, 5.0, 6.0
Soil width, [m]	B_b	6.0
Soil height, [m]	H_b	1.5, 2.0, 2.5, 3.0, 3.5, 4.0
Soil length, [m]	L_b	8.0

and modeling granular flow).

The primary goal of this study is to evaluate the magnitude of the forces imparted on the rigid column/wall due to the soil surge. Secondary emphasis is placed on identifying trends in the resulting force profiles. The study is parametric in nature and investigates the role that both geometry and material properties have on the net reaction force. From the geometry side, the column width and body height are varied over a specified range. For each column width and body height pair the effective friction angle of the granular soil is changed to capture a broad range of flow-like states.

A full geometric description is contained in Table 7.9. The initial gap between the soil mass and the column is set to 1 [m]. This value is chosen somewhat arbitrarily and is based on findings from preliminary studies that targeted appropriate ranges for the geometry parameters. This short gap allows the action of gravity, in concert with the applied velocity, to create a flow-like impact as opposed to a flat wall of soil impacting the column. The body length is fixed—providing a sufficiently small aspect ratio compared to the height of the surge. Gravity is aligned with the vertical direction and has a magnitude of $|\mathbf{g}| = 10$ [m/s^2]. The initial study considers only a single approach velocity of 1.0 [m/s]. Note that a column width of 6.0 [m] effectively turns the structure into a rigid wall. In such cases the term *column* is used interchangeably with *wall*.

The material and MPM parameters are given in Table 7.10. The material model employed for these analyses is the smooth-cap two surface Drucker-Prager model described in Section 3.6.2. Here the yield stress parameter, μ, is taken as very small but non-zero which reaps the numerical benefits of the circular cap. A node-based averaging scheme is used to construct the volumetric portion of the deformation and stress field[7]. The parameters listed in Tables 7.9 and 7.10 account for a total of 180 separate analyses—each one containing between 36,864–98,304 particles. Obviously all the possible results cannot be presented here.

[7]See Section 7.4.3 for an additional discussion regarding the use of a node-based scheme.

Table 7.10: Material and MPM parameters for granular flow into a single column/wall.

Description	Symbol	Value(s)
Macroscopic density, [kg/m^3]	ρ_0	1950.55
Bulk modulus, [Pa]	K	$8.33\,(10)^6$
Shear modulus, [Pa]	G	$3.85\,(10)^6$
Friction angle, [deg°]	ϕ_F	$5°, 10°, 20°, 30°, 40°$
Yield stress, [Pa]	μ	10
Associativity	ϱ_G/ϱ_F	0.05
Time step, [s]	$\Delta\, t$	$5.00\,(10)^{-4}$
Duration, [s]	t_f	3.5
Cell size, [m]	$h_x = h_y = h_z$	0.25
Particles per cell	PPC	8

An attempt is made to identify trends and present the data in an economical fashion.

The star quantity of this study is ultimately the reaction force the surge induces on the column. As a result the main emphasis is not on the soil body itself (the material points); rather, the focus is shifted to the column and those nodes that make up this bounding surface. Prior to delving into the force topic, however, it is worth examining the material points themselves—as they too have an interesting story to tell.

7.4.1 Dynamic Description, Stress Field, and Total Deformation

From a material standpoint there are multiple fields of interest. Only three such fields are briefly examined here: the velocity, stress, and plastic deformation fields. The particle velocity is first up and several plan views are shown in Figure 7.30. Here the velocity magnitude at three sequential times is shown for three different friction angles, namely $\phi_F =$ 10°, 20°, and 30°. The reference time, $t = 0.0\ s$, corresponds to the initial condition as described in Figure 7.29. These images are from simulations in which the column obstructs half of the available channel, i.e., $w_c = 3.0$ [m], and the initial particle height is 3.0 [m]. Only particles in the immediate vicinity of the barrier are shown.

Clearly the friction angle of the material dictates the flow as the soil mass spreads around the column. This observation is an ever-present theme and will be revisited time and again throughout this discussion. Shortly into the analysis a majority of the mass has slowed from the initial 1.0 [m/s]. Only regions free to flow near the column are experiencing an increase in velocity due to the momentum and action of gravity. For the fluid-like case of $\phi_F = 10°$, the area reduction is leading to a noticeable increase in velocity to conserve

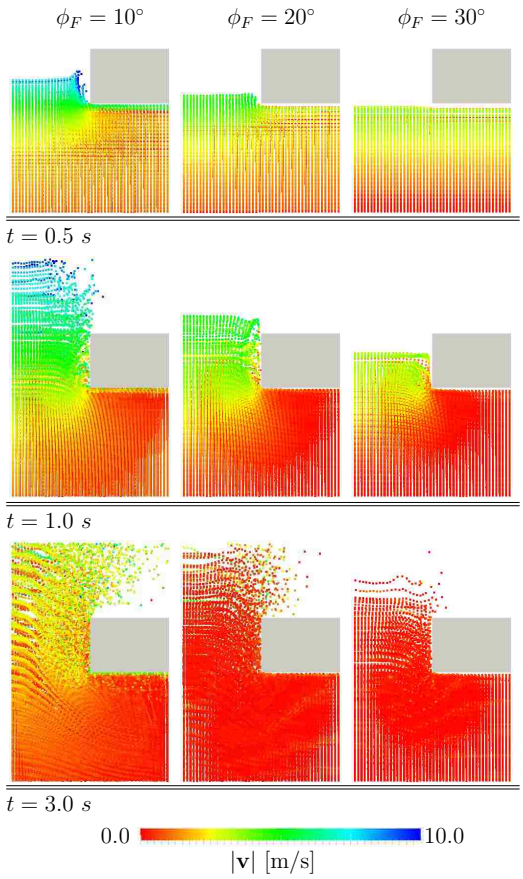

Figure 7.30: Plan view as the soil flow wraps around the column. The color map shows magnitude of the particle velocity.

energy. The phenomenon is most noticeable in the region directly adjacent to the column corner. This is in stark contrast to the $\phi_F = 20°$ and $\phi_F = 30°$ simulations. For these latter two cases the flow is moving at a slower rate and has not progressed appreciably around the column. A similar evolution is observed as the flow time increases through $t = 1.0\ s$. By the time $t = 3.0\ s$ the full disparity between the flow regimes is observed and appreciated. The 10° flow dynamically evolves as the flow engulfs the structure and proceeds around the backside. On the other end of the spectrum is the 30° debris pile, whose motion has ceased and is stationary. Generally speaking the flow dynamics match intuitive expectations regarding the flow-like nature and the corresponding link to friction angle. As will be shown in due course, a friction angle of 20° serves as the pseudo delimiter between a liquid-like response and a more traditional solid/granular flow response.

The vertical stress component σ_{22} is shown in Figure 7.31. At time $t = 0.0\ s$ the

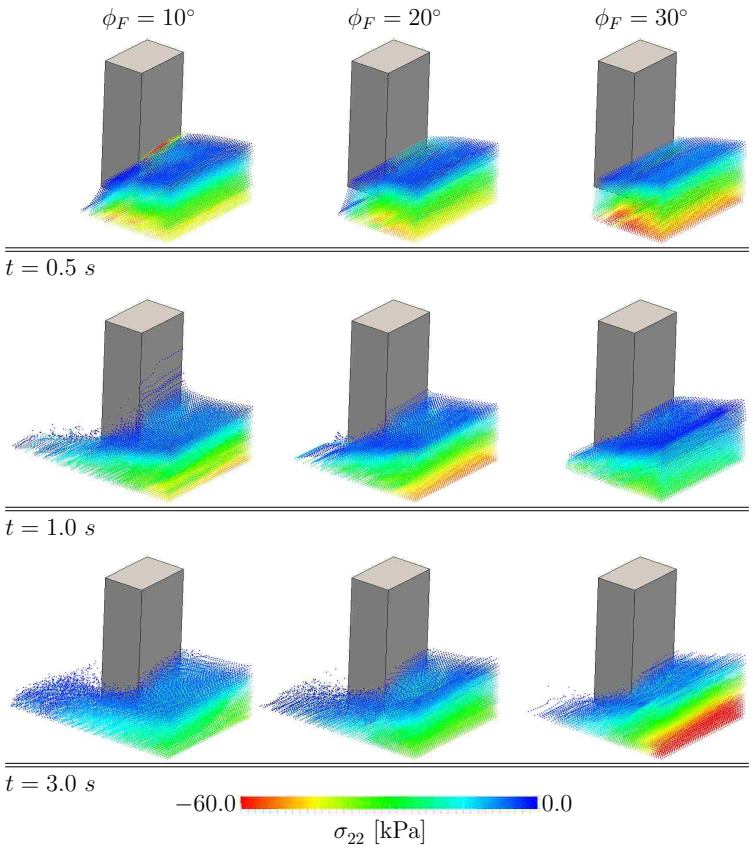

Figure 7.31: Isometric view as the soil flow wraps around the column. The color map shows the vertical stress, σ_{22}.

particles are assigned an initial state consistent with a static configuration. As the flow proceeds the regions near the front assume a nearly stress free condition. Shortly after impact at $t = 0.5\ s$, an increase in stress magnitude is observed for $\phi_F = 10°$ as the mass is compressed into the column face. Note that the smaller the friction angle, the smaller the magnitude of the vertical stress is for regions in the vicinity of the flow channel. This is due to the decreased depth of the soil as the flow proceeds around the column. At $t = 1.0\ s$ the forward momentum results in a splash for the 10° flow. Neither the 20° or 30° simulations experience anything resembling a splash of this nature. The analyses employing a friction angle of 5° (not shown) have a spectacular splash that trumps even the 10° counterpart. As time moves on to $t = 3.0\ s$, the stress reduces in magnitude to values consistent with the depth of the flow for both the 10° and 20° flows. Once static the stress state resembles the initial state for regions away from the leading edge. Though Figure 7.31 represents only a small sample of the flows, the findings for the particle stress distribution are very good for all

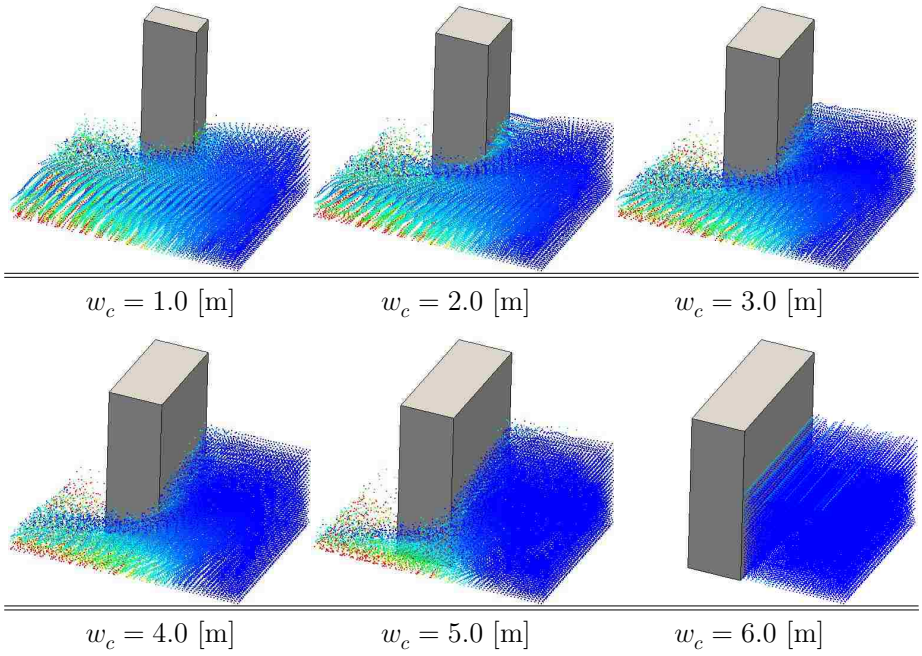

Figure 7.32: Isometric view of plastic deformation at $t = 3.0\ s$ for $\phi_F = 10^\circ$ and $H_b = 3.5$ [m]. The column width increases until it forms a rigid barrier. The red particles have $|\boldsymbol{\varepsilon}_p| = 10.0$ while the blue particles have $|\boldsymbol{\varepsilon}_p| \approx 0.0$.

soil depths, column widths, and friction angles examined. The volumetric approximation outlined in Section 4.5 for elastoplastic materials ensures quality stress measures for all stress components and invariants.

Figure 7.32 shows the total magnitude of the plastic strain tensor, $|\boldsymbol{\varepsilon}_p|$, in an effort to capture what regions of flow are deforming the most. This scalar effectively serves as the total deformation measure—as the elastic portion of the deformation is significantly smaller than the plastic portion. Only a single height and friction angle ($\phi_F = 10^\circ$ and $H_b = 3.5$ [m]) are shown. The snapshot is at $t = 3.0\ s$ for column widths ranging from $1.0 - 6.0$ [m]. Obviously the flow behaves differently for different column widths. The extreme case being $w_c = 6.0$ [m], in which case the column is actually a rigid wall. For this geometry there is very little plastic deformation and the mass remains more or less elastic. As the flow channel opens wider and wider the net deformation increases. This in itself is not all that interesting; what is more interesting is seeing which regions of the debris flow experience the largest deformation. This occurs primarily at the leading edge where the continuum is in immediate contact with the rough surface. These particles deform and provide the base for other particles to slide over. Said regions are indicated by the red colomap in Figure 7.32. The freeriders—the particles shown in blue—are those that experience little deformation

but excessive displacement at the front of the flow. These enviable constituents ride the stress-free wave of momentum as the soil makes its way around the obstruction. This deformation pattern is consistent with the MPM findings and experimental observations of the sand column collapse outlined in Section 7.2.

The mechanical fields discussed above highlight a few capabilities of the current implementation when the focus is on the continuum body itself. As a whole, the quality of these fields—be it the velocity, stress, or deformation (or almost any other tensor field for that matter)—is quite high. Bridging the gap between solid- and fluid-like behavior for an elastoplastic body is an excellent example of the types of analyses MPM is best suited for: large deformation of history dependent materials. Successfully obtaining the values shown in Figures 7.30–7.32 is beyond the ability of many traditional continuum based methods.

7.4.2 Reaction Force on Column

The primary quantity of interest is the reaction force the surge induces on the column. This force is obtained by ensuring all nodes representing a surface satisfy $\mathbf{v}_i \cdot \mathbf{n} = 0$ and $\dot{\mathbf{v}}_i \cdot \mathbf{n} = 0$ for the nodal velocity and acceleration, respectively. The unit normal, $\mathbf{n}$, is defined perpendicular to the surface. Here the column surface is assumed to be smooth and friction is neglected. In the context of the MPM, the above constraints on the velocity and acceleration field build a reaction force profile at the computational nodes. By tracking these values the net reaction force distribution is determined.

Sample force profiles are shown in Figure 7.33. These images are from the same analyses showing particle stress in Figure 7.31. The viewing angle is the same but the particles are removed so the nodal force vectors can be seen. The scale of the max force is different for each friction angle of the flow. The maximum value the colormap corresponds to is found just below the upper row of the diagram. A force profile is observed on both the primary impact and the side faces as the particles wrap around the obstruction. The shape of these profiles is important. At the start of the interaction the profile on the impact face tends to be more constant as the soil surges against the barrier. At later times the profile assumes a force prism that is triangular in nature. However, while these observations do hold in general, significant deviation is possible for individual time steps—as the stress wave propagations cause local fluctuations in profile geometry.

Figure 7.33 is beneficial for understanding the reaction force distribution and determining local regions where the force effects are amplified. However, of much greater interest is the net or total force value acting on a structure due to the interaction of the soil surge. This value is computed simply by summing those nodes on a common face and examining the

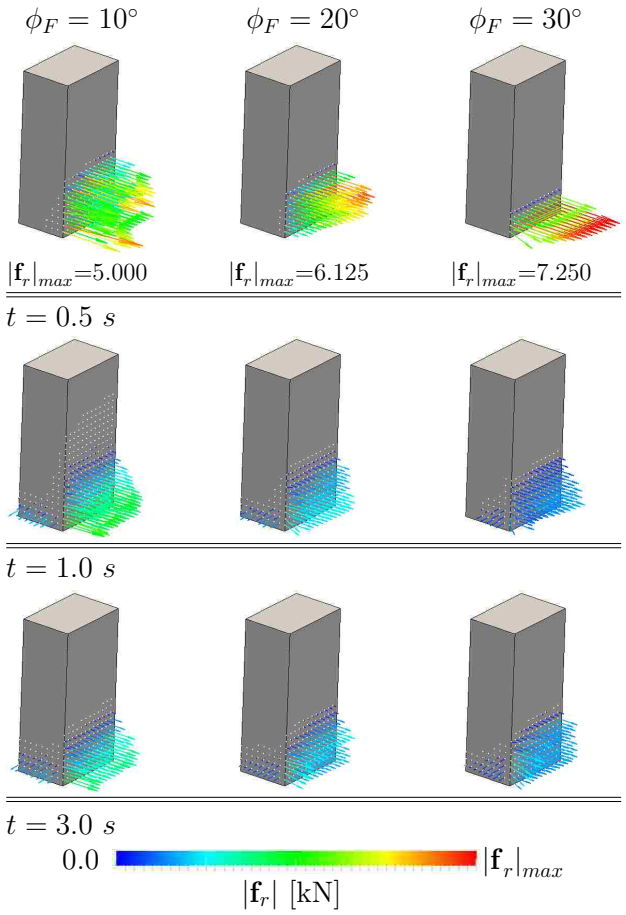

Figure 7.33: Isometric view as the soil flow wraps around the column. The color map shows the magnitude of the reaction force, $|\mathbf{f}_r|$, normal to the bounding surface. Each individual boundary node can be seen with corresponding reaction force vector.

resulting vector. For the cases examined here the force on the impact face is several times larger than on the side face. Thus, this discussion takes into account only the net force on the impact face. And, since the column is smooth, the largest component is perpendicular to the impact face (or parallel with $\mathbf{v}_0$). It is this component that is examined in detail in what follows.

A typical reaction force time history is shown in Figure 7.34. These force histories are for a column width, $w_c = 4.0$ [m]. Three different friction angles are considered: $\phi_F = 5°,\ 10°$, and $20°$. For each effective friction angle three heights are shown, with $H_b = 2.0,\ 3.0$, and 4.0 [m]. It is immediately apparent there are identifiable trends. The first observation is the existence of a peak force value. The peak occurs early in the interaction as the surge makes contact with the column. A sharp decrease in magnitude is observed a short duration

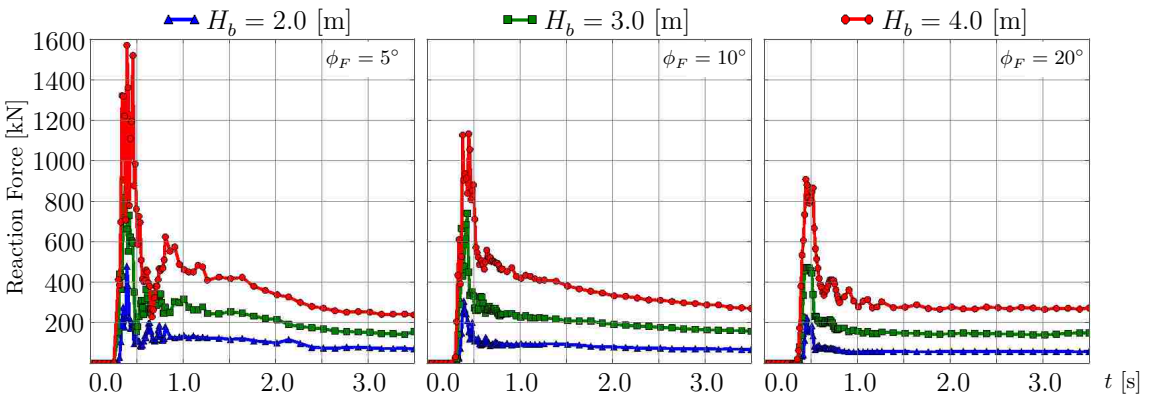

Figure 7.34: Net reaction force as a function of time for $w_c = 4.0$ [m]. Positive value indicates force directed against flow.

after the initial peak. As time proceeds the magnitude of the force diminishes until the value becomes more or less constant. This constant magnitude is referred to here as the steady state force. Although the force is constant the flow may still be moving as the velocity profiles in Figure 7.30 indicates. These two key forces—the peak and steady state—are observed for all soil heights, columns widths, and material parameters considered in this study.

Obtaining an accurate peak force is not entirely straight forward. The nature of the implementation only records snapshots of the simulation at user-specified time intervals. Unfortunately, it is quite unlikely the peak force experienced by the surface will occur precisely during a time step in which data is being collected. The boundary class is modified to collect the largest magnitude force exerted during a given analysis in order to resolve this issue. Every boundary instance (each flat surface in this case) keeps track of the total sum of all nodes it contains and the maximum over the entire interval is isolated and reported. Thus, peak force values presented here are often slightly larger than the force history plots indicate.

Collecting a reasonable steady state force also requires attention. While the existence of a constant, steady state force is discernible from Figure 7.34, there are in fact small fluctuations due to stress wave propagation in the medium. To combat these fluctuations a modified running average is used. The average window (anywhere from 1-3 sample steps) is computed to obtain an average profile. This profile is then modified such that the impulse from the original signal is conserved. The final result is a very close fit to the data that also maintains the momentum from the original signal. This scheme is highlighted in Figure 7.35. Here the dashed lines represent the original signal and the solid line is the

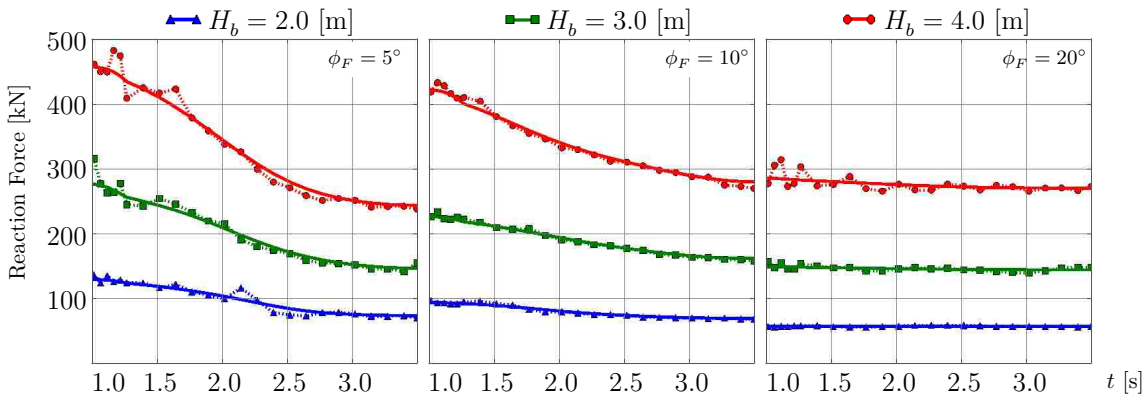

Figure 7.35: Moving average of reaction force as a function of time for $w_c = 4.0$ [m]. Positive value indicates force directed against flow. The averaged value is used to obtain the steady state force measure.

modified running average. Ostensibly such a scheme could be used to reconstruct the entire force-time signal from each surface. There is a lot of literature on signal processing an undoubtedly a reasonable method could be adopted to preserve the peak and steady state values all the while eliminating a majority of the fluctuations. This, however, is beyond the scope of this study. Instead the modified moving average is used only to compute the steady state force values.

It is tempting to begin using Figure 7.34 to draw conclusions about the links between geometry and material parameters. For example, as the initial height of the soil surge is decreased so is the magnitude of the peak force. This figure also seems to indicate that increasing the friction angle reduces the magnitude of the peak force for a given soil height. While these are certainly valid observations, they are based on a very small subset of the available data. Furthermore, plots like Figure 7.34 make it challenging to quantify changes and answer trend-related questions. How is the peak force changing with friction angle? What is the nature of the link between column width and initial soil depth when examining the steady state force? Can the peak force be predicted for a given column width?

To answer these questions and others it is helpful to look at a multi-dimensional plot. Overall there are three variables that change in these analyses: the column width, w_c, the initial soil depth, H_b, and the effective friction angle ϕ_F[8]. There is value in examining any pair of these variables in the x-y plane and plotting a corresponding scalar value (such as

[8]This list could be extended indefinitely to include additional variables. For example, the initial velocity could be varied, or the mechanical properties of the soil altered. This flexibility provides additional avenues of focus for future studies.

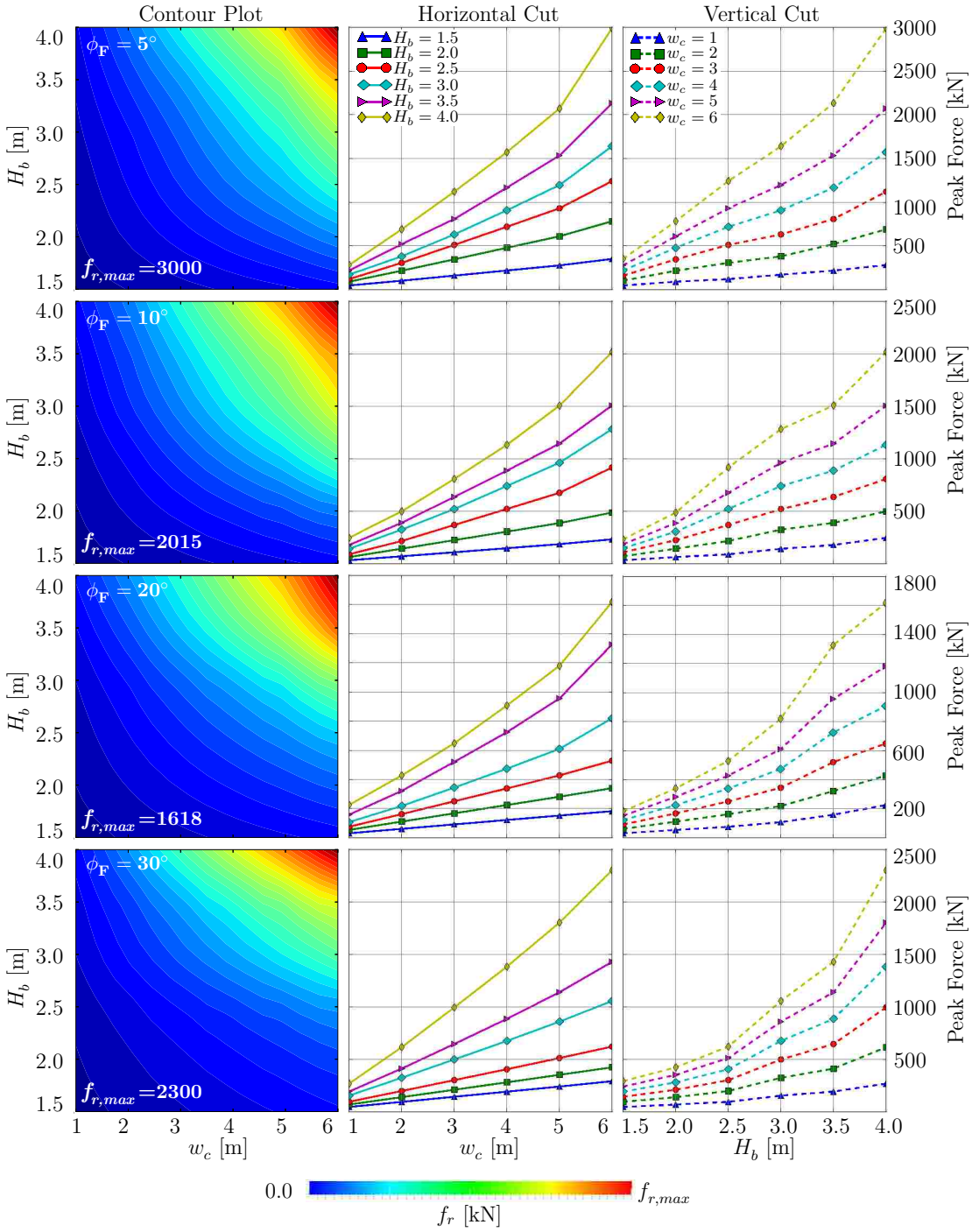

Figure 7.36: Peak force values as a function of column width, w_c, and initial height, H_b. Each row represents a single friction angle. The center and right columns are horizontal and vertical cuts, respectively, through the contour plot shown in the left column.

the peak force) in the third direction. When viewed in the x-y plane this effectively creates a contour plot. For example, Figure 7.36 shows a series of plots highlighting the variation in peak force as a function of column width and initial soil depth. Each row of plots represents a specified friction angle. The far left stack of images is the aforementioned contour plot. For these images the horizontal axis contains the column width and the vertical direction shows the dependence on initial soil depth. The colomap indicates the magnitude of the peak reaction force. Note that the peak value is different for each friction angle as identified by the $f_{r,max}$ label located in the lower left portion of each contour plot. The center and right stacks depict horizontal and vertical *slices*, or *cuts*, through the contour plot for a given row.

As a whole the the peak force behaves as expected; for a given soil depth the magnitude of the peak force increases as the column width increases. An equally valid but alternative interpretation is to consider a single column width. From this viewpoint the magnitude of the peak force increases as the depth of the soil increases. Regardless of interpretation, the results are in agreement with physical intuition. This observation is reassuring and helps to establish the MPM as a valid tool for recovering the reaction force in this context.

The other raw force measure of interest is the magnitude of the steady state force. This value is computed from the data set for each analysis using the modified moving average technique outlined earlier. In Figure 7.37 the steady state force values are shown in relation to column width, w_c, and initial height, H_b. Each row of plots represents a specified friction angle. The left, center, and right columns depict the the contour plot as well as the corresponding horizontal and vertical slices, respectively. A series of observations are made here that recount the peak force discussion. As a whole the steady state magnitudes agree with physical intuition—that is, increasing the column width and/or the initial soil depth leads to a higher steady state force value. For smaller friction angles ($\phi_F \lesssim 10^\circ$) there is a high degree of symmetry with respect to column geometry and initial height. This relation diminishes as the soil friction angle increases. For the 30° and 40° (not shown) analyses, the link between height and steady state force is verging on quadratic, whereas the link is linear with respect to column width.

According to Figure 7.35 the magnitude of the steady state force is relatively constant for a given height and column width. That is, the friction angle has little influence on the final values for a given set of geometry parameters. A similar observation is made here. In Figure 7.37 the relative scale is nearly identical for all friction angles. This is in stark contrast to the peak force values shown in Figure 7.36, where there is a significant disparity

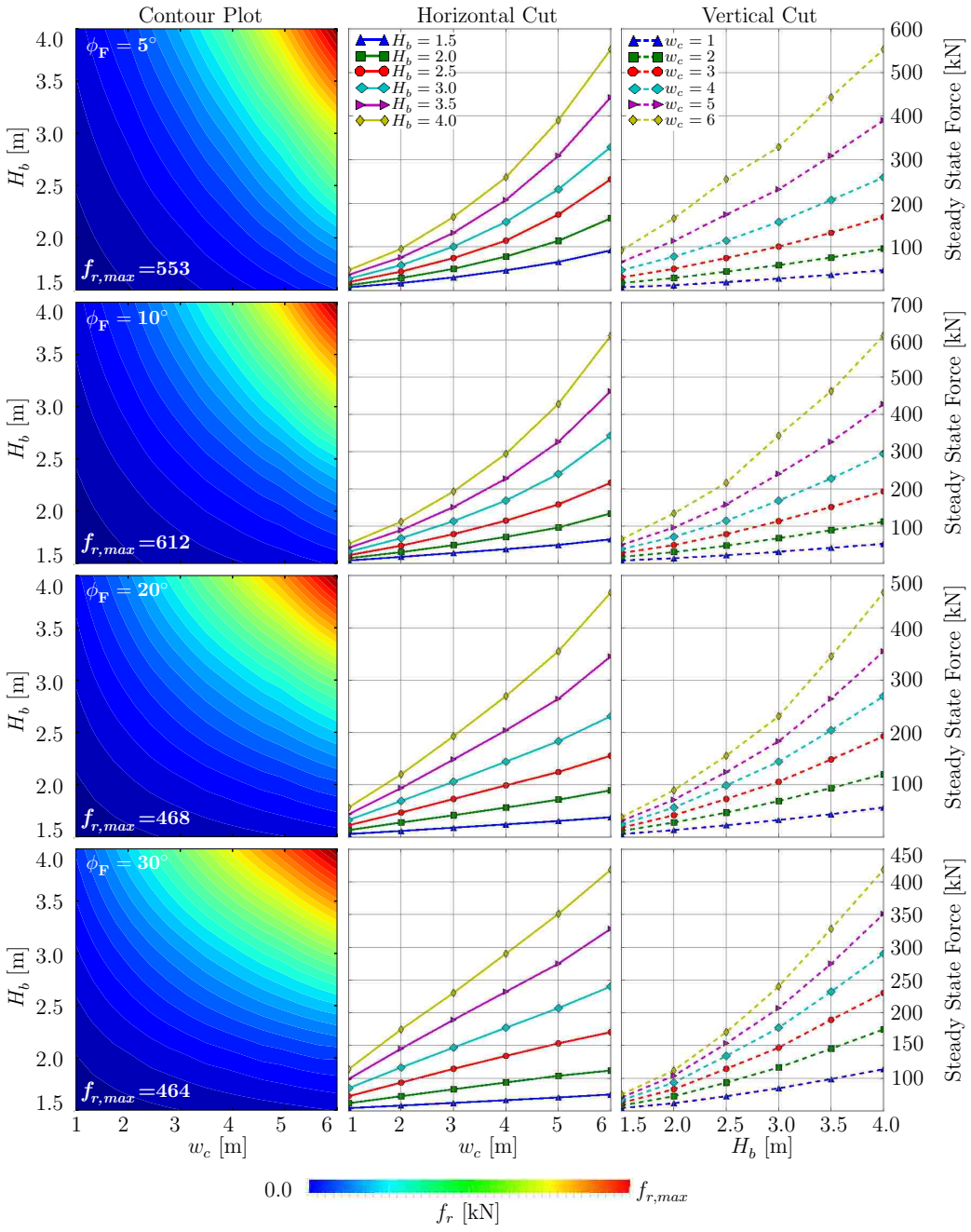

Figure 7.37: Steady state force values as a function of column width, w_c, and initial height, H_b. Each row represents a single friction angle. The center and right columns are horizontal and vertical cuts, respectively, through the contour plot shown in the left column.

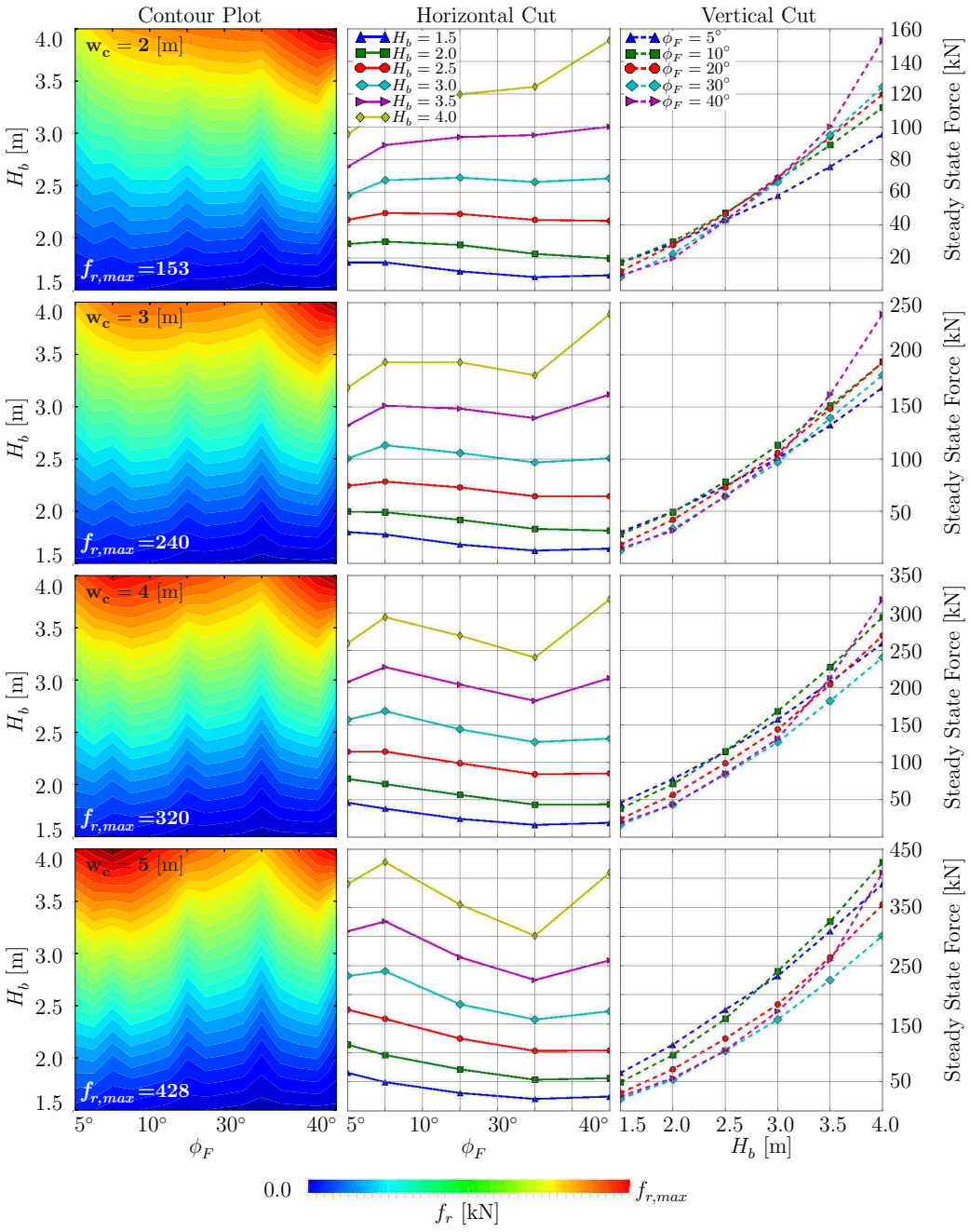

Figure 7.38: Steady state force values as a function of friction angle, ϕ_F, and initial height, H_b. Each row represents a different column width. The center and right columns are horizontal and vertical cuts, respectively, through the contour plot shown in the left column.

in the range of forces and a strong dependence on friction angle[9]. The steady state force magnitudes are examined from an alternative viewpoint in an effort to isolate the effect of friction angle. Figure 7.38 shows how the steady state force value varies as a function of friction angle, ϕ_F, and initial height, H_b. In this configuration each row of plots represents a specified column width. From an engineering perspective this alternative presentation is appealing—as column geometry is likely to be specified regardless of soil parameters and surge geometry. From this figure it is clear that the steady state force is a function of only the initial depth. This reasoning follows from the fact that lines collapse upon themselves for a given column width, w_c, as shown on the right side of Figure 7.38. This trend is confirmed by examining the center column of plots[10].

So far the focus has been on actual force magnitudes. If the end goal of an analysis is to determine the net force effects due to a flow event, then the types of results presented thus far are sufficient. However, parametric studies of this nature are often beneficial for their ability to identify trends and develop predictive models for general design procedures. It is to this end that the focus now shifts.

The study of flow around/over an immersed body is one of the pillars of fluid mechanics. Of particular emphasis is categorizing and quantifying the dynamic force interaction between the body and flow. This is accomplished by expressing the net force as

$$f = \rho_0 \, v^2 \, A \, C \, , \tag{7.13}$$

where f is the force magnitude [N], ρ_0 is the initial mass density [kg/m^3], v is the upstream (initial) velocity [m/s], and A [m^2] is the characteristic area of the object interacting with the flow. When the force coefficient of interest is parallel to v—as is the present case—A is most often taken to be the frontal area, or the projected area of the immersed body perpendicular to the flow direction, Munson et al. (2002); Panton (2005). The empirical factor C is a dimensionless quantity that is a function of several variables, including the fluid properties as well as the object geometry and roughness. The product $\rho_0 \, v^2$ is the

[9]Figures 7.36 and 7.37 could potentially benefit by having the same force scale for each figure. However, doing so diminishes the readers ability to spot the shape of the underlying trend and are more beneficial in their current form.

[10]A word of caution regarding trends as a function of friction angle: while it is tempting to use Figure 7.38 and similar plots to identify underlying tendencies, it also is dangerous and potentially misleading—as different materials are being compared. Different materials obviously have different responses to mechanical forces; the underlying mechanisms can be drastically different over the range of friction angles considered here. It is not rational to compare, say, a fluid-like soil to concrete. However, both responses can be achieved with the current material model simply by changing the effective friction angle.

dynamic pressure. In traditional fluid mechanics the dynamic pressure is usually proceeded by a factor of 1/2. Here this factor is absorbed in C.

The current study assumes the characteristic area is the area of the flow projected onto the column, i.e., $A = w_c\, H_b$. Equation (7.13) is used to identify C_{pk} and C_{ss}, the peak and steady state force coefficients, respectively, from the relations

$$C_{pk} = \frac{f_{pk}}{\rho_0\, v^2\, w_c\, H_b} \qquad \text{and} \qquad C_{ss} = \frac{f_{ss}}{\rho_0\, v^2\, w_c\, H_b}\ . \tag{7.14}$$

The terms f_{pk} and f_{ss} are the peak and steady state force magnitudes presented in Figures 7.36 and 7.37.

Figure 7.39 presents the peak force coefficients defined in Equation $(7.14)_1$ as a function of column width and initial soil height. For lower friction angles ($\phi_F \lesssim 10^\circ$) the contour plots appear to have a symmetry about the diagonal. As a result the peak force coefficients have a linear dependence with both the column width and body hight. As the friction angle of the material increases the contour plots change their shape—much more so than previously observed with the force magnitudes. In particular, the peak force coefficients become constant with column width. This trend is identified by the nearly flat plot lines associated with each soil height. Moreover, the vertical spacing between each soil height is more uniform. This leads to the very well defined curves shown for $\phi_F = 20^\circ$ and $\phi_F = 30^\circ$ in the lower right portion of Figure 7.39. The coefficients for each column width are collapsing to form a single curve that is linear in H_b. A unique curve is highly-sought in this context and indicates the underlying relationship between column geometry, initial height, and peak force is well defined. Here a least-squares fit or simple average could suffice to describe the evolution of C_{pk} for $\phi_F \gtrsim 20^\circ$. For $\phi_F \lesssim 20^\circ$ the coefficients are not as well behaved and a discernible trend is not as easily identified.

The steady state force coefficients, C_{ss}, defined in Equation $(7.14)_2$ are displayed in Figure 7.40. These coefficients form a very well behaved series of plots. Again the flow-like states have a dependence on both w_c and H_b. From the center column it is apparent for the $\phi_F = 5^\circ$ and $\phi_F = 10^\circ$ cases that the steady state force coefficients are linear or quadratic in w_c. Regardless of their shape, the spacing between each soil height is very consistent. The uniformity of the height spacing remains as the friction angle increases. For the 30° and 40° (not shown) cases the steady state dependence on column width is all but eliminated—leading to a C_{ss} that is only a function of H_b. This is shown in the lower right portion of Figure 7.40. For both the $\phi_F = 20^\circ$ and $\phi_F = 30^\circ$ analyses the points fall on a single, linear line. Although the coefficients for the flow-like states do not collapse to a single line they maintain a very regular structure/shape.

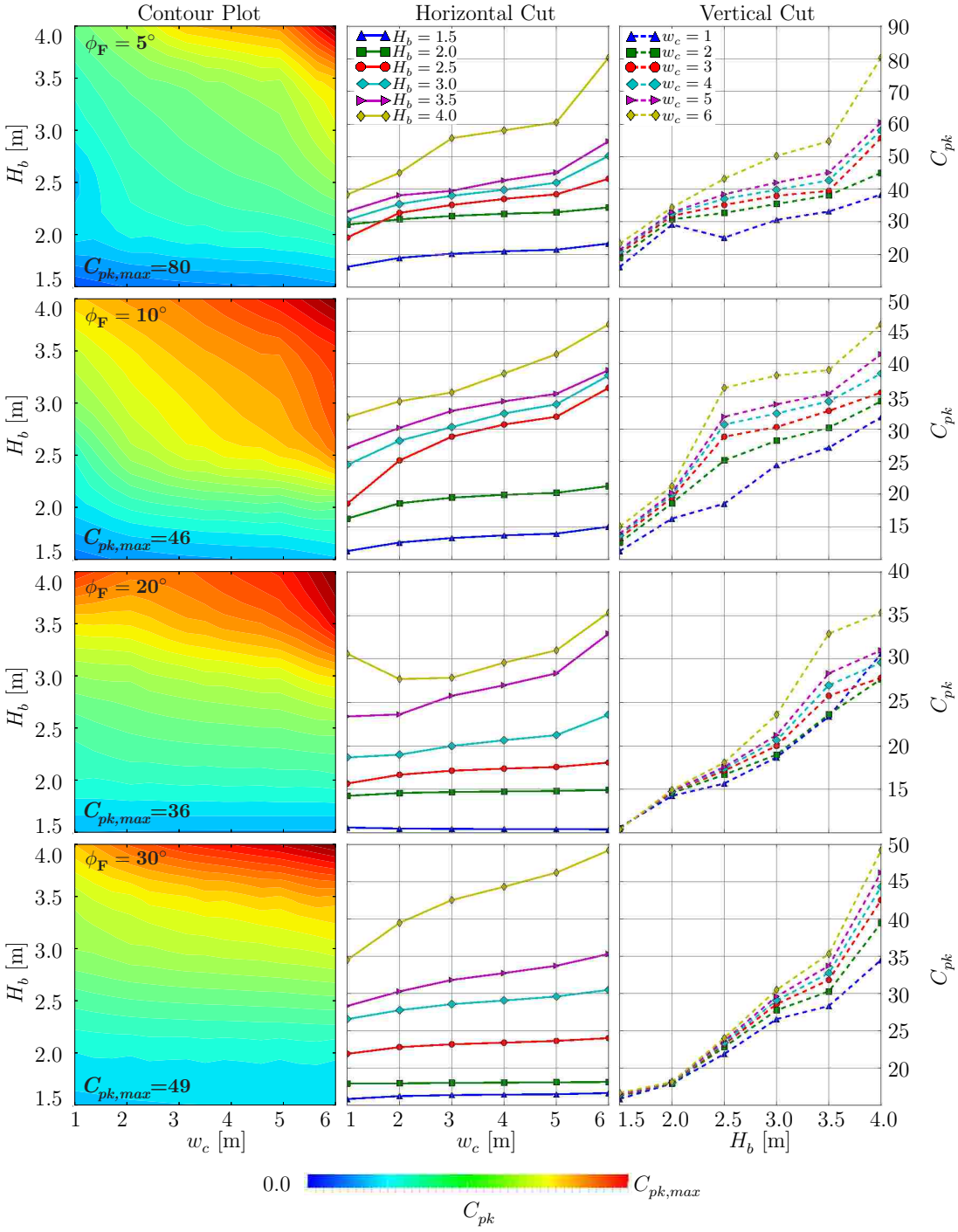

Figure 7.39: Peak force coefficients, C_{pk}, as a function of column width, w_c, and initial height, H_b. Each row represents a single friction angle. The center and right columns are horizontal and vertical cuts, respectively, through the contour plot shown in the left column.

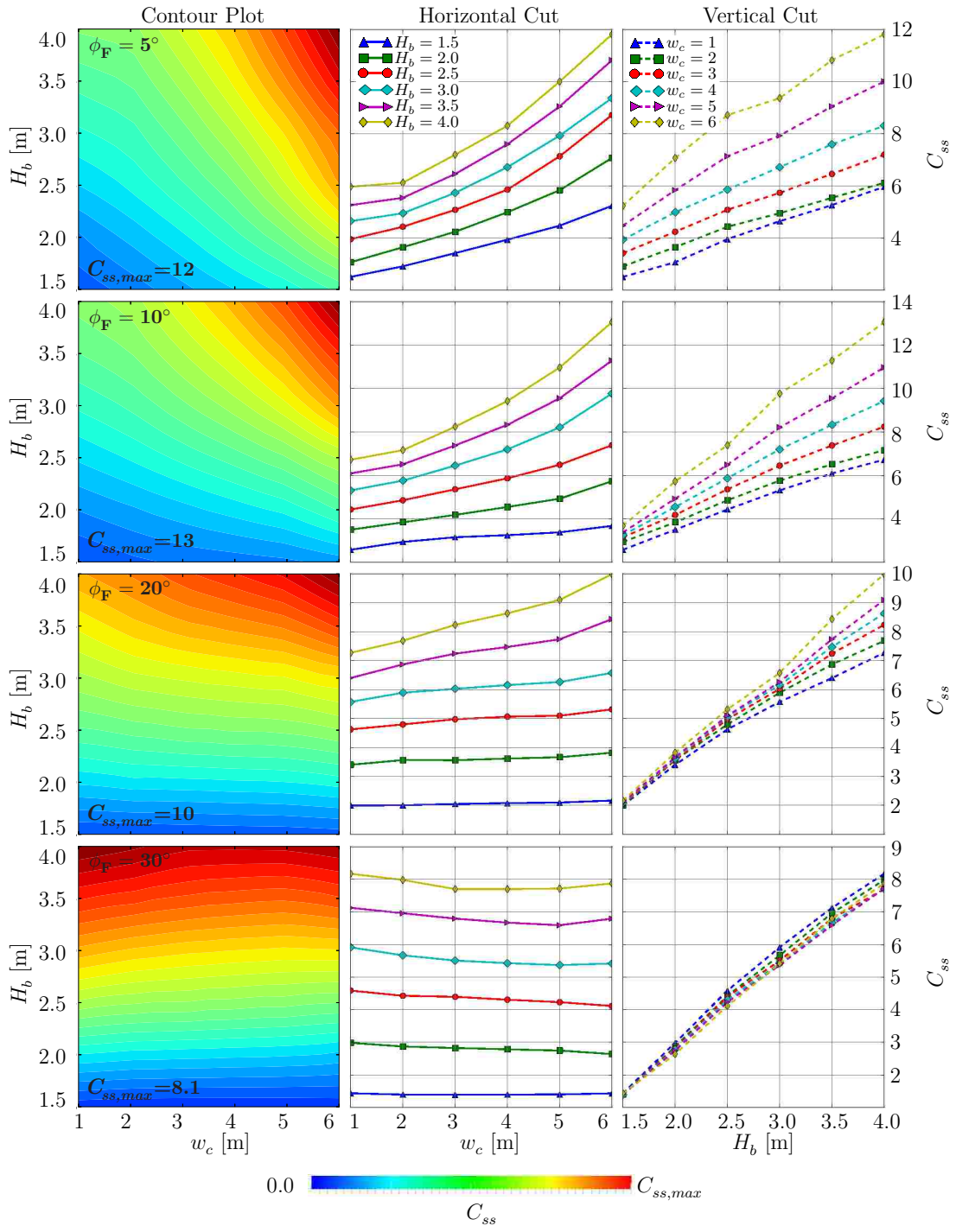

Figure 7.40: Steady state force coefficients, C_{ss}, as a function of column width, w_c, and initial height, H_b. Each row represents a single friction angle. The center and right columns are horizontal and vertical cuts, respectively, through the contour plot shown in the left column.

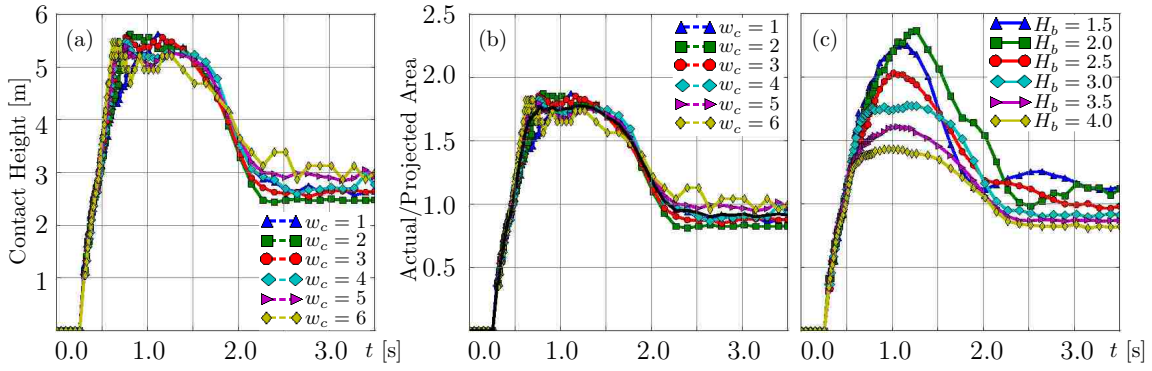

Figure 7.41: Comparison of actual contact geometry to initial values. (a) The height of soil in contact with barrier for $H_b = 3.0$ and $\phi_F = 5°$. (b) Ratio of actual contact to projected area for $H_b = 3.0$ and $\phi_F = 5°$. (c) Average ratio of actual contact to projected area for all soil depths and $\phi_F = 5°$.

The trends identified in Figures 7.39 and 7.40 indicate the presence of an underlying trend linking the column forces to soil geometry and material properties. These values have been computed using the characteristic area as the area of the flow projected onto the column, i.e., $A = w_c\, H_b$. However, depending on the friction angle, this area can be grossly inaccurate; the analyses using higher friction angles do not experience the same fluid like state as their lower friction angle counterparts. As a result the actual contact area is typically much less than the initial flow depth projected onto the column. On the other end of the spectrum, highly fluid-like soil flows experience a large splash and significant increase in contact area. Thus, there is merit in looking at the actual depth of the soil surge in contact with the column/wall. This is accomplished by tracking the nodes that make up a contact face. The net contact area is the sum of the nodal contact areas. For cubic cells of dimension $h_x = h_y = h_z = h$, the contact area for node i is $A_i = h^2$. The actual soil depth at the column face is determined using

$$H_{act} = \frac{\sum_i^m A_i}{w_c} = \frac{A_{act}}{w_c}\,, \tag{7.15}$$

where m is the nodes that make up the contact face and contain mass. Here an additional parameter is identified, A_{act}, which represents the actual area in contact at any given time.

In Figure 7.41(a) the actual contact height, H_{act} [m], is shown for an initial depth $H_b = 3.0$ [m] and friction angle $\phi_F = 5°$. This figure includes all column widths. At the outset of the analyses and prior to contact, the depth of the surge on the column is 0.0. As time goes on things begin to change. Initially there is a sharp increase in the depth as the soil makes contact. The depths continues to grow until it reaches a peak of approximately

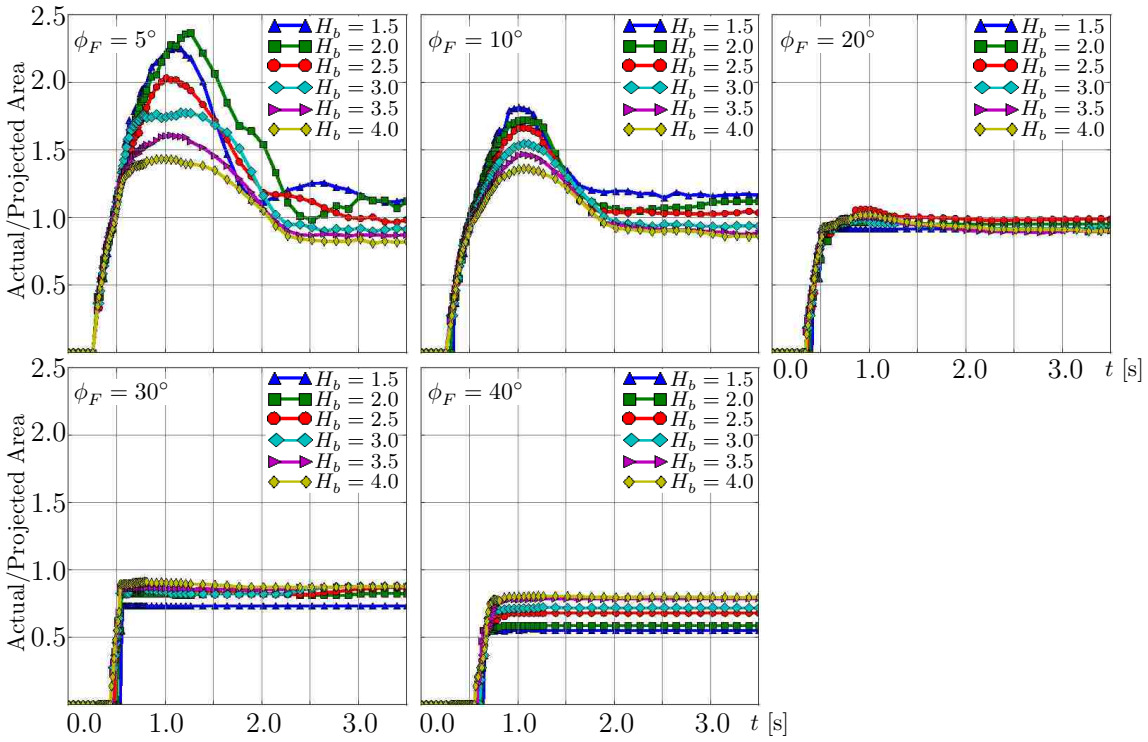

Figure 7.42: Comparison of actual contact geometry to initial values. Average ratio of actual contact to projected area for all soil depths and all friction angles examined.

5.5 [m]. The values decline until they steady off around 3.0 [m]. There are a few key observations to be discussed here. First, the height of the soil surge is nearly constant regardless of column width. Second, the sharp increase in height beyond the initial depth is really nothing more than a splash as the surge hits the interface. Plots of this nature can be used to identify which materials splash on contact with the structure. Finally, tracking the contact height allows the depth of the surge during the steady state interaction to be determined. For this particular friction angle the steady state soil depth is essentially the same as the initial depth. This is indicative of a true fluid-like response.

Figure 7.41(b) is introduced to show how the changing depth affects the net contact area. Here the actual to projected area ratio

$$A_{ratio} = \frac{A_{act}}{A} = \frac{A_{act}}{w_c\, H_b} \tag{7.16}$$

is plotted. Again, these plots are for $H_b = 3.0$ [m] and friction angle $\phi_F = 5°$. The ratio for each column width appears to collapse to a single curve. Taking the average of the area ratios for each column width, at each point in time, yields a master curve for the actual to projected area ratio for a given friction angle. This value is plotted as the solid black

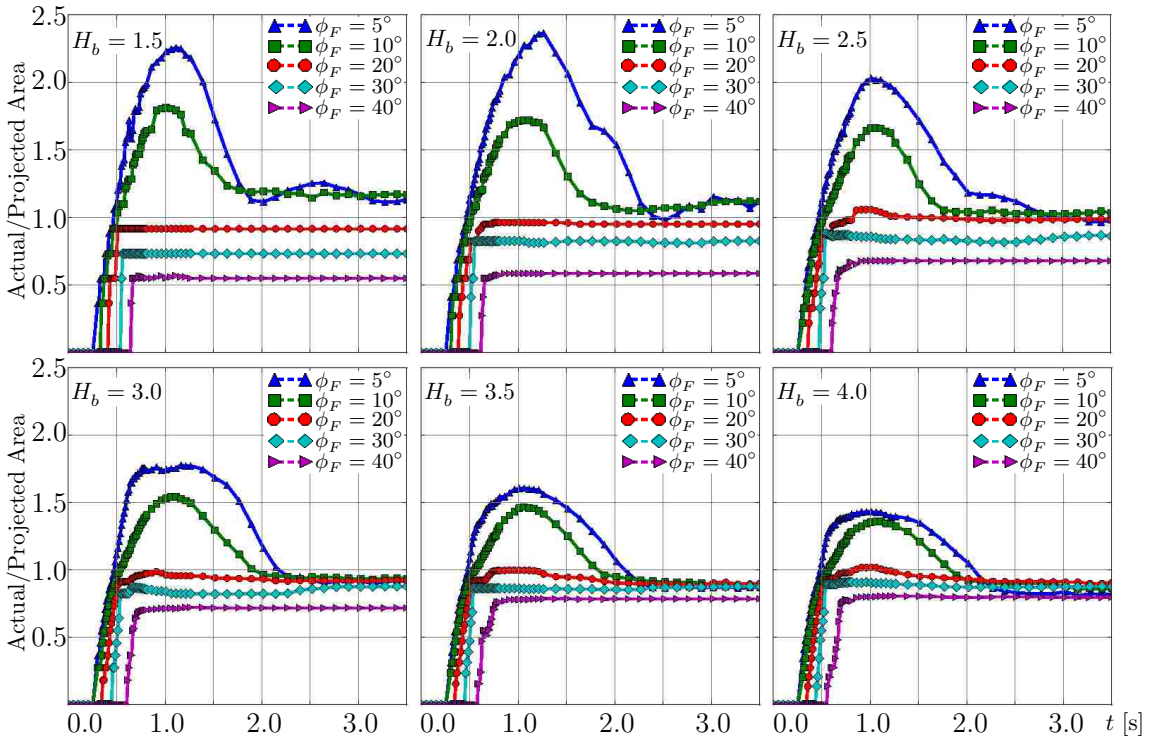

Figure 7.43: Comparison of actual contact geometry to initial values. Average ratio of actual contact to projected area for all soil depths and all friction angles examined.

line in Figure 7.41(b). In a similar manner a master curve is computed for each initial soil depth examined in this study. Collectively all the curves are displayed in Figure 7.41(c). This single figure is valid for $\phi_F = 5°$.

The actual to projected area ratios are shown in Figures 7.42 and 7.43. In Figure 7.42 the curves are grouped according to friction angle. Each individual subplot shows the ratio's dependence on initial height, H_b, as a function of time. Here it is easy to identify the $\phi_F = 20°$ as a pseudo demarcation value separating a liquid-like response and a more traditional granular flow. For friction angles less than 20° a splash occurs as indicated by an area ratio greater than 1.0. Friction angles of 5°, 10° and 20° experience a steady state depth essentially equal to the initial flow depth, as indicated by $A_{ratio} \approx 1.0$. Contrary to this finding are those with $\phi_F > 20°$. These cases experience a reduction in contact area as the majority of the mass comes to a stop before interacting with the column. In some cases the contact area is reduced from the projected area by as much as 50%, although the reduction is typically closer to $25\% - 35\%$. An alternative presentation of the same data is provided in Figure 7.43. There the area ratios are grouped by initial height, H_b. In general, for the fluid-like states, the increase in contact area is inversely related to initial depth; i.e.,

a more shallow soil surge has a larger relative splash compared to an initially deeper surge. This finding is somewhat counterintuitive.

The primary advantage of tracking the contact area is that the soil depth is realized during steady state conditions. This depth provides yet another measure to correlate with to the peak and steady state force magnitudes presented earlier. In an effort to tie these dynamic forces to something familiar, the static equivalent force per column length is computed as

$$b_{st} = \frac{1}{2} K_0 \rho_0 |\mathbf{g}| H_{act}^2 \ . \tag{7.17}$$

The term K_0 is coefficient of at-rest earth pressure and represents the ratio of horizontal to vertical stress. Often times for granular material this coefficient is expressed as a function of ϕ_F. Here, however, the material parameters listed in Table 7.10 dictate this value as $K_0 = 0.429$. The leading coefficient of 1/2 follows from the assumption of a triangular force distribution against the column (Das, 1984). Using Equation (7.17) the net, or total static force equivalent acting on a column of width w_c is computed according to

$$f_{st} = b_{st} w_c = \frac{1}{2} K_0 \rho_0 |\mathbf{g}| H_{act}^2 w_c. \tag{7.18}$$

Equation (7.18) represents the net force a dry soil mass of depth H_{act} would exert on the structure in static conditions. And, more importantly, it provides a reference quantity by which the dynamic peak and steady state forces can be compared to. The two ratios

$$R_{pk} = \frac{f_{pk}}{f_{st}} \qquad \text{and} \qquad R_{ss} = \frac{f_{ss}}{f_{st}} \tag{7.19}$$

are defined for the peak and steady state force magnitudes depicted in Figures 7.36 and 7.37, respectively.

The peak ratio is plotted in Figure 7.44 as a function of column width and initial height H_b. The fact that no discernible trend is apparent in the contour plots is not problematic—as the peak ratios are more or less constant for all friction angles. The steady state ratio R_{ss} is plotted in Figure 7.45. Again, these values are tending towards a relatively narrow range, indicating the equivalent static force parameter is ideal for normalization. Further examination of Figures 7.44 and 7.45 indicates that, as a whole, the analyses with $H_b = 1.5$ [m] and $w_c = 1.0$ [m] are causing significant deviation in the force ratios and something is amiss. It is presumed that these two data series are suffering from refinement issues—as they both represent the course end of their respective spectrum. For the remainder of this discussion these values, as well as the single series of results with $H_b = 4.0$ and $\phi_F = 5.0$ are omitted. Obviously removing questionable data from a given set is ill

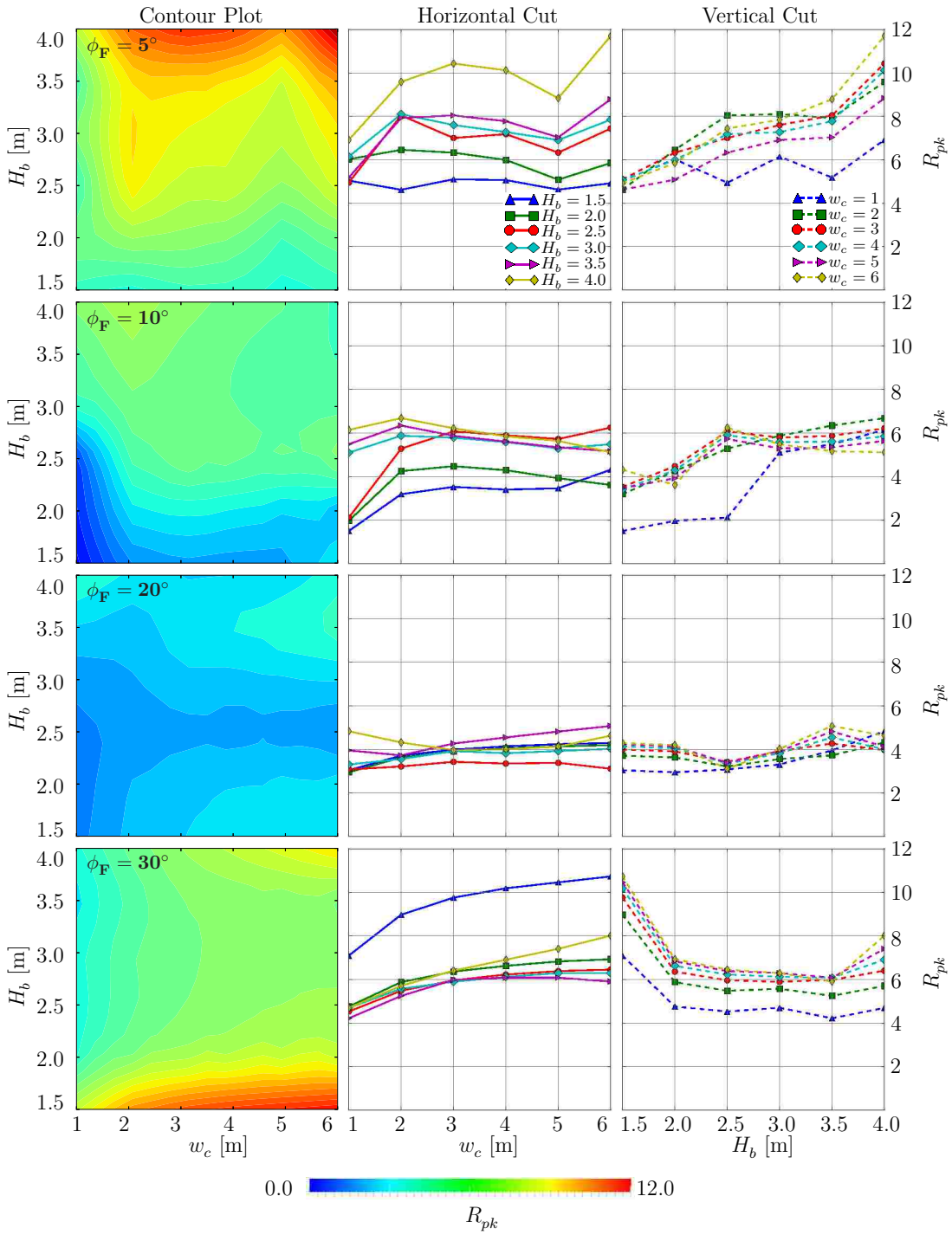

Figure 7.44: Ratio of peak force to static equivalent, R_{pk}, as a function of column width, w_c, and initial height, H_b. Each row represents a single friction angle. The center and right columns are horizontal and vertical cuts, respectively, through the contour plot shown in the left column.

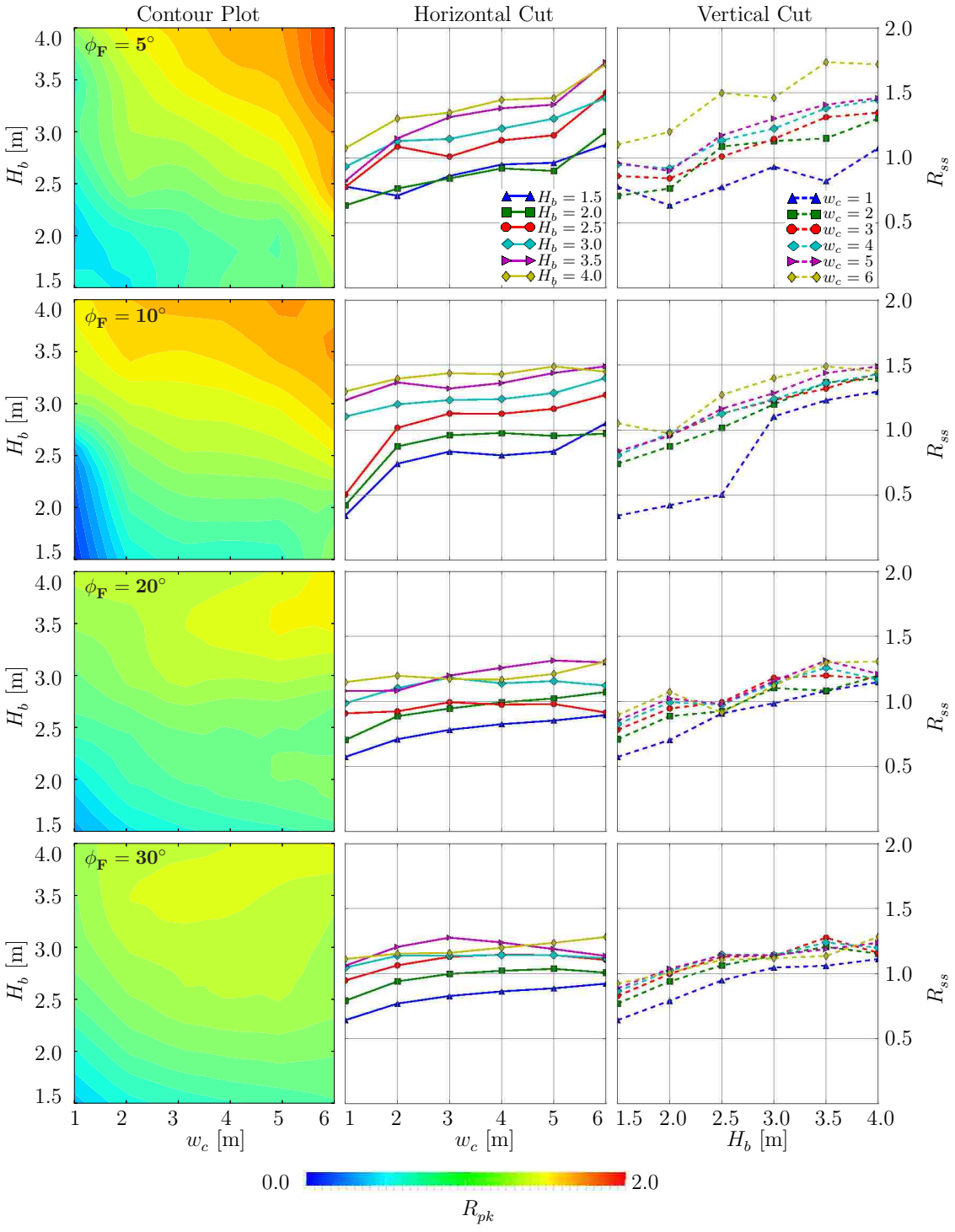

Figure 7.45: Ratio of steady state force to static equivalent, R_{ss}, as a function of column width, w_c, and initial height, H_b. Each row represents a single friction angle. The center and right columns are horizontal and vertical cuts, respectively, through the contour plot shown in the left column.

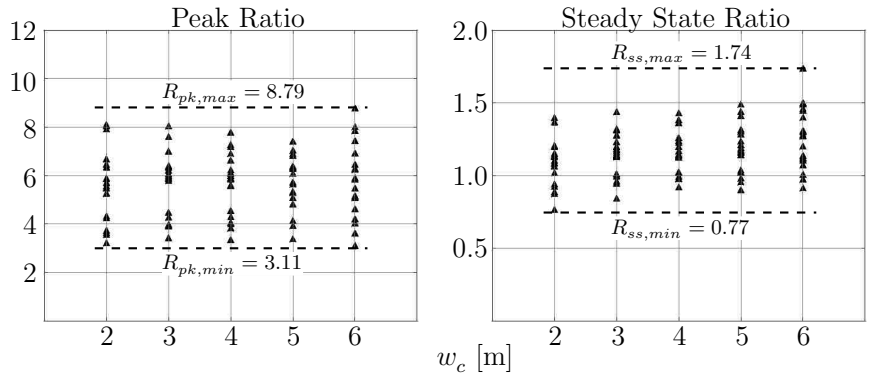

Figure 7.46: Peak and steady state to static force equivalent for select data points.

advised. However, these exclusions represent a small portion of the data set and experience shows that the MPM can yield poor results for no obvious reason.

The remaining data series are collected and plotted in Figure 7.46. This points represent all friction angles and all initial heights (save the omitted sets previously discussed). The R_{pk} coefficients are shown on the left hand side. All the peak ratios fall between $3-9$ times the static force. In an ideal world this range would be smaller, but nonetheless provides valuable insight into the magnitude of the peak reaction force compared to a commonly used quantity. The static coefficients are, not surprisingly, lumped in a much narrower range centered just above 1.0. This is welcome news—as it verifies the steady state force is similar to the static equivalent. Cross checking with Figure 7.45 shows that most of the cases with $R_{ss} < 1.0$ have narrow column widths, i.e., $w_c \lesssim 3.0$. This causes a reduction in force as the flow goes around the column as opposed to resting against it. The fact that $R_{ss} > 1.0$ for some cases means one of two things. Either the impact is amplified beyond the static equivalent due to inertia—as the $\phi_F \lesssim 20^\circ$ cases are not actually static even thought the steady state force is constant—or the actual force distribution is not triangular in nature, as Figure 7.33 shows is possible. If the actual force distribution is somewhere between constant and triangular, then normalizing using Equation (7.18) will amplify the steady state ratio.

7.4.3 Conclusions

The primary goal of this study was to evaluate the magnitude of the forces imparted on the rigid column/wall due to a soil surge. The column geometry, initial soil depth, and material properties were varied in an effort to isolate key relationships amongst these variables and the net column force. This goal has been met and Figures 7.33–7.38 highlight the nature,

shape, orientation, and magnitude of the column forces during the soil-structure interaction. Some general observations are listed below.

- The column/wall experiences a definitive peak and steady state (constant) force during the interaction. The existence of a constant force does not imply a static flow state.
- Peak and steady state force magnitude increase linearly with column size.
- Peak and steady state force magnitude increases linearly with initial depth for $\phi \lesssim 10°$. For friction angles greater than 10° the magnitude tends to increases quadratically.
- The steady state force magnitude is largely independent of friction angle.

In addition to the column forces the soil particles themselves provide great data. The velocity, stress, and total deformation fields are displayed in Figures 7.30–7.32. The ability to maintain these quality fields throughout the simulation exemplifies the MPM's ability to bridge the gap between solid- and fluid-like behavior for history dependent, large deformation analyses.

A secondary goal was to identify force related measures that aid in the development of predictive models for general design procedures. Initially two coefficients were discussed: C_{pk} and C_{ss}. These values are plotted in Figures 7.39 and 7.40. In both cases trends were beginning to take shape for the various parameters investigated. Both C_{pk} and C_{ss} were based off A, the initial projected frontal area of the soil. Figures 7.41–7.43 show that the actual area in contact with the column, A_{act}, can be quite different than the projected area A. This observation motivated the definition of a static equivalent net force, f_{st}, which was used as a normalization factor. This yielded the coefficients R_{pk} and R_{ss} which represent the expected increase in the dynamic forces compared to their static state counterparts. These are appealing coefficients in that the static force is a tangible quantity more easily realized than alternative measures. These latter coefficients are plotted in Figures 7.44–7.46.

The trends identified in this section for C_{pk}, C_{ss}, R_{pk} and R_{ss} highlight the potential for using the MPM as a predictive tool for identifying and quantify debris flow loadings on rectangular columns. Clearly this study is preliminary and significant steps need to be taken to validate and expand the results base before any additional conclusions can be drawn. This includes studies examining the effects of initial velocity, as well as studies investigating alternate material and MPM parameters, such as particles per cell, time step, and/or cell size. Ultimately the numerical results need to be validated experimentally before any real progress can take place.

Several additional results have not been presented in the interest of space. In most cases the omitted findings do not provide any additional insight beyond what has already been shown. Notable omissions include the coefficients $C_{pk,actual}$ and $C_{ss,actual}$ which are

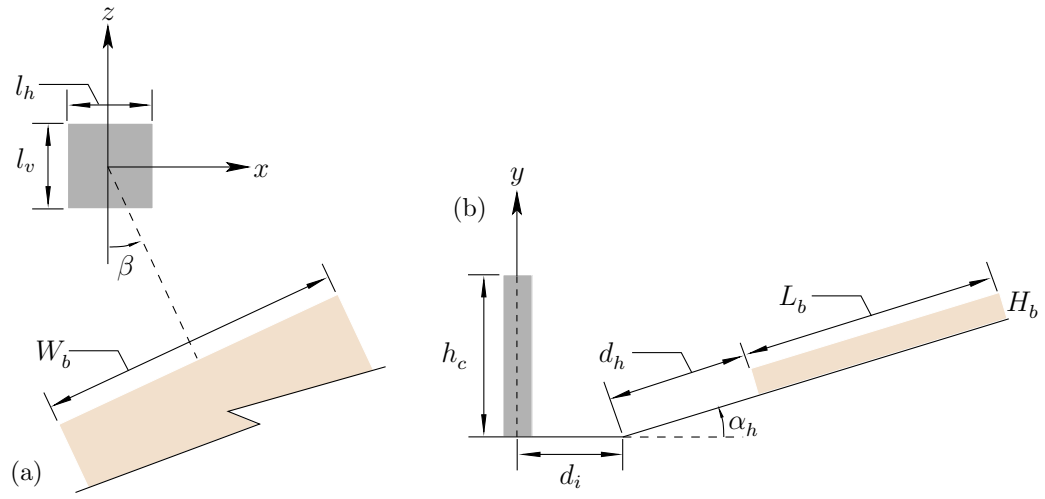

Figure 7.47: Schematic drawing of a debris flow approaching a column at an arbitrary angle. (a) Plan view. (b) Side view.

based on the actual area, A_{act}, as opposed to the initial projected frontal area, and the ratio f_{pk}/f_{ss} (and consequently C_{pk}/C_{ss}).

A final note regarding this study: one of the major focal points has been the peak force exerted on the column. From the design standpoint of protective structures this is the value of interest; the steady state force is more or less irrelevant. Unfortunately the steady state force trends are more consistent/uniform than the peak force data. This is due in part to cell crossing issues that arise from linear shape functions on the background grid as the surge initiates contact with the column. In particular, certain geometric configurations artificially inflate the peak force, and refinement can actually exacerbate the issue, as this increases the number of cell crossings. The cell-based anti-locking formulation presented in Chapter 4 can help mitigate this problem but provides little-to-no assistance at the edge of the body—where the reaction force is occurring. An extensive amount of time was invested in reducing the artificial inflation of the peak force values due to the cell crossing phenomenon . Preliminary studies identified that approximating the volumetric portion of the strain fields using a node-based approach significantly improved this problem and afforded reasonable results. For this reason a node-based anti-locking strategy was employed for this study despite the increased time overhead.

7.5 Soil-Column Impact: Varying Approach Angle

The gravity field modification described in Section 7.3.1 yields several additional analysis capabilities that were previously dismissed due to the restrictions imposed by a regular grid.

Table 7.11: Initial soil configuration for bi-planar domain description.

Description	Symbol	Value
Soil length, [m]	L_b	8.0
Soil width, [m]	W_b	4.0
Soil depth, [m]	H_b	4.0
Slope angle [deg °]	α_h	25.0
Approach angle [deg °]	β	$0°, 15°, 30°, 45°, 60°, 75°, 90°$
Hill length [m]	d_h	10.0
Column distance from hill [m]	d_i	4.75
Column height [m]	h_c	8.0
Vertical column length [m]	l_v	1.5
Horizontal column length [m]	l_h	1.5

The technique is used to emulate a hillside whose slope varies with global position. Here the feature is taken a step further by introducing an additional directional dependence. The plan view shown in Figure 7.47 identifies an approach angle β, which, when coupled with the hill slope α_h, grants additional freedom in capturing a soil-column interaction. In the present case the gravitational body force is modified to read

$$\mathbf{g} = g\ (\sin\alpha_h\ \sin\beta\,\mathbf{i} - \cos\alpha_h\ \mathbf{j} + \sin\alpha_h\ \cos\beta\ \mathbf{k})\ , \tag{7.20}$$

where g is the magnitude of the initial gravity vector. In Figure 7.47 the hill slope, α_h, is assumed to vanish at a radial distance d_i from the center of the column.

The goal of this analysis is to capture the force interaction between the single column and the granular flow. For the time being only the flow angle, β, is varied in increments of 15° on or between the baseline values of $\beta = 0°$ and $\beta = 90°$. Depending on the soil geometry, there is a potential line of symmetry about the diagonal $\beta = 45°$. However, this line is more or less ignored in the current study and a full $\beta = 90°$ rotation of the soil mass is explored. The smooth, two surface tension cap material model of Section 3.6.2 is used in concert with a cell-based anti-locking technique. In this study only the volumetric portion of the deformation field[11] is approximated using the anti-locking approach identified

[11]In terms of global behavior, it turns out that approximating the strain field is all that is necessary to obtain desirable results and realize most of the benefits of the anti-locking routines. That is, approximating the stress field in addition to the strain leads to nearly indistinguishable kinematics in most scenarios and effectively doubles the computational overhead. By eliminating the stress approximation, the benefits of the anti-locking algorithms are optimized in terms of performance and realized benefits. Of course the stress field

Table 7.12: Material and MPM parameters for angled granular flow simulation.

Description	Symbol	Value(s)
Macroscopic density, [kg/m^3]	ρ_0	1950.55
Bulk modulus, [Pa]	K	$8.33\,(10)^6$
Shear modulus, [Pa]	G	$3.85\,(10)^6$
Friction angle, [deg°]	ϕ_F	15°
Yield stress, [Pa]	μ	500
Associativity	ϱ_G/ϱ_F	0.025
Time step, [s]	Δt	$5.00\,(10)^{-4}$
Duration, [s]	t_f	10.0
Cell size, [m]	$h_x = h_y = h_z$	0.25
Particles per cell	PPC	15.625 (average)

in Chapter 4. The geometric and material parameters are listed in Table 7.11 and 7.12, respectively.

7.5.1 Velocity Field and Dynamic Description

The interaction is shown in Figure 7.48 at $t = 2.50\ s$ for all angles considered in this study. This plan view depicts the flow wrapping around the column in an aesthetically pleasing fashion. The resulting spray pattern is similar for each angle. In Figure 7.49 a sequence of images shows the flow progression as a function of time. The slide front reaches a peak velocity shortly before impact at $t = 1.25\ s$. The contact and splash are observed at both $t = 2.50\ s$ and $t = 3.50\ s$. By the time $t = 5.0\ s$ the granular medium is coming to rest. Those regions of the flow opposite of the impact faces have settled and the accumulation of the remaining matter is propagating back up the hill as seen in the snapshot with $t = 7.50\ s$. The final deposit is shown in the last image, where the nearly static state at $t = 10.00\ s$ conforms nicely with the desired domain geometry.

7.5.2 Force Interaction

The reaction force that develops as a result of the soil-column interaction is of interest as has been the case with several of the studies discussed in this dissertation. The reaction

is not quite as smooth as it would be if an approximation is constructed, but it does represent a significant improvement to what the standard algorithm is capable of providing. As noted previously, if the goal is to only visualize a smooth stress field, then averaging techniques exist that will make even the standard MPM stress field look good.

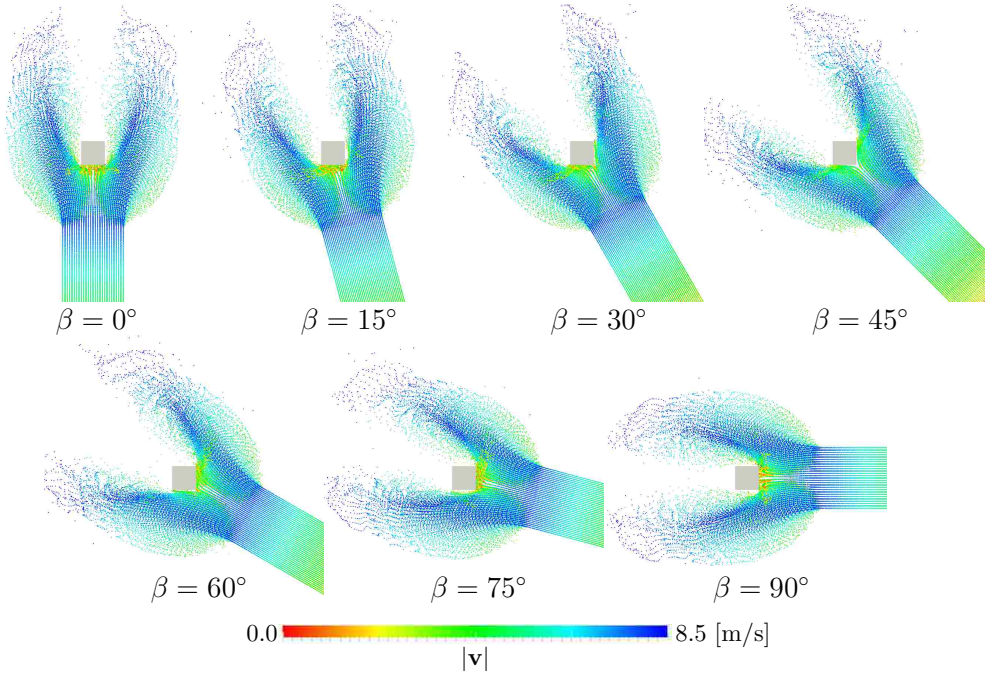

Figure 7.48: Plan view of the particle velocity magnitude for varying approach angles. The snapshot coincides with the time that the peak reaction force occurs.

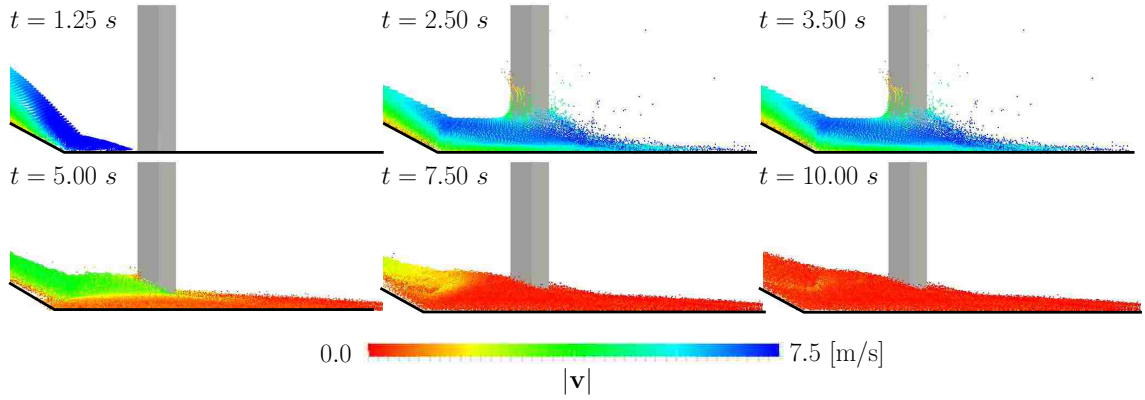

Figure 7.49: Side view of impact for $\beta = 30°$.

force vectors are shown in Figure 7.51 for select approach angles. The upper row of images highlights the distribution from an isometric vantage point while the lower row depicts the same data in plan view. In both cases the black arrow indicates the initial flow direction. These values correspond to $t = 2.50\ s$ which, as will be shown shortly, represents (approximately) the time in which the net column force is at a peak. As a whole these forces are consistent with previous observations and are in line with intuitive notions regarding the behavior of the interaction. The face bearing the brunt of the impact experiences larger

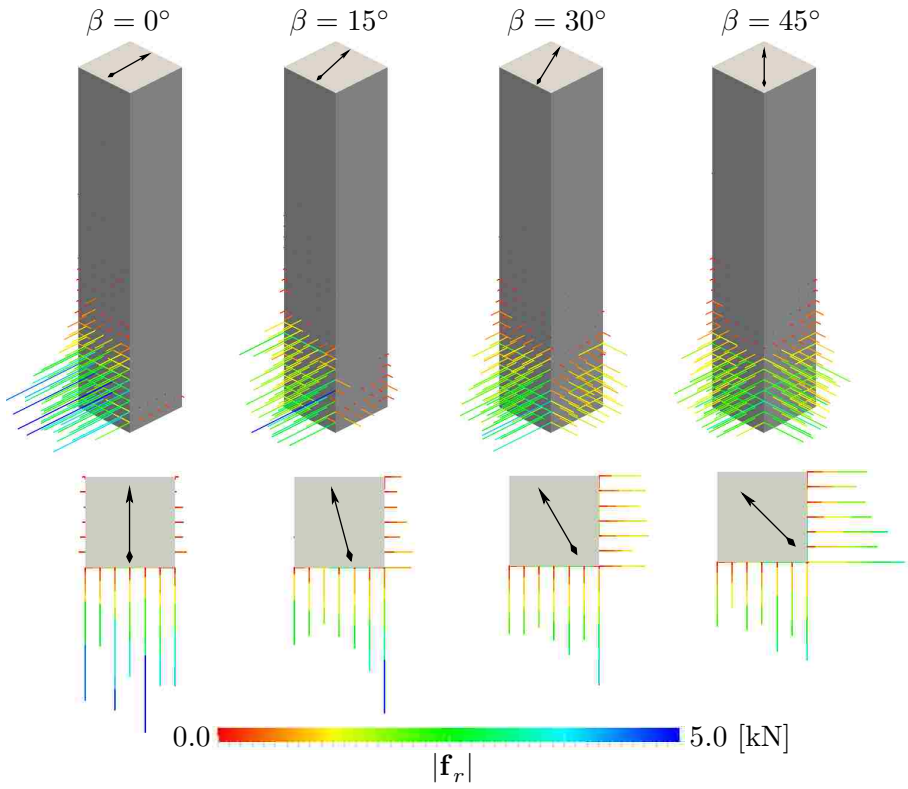

Figure 7.50: Reaction force distribution for $\beta = 0.0° - 45°$. The upper row is an isometric view and the lower row a plan view. The arrow indicates the flow direction around the column.

forces. As the flow pattern approaches the symmetric case of $\beta = 45°$, the vectors exhibit a high degree of symmetry and the distribution is nearly identical on both impact faces.

Summing the net reaction force for all nodes comprising the column leads to the plots shown in Figure 7.51(a). Again the force response can be categorized by a peak and steady state value. This trend will always be present when an impact occurs between a flow and resisting structure. As was discussed at the end of Section 7.4.3, the standard MPM or any cell-based averaging scheme leads to artificially inflated reaction forces. This is not due to an inherent flaw in the formulation, rather, this is due to known issues regarding linear shape functions at the edge of a body. Thus, one way of dealing with this artificial increase when cell-based averaging schemes are used is to apply a smoothing filter over the original force signal. This results in the smooth force depicted next to the original signal in Figure 7.51(a). Obviously the peak force will be diminished when any averaging scheme is used. There are, however, several acceptable options that do a very good job in maintaining the integrity of the original signal while eliminating outlying fluctuations. In addition to the

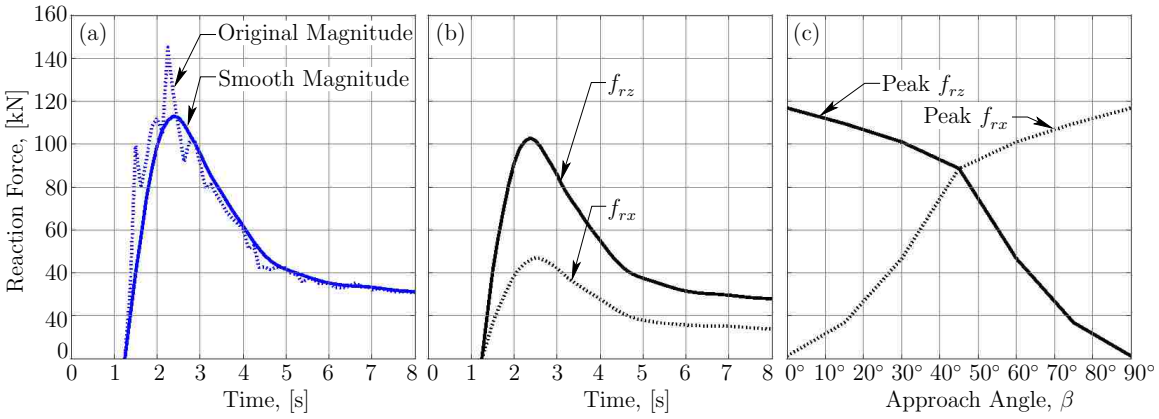

Figure 7.51: Reaction force comparison. (a) Reaction force magnitude before and after smoothing as a function of time. (b) The x and z components of the reaction force as a function of time for $\beta = 30°$. (c) Peak force as a function of approach angle.

traditional constant moving average, linear and exponential averaging schemes exist that weight each point differently. This topic is largely out of the current scope but is nonetheless an avenue worth pursuing at some point should this work continue forward.

This study provides an opportunity to decompose the net reaction force into the x- and z-components. The values for f_{rx} and f_{rz} are plotted in Figure 7.51(b) for the $\beta = 30°$ case. These plots depict a smoothed version of the original signal. Plotting the peak values for f_{rx} and f_{rz} for each approach angle considered yields Figure 7.51(c). Here a high degree of symmetry is observed as there should be. While the net magnitude of each case is nearly identical, there is a considerable difference in the component values. For example, a $\beta = 45°$ reduces the force components by more than 25%. Such a reduction could potentially have large design implications for columns in the path of debris flows.

7.5.3 Conclusions

This study highlighted another facet of the body force modification technique originally presented in Section 7.3.1. By adding a second directional dependence in the form of the approach angle β, not only was a bi-planar slope described but a preferred flow direction emerged. The final result was a series of impacts directed around a square column. The flow wrapped around the column as the slide proceeded down the hill, eventually coming to rest in a static state consistent with the emulated geometry. The reaction force profiles were summed to obtain net total force curves. The effects of smoothing the original signal were displayed and the total force was decomposed into the corresponding x- and z-components. A high degree of symmetry was observed for the peak force values.

Among other things, this study identifies the benefits of an angled flow protector for columns and bents in the path of a moving mass, be it soils, snow, or liquid. A reduction in force components of more than 25% can be achieved simply by altering the orientation of a square column or ensuring an angled geometry in the path of the flow.

Chapter 8

CONCLUSIONS

This document provides a comprehensive discussion and applications of the Material Point Method, a numerical technique that is best suited for modeling history dependent materials in a dynamic, large deformation setting. The formulation tracks moving points relative to stationary nodes, and can be used to capture the behavior of both fluids and solids in a unified framework.

In this closing chapter conclusions about this work are identified and discussed following a brief summary of the dissertation. In general these conclusions are about the work as a whole and are not necessarily application specific. Each example presented in Chapters 6 and 7 contains concluding remarks and the reader is referred to these chapters for specific conclusions and future work regarding individual examples.

8.1 Summary

In Chapter 2 the method was outlined in moderate detail, providing a basic explanation along with implementation details for the standard framework. A comparison to other numerical techniques was made, in particular with regards to Smoothed Particle Hydrodynamics and the Discrete Element Method. The latter was made from the perspective of granular media, one of the key focal points throughout this dissertation. The overview chapter concluded with a literature review, highlighting past and current applications of the MPM and its close friend, the Generalized Interpolation Material Point method. Additional implementation details are given in Appendix B, where an overview of the computational framework is discussed. From a global perspective the code was broken down into three components: Pre-Processing, Model Analysis, and Post-Processing. Each component was addressed and a particular emphasis was placed on how to construct input files from the available features. Appendix B also contains example input files as well as instructions for viewing existing MPM simulations using ParaView.

Multiple material model considerations were identified in Chapter 3. This included a discussion of computational inelasticity, cast in terms of small and large deformations. The return mapping integration algorithm was discussed in detail and a general framework for isotropic media was outlined. Multiple material models were described for capturing the

response of isotropic solids, aggregates, composites, and cohesive-frictional materials, several of which are appropriate for simulating ductile metals, concrete, and various soils (most notably dry sands and gravels). The chapter concludes with biaxial and pure shear simulations.

Both Chapters 4 and 5 highlight enhancements to the Material Point Method algorithm. The latter provided an anti-locking strategy that helps mitigate the accumulation of fictitious strains that result from the use of linear shape function. This is accomplished by building separate approximations for the stress and strain fields in addition to displacement related fields. Three strategies were introduced: a cell- and node-based approach, followed by a third variant that effectively combines the first two strategies. The second major addition was a volume constraint for use in multiphase simulations. This technique was outlined in Chapter 5, where the background theory and implementation were discussed.

The culmination of all things MPM discussed in Chapters 2–5 resides in Chapters 6 and 7, where a series of examples shows the broad range of applications the Material Point Method is capable of modeling. The first of these two chapters focused exclusively on linear elastic applications, and included validation of both the anti-locking and volume constraint algorithms. The latter chapter emphasized the elastoplastic material models presented in Chapter 3 and included large-deformation ductile impact simulation, planar sand flow, snow and avalanche diversion, as well as debris flow interaction with protective structures. Many of the elastoplastic investigations were parametric in nature and attempted to identify key relationships between analysis parameters and values of interest.

8.2 Key Findings

Throughout Chapters 2–7 several noteworthy observations were made regarding MPM, its capabilities and limitations, and overall performance when applied to a broad spectrum of problem types.

8.2.1 Enhancements to the MPM

There is little doubt the single most valuable contribution this work provides to the academic community is the anti-locking framework discussed in Chapter 4. The extension is applicable to both elastic and elastoplastic materials and is essential for improving the kinematics and stress field for MPM simulations. Currently the approximation schemes allow the volumetric or full tensor field to be constructed of both the strain and stress measures. This is accomplished using a cell- or node-based approach, or a third variant that effectively combines the first two techniques. However, even this enhancements has its prac-

tical limitations and shortcomings. The Taylor Bar simulation of Section 7.1 indicates the computational overhead incurred by using the anti-locking extensions is not justified with the realized benefits of the full tensor approximation schemes. In general it is sufficient to use the volumetric approximation for both the stress and strain. This trend was observed for nearly all problems presented in Chapter 7. Here it is recommended that a cell based approach be used unless the reaction force at nodes is desired. For the latter case a node based approximation may be the best choice. Of course, it is always possible to fashion examples that contradict the claim that a volumetric approximation is all that is necessary. However, for those simulations the MPM is best suited to capture, i.e., large deformations and displacements of history dependent materials, this claim holds true.

Another enhancement was the volume constraint of Chapter 5. This extension was originally conceived to combat volume overloading of a spatial region that can occur due to the point-wise material point description. From a qualitative perspective, the physical basis for such a constraint was appealing, as it matched everyday intuitions regarding the physical world. However, there are limitations to what having an appropriate amount of matter in a given space can provide in a numerical context, and the expected capabilities of the volume constraint were shown to be unobtainable. Specific problems associated with this approach were identified final sections of Chapter 5.

Interestingly, in the author's experience with MPM and the coding framework, some of the most valuable extensions have followed from ad-hoc enhancements, quick fixes to problems that cannot be cast in terms of variational principals but follow from code hacks that have little or no theoretical justification. Often these tricks are the sole reason a particular analysis yields good results. This has been termed *technology* by those working close to the author, and there is reason to believe such technology is ever-present in any numerical analysts' tool belt. In the present case two such examples exist. The first being artificial viscous damping. Regardless of the anti-locking routine, cell size, time step, particle density, etc., linear elastic simulations must employ damping to control the propagation of stress waves and maintain valid stress fields. This is done using the `ViscousDamping` option described in Appendix B. The second critical enhancement is the `FrontSmoothing` option, responsible for detecting the edge of a body. The affected region(s) are updated using only kinematic field variables from time t_n to avoid problems associated with linear shape functions. Neither of these tricks are needed if using higher order shape functions. It is postulated here that the desired phase mixing and separation capabilities the volume constraint was intended to provide will be solved by ad-hoc extensions that use multigrid contact algorithms coupled with the appropriate phase volume fractions and mixture theories built using common grid

values (in addition to the individual phase motions).

8.2.2 Linear Elastic Simulations

The primary focus of Chapter 6 was to discuss a series of MPM simulations from fluid and solid mechanics. The different examples were designed to show the effectiveness of the anti-locking approach applied to a wide variety of problem types. Large deformation, nearly incompressible flow simulations were examined in order to validate the anti-locking strategy from a kinematic viewpoint. The ensuing pressure field and interaction between fluid and bounding surface were examined. It is apparent from this chapter that an anti-locking strategy is indispensable for modeling nearly incompressible flow. Failure to alleviate the fictitious stress and strains that accumulate in the standard implementation leads to nonphysical and unusable results. The anti-locking algorithms employed in these analyses successfully eliminate the volumetric locking and lead to improved findings with respect to all field variables, including the particle pressure and nodal/particle velocity. Here it was shown that the MPM with appropriate anti-locking extension is a valid tool for recovering or assessing the magnitude of the reaction force/traction between a body and a rigid surface.

On the solid mechanics end of the spectrum, MPM's ability to capture a linear elastic response for a material with finite shear stiffness was investigated in the form of free vibration. In particular, the effectiveness of the anti-locking approach presented in Chapter 4 was key to mitigating shear locking for a cantilever beam subjected to a prescribed velocity field. Both normal and shear stresses were successfully recovered, and represent a significant improvement over the standard MPM algorithm. The example also showed that the proposed anti-locking technique exhibits ideal convergence behavior. Volumetric locking in the context of solid mechanics was addressed by examining the algorithmic performance when approaching the incompressible material limit. A single anti-locking variant (ALCV) is identified that is capable of mitigating both shear and volumetric locking, making it an ideal candidate for both fluid and solid mechanics simulations when using linear elastic material models.

Chapter 6 also presented three examples highlighting the capabilities of the volume constraint algorithm. The saturated soil simulations were performed in a multigrid, multiphase framework. The 1D hydrostatic test cases produced accurate distributions of the constituent, bulk, and mixture stresses. Solid phase displacements were shown to converge to an analytical solution. The pressure head drawdown simulations showed how prescribed conditions could potentially be used to capture the liquefaction process. The drawdown examples emphasized the need for additional momentum exchange mechanisms beyond the

pressure obtained from the volume constraint algorithm; there it was shown that the alternative exchange processes are largely more important in a saturated soil context. The final example considered a 2D saturated panel subject to a distributed foundation loading. Pore pressure distribution and surface displacements were compared to the $u - p$ CMPM formulation and an FEM implementation using stabilized elements. All results compared favorably with respect to pore pressure.

8.2.3 Elastoplastic Simulations

A Taylor Bar Impact problem was used to validate the anti-locking routines in the nonlinear material regime. The deformed geometry and stress field were compared to results obtained using commercial Finite Element Method software. The anti-locking algorithms yielded higher quality results with respect to geometric parameters than the original algorithm with linear shape functions. Each anti-locking technique yielded very similar values that were consistent with the FEM model. This latter point should not be taken lightly; the FE model employs higher order shape functions that are not subject to locking. The locking free variants result in a net time increase on the order of 27%–294%. Comparing all aspects of the findings—geometric, mechanical fields, efficiency, etc.—a picture emerged that suggested the use of a full-tensor averaging technique is superfluous in a nonlinear material context. The volumetric averaging scheme, be it cell- or node-based, provides the same benefits at a significant reduction in cost. This observation is not limited to the Taylor Bar impact problem analyzed in this section.

A series of simulations were designed to show the MPM is a valuable tool for modeling granular flow and landslides when coupled with an appropriate constitutive framework. The first series of tests targeted a planar sand column collapse, where the MPM simulations reproduced key geometric observations from published experiments. These analyses identified the peak material strength as being the most influential factor in determining the final shape of the collapsed profile. In addition to the geometric aspects, it was shown that the MPM can be used to visualize other field variables of interest; the velocity and stress fields were used as examples but many other options exist. The reaction force between the planar surface and the body of sand was investigated and found to be parabolic in shape. A second problem modeled a series of earthen mounds as energy dissipating devices to protect civil infrastructure. The mounds proved to be quite efficient in impeding the flow, and the resulting interaction was captured by way of a reaction force field. This study shows the potential for the MPM in this context, and opens the door for several quantitative parametric studies of landslides. Also of importance from this study was the idea of a modified

gravitational field. By altering the direction of gravity—and in some cases the underlying normal boundary definition—complex surface shapes can be created within the confines of a regular grid.

The repetitive structure of the mounds described in the previous paragraph motivated a quantitative study identifying the underlying link between reaction force magnitude and geometric, material, and analysis parameters. To this end a parametric study consisting of 180 separate analysis was conducted, each evaluating the impact of a soil mass with a rectangular column. The column geometry and soil depth were varied, along with the soil properties. Two distinct force regimes were observed in the force profiles, namely, a peak force and steady state force. Several trends were identified between the flow parameters and these two force measures. A method establishing the ratio between the dynamic force magnitude and static design force was identified and found to be as high as 8. A final study investigated soil structure interaction by varying the approach angle of the flow as it impacts a lone column. The net force remains constant as the approach angle varies, yet the force components in the axis directions varied appropriately with the approach angle. This study identified the benefits of an angled flow protector for columns and bents in the path of a moving soil, snow, or liquid mass.

8.3 Moving Forward

This work has identified different research options for future students to pursue. The following discussion categorizes potential work by topic.

8.3.1 Computational Framework

By and large the current framework is a development code. As such the focus was always on adding features and capabilities. Considerable algorithmic issues that will arise if the intent is to move towards an efficiency-centric implementation using the existing code. This includes a troublesome transition to a parallel implementation with multiple processors or computational nodes for a single simulation. On the other hand, running serial simulations simultaneously has proven to be quite efficient and sufficient for the scale of analyses ran to date. Beyond this, additional parallelization should not be pursued until there is a significant need for speed up.

At one point there was talk of building an MPM specific GUI. The recent use of ParaView as largely negated the need for a specialized visualization environment. This software is advanced beyond what could feasibly be created and built specifically for viewing mechanics-based analyses; thus there is little benefit in building a custom GUI. All that being said, it

is possible to embed ParaView scenes and features in custom built applications. Such an approach is perhaps the most appropriate for the current situation if an MPM specific GUI is built. There would be considerable benefit in developing a custom particle discretization tool. That is, the ability to construct (or read in) arbitrary shapes and objects, then build a particle based discretization of these entities according to user specified parameters (particle density, max/min spacing, etc.).

Unfortunately the type of student capable of providing the computational extensions discussed in this subsection is more likely to be found outside of civil engineering. This may be an inaccurate statement. But at this point leaps in the coding framework are going to be achieved by someone who a.) is very knowledgeable in efficient programing techniques, or b.) already knows the MPM and can focus more on the efficient implementations as opposed to trying to develop code (while learning good programming as well) and learn the MPM at the same time.

8.3.2 Additional Capabilities

There is always room for improvement and additional simulation features. However, at this point features should be added for specific reasons. Before adding a feature there should be a sufficient need, or void, or hole, the current coding framework cannot meet.

There still remains a need for more general bounding surfaces within the current framework. As a first step, existing multigrid contact algorithms could be added. The code setup is well suited to handle this type of extension and would allow for particle based boundary definitions and multibody contact. Alternatively, an irregular grid could be utilized. This has already been addressed in this chapter but will allow for general boundary definitions. The larger issue with an irregular grid in the context of structural engineering is the perfectly rigid requirement imposed by the node-based boundary. This is unrealistic for a structure. Perhaps the best solution is to couple the MPM with FEM. There are existing strategies in place for this approach, and in the author's opinion will provide the most flexible framework for moving forward.

The use of higher order b-splines could also be quite beneficial if sticking with a regular grid (assumes FEM will be added to deal with boundaries). These shape functions are superior to the traditional quadratic element primarily because the don't reduce node spacing (and thus time step) and do not pose a problem with the lumped mass matrix. Furthermore, using such functions eliminates the locking phenomena associated with linear shape functions. Higher order shape functions also eliminate problems at the edge of a body and other stalwart problems like internal cell crossing errors that the anti-locking routines alone

cannot resolve. While there is no doubt an increase is incurred using higher order shape functions, in the author's opinion this additional computational cost is worth the better results in several situations.

8.3.3 Applications

It is the author's sincere hope that the coding framework is used more for additional applications in the future. These pages have demonstrated that even with the restrictions of a regular grid, a single phase, or with the simple material models employed in these studies, there are several opportunities to simulate complex engineering problems—problems that the MPM community finds interesting and problems that can benefit the geotechnical engineering community at large. Potential future studies include a debris flows and placing rigid objects in the flow path, a comparison of landslide runout to existing runout models, the use of MPM as a tool to assess the loads on pipeline structures, and additional parametric studies quantifying the force reaction between flows and columns.

In looking at the diverse applications of the MPM and observing trends in recent publications, it is only a matter of time until other researchers begin using the MPM to simulate landslide and debris flows in a context very similar to the work presented in this document. The immediate focus following this research should be on sharing existing findings and establishing the current MPM group at the University of Washington as team modeling landslides and debris flows and their interactions with structures.

BIBLIOGRAPHY

Manual on Estimating Soil Properties for Foundation Design (EPRI), 1990. Cornel University.

H. Alawaji, K. Runesson, S. Sture, and K. Axelsson. Implicit integration in soil plasticity under mixed control for drained and undrained response. *International Journal for Numerical and Analytical Methods in Geomechanics*, 16(10):737–756, 1992. ISSN 1096-9853.

U. Andelfinger and E. Ramm. EAS-elements for two-dimensional, three-dimensional, plate and shell structures and their equivalence to HR-elements. *International Journal for Numerical Methods in Engineering*, 36(8):1311–1337, 1993.

S. Andersen and L. Andersen. Analysis of spatial interpolation in the material point method. *Computers & Structures*, 88(7-8):506 – 518, 2010a.

S. Andersen and L. Andersen. Modelling of landslides with the material-point method. *Computational Geosciences*, 14:137–147, 2010b.

J. E. Andrade and X. Tu. Multiscale framework for behavior prediction in granular media. *Mechanics of Materials*, 41(6):652 – 669, 2009. ISSN 0167-6636.

P. Arduino, P. Mackenzie-Helnwein, and G. R. Miller. Modeling multi-scale flow using the material point method. In R. I. Borja, editor, *Multiscale and Multiphysics Processes in Geomechanics. Results of the Workshop on Multiscale and Multiphysics Processes in Geomechanics, Stanford, June 23–25, 2010*. Springer, 2011.

B. Ataie-Ashtiani and G. Shobeyri. Numerical simulation of landslide impulsive waves by incompressible smoothed particle hydrodynamics. *International Journal for Numerical Methods in Fluids*, 56(2):209 – 32, 2008. ISSN 0271-2091. URL `http://dx.doi.org/10.1002/fld.1526`.

N. J. Balmforth and R. R. Kerswell. Granular collapse in two dimensions. *Journal of Fluid Mechanics*, 538:399–428, 2005.

S. G. Bardenhagen. Energy conservation error in the material point method for solid mechanics. *J. Comput. Phys.*, 180(1):383–403, 2002. ISSN 0021-9991.

S. G. Bardenhagen and E.M. Kober. The generalized interpolation material point method. *Computer Modeling in Engineering & Sciences*, 5(6):477 – 495, 2004.

S. G. Bardenhagen, J. U. Brackbill, and D. Sulsky. The material point method for granular materials. *Computer Methods in Applied Mechanics and Engineering*, 187(3–4):529–541, 2000.

S. G. Bardenhagen, J. E. Guilkey, K. M. Roessig, J. U. Brackbill, W. M. Witzel, and J. C. Foster. An improved contact algorithm for the material point method and application to stress propagation in granular material. *Computer Modeling in Engineering & Sciences*, 2:509–522, 2001.

K.J Bathe. *Finite Element Procedures*. Prentice Hall, 1996.

T. Belytschko, Y. Krongauz, D. Organ, M. Fleming, and P Krysl. Meshless methods: An overview and recent developments. *Computer Methods in Applied Mechanics and Engineering*, Vol. 139: 3–47, 1996.

T. Belytschko, W. K. Liu, and B. Moran. *Nonlinear Finite Elements for Continua and Structures*. John Wiley & Sons, Ltd., West Sussex, England, 2000.

D. Benson. Computational methods in Lagrangian and Eulerian hydrocodes. *Computer Methods in Applied Mechanics and Engineering*, Vol. 99(2-3):235–394, 1992.

L. Beuth, T. Benz, and P. A. Vermeer. Large deformation analysis using a quasi-static material point method. *Journal of Theoretical and Applied Mechanics*, 38(1–2):45–60, 2008.

L. Beuth, Z. Wieckowski, and P. A. Vermeer. Solution of quasi-static large-strain problems by the material point method. *International Journal for Numerical and Analytical Methods in Geomechanics*, 2010. ISSN 1096-9853.

R. I. Borja, K. M. Sama, and P. F. Sanz. On the numerical integration of three-invariant elastoplastic constitutive models. *Computer Methods in Applied Mechanics and Engineering*, 192(910):1227 – 1258, 2003. ISSN 0045-7825.

J. U. Brackbill and H. M. Ruppel. Flip: A method for adaptively zoned, particle-in-cell calculations of fluid flows in two dimensions. *Journal of Computational Physics*, 65(2):314–343, 1986. ISSN 0021-9991.

R. L. Brown, T. E. Lang, W. F. St. Lawrence, and C. C. Bradley. A failure criterion for snow. *Journal of Geophysical Research*, 78(23):4950–4958, 1973. ISSN 2156-2202.

O. Buzzi, D. Pedroso, and A. Giacomini. Caveats on the implementation of the generalized interpolation material point method. *Computer Modeling in Engineering & Sciences*, 31(2):85 – 106, 2008.

S.-C. Chen, S.-H. Peng, and H. Capart. Two-layer shallow water computation of mud flow intrusions into quiescent water. *Journal of Hydraulic Research*, 45(1):13 – 25, 2007. ISSN 0022-1686.

W.F. Chen. *Constitutive Equations for Engineering Materials*, volume 1: Elasticity and Modeling. Elsevier, 1994a.

W.F. Chen. *Constitutive Equations for Engineering Materials*, volume 2: Plasticity and Modeling. Elsevier, 1994b.

Z. Chen, W. Hu, L. Shen, X. Xin, and R. Brannon. An evaluation of the MPM for simulating dynamic failure with damage diffusion. *Engineering Fracture Mechanics*, 69(17):1873 – 1890, 2002. ISSN 0013-7944.

C. Coetzee, P. Vermeer, and A. Basson. The modeling of anchors using the material point method. *International Journal for Numerical and Analytical Methods in Geomechanics*, Vol. 29(9):879–895, 2005.

N. Daphalapurkar, H. Lu, D. Coker, and R. Komanduri. Simulation of dynamic crack growth using the generalized interpolation material point (gimp) method. *International Journal of Fracture*, 143:79–102, 2007.

B. M. Das. *Principles of Foundation Engineering*. Wadsworth, Inc., 1984.

R.P. Denlinger and R.M. Iverson. Flow of variably fluidized granular masses across three-dimensional terrain. 2. numerical predictions and experimental tests. *Journal of Geophysical Research*, 106 (B1):553 – 66, 2001. ISSN 0148-0227.

S. Diebels and W. Ehlers. Dynamic analysis of a fully saturated porous medium accounting for geometrical and material non-linearities. *International Journal for Numerical Methods in Engineering*, 39(1):81–97, 1996. ISSN 1097-0207.

J. Donea, A. Huerta, J.-Ph. Ponthot, and A. Rodríguez-Ferran. *Arbitrary Lagrangian-Eulerian Methods*, chapter 14. John Wiley & Sons, Ltd., 2004.

T. P. Fries and H. G. Matthies. Classification and overview of meshfree methods. *Informatikbericht-Nr*, 2003-03.

M. G. Geers, R. L. Ubachs, R. A. Engelen, and W.A.M.Brekelmans. Large deformation gradient-enhanced hyperelasto-plasticity for ductile failure. Barcelona, Spain, 2000. European Congress on Computational Methods in Applied Sciences and Engineering (ECCOMAS), incorporating the VI International Conference on Computational Plasticity (COMPLAS VI).

J. Ghaboussi and R. Barbosa. Three-dimensional discrete element method for granular materials. *International Journal for Numerical and Analytical Methods in Geomechanics*, 14:451–472, 1990.

J. E. Guilkey and J. A. Weiss. Implicit time integration for the material point method: Quantitative and algorithmic comparisons with the finite element method. *International Journal for Numerical Methods in Engineering*, 57:1323–1338, 2003.

J.E. Guilkey, J.B. Hoying, and J.A. Weiss. Computational modeling of multicellular constructs with the material point method. *Journal of Biomechanics*, Vol. 39(11):2074 – 2086, 2006.

R.F. Guimaraes, R.A. Trancoso, G.E.O.A. De Carvalho Jr., N.F. Fernandes, E. Do Amaral Vargas Jr., and E.S. De Martins. Identification of the affected areas by mass movement through

a physically based model of landslide hazard combined with a two-dimensional flood routing model for simulating debris flow. In *International Geoscience and Remote Sensing Symposium (IGARSS)*, pages 3035 – 3038, Barcelona, Spain, 2008. URL `http://dx.doi.org/10.1109/IGARSS.2007.4423484`.

Y.J. Guo and J.A. Nairn. Calculation of J-integral and stress intensity factors using the material point method. *Computer Modeling in Engineering & Sciences*, 6:295–308, 2004.

Y.J. Guo and J.A. Nairn. Three-dimensional dynamic fracture analysis using the material point method. *Computer Modeling in Engineering & Sciences*, 1:11–25, 2006.

F. H. Harlow. Hydrodynamic problems involving large fluid distortions. *J. ACM*, 4(2):137–142, 1957. ISSN 0004-5411.

E. W. Heller. Extension of the material point method for the consideration of boundaries at arbitrary locations. Master's thesis, University of Washington, 2003.

P. Helnwein. Some remarks on the compressed matrix representation of symmetric second-order and fourth-order tensors. *Computer Methods in Applied Mechanics and Engineering*, 190(2223):2753 – 2770, 2001. ISSN 0045-7825.

L. M. Highland. Estimating landslide losses—preliminary results of a seven-state pilot project. Technical Report 2006:1032, USGS, http://pubs.usgs.gov/of/2006/1032/pdf/OFR-2006-1032.pdf, 2006.

Y. Higo, F. Oka, S. Kimoto, Y. Morinaka, Y. Goto, and Z. Chen. A coupled MPM-FDM analysis method for multi-phase elasto-plastic soils. *Soils and Foundations*, 50(4):515–532, 2010.

R. Hill. On constitutive inequalities for simple materials I. *Journal of the Mechanics and Physics of Solids*, 16(4):229 – 242, 1968a.

R. Hill. On constitutive inequalities for simple materials II. *Journal of the Mechanics and Physics of Solids*, 16(5):315 – 322, 1968b.

R. Hill. Constitutive inequalities for isotropic elastic solids under finite strain. *Proceedings of the Royal Society of London. Series A, Mathematical and Physical Sciences*, 314(1519):457–472, 1970.

R. D. Holtz and W. D. Kovacs. *An Introduction to Geotechnical Engineering*. 1981.

G. A. Holzapfel. *Nonlinear Solid Mechanics - A Continuum Approach for Engineering*. John Wiley and Sons Ltd, 2000.

H. Htike, W. Chen, Y. Gu, and J. Yang. Material point method with RBF interpolation. *Computer Modeling in Engineering & Sciences*, 72(4):247–272, 2011.

W. Hu and Z. Chen. A multi-mesh MPM for simulating the meshing process of spur gears. *Computers & Structures*, 81(20):1991–2002, 2003.

P. Huang, X. Zhang, S. Ma, and H.K. Wang. Shared memor OpenMP parallelization of explicit MPM and its application to hypervelocity impact. *Computer Modeling in Engineering & Sciences*, 38 (2):119–147, 2008.

P. Huang, X. Zhang, S. Ma, and X. Huang. Contact algorithms for the material point method in impact and penetration simulation. *International Journal for Numerical Methods in Engineering*, 85(4):498–517, 2011.

A. Huerta and F. Casadei. New ALE applications in non-linear fast-transient solid dynamics. *Engineering Computations*, Vol. 11(4):317–345, 1994.

T. R. Hughes. *The Finite Element Method: Linear Static and Dynamic Finite Element Analysis*. 1987.

R.M. Iverson and R.P. Denlinger. Flow of variably fluidized granular masses across three-dimensional terrain. 1. coulomb mixture theory. *Journal of Geophysical Research*, 106(B1):537 – 52, 2001. ISSN 0148-0227.

R.M. Iverson and J.W. Vallance. New views of granular mass flows. *Geology*, 29(2):115 – 118, 2001. ISSN 0091-7613. URL `http://dx.doi.org/10.1130/0091-7613(2001)029<0115:NVOGMF>2.0.CO;2`.

R.M. Iverson, J.E. Costa, and R.G. LaHusen. Debris-flow flume at H.J. Andrews Experimental Forest, Oregon, open-file report 92-483. Technical report, U.S. Geological Survey, 1992. http://vulcan.wr.usgs.gov/Projects/ MassMovement/Publications/OFR92-483.

P. V. Lade. *The stress-strain and strength characteristics of cohesionless soils*. PhD thesis, University of California, Berkeley, 1972.

P. V. Lade and J. M. Duncan. Elastoplastic stress-strain theory for cohesionless soil. *Journal of the Geotechnical Engineering Division*, 101(10):1037–1053, 1975.

E. Lajeunesse, A. Mangeney-Castelnau, and J. P. Vilotte. Spreading of a granular mass on a horizontal plane. *Physics of Fluids*, 16(7):2371–2381, 2004.

R. J. LeVeque. *Finite Difference Methods for Ordinary and Partial Differential Equations*. Society for Industrial and Applied Mathematics, 2007.

R. W. Lewis and B. A. Schrefler. *The Finite Element Method in the Static and Dynamic Deformation and Consolidation of Porous Media*. John Wiley and Sons Ltd, 1998.

Y.P. Lian, X. Zhang, X. Zhou, S. Ma, and Y.L. Zhao. Numerical simulation of explosively driven metal by material point method. *International Journal of Impact Engineering*, 38(4):238 – 246, 2011.

M.-L. Lin and K.-L. Wang. Seismic slope behavior in a large-scale shaking table model test. *Engineering Geology*, 86(2-3):118 – 133, 2006. ISSN 0013-7952. URL `http://dx.doi.org/10.1016/j.enggeo.2006.02.011`.

G.R. Liu. *Mesh Free Methods*. CRC Press, 2003.

G.R. Liu and M.B. Liu. *Smoothed Particle Hydrodynamics: A Meshfree Particle Method*. World Scientific Publishing Co., 2003.

E. Love and D. Sulsky. An energy-consistent material point method for dynamic finite deformation plasticity. *International Journal for Numerical Methods in Engineering*, 65(10):1608 – 1638, 2006a.

E. Love and D.L. Sulsky. An unconditionally stable, energy-momentum consistent implementation of the material-point method. *Computer Methods in Applied Mechanics and Engineering*, 195 (33-36):3903 – 3925, 2006b.

G. Lube, H. E. Huppert, R. S. J. Sparks, A. Freundt, and M. A. Hallworth. Axisymmetric collapses of granular columns. *Journal of Fluid Mechanics*, 508:175–199, 2004.

G. Lube, H. E. Huppert, R. S. J. Sparks, and A. Freundt. Collapses of two-dimensional granular columns. *Phys. Rev. E*, 72:041301, 2005.

J. Ma, Y. Liu, H. Lu, and R. Komanduri. Multiscale simulation of nanoindentation using the generalized interpolation material point (GIMP) method, dislocation dynamics (DD), and molecular dynamics (MD). *Computer Modeling in Engineering & Sciences*, 16(1):41 – 55, 2006a.

J. Ma, H. Lu, and R. Komanduri. Stuctured mesh refinement in generalized interpolation material point method (GIMP) for simulation of dynamic problems. *Computer Modeling in Engineering & Sciences*, 12(3):213 – 227, 2006b.

J. Ma, H. Lu, B. Wang, R. Hornung, A. Wissink, and R. Komanduri. Multiscale simulation using the generalized interpolation material point (GIMP) method and molecular dynamics (MD). *Computer Modeling in Engineering & Sciences*, 14(2):101 – 117, 2006c.

S. Ma and X. Zhang. Material point method for impact and explosion problems. In *Computational Mechanics*, pages 156–166. Springer Berlin Heidelberg, 2009. ISBN 978-3-540-75999-7.

S. Ma, X. Zhang, and X.M. Qiu. Comparison study of MPM and SPH in modeling hypervelocity impact problems. *International Journal of Impact Engineering*, 36(2):272 – 282, 2009.

X. Ma, P. T. Giguere, B. Jayaraman, and D. Z. Zhang. Distribution coefficient algorithm for small mass nodes in material point method. *Journal of Computational Physics*, 229(20):7819 – 7833, 2010a.

Z.T. Ma, X. Zhang, and P. Huang. An object oriented MPM framework for simulation of large deformation and contact of numerous grains. *Computer Modeling in Engineering & Sciences*, 55 (1):61–87, 2010b.

P. Mackenzie-Helnwein, P. Arduino, W. Shin, J. A. Moore, and G. R. Miller. Modeling strategies for multiphase drag interactions using the material point method. *International Journal for Numerical Methods in Engineering*, 83(3):295 – 322, 2010.

P. Mackenzie-Helnwein, P. Arduino, C. M. Mast, G. R. Miller, and W. Shin. Landslide and debris-flow induced static and dynamic loads on protective structures—modeling framework within the Material Point Method. In *National Science Foundation Engineering Research and Innovation Conference, Atlanta, GA., Jan. 4–7*, page 14 pages, 2011. 14 pages.

L. E. Malvern. *Introduction to the Mechanics of a Continuous Medium*. Prentice Hall, 1969.

J. E. Marsden and T. J. R. Hughes. *Mathematical Foundations of Elasticity*. Prentice-Hall, 1983.

J.C. Martin and W.J. Moyce. Part IV: An experimental study of the collapse of liquid columns on a rigid horizontal plane. *Philosophical Transactions of the Royal Society of London*, Vol. 244: 312–324, 1952.

C. M. Mast. Extension of the material point method for the consideration of boundaries at arbitrary locations. Master's thesis, University of Washington, December 2008.

C.M. Mast, P. Mackenzie-Helnwein, P. Arduino, G.R. Miller, and W. Shin. Mitigating kinematic locking in the material point method. *Journal of Computational Physics*, 231(16):5351 – 5373, 2012.

H. Matsuoka and T. Nakai. Stress-deformation and strength characteristics of soil under three different principal stresses. *Proceedings, JSCE*, (232):59–70, 1974.

H. Matsuoka and T. Nakai. A new failure criterion for soils in three-dimensional stresses. International Union of Theoretical and Applied Mechanics (IUTAM) Symposium on Deformation and Failure of Granular Materials, Aug. 31- Sep. 3 1982.

H. Matsuoka and T. Nakai. Relationship among tresca, mises, mohr-coulomb and matsuoka-nakai failure criteria. *Soils and Foundations*, 25(4):123–128, 1985.

S. McDougall and O. Hungr. A model for the analysis of rapid landslide motion across three-dimensional terrain. *Canadian Geotechnical Journal*, 41(6):1084 – 1097, 2004. ISSN 0008-3674. URL `http://dx.doi.org/10.1139/T04-052`.

ChristopherR. McGann, Pedro Arduino, and Peter Mackenzie-Helnwein. Stabilized single-point 4-node quadrilateral element for dynamic analysis of fluid saturated porous media. *Acta Geotechnica*, 7:297–311, 2012. ISSN 1861-1125.

Shuji Moriguchi, Ronaldo I. Borja, Atsushi Yashima, and Kazuhide Sawada. Estimating the impact force generated by granular flow on a rigid obstruction. *Acta Geotechnica*, 4(1):57–71, 2009. ISSN 1861-1125.

B. R. Munson, D. F. Young, and T. H. Okiishi. *Fundamentals of Fluid Mechanics*. John Wiley and Sons Ltd, 2002.

J. A. Nairn. Material point method calculations with explicit cracks. *Computer Modeling in Engineering & Sciences*, 4:649–664, 2003.

F. Nicot. Constitutive modelling of snow as a cohesive-granular material. *Granular Matter*, 6:47–60, 2004. ISSN 1434-5021. doi: 10.1007/s10035-004-0159-9.

X.-F. Pan, A.-G. Xu, G.-C. Zhang, P. Zhang, J.-S. Zhu, S. Ma, and X. Zhang. Three-dimensional multi-mesh material point method for solving collision problems. *Communications in Theoretical Physics*, 49(5):1129–1138, 2008.

R. L. Panton. *Incompressible Flow*. John Wiley and Sons Ltd, 2005.

K. Petek. *Development and Application of Mixed Beam-Solid Models for Analysis of Soil-Pile Interaction Problems*. PhD thesis, University of Washington, Seattle, WA, 2006.

J. J. Petrovic. Review mechanical properties of ice and snow. *Journal of Materials Science*, 38:1–6, 2003. ISSN 0022-2461.

F. Radjai and F. Duboi. *Discrete-element Modeling of Granular Materials*. Wiley, 2011.

S. S. Rao. *Applied Numerical Methods for Engineers and Scientists*. Prentice Hall, 2002.

D. Rees. *Basic engineering plasticity: an introduction with engineering and manufacturing applications*. Elsevier, 2006.

M.E. Reid, D.L. Brien, R.G. LaHusen, J.J. Roering, J. De La Fuente, and S.D. Ellen. Debris-flow initiation from large, slow-moving landslides. In *International Conference on Debris-Flow Hazards Mitigation: Mechanics, Prediction, and Assessment, Proceedings*, volume 1, pages 155 – 166, Davos, Switzerland, 2003.

A. Sadeghirad, R.M. Brannon, and J. Burghardt. A convected particle domain interpolation technique to extend applicability of the material point method for problems involving massive deformations. *International Journal for Numerical Methods in Engineering*, 86(12):1435–1456, 2011a.

A. Sadeghirad, R.M. Brannon, and J. Burghardt. A convected particle domain interpolation technique to extend applicability of the material point method for problems involving massive deformations. *International Journal for Numerical Methods in Engineering*, 86(12):1435–1456, 2011b.

B. Salm. Mechanical properties of snow. *Reviews of Geophysics*, 20(1):1–19, 1982. ISSN 1944-9208.

S.B. Savage and R.M. Iverson. Surge dynamics coupled to pore-pressure evolution in debris flows. In *International Conference on Debris-Flow Hazards Mitigation: Mechanics, Prediction, and Assessment, Proceedings*, volume 1, pages 503 – 514, Davos, Switzerland, 2003.

H. L. Schreyer, D. L. Sulsky, and S. J. Zhou. Modeling delamination as a strong discontinuity with the material point method. *Computer Methods in Applied Mechanics and Engineering*, 191(23-24): 2483 – 2507, 2002.

B. R. Seth. *Generalized strain measure with applications to physical problems.* Defense Technical Information Center, 1961.

L. Shen. A rate-dependent damage/decohesion model for simulating glass fragmentation under impact using the material point method. *Computer Modeling in Engineering & Sciences*, 49(1): 23–45, 2009.

L. Shen and Z. Chen. A silent boundary scheme with the material point method for dynamic analyses. *Computer Modeling in Engineering & Sciences*, 7(3):305–320, 2005.

W. Shin. *Modeling Mixing and Separation of Solid Matter and Fluid in Landslides and Debris Flows by Representing the Multiphase Material through Distinct Phases.* PhD thesis, University of Washington, Seattle, WA, 2009.

W. Shin, G. R. Miller, P. Arduino, and P. Mackenzie-Helnwein. Dynamic meshing for material point method computations. *International Journal of Computational and mathematical Sciences*, 4(8): 379–387, 2010.

J. C. Simo. Numerical analysis and simulation of plasticity. In P.G. Ciarlet and J.L. Lions, editors, *Numerical Methods for Solids (Part 3) Numerical Methods for Fluids (Part 1)*, volume 6 of *Handbook of Numerical Analysis*, pages 183 – 499. Elsevier, 1998.

J. C. Simo and T. J. R. Hughes. *Computational Inelasticity.* Springer, New York, 1998.

J.C. Simo. A framework for finite strain elastoplasticity based on maximum plastic dissipation and the multiplicative decomposition: Part i. continuum formulation. *Computer Methods in Applied Mechanics and Engineering*, 66(2):199 – 219, 1988.

J.C Simo, F Armero, and R.L Taylor. Improved versions of assumed enhanced strain tri-linear elements for 3d finite deformation problems. *Computer Methods in Applied Mechanics and Engineering*, 110(34):359 – 386, 1993.

L. Staron and E. J. Hinch. Study of the collapse of granular columns using two-dimensional discrete-grain simulation. *Journal of Fluid Mechanics*, 545:1–27, 2005.

M. Steffen, R. Kirby, and M. Berzins. Analysis and reduction of quadrature errors in the material point method MPM. *International Journal for Numerical Methods in Engineering*, 76(6):922–948, 2008a.

M. Steffen, P. Wallstedt, J. Guilkey, R. Kirby, and M. Berzins. Examination and analysis of implementation choices within the material point method (MPM). *Computer Modeling in Engineering & Sciences*, 32(2):107–127, 2008b.

M. Steffen, R. M. Kirby, and M. Berzins. Decoupling and balancing of space and time errors in the material point method (MPM). *International Journal for Numerical Methods in Engineering*, 82 (10):1207–1243, 2010.

D. Sulsky and A. Kaul. Implicit dynamics in the material-point method. *Computer Methods in Applied Mechanics and Engineering*, 193(12-14):1137 – 1170, 2004.

D. Sulsky and H. L. Schreyer. Axisymmetric form of the material point method with applications to upsetting and taylor impact problems. *Computer Methods in Applied Mechanics and Engineering*, 139:409–429, 1996.

D. Sulsky and H. L. Schreyer. MPM simulation of dynamic material failure with a decohesion constitutive model. *European Journal of Mechanics - A/Solids*, 23(3):423 – 445, 2004. ISSN 0997-7538.

D. Sulsky, Z. Chen, and H.L. Schreyer. A particle method for history-dependent materials. *Computer Methods in Applied Mechanics and Engineering*, 118(1-2):179 – 196, 1994.

D. Sulsky, S. Zhou, and H. L. Schreyer. Application of a particle-in-cell method to solid mechanics. *Computer Physics Communications*, 87(1–2):236–252, 1995.

D. Sulsky, H. L. Schreyer, K. Peterson, R. Kwok, and M. Coon. Using the material point method to model sea ice dynamics. *Journal of Geophysical Research*, 112(c2), 2007.

C. C. Swan and Y. K. Seo. A smooth, three-surface elasto-plastic cap model: Rate formulation, integration algorithm, and tangent operators. 2006.

H. Tan and J. A. Nairn. Hierarchical, adaptive, material point method for dynamic energy release rate calculations. *Comput. Meths. Appl. Mech. Engrg*, 191:2095–2109, 2001.

G. Taylor. The use of flat-ended projectiles for determining dynamic yield stress. i. theoretical considerations. *Proceedings of the Royal Society of London. Series A, Mathematical and Physical Sciences*, 194(1038):289–299, 1948.

H. Teufelsbauer, Y. Wang, S.P. Pudasaini, R.I. Borja, and W. Wu. DEM simulation of impact force exerted by granular flow on rigid structures. *Acta Geotechnica*, 6(3):119–133, 2011. ISSN 1861-1125.

E. L. Thompson and H. .E Herbert. Granular column collapses: further experimental results. *Journal of Fluid Mechanics*, 575:177–186, 2007.

Adrin Tohari, Makoto Nishigaki, and Mitsuru Komatsu. Laboratory rainfall-induced slope failure with moisture content measurement. *Journal of Geotechnical and Geoenvironmental Engineering*, 133(5):575 – 587, 2007. ISSN 1090-0241. URL `http://dx.doi.org/10.1061/(ASCE)1090-0241(2007)133:5(575)`.

C. Truesdell and W. Noll. *The Non-Linear Field Theories of Mechanics*. Springer-Verlag, 1965.

X. Tu, J. E. Andrade, and Q. Chen. Return mapping for nonsmooth and multiscale elastoplasticity. *Computer Methods in Applied Mechanics and Engineering*, 198(3032):2286 – 2296, 2009. ISSN 0045-7825.

P. C. Wallstedt and J. E. Guilkey. Improved velocity projection for the material point method. *Computer Modeling in Engineering & Sciences*, 19(3):223 – 232, 2007.

P. C. Wallstedt and J. E. Guilkey. An evaluation of explicit time integration schemes for use with the generalized interpolation material point method. *Journal of Computational Physics*, 227:9628 – 9642, 2008.

B. Wang, V. Karuppiah, H. Lu, S. Roy, and R. Komanduri. Two-dimensional mixed mode crack simulation using the material point method. *Mechanics of Advanced Materials and Structures*, 12:471–484, 2005.

K. Washizu. *Variational Methods in Elasticiy and Plasticity*. Pergamon Press, 1982.

Z. Wieckowski. Modeling of silo discharge and filling problems by the material point method. *Task Quarterly*, 7(4):701 – 721, 2003.

Z. Wieckowski. The material point method in large strain engineering problems. *Computer Methods in Applied Mechanics and Engineering*, 193(39-41):4417 – 4438, 2004a.

Z. Wieckowski. The material point method in soil mechanics problems. In *XXI International Congress of Theoretical and Applied Mechanics—Proceedings*, Warsaw, Poland, August 2004b.

Z. Wieckowski, S.-K. Youn, and J.-H. Yeon. A particle-in-cell solution to the silo discharging problem. *International Journal for Numerical Methods in Engineering*, 45:1203–1225, 1999.

D. M. Wood. *Soil Behaviour and Critical State Soil Mechanics*. Cambridge University Press, 1990.

D. M. Wood. *Geotechnical Modelling*. Spon Press, 2004.

P. Wriggers. *Nonlinear Finite Element Methods*. Springer-Verlag, Berlin, 2008.

A. R. York, D. Sulsky, and H. L. Schreyer. The material point method for simulation of thin membranes. *International Journal for Numerical Methods in Engineering*, 44(10):1429–1456, 1999.

A. R. York, D. Sulsky, and H. L. Schreyer. Fluid–membrane interaction based on the material point method. *International Journal for Numerical Methods in Engineering*, 48(6):901–924, 2000. ISSN 1097-0207.

D. Z. Zhang, Q. Zou, W. B. VanderHeyden, and X. Ma. Material point method applied to multiphase flows. *Journal of Computational Physics*, 227(6):3159 – 3173, 2008.

D. Z. Zhang, X. Ma, and P. T. Giguere. Material point method enhanced by modified gradient of shape function. *Journal of Computational Physics*, 230(16):6379 – 6398, 2011.

H.W. Zhang, K.P. Wang, and Z. Chen. Material point method for dynamic analysis of saturated porous media under external contact/impact of solid bodies. *Computer Methods in Applied Mechanics and Engineering*, 198(17-20):1456 – 1472, 2009.

S. Zhou, J. Stormont, and Z. Chen. Simulation of geomembrane response to settlement in landfills by using the material point method. *International Journal for Numerical and Analytical Methods in Geomechanics*, 23:1977–1994, 1999.

O. C. Zienkiewicz and T. Shiomi. Dynamic behaviour of saturated porous media; the generalized biot formulation and its numerical solution. *International Journal for Numerical and Analytical Methods in Geomechanics*, 8(1):71–96, 1984.

O.C. Zienkiewicz, R.L. Taylor, and P. Nithiarasu. *The Finite Element Method for Fluid Dynamics*, volume 3. Elsevier Butterworth-Heinemann, 6 edition, 2005a.

O.C. Zienkiewicz, R.L. Taylor, and P. Nithiarasu. *The Finite Element Method: Its Basis and Fundamental*, volume 1. Elsevier Butterworth-Heinemann, 6 edition, 2005b.

O.C. Zienkiewicz, R.L. Taylor, and P. Nithiarasu. *The Finite Element Method for Solid and Structural Mechanics*, volume 2. Elsevier Butterworth-Heinemann, 6 edition, 2005c.

Appendix A

YIELD SURFACE EXAMPLES

This appendix outlines a scheme to generate points on a yield surface and shows how to obtain the yield function or plastic potential directional derivatives with respect to the stress tensor. The Drucker-Prager and Matsuoaka-Nakai models are used as examples throughout the appendix.

A.1 Generating Points on a Yield Surface

This section outlines a scheme to obtain points on a given yield surface, $F(\boldsymbol{\sigma}, \boldsymbol{\kappa})$. The following formulation assumes that the yield function can be written in terms of the three invariants of the stress tensor: I_1, I_2, and I_3 as defined in Equations (3.52)–(3.54). In what follows, a transformation of coordinates is used to construct slices in principal stress-space that are perpendicular to the hydrostatic axis. This allows the points that reside on the surface to be quickly computed and used for other purposes, such as plotting and visualization. The technique discussed here is certainly not the only option; there are, perhaps, easier ways—such as contour plots using Matlab and Mathematic—but this particular approach is general and more powerful than brute-force shortcuts and is used to generate surface data for all failure surfaces appearing in this document

A.1.1 Coordinate Systems

The first order of business is to determine a convenient choice of coordinates to represent the yield function. This function is often cast in terms of stresses that represent the elastic limit of the material in question. As such, principal stress space is a physically intuitive and meaningful option. Principal stress space is not the most convenient choice if the intent is to determine or solve for the collection of points that represent the yield surface. To this end it is beneficial to seek an alternative set of coordinates and define their relation to principal stress space.

One such option is to create an orthonormal bases that has a single direction aligned with the hydrostatic axis. This is depicted in Figure A.1(a). This discussion adopts the

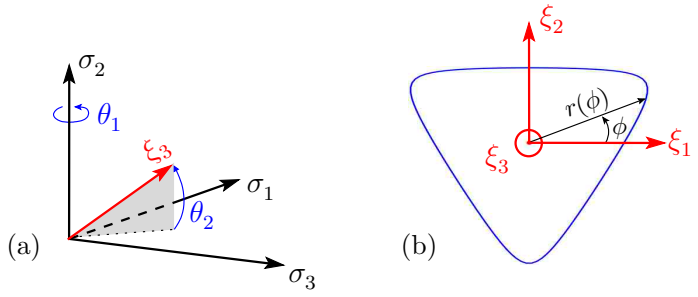

Figure A.1: Needed ingredients to compute points on a yield surface. (a) Transformation from principal space to orthonormal coordinate system aligned with hydrostatic axis. (b) Slice of yield surface perpendicular to the hydrostatic axis.

following vector notation

$$\boldsymbol{\sigma} = \{\, \sigma_1 \,,\, \sigma_2 \,,\, \sigma_3 \,\}^T \qquad \text{and} \qquad \boldsymbol{\xi} = \{\, \xi_1 \,,\, \xi_2 \,,\, \xi_3 \,\}^T \tag{A.1}$$

for the two coordinate spaces. The two coordinate systems are linked by the rotation matrices $\mathbf{R}_1$ and $\mathbf{R}_2$ via

$$\boldsymbol{\xi} = \mathbf{R}_2 \cdot \mathbf{R}_1 \cdot \boldsymbol{\sigma} \qquad \text{and} \qquad \boldsymbol{\sigma} = \mathbf{R}_1^T \cdot \mathbf{R}_2^T \cdot \boldsymbol{\xi} \;. \tag{A.2}$$

The rotation matrices are

$$\mathbf{R}_1 = \begin{bmatrix} \cos\theta_1 & 0 & -\sin\theta_1 \\ 0 & 1 & 0 \\ \sin\theta_1 & 0 & \cos\theta_1 \end{bmatrix} \qquad \text{and} \qquad \mathbf{R}_2 = \begin{bmatrix} 1 & 0 & 0 \\ 0 & \cos\theta_2 & -\sin\theta_2 \\ 0 & \sin\theta_2 & \cos\theta_2 \end{bmatrix} \;. \tag{A.3}$$

By selecting $\theta_1 = \pi/4$ and $\theta_2 = \cos^{-1}\sqrt{2/3}$, the final relationship between the two coordinate systems is expressed as

$$\begin{Bmatrix} \sigma_1 \\ \sigma_2 \\ \sigma_3 \end{Bmatrix} = \begin{bmatrix} \sqrt{2}/2 & -\sqrt{6}/6 & \sqrt{3}/3 \\ 0 & \sqrt{2/3} & \sqrt{3}/3 \\ -\sqrt{2}/2 & -\sqrt{6}/6 & \sqrt{3}/3 \end{bmatrix} \cdot \begin{Bmatrix} \xi_1 \\ \xi_2 \\ \xi_3 \end{Bmatrix} \;. \tag{A.4}$$

From Figure A.1(b) the following relations are derived:

$$\xi_1 = r(\phi)\cos(\phi) \qquad \text{and} \qquad \xi_2 = r(\phi)\sin(\phi) \;, \tag{A.5}$$

where ϕ is commonly known as the lode angle. The rational for using yet another set of coordinates will become clear shortly. Utilizing Equations (A.4) and (A.5), the invariants of $\boldsymbol{\sigma}$ are expressed as

$$I_1 = \sigma_1 + \sigma_2 + \sigma_3 = \sqrt{3}\;\xi_3, \tag{A.6}$$

$$I_2 = \sigma_1\sigma_2 + \sigma_1\sigma_3 + \sigma_2\sigma_3 = \xi_3^2 - \frac{r^2}{2}, \qquad \text{and} \tag{A.7}$$

$$I_3 = \sigma_1\sigma_2\sigma_3 = \frac{\xi_3^3}{3\sqrt{3}} - \frac{r^2\,\xi_3}{2\sqrt{3}} - \frac{r^3\,\sin 3\phi}{3\sqrt{6}}\ . \tag{A.8}$$

The expressions given in Equations (A.6)–(A.8) provide a means to determine the points residing on the yield surface. By prescribing points along the hydrostatic axis, ξ_3, the domain can be thought of as a series of slices; for each slice the lode angle, ϕ, is varied between 0 and $2\,\pi$. At each $\{\xi_3, \phi\}$ pair, the yield function provides the constraint necessary to determine the radius—i.e., the condition $F(\boldsymbol{\sigma}, \boldsymbol{\kappa}) = 0$ is used to determine $r(\phi)$. Equations (A.5) uniquely link each $\{\phi, r(\phi)\}$ pair to a corresponding $\{\xi_1, \xi_2\}$ pair, while the expression in (A.4) provides the final map to principal stress space. Note that throughout this process it is assumed that the hardening parameters, $\boldsymbol{\kappa}$, are constant. This is a reasonable assumption since the goal is, after all, to determine which points are on the surface for a given state.

Generally speaking, the resulting equation for the radius will be non-linear and require iteration to determine $r(\phi)$. For some simpler models determining the radius is straightforward and can be done in closed form. The latter includes the traditional J2 and Drucker-Prager models described in Sections 3.5 and 3.6.1, respectively.

A.1.2 Example Formulation: Matsuoka-Nakai Yield Surface

The procedure is outlined here for the Matsuoka-Nakai material model. This particular yield function requires iteration to determine $r(\phi)$. The detailed formulation for this criterion is presented in Section 3.7. Here the yield function is repeated for completeness and is given by

$$F(\bar{\boldsymbol{\sigma}}, \kappa_F) = 6\,\bar{I}_3\,\kappa_F + 3\,\bar{I}_1\,\|\mathbf{s}\|^2 - 2\,\bar{I}_1^3\ . \tag{A.9}$$

The overbar on the invariants was introduced in Equations (3.55)–(3.57) and represents a shift along the hydrostatic axis by a distance c. The yield function is re-written by eliminating the shifted invariants and utilizing the relations given in (A.6)–(A.8):

$$\begin{aligned} F(\xi_3, \phi, r, \kappa_1) &= r^2\,c\,(3\,\kappa_F - 9) + r^2\,\xi_3\,\sqrt{3}\,(3 - \kappa_F) - r^3\,\kappa_F\,\sqrt{2/3}\,\sin 3\phi \\ &+\xi_3^3\,(2\,\kappa_F/\sqrt{3} - 6\,\sqrt{3}) + c\,\xi_3^2\,(54 - 6\,\kappa_F) + c^2\,\xi_3\,\sqrt{3}\,(6\,\kappa_F - 54) + c^3\,(54 - 6\,\kappa_F)\ . \end{aligned} \tag{A.10}$$

This is non-linear in $r(\phi)$ so the Newton-Raphson iteration technique outlined in Table 3.2 is used to determine a converged value for the radius. The unknown and residual 'vectors'

are

$$\mathbf{x} = \{r(\phi)\} \qquad \text{and} \qquad \mathbf{r}(\mathbf{x}) = \{F(\xi_3, \phi, r, \kappa_1)\} \ , \tag{A.11}$$

respectively. The corresponding Jacobian 'matrix' is

$$\mathbf{J}(\mathbf{x}) = \left[\frac{\partial \mathbf{r}}{\partial \mathbf{x}}\right] = \left[2\,r\,c\,(3\,\kappa_F - 9) + 2\,r\,\xi_3\,\sqrt{3}\,(3 - \kappa_F) - r^2\,\kappa_F\,\sqrt{6}\,\sin 3\phi\right] \ . \tag{A.12}$$

A good guess for the initial radius is helpful for this model (and perhaps others). Since the Matsuoka-Nakai failure plane circumscribes the Mohr-Coulomb failure plane, a quality starting choice is the radius that corresponds to pure triaxial extension in Mohr-Coulomb theory. This value is given by Wood (1990) as

$$\mathbf{x}^0 = r_{min} = \frac{-2\,\sqrt{2}\,(\xi_3 - 3\,c/\sqrt{3})\sin\phi_F}{3 + \sin\phi_F} \tag{A.13}$$

and represents the minimum possible value for $r(\phi)$. Note that ϕ_F in (A.13) corresponds to the effective friction angle and is *not* the lode angle.

A.2 Directional Derivatives of the Yield Surface

This section outlines how to obtain the yield function or plastic potential directional derivatives with respect to the stress tensor for the Drucker-Prager and Matsuoaka-Nakai models. These derivations make extensive use of the relationships defined in Section 3.4. Of primary interest is the first and second derivatives. When considering the yield function, the first derivative yields a tensor that is tangent to the surface[1]. With regards to the plastic potential, the first derivative represents the plastic flow direction, $\mathbf{g}$. The second derivative of this function is used extensively in the return mapping algorithm, e.g., the Jacobien definition of Equation (3.42).

A.2.1 Drucker-Prager Derivatives

The Drucker-Prager plastic potential reads

$$G(\boldsymbol{\sigma}, \psi_G) = \|\mathbf{s}\| + \varrho_G\,I_1 - C_G = 0 \ , \tag{A.14}$$

[1]When visualized in principal stress space the notion of a tensor being tangent to a surface is easier realized.

where each term is defined in Section 3.6.3. The flow direction is obtained from the notion of a directional derivative as

$$\begin{aligned} dG &= d\|\mathbf{s}\| + d(\varrho_G\, I_1) - dC_G \\ &= d\,(\mathbf{s} : \mathbf{s})^{1/2} + \varrho_G\, dI_1 \\ &= \frac{1}{2}\,\|\mathbf{s}\|^{-1/2}\,(d\mathbf{s} : \mathbf{s} + \mathbf{s} : d\mathbf{s}) + \varrho_G\,\mathbf{1} \\ &= \frac{d\mathbf{s} : \mathbf{s}}{\|\mathbf{s}\|} + \varrho_G\,\mathbf{1}\ . \end{aligned}$$

The term $d\mathbf{s}$ is obtained from

$$\begin{aligned} d\mathbf{s} &= d\left(\boldsymbol{\sigma} - \frac{1}{3}\,I_1\,\mathbf{1}\right) \\ &= d\boldsymbol{\sigma} - \frac{1}{3}\,dI_1\,\mathbf{1} \\ &= \mathbb{I} - \frac{1}{3}\mathbf{1}\otimes\mathbf{1} = \mathbb{I}_{dev}\ , \end{aligned} \tag{A.15}$$

where the 4^{th} order tensor, $\mathbb{I}_{dev}$, is a purely deviatoric operator. The relationship in (A.15) leads to the important conclusion $d\mathbf{s} : \mathbf{s} = \mathbf{s}$, or, in words: extracting the deviatoric component of a purely deviatoric tensor leaves the original tensor. Armed with this knowledge the final definition of the first derivative is

$$\frac{dG}{d\boldsymbol{\sigma}} = \mathbf{g} = \frac{\mathbf{s}}{\|\mathbf{s}\|} + \varrho_G\,\mathbf{1}\ . \tag{A.16}$$

The second derivative follows accordingly as

$$\begin{aligned} d^2G &= d\left(\frac{\mathbf{s}}{\|\mathbf{s}\|} + \varrho_G\,\mathbf{1}\right) \\ &= d\,\frac{\mathbf{s}}{\|\mathbf{s}\|} \\ &= \frac{\|\mathbf{s}\|\,d\mathbf{s} - \mathbf{s}\,d\|\mathbf{s}\|}{\|\mathbf{s}\|^2} \\ &= \frac{d\mathbf{s}}{\|\mathbf{s}\|} - \frac{1}{\|\mathbf{s}\|}\left(\frac{\mathbf{s}}{\|\mathbf{s}\|}\,d\|\mathbf{s}\|\right)\ . \end{aligned}$$

Making the appropriate substitutions yields the final expression for the second derivative

$$\frac{d^2G}{d\boldsymbol{\sigma}\otimes d\boldsymbol{\sigma}} = \frac{1}{\|\mathbf{s}\|}\left(\mathbb{I} - \frac{1}{3}\mathbf{1}\otimes\mathbf{1} - \frac{\mathbf{s}}{\|\mathbf{s}\|}\otimes\frac{\mathbf{s}}{\|\mathbf{s}\|}\right)\ . \tag{A.17}$$

A.2.2 Matsuoka-Nakai Derivatives

The Matsuoka-Nakai derivatives are presented in this appendix section. A coordinate free formulation is presented for the first and second derivatives. Each term is then simplified

for use in principal stress space. The plastic potential for the Matsuoka-Nakai model is given by

$$G(\bar{\boldsymbol{\sigma}}, \kappa_G) = 6\,\bar{I}_3\,\kappa_G + 3\,\bar{I}_1\,\|\mathbf{s}\|^2 - 2\,\bar{I}_1^3 \ , \tag{A.18}$$

where κ_G is a hardening parameter related to the plastic dilation angle, ψ_G, via

$$\kappa_G = \frac{\sin^2\psi_G - 9.0}{\sin^2\psi_G - 1.0} \ . \tag{A.19}$$

The overbar on the invariants was introduced in Equations (3.55)–(3.57) and represents a shift along the hydrostatic axis by a distance c_G. The directional derivative of the potential with respect to the stress tensor is

$$dG = 6\,d\bar{I}_3\,\kappa_G + 3\,d\bar{I}_1\,\|\mathbf{s}\|^2 + 6\,\bar{I}_1\,d\|\mathbf{s}\| - 6\,\bar{I}_1^2\,d\bar{I}_1 \ . \tag{A.20}$$

The derivative is expanded to read

$$\begin{aligned}
\frac{dG}{d\boldsymbol{\sigma}} &= 6\,\kappa_G\left(I_3\,\boldsymbol{\sigma}^{-1} - c_G\,(I_1\,\mathbf{1} - \boldsymbol{\sigma}) + c_G^2\,\mathbf{1}\right) + 3\,\|\mathbf{s}\|^2\,\mathbf{1} + 6\,(I_1 - 3\,c_G)\,\mathbf{s} - 6\,(I_1 - 3\,c_G)^2\,\mathbf{1} \\
&= 6\,\kappa_G\,I_3\,\boldsymbol{\sigma}^{-1} - 6\,\kappa_G\,c_G\,I_1\,\mathbf{1} + 6\,\kappa_G\,c_G\,\boldsymbol{\sigma} + 6\,\kappa_G\,c_G^2\,\mathbf{1} + 3\,\|\mathbf{s}\|^2\,\mathbf{1} - 6\,I_1^2\,\mathbf{1} + 36\,I_1\,c_G\,\mathbf{1} \\
&\quad -54\,c_G^2\,\mathbf{1} + 6\left(\boldsymbol{\sigma} - \frac{I_1}{3}\,\mathbf{1}\right) - 18\,c_G\left(\boldsymbol{\sigma} - \frac{I_1}{3}\,\mathbf{1}\right) \ .
\end{aligned}$$

Rearranging and combining like terms yields the final form of the first derivative:

$$\begin{aligned}
\frac{dG}{d\boldsymbol{\sigma}} &= 6\,\kappa_G\,I_3\,\boldsymbol{\sigma}^{-1} + 3\,\|\mathbf{s}\|^2\,\mathbf{1} - 8\,I_1^2\,\mathbf{1} + 6\,I_1\,\boldsymbol{\sigma} \\
&\quad +6\,c_G\,(\kappa_G\,\boldsymbol{\sigma} + 7\,I_1\,\mathbf{1} - 3\,\boldsymbol{\sigma} - \kappa_G\,I_1\,\mathbf{1}) \\
&\quad +6\,c_G^2\,(\kappa_G\,\mathbf{1} - 9\,\mathbf{1}) \ ,
\end{aligned} \tag{A.21}$$

in which the contribution from the hydrostatic shift c_G can clearly be seen when compared to the from presented in Equations (A.18).

The second derivative is obtained by taking the directional derivative with respect to the stress tensor of Equation (A.21):

$$\begin{aligned}
d^2G &= d\,(dG/d\boldsymbol{\sigma}) \\
&\quad 6\,\kappa_G\,dI_3\,\boldsymbol{\sigma}^{-1} + 6\,\kappa_G\,I_3\,d\boldsymbol{\sigma}^{-1} + 6\,\|\mathbf{s}\|d\|\mathbf{s}\|\,\mathbf{1} - 16\,I_1\,dI_1\,\mathbf{1} + 6\,dI_1\,\boldsymbol{\sigma} + 6\,I_1\,d\boldsymbol{\sigma} \\
&\quad +6\,c_G\,(\kappa_G\,d\boldsymbol{\sigma} + 7\,dI_1\,\mathbf{1} - 3\,d\boldsymbol{\sigma} - \kappa_G\,dI_1\,\mathbf{1}) \ .
\end{aligned} \tag{A.22}$$

Introducing the tensor product and making the appropriate substitutions for the directional derivatives of the invariants, the second derivative is written as

$$\begin{aligned}
\frac{d^2G}{d\boldsymbol{\sigma}\otimes d\boldsymbol{\sigma}} &= 6\,\kappa_G\,I_3\left(\boldsymbol{\sigma}^{-1}\otimes\boldsymbol{\sigma}^{-1} + \frac{d\boldsymbol{\sigma}^{-1}}{d\boldsymbol{\sigma}}\right) + 6\left(\boldsymbol{\sigma} - \frac{I_1}{3}\,\mathbf{1}\right)\otimes\mathbf{1} \\
&\quad -16\,I_1\,\mathbf{1}\otimes\mathbf{1} + 6\,\mathbf{1}\otimes\boldsymbol{\sigma} + 6\,I_1\mathbb{I} \\
&\quad +6\,c_G\,(\kappa_G\,\mathbb{I} + 7\,\mathbf{1}\otimes\mathbf{1} - 3\,\mathbb{I} - \kappa_G\,\mathbf{1}\otimes\mathbf{1}) \ .
\end{aligned} \tag{A.23}$$

Expanding and combining like terms yields the final form of the second derivative:

$$\frac{d^2G}{d\boldsymbol{\sigma}\otimes d\boldsymbol{\sigma}} = 6\,\kappa_G\,I_3\,\left(\boldsymbol{\sigma}^{-1}\otimes\boldsymbol{\sigma}^{-1}+\frac{d\boldsymbol{\sigma}^{-1}}{d\boldsymbol{\sigma}}\right)+6\,\left(\boldsymbol{\sigma}\otimes\mathbf{1}+\mathbf{1}\otimes\boldsymbol{\sigma}\right)-18\,I_1\,\mathbf{1}\otimes\mathbf{1}+6\,I_1\mathbb{I}$$
$$+6\,c_G\,\left(\kappa_G\,\mathbb{I}+7\,\mathbf{1}\otimes\mathbf{1}-3\,\mathbb{I}-\kappa_G\,\mathbf{1}\otimes\mathbf{1}\right)\ . \tag{A.24}$$

These derivatives are quite cumbersome and awkward to work with, particularly so for Equation (A.24). Their complexity—not to mention physical size—is significantly reduced if working in principal stress space. Doing so reduces the first derivative to a vector and the second derivative becomes

$$\frac{d^2G}{\sigma_I\,\sigma_J} = 6\,\kappa_G\,I_3\,\left(\frac{1}{\sigma_I\,\sigma_J}-\frac{\delta_{IJ}}{\sigma_I\,\sigma_J}\right)+6\,\left(\sigma_I+\sigma_J\right)+6\,I_1\delta_{IJ}-18\,I_1$$
$$+6\,c_G\,\left(\kappa_G-3\right)\,\delta_{IJ}+6\,c_G\,\left(7-\kappa_G\right)\ . \tag{A.25}$$

Here I and J are free indices ranging from 1–3 denoting the principal values. This form is advantageous because numerical difficulties associated with a zero principal stress are eliminated. For example, the definition $I_3=\sigma_1\,\sigma_2\,\sigma_3$ in principal space is exploited to avoid a disastrous division by zero in the first term by simply canceling out the appropriate values of the stress tensor.

Appendix B

COMPUTATIONAL FRAMEWORK

At the core of any numerical simulation is the computational framework that effectively reads in data, performs the relevant calculations, and generates useful results for analysis and visualization. The implementation developed for the present study employs the C++ and Python programming languages. Visualization is accomplished using the `matplotlib` Python module, as well as the 3rd party software ParaView [1] , an interactive application that relies on the Visualization Toolkit (VTK) library. The goal of this chapter is to present an overview of the computational framework so others using this coding base have a starting point for future work. There are limitations in the extent to which the code can be documented here. As such, primary emphasis is placed on defining input data and viewing results.

B.1 Overview

The computational framework, referred to from here on as *the code*, contains approximately 22,500 lines of code [2] (loc). This metric and others are easily obtainable for any project using the free utility `cloc`. Of course, loc is a bit vague and subject to change based on coding style and the efficiency of the implementation, but does provide some frame of reference as to the size of the application. The code is split naturally into three categories: pre-processing, model analysis, and post-processing, each of which accounts for 5%, 70%, and 25% of the total 22.5 kloc, respectively.

These code components are shown schematically in Figure B.1. In this perspective the three entities create a pipeline directing the flow of data. Raw data comprising the spatial domain and body is organized and used to generate an input file. The model analysis portion, an object-oriented implementation written exclusively in C++ , does the primary numerical analysis and writes a stream of values to an output file at user prescribed increments. A typical data set ranges in size from a few kilobytes to several gigabytes, and can contain customizable input and output types unique to each analysis. The lack of a pre-

[1] http://www.paraview.org/

[2] This figure does not include comments and blank lines. Adding these yields approximately 41,000 loc.

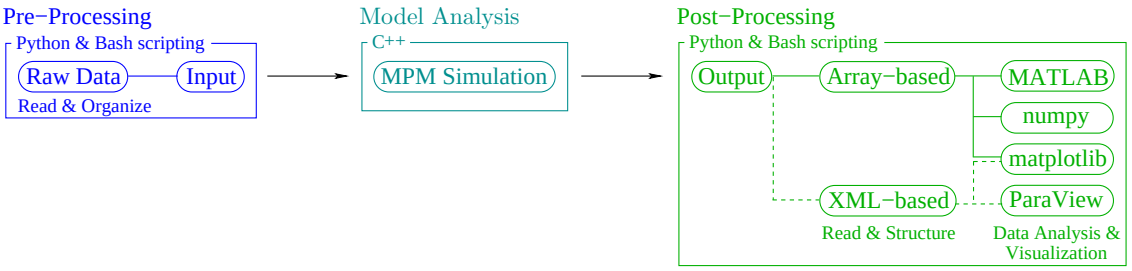

Figure B.1: The code components that make up the computational framework and dictate the flow of data.

defined structure means the post-processors must read, interpret, and organize the data in such a manner that is useful for analysis and visualization. The latter is accomplished with a series of Python scripts that dissect an output file line by line, essentially transforming the stream of numbers into useful constructs. Each component of this process is now explored in additional detail.

B.2 Pre-Processing

The input file serves as the sole data source linking the user to the MPM algorithm and the enhancements described in this dissertation. As such, the ability to generate input files is the single most important aspect of this chapter and is critical for any individual trying move forward with this particular coding framework. To this end the input file structure is discussed in detail, in the process highlighting the many features of the code.

B.2.1 Input File Basics

An input file should end with the extension `.inp`. This is not a requirement. In fact, as will be discussed in due course, the code also accepts the extension `.rst` indicating a restart file. The input framework does not care or respond differently if the file represents a new analysis or a restart from a previous state. However, a consistent naming scheme easily identifiable to the user should be employed and hence the suggested extension `.inp`.

The parser reads an input file line by line, searching for keywords and responding appropriately. Keywords can be nested within keywords. This approach creates a hierarchical structure that is best explained from the top down. Thus, the typical root keywords appearing in an input file are given in Figure B.2. The symbol `[...]` indicates nested keywords or options. Additional keywords will receive attention shortly, but in the meantime there are some important points to make about the base keywords. First and foremost order is not important, that is, each keyword can appear anywhere in an input file as long as it

```
// This serves as the comment symbol for an input file.
//
// Common Keywords
AnalysisOptions
  [...]
End
//
Parameters
  [...]
End
//
Material
 // Mat_ID       ModelName      V_Frac    Density     Params
End
//
Boundary
  // Type    ID    l_x    l_y    l_z    n_x    n_z    n_z
  [...]
End
//
OutputData
  [...]
End
//
Particles    MaterialID    PhaseID
  // p_ID     p_mass    p_x    p_y    p_z
End
//
ParticleState
  // p_ID    [...]
End
//
// Less common keywords (or those only appearing in .rst file)
//
ParticlePrescribedTraction
  // p_ID  A_p    MagTraction   n_x    n_y    n_z
End
//
ParticleShape
  // p_ID  r1_x  r1_y  r1_z  r2_x  r2_y  r2_z  r3_x  r3_y  r3_z
End
//
ParticleVelocity
  // p_ID    v_x    v_y    v_z
End
//
ParticleBodyForce
  // p_ID    b_x    b_y    b_z
End
// Be careful about blank lines!
```

Figure B.2: Base keywords for input file.

```
AnalysisOptions
  //Version   float_ver   (0.0)
  //DontDeleteNodes   (false)
  //CPDI   (false)
  //SFType string_type (Linear)
  //HybridCPDI   float_s   float_n  (false)
  //LargeDeformation   (false)
  //ViscousDamping   float1  (false)
  //PlaneStrain   (false)
  //PlaneStress   (false)
  //TriLinearAntiLocking   string_shape   string_type (false)
  //ConstantAntiLocking   string_shape   string_type (false)
  //IncrementalUpdate (false)
  //DCA (false)
  //FrontSmoothing (false)
  //VolumeConstraint (false)
  //CMPM float_n float_B float_k float_g float_d float_s (false)
End
```

Figure B.3: AnalysisOptions keywords for input file.

is followed by `End`. However, some locations make more sense than others. For example, it is nice to open a file and see which `AnalysisOptions` and `Parameters` are employed in the current simulation. This information is hard to find if a list of `Particles`, possibly in excess of 10,000 lines, appears before these keywords. The order presented in Figure B.2 has proven quite useful and is recommended. Second, not all keywords are required. It is only necessary to specify `Particles` and `Material`. There are, however, common keywords that appear in most analyses. In fact, every analysis appearing in this document follows from input files using only the Common Keywords. That is not to say things like body force are not used, but there are other ways to apply forces, velocity, position shift, etc., to all particles and these will be addressed shortly. And finally, the input file does not support blank lines (this can be problematic at the end of an input file). If a blank line is desired use the comment symbol `\\`, as this seems to be the only effective solution to this problem. Each base keyword is addressed in additional detail in the next several subsections.

B.2.2 `AnalysisOptions`

The nested keywords available from within this base option are shown in Figure B.3. Note that in practice the leading '`//`' should be removed if an option is desired (otherwise it will be interpreted as a comment). Values in parenthesis (•) indicate the default value. Some features are activated simply by adding them as an analysis option. For example, invoking `PlaneStrain` will automatically change the value to `true` and it is not necessary to do anything else. Other keywords might require additional values. The expected type of these additional parameters is given by `float` or `string` (the latter does *not* need to be given in

quotes).

- `Version float_ver`
  This is the Version number with 0.0 the default. This feature is not important since nothing special is done for different versions. Obviously this could be a powerful feature with additional code releases.

- `DontDeleteNodes`
  Nodes with no mass are subject to deletion by default. By activating this option nodes will *not* be removed even if they have no mass. The frequency with which nodes are removed can be adjusted in `OutputData`.

- `CPDI`
  This is the Convected Particle Domain Interpolation feature by Sadeghirad et al. (2011b). If this feature is active then the `ParticleShape` should be specified for each particle in the input file. If not specified default shapes are assumed and may not match the desired particle structure.

- `SFType string_type`
  Standard shape function type. Defaults to `Linear` , an 8-noded brick. Type `Quadratic` is a 27-noded element. The solution scheme uses a lumped mass. This is problematic for the quadratic element if particles are changing cells, thus `Quadratic` is only recommended for small displacements.

- `HybridCPDI float_s float_n`
  False by default. This feature was developed in house and utilizes the `CPDI` option only for particles actively crossing a cell boundary. `float_s` is a scalar multiplier that decreases (or increases) the shape vectors that make up the particle. `float_n` is the max number of particles in the new cell that will turn off this feature.
  For example: `HybridCPDI 0.75 8` will reduce the particle shape size by 25% and only activate `CPDI` if 8 or less particles are in the new cell the particle is headed into. Note that the size reduction is only applied in the search algorithm to see if a particle is in multiple cells. This does not affect the actual particle mass or volume.

- `LargeDeformation`
  Small deformation by default, see Equation (3.10). Activating this feature changes the deformation measure to the left Cauchy-Green deformation tensor, for use with the logarithmic strain in (3.33).

- `PlaneStrain`
  False by default. Restricts deformation in the z-direction. Particles must reside in the xy plane to use this feature. If activated the particles are automatically shifted to the center of the cell in the z-direction. This feature impacts the anti-locking routines, as the shape and filter matrices are changed by plane strain conditions.

- `PlaneStress`
  False by default. Restricts stress accumulation in the z-direction. Particles must reside in the xy plane to use this feature. If activated the particles are automatically shifted to the center of the cell in the z-direction. This feature impacts the anti-locking routines, as the shape and filter matrices are changed by plane stress conditions. This feature is valid only for linear elastic materials.

- `TriLinearAntiLocking string_shape string_type`
  False by default. `string_shape` can be *either* `AS1,AS2,`or `AS3CV`. Shape `AS1` utilizes those definitions in Section 4.3.1, shape `AS2` uses those given in Section 4.3.2, while shape `AS3CV` forces a constant volumetric approximation. `string_type` can be either `CellBased, NodeBased,` or `HybridBased`. See Sections 4.4.1–4.4.3 for a discussion.

- `ConstantAntiLocking string_shape string_type`
  False by default. `string_shape` can be either `AS1,`or `AS2`. This option does not utilize the diagonal terms in shape matrix definition.

- `ViscousDamping float1`
  This feature adds artificial volumetric damping similar to the approach given in Chen et al. (2002) and is false by default. Note that this feature is not the same as adding overall viscosity. This feature is the single most important feature for simulating nearly incompressible fluids or elastic solids. Anti-locking alone cannot achieve the degree of stabilization that this feature provides.

- `DCA`
  False by default. This is the Distributed mass Coefficient Algorithm as presented by Ma et al. (2010a). This approach is useful for nodes that have small mass and redistributes mass to regions near the edge of the body. This feature has not been extensively evaluated and has shown to be problematic when large regions of a body are moving into a new cell.

- `FrontSmoothing`
  False by default. This feature that automatically detects which nodes have a volume

```
Parameters
  //TimeStep float_t (1e-5)
  //ExternalForceRamp  float_c   (0.0)
  //ThetaIntegration float_t (0.0)
  //StartTime float_t (0.0)
  //AnalysisDuration float_t (1.0)
  //RecordStartTime float_t (0.0)
  //globalVelocity  [int_phase]  float_vx  float_vx  float_vx
  //globalVelocityMultiplier float_t (1.0)
  //globalPosition [int_phase]  float_px  float_px  float_px
  //globalBodyForce [int_phase]  float_bx  float_bx  float_bx
  //CellSize float_lx  float_lx  float_lx
  //DeleteNodesEvery int (5000)
  //DragInteraction int_phase_1 int_phase_2 float_coeff
  //BouyantForce int_phase_1 int_phase_2 float_gmag
End
```

Figure B.4: Parameters keywords for input file.

fraction less than a prescribed value. If so, then all particle in the support of this node are updated using only time t_n quantities and are temporarily designated as ALONE. This feature prevents large strain rates at the edge of bodies. This feature is the second most important feature (and very close to first) for simulating nearly incompressible fluids or elastic solids.

- `VolumeConstraint`
  False by default. Turns on the Volume Constraint algorithm described in Chapter 5.

- `CMPM  float_n  float_B  float_k  float_g  float_d  float_s`
  False by default. Activates the CMPM as presented by Zhang et al. (2008). Each variable above is as follows: `float_n` is the porosity, `float_B` is Biot's constant, `float_k` is the permiability, `float_g` is the magnitude of gravity, `float_d` is the pore fluid density, `float_s` is the pore fluid bulk stiffness.

B.2.3 `Parameters`

The nested keywords available from within the `Parameters` option are shown in Figure B.4. Again, default values are indicated by parenthesis. Values in brackets [•] are optional. The keyword `CellSize` is the only required parameter option.

- `TimeStep  float_t`
  The time step Δt.

- `ExternalForceRamp  float_c`
  A linear load ramp with maximum magnitude of 1.0 over the duration from 0.0 to

`float_c`. Multiplies only the external force at a node. This parameters is used to slowly apply gravity.

- `ThetaIntegration float_t`
  The integration parameter $\theta \in [0, 1]$. See Equation (2.15).

- `StartTime float_t`
  Analysis start time. Defaults to zero. Will likely only be non-zero for restart files.

- `AnalysisDuration float_t`
  Analysis duration. Appended to the start time to get absolute end time.

- `RecordStartTime float_t`
  Minimum time at which data is to be recorded. Defaults to 0.0. This feature is useful if early portions of an analysis are not of interest.

- `globalVelocity [int_phase] float_vx float_vx float_vx`
  This parameter is optional. Sets all particles of phase `[int_phase]` to velocity $\mathbf{v} = (vx, vy, vz)$. If `[int_phase]` is not provided this vector is applied to all particles. By making it phase specific differing fields can be applied to different phases.

- `globalVelocityMultiplier float_t`
  Multiplies a given velocity field by the factor `float_t`. This is useful when the shape of a profile—such as a vibrating beam—is known and the user wants to quickly change the max magnitude of the motion.

- `globalPosition [int_phase] float_px float_px float_px`
  This parameter is optional and *shifts* all particles of phase `[int_phase]` by a distance $\mathbf{d} = (px, py, pz)$. If `[int_phase]` is not provided this vector shift is applied to all particles. By making it phase specific differing fields can be applied to different phases. Note this is a shift and not an override like was the case for `globalVelocity`.

- `globalBodyForce [int_phase] float_bx float_bx float_bx`
  This parameter is optional and applies a body force to Particles of phase `[int_phase]` with components $\mathbf{v} = (bx, by, bz)$. If `[int_phase]` is not provided this vector is applied to all particles. By making it phase specific differing fields can be applied to different phases. This is how gravity is applied to all particles.

- `CellSize float_lx float_lx float_lx`
  Sets the cell size. This is parameter is required.

```
Material
  //Mat_ID ModelName                    V_Frac Dens Params
  //
  //int_ID LinearElasticSolid           float  float [...]
  //int_ID IncompressibleFluid          float  float [...]
  //int_ID J2Solid                      float  float [...]
  //int_ID DruckerPragerSolid           float  float [...]
  //int_ID SmoothCapDPSolid             float  float [...]
  //int_ID ModifiedDruckerPragerSolid float  float [...]
  //int_ID MatsuokaNakaiSolid           float  float [...]
End
```

Figure B.5: Material keywords for input file.

- `DeleteNodesEvery int`
  Controls how frequently the active nodes are searched and massless nodes deleted from the computation. This process occurs every `int` time steps. By default nodes are checked and deleted (if necessary) every 5000 steps.

- `DragInteraction int_phase_1 int_phase_2 float_coeff`
  Activates the multiphase drag interaction algorithm as outlined in Mackenzie-Helnwein et al. (2010). The phase id values `int_phase_1` and `int_phase_2` have an interaction coefficient `float_coeff`.

- `BouyantForce int_phase_1 int_phase_2 float_gmag`
  Accounts for the buoyancy between two phases `int_phase_1` and `int_phase_2` . Computed using volume fractions if both phases are occupying the same space.

B.2.4 `Material`

Each material used in the analysis must be specified within the base keyword `Material`. An arbitrary integer identification number, `int_ID`, is used to link materials with a certain group of `Particles`. Each `ModelName` is initialized from the base class `Material.cpp`. The `V_Frac` and `Dens` are the volume fraction and density, respectively. Depending on the application these values mean different things. For a general continuum analysis, `V_Frac` should be 1.0 and `Dens` assumes the bulk value. On the other hand, for multiphase analyses employing porous soils then an appropriate volume fraction must be supplied and the `Dens` value represents the *constituent* density. Each material requires different parameters as outlined below. Since it may be necessary to distinguish between bulk values and constituent quantities the following notation is used: a superscript character denotes a *bulk*, or *partial*, quantity while subscript indicates a *constituent* quantity. Note that the constituent terms

are needed exclusively for the `VolumeConstraint` algorithm. Constitutive parameters are made mass-specific internally, as such the user should not attempt to account for this in the input file.

- `LinearElasticSolid`
  This is a traditional linear elastic material in which
  `[...]`= [K_α, K^α, G^α]
  with K_α and K^α as the constituent and bulk stiffness, respectively, and G^α as the bulk shear modulus.

- `IncompressibleFluid`
  Fluids derived from this material are bound to the `LinearElasticSolid`class. This concept is illustrated in Equation (6.1) and corresponding discussion. The input parameters are
  `[...]`= [K_α, K^α, μ]
  with μ as the dynamic viscosity. Obviously the notion of constituent vs. bulk properties can lose meaning when dealing with a fluid. See Section 6.3 for how to interpret these quantities in the context of a fluid.

- `J2Solid`
  See Section 3.5 for a discussion of this model and implementation details. This model contains optional input parameters designated by the | and ‖ symbol.
  `[...]`= [K_α, K^α, G^α, σ_Y, | k, ‖ H]
  Everything to the left of | is a required input, including the yield stress σ_Y. If no hardening is desired then these are the only inputs. Alternatively, isotropic hardening is obtained by adding the modulus k to the parameters and including everything to the left of ‖ symbol. Finally, by adding H, kinematic hardening is included and the parameter vector is fully populated.

- `DruckerPragerSolid`
  See Section 3.6.1 for a discussion of this model and implementation details. For this model the parameters are
  `[...]`= [K_α, K^α, G^α, ϱ_F, σ_Y, | ϱ_G, ‖ k, H]
  where ϱ_F and ϱ_G are additional model parameters related to the internal friction angle and dilation angle, respectively. Again, the | and ‖ work as they did for the `J2Solid`input.

- `SmoothCapDPSolid`
  See Section 3.6.2 for a discussion of this model and implementation details. The

```
Boundary
  //Type     ID     l_x     l_y     l_z     n_x     n_z     n_z
  //
  //Fixed      int_ID  fl_lx fl_ly fl_lz fl_nx fl_ny  fl_nz
  //Planar     int_ID  fl_lx fl_ly fl_lz fl_nx fl_ny  fl_nz
  //Eliminate int_ID  fl_lx fl_ly fl_lz fl_nx fl_ny  fl_nz
  //Size       int_ID  fl_sx fl_sy fl_sz
  //ForceTolerance    int_ID  float_tol
  //FrictionCoefficient    int_ID   float_coeff
  //Phase     int_ID       int_PhaseID
End
```

Figure B.6: Boundary keywords for input file.

parameters are
`[...]`= [K_α, K^α, G^α, ϱ_F, μ, | ϱ_G]
with μ as an effective yield stress. Currently no material hardening or softening is implemented in this model.

- `ModifiedDruckerPragerSolid` and `MatsuokaNakaiSolid`
  See Sections 3.6.3 and 3.7 for a discussion of these models and implementation details. Both use identical parameters vectors by design and are as follows:
  `[...]`= [K_α, K^α, G^α, c_F, a_0, a_1, a_2, a_3, a_4, a_5]
  where c_F is a cohesion parameter and a_{0-5} are the constants used to define the internal friction and critical state angles.

B.2.5 `Boundary`

The current implementation is capable of modeling horizontal surfaces with arbitrary locations and orientations. Each flat surface is an instance of the `Boundary.cpp` object. At this point only displacement boundary conditions are supported in a general sense. Other conditions, such as force and velocity, can be added to the code to obtain certain effects depending on the application. The two supported boundary types are `Fixed` and `Planar`. Physical boundaries must be one of these two types. A third option exists and is outlined below. Boundaries work best when they align with the grid. However, there is no requirement that boundary objects align with the grid. Indeed, by making many small boundary objects, each with changing normal, curves and arbitrary surfaces can be composed. Of course, the quality of the representation is still subject to the spatial discretization and the cell size. Given the arbitrary nature of the boundary in MPM, a single node can have multiple boundary objects. In this case an equivalent normal vector representing all surfaces is computed.

- `Fixed int_ID fl_lx fl_ly fl_lz fl_nx fl_ny fl_nz`
  This condition inhibits the motion of all nodes residing on (or within a buffer zone related to cell size) this surface. Each boundary object needs a unique `int_ID`. The coordinate position of the boundary is determined by the floating point numbers (`fl_lx` , `fl_ly`, `fl_lz`). This point represents the center of the surface. The orientation is specified using the vector (`fl_nx` , `fl_ny`, `fl_nz`), which is assumed to be perpendicular to the boundary. Internally the vector is normalized so the user does not have to enter normalized components.

- `Planar int_ID fl_lx fl_ly fl_lz fl_nx fl_ny fl_nz`
  A `Planar` boundary restricts acceleration and velocity in the normal direction. The surface is assumed to be smooth.

- `Eliminate int_ID fl_lx fl_ly fl_lz fl_nx fl_ny fl_nz`
  This entity is not a physical boundary in the sense that `Planar` and `Fixed` are. Instead this surface is used to identify particles that have left the area of interest. These particles are immediately removed from the computation.

- `Size int_ID fl_sx fl_sy fl_sz`
  This is an optional addendum to a `Fixed`, `Planar`, or `Eliminate` boundary object. By default the rectangular bounding surface is assumed to be quite large. The `Size` feature allows the user to define the extents of the surface by specifying three floats: (`fl_sx` , `fl_sy`, `fl_sz`). These are used in the *local* coordinate system of the boundary object. Thus, the size `fl_sx` represents the thickness of the boundary *in the normal direction*. The terms `fl_sy` and `fl_sz` can be interpreted as the length and width of the rectangular surface, centered about the initial boundary object location (`fl_lx` , `fl_ly`, `fl_lz`).

- `ForceTolerance int_ID float_tol`
  This is an optional addendum to a `Fixed` or `Planar` boundary object. The force tolerance compares the quantity $\mathbf{f}_r \cdot \mathbf{n}$, with $\mathbf{f}_r$ as the reaction force and $\mathbf{n}$ as the effective unit normal. If this value is greater than 0.0 then the body is pushing against the boundary. Alternatively, if less than zero the body is pulling on the surface. By default each boundary object does *not* release in tension. This is by design. The user can dictate a tension release condition by setting `ForceTolerance` to 0.0 (it is recommended a value slightly less than zero be used to allow for fluctuations. The term *slightly less* is relative to the units used and the magnitude of force in the analysis).

- `FrictionCoefficient int_ID float_coeff`
  This is an optional addendum to a `Planar` boundary object. By default a planar surface is smooth and no friction develops. The current implementation employs a Coulomb friction model with frictional magnitude proportional to the normal force multiplied by a coefficient. This coefficient is commonly referred to using the symbol μ in the literature and can be computed from an external friction angle as $\mu = \tan(\phi_{fr})$.

- `Phase int_ID int_PhaseID`
  This is an optional addendum to a `Fixed`, `Planar`, or `Eliminate` boundary object. This feature allows the user to use different boundary conditions for different phases. The user **must** use this option when multiple phases are present (not necessary if only a single phase is used), even if the same boundary conditions are desired for all phases. While seemingly annoying, this is done for very specific reasons. In multiphase applications, it is best practice to create the boundary, and immediately assign it to a specific phase.

B.2.6 `OutputData`

The output options are shown in Figure B.7. The first two listings do not result in data being output to file. Rather, `WriteToFile` requires an integer for the number of time steps between successive file dumps and defaults to 1000 steps. Likewise, the option `RestartToFile` specifies the frequency a restart file is generated. A restart file essentially captures the current state of the model, and creates an input file to reflect this state in terms of particle data, boundaries, material state, etc.

By default the particle ID, phase, and position are always written to file. The rest of the output options are custom selected from the list in Figure B.7. Particle, node, and boundary nodes (those nodes that reside on a boundary) output is designated by `P`, `N`, or `B` as the first letter, respectively. The value listed in brackets [•] is *not* part of the input and should not be included in the file. These are shown to indicate the size, or number of values, that each output option writes. This is important when parsing the output files (more on the output structure in Section B.3). An option that is boolean operates under standard protocol: 0 is false and non-zero is true (1 is used for true by C++). By and large these options are self explanatory and many do not warrant additional discussion. Only options requiring an explanation are reviewed in further detail in what follows. In the case of time step dependent data, such as the velocity, where t_n and t_{n+1} (or even $t_{n+\theta}$) data exists, only the updated and/or relevant value is written to file.

```
OutputData
  //WriteToFile  int (1000)
  //RestartToFile  int  (5000)
  //PVelocity [3]
  //PDisplacement [3]
  //PMass [1]
  //PMatID [1]
  //PPorePressure [1]
  //PVolumeFraction [1]
  //PDensity [1]
  //PStress [6]
  //PEffectiveStress [6]
  //PJacobian [1]
  //PStrain [6]
  //PElasticStrain [6]
  //PPlasticStrain [6]
  //PDefGradient [9]
  //PRateDef [6]
  //PEnergy [1]
  //PBodyForce [1]
  //PShape [9]
  //PCPDI [bool, 1]
  //PALONE [bool, 1]
  //PPLASTIC [bool, 1]
  //NGoodVF [bool, 1]
  //NMass [1]
  //NForce [3]
  //NForceExt [3]
  //NForceInt [3]
  //NReactionForce [3]
  //NTraction [3]
  //NAcceleration [3]
  //NVelocity [3]
  //NMomentum [3]
  //BMass [1]
  //BForce [3]
  //BReactionForce [3]
  //BReactionForce_Max [3]
  //BReactionForce_CurrentTotal [3]
  //BTraction [3]
  //BAcceleration [3]
  //BVelocity [3]
  //BArea [1]
End
```

Figure B.7: OutputData keywords for input file.

Tensor and vector quantities are output in their entirety (as opposed to the magnitude/norm, individual components, etc.). Here it is assumed that if a norm, component, or scalar measure is desired, then the analyst can be obtained in the post-processing phase.

- `PPorePressure` and `PVolumeFraction`
  These are the p_{n+1} and θ^{α} values from the volume constraint algorithm of Chapter 5. These quantities are also active when the `CMPM` analysis option is active.

- `PStress` and `PEffectiveStress`
  For non-porous media related analysis these quantities will be identical, as the member variable $p_p = 0.0$. However, if the volume constraint or CMPM is active then

- `PStress` represents the total stress tensor while `PEffectiveStress` reflects the existence of a finite p.

- `PEnergy`
  Contains both the kinetic and elastic potential energy of a particle. Does not and cannot account for things like gravitational potential energy.

- `PShape`
  Outputs 9 values (three vectors) for $\mathbf{r}_1$, $\mathbf{r}_2$ and $\mathbf{r}_3$. See Figure 2.3.

- `PCPDI`
  Boolean output. If `PCPDI` is active this will be a 1 for all particles. Not really of use until the analysis option `HybridCPDI` is employed, and those particles currently using CPDI over a specific time step can be viewed.

- `PALONE`
  This is a boolean flag that follows from the analysis option `FrontSmoothing`, and identifies those particles using only t_n values for the current time step.

- `PPLASTIC`
  A boolean flag that is true if a particle has undergone *any* plastic deformation. A quick alteration in the code can change this to particles *currently* experiencing plastic loading, i.e., $F^{tr} \neq 0.0$.

- `NGoodVF`
  This is a boolean flag that follows from the analysis option `FrontSmoothing`, which identifies those nodes with dangerously low volume fractions at the edge of a body. If true for a given time step, all particles in the support of the node are designated as `PALONE`.

- `NTraction`
  The traction that develops at a node is in response to those particles carrying a prescribed external traction. This feature is seldom used but available.

- `BReactionForce`
  This is the nodal reaction force that develops in order to satisfy the boundary conditions. Takes into account friction on rough surfaces.

- `BReactionForce_CurrentTotal`
  Unlike most other nodal (and boundary node) outputs that correspond to the individual node, this value is dependent on all nodes residing on a given boundary surface. This value sums all reaction forces present on a given face. If this surface and corresponding nodes were to be visualized, each node on said surface would carry the same vector for `BReactionForce_CurrentTotal`. Nodes residing on more than one surface hold the largest magnitude force from the contributing boundary object.

- `BReactionForce_Max`
  Unlike most other nodal (and boundary node) outputs that correspond to the individual node, this value is dependent on all nodes residing on a given boundary surface. Like its counterpart `BReactionForce_CurrentTotal`, this output variable represents all boundary nodes on a given surface, but stores the maximum magnitude over the entire time history of this nodes existence. This feature is useful for capturing the peak reaction force on a given boundary face, even it the peak does not coincide in time with writing the data to file. Nodes residing on more than one surface hold the largest magnitude maximum force from the contributing boundary object.

- `BArea`
  Unlike most other nodal (and boundary node) outputs that correspond to the individual node, this value is dependent on all nodes residing on a given boundary surface. This feature computes the total *active* area of a surface using the cell size and only boundary nodes that have mass. Nodes residing on more than one surface hold the largest area from the contributing boundary object.

A note regarding nodal output: data values reflect a *single* Node object, which is itself a Degree of Freedom (DOF) object containing other multiple DOF's for each phase present. Originally the implementation generated each DOF corresponding to each phase. While strictly correct, this creates more trouble than it is worth to parse. Thus, nodal output is suppressed to a single Node object. This means that nodal data in multiphase analyses

reflects all phases present at a particular node. This could be changed in the future but will require modifying all post processing files as well.

The remaining base keywords do not contain nested features, and are thus presented without the itemized format of the previous subsections. The reader is referred to Figure B.2 for a quick reminder as to what the remaining base keywords represent.

B.2.7 `Particles`

A particle group must be flagged with an integer `MaterialID` and `PhaseID` as indicated in Figure B.2. The `MaterialID` must correspond to the `int_ID` in Figure B.5. The `PhaseID` is also required for multiphase analyses. These can be arbitrary and do not need to be any specific value. Each phase is assumed to have its own motion, and thus its own grid. A single phase can have multiple materials, designated by multiple groups of `Particles` statements. Each particle gets its own line containing:
`p_ID p_mass p_x p_y p_z`.
where `p_ID` is an integer. The mass and position components are floats.

B.2.8 `ParticleState`

Each particle gets its own line in the input file of the form
`p_ID [...]`
where `[...]` indicates a list of state parameters needed for a full definition of the material. This includes the current elastic and plastic deformation, deformation gradient, and all state variables required to compute the current stress state. As such, this parameter list is long. In the interest of saving space the user is referred first to the virtual functions `matGetState()` and `matReadState([...])` , defined in the general `Material.cpp` class. Each of these functions are overloaded by the individual material class indicating the order and contents of `[...]`.

B.2.9 `ParticlePrescribedTraction`

This base option is used for prescribed tractions on a body's surface. Since the particles represent the body—and *not* the nodes like in the FEM—force-like boundary conditions should (does not mean they always are) be applied to the particles. This option adds an external traction to select particles using
`p_ID A_p MagTraction n_x n_y n_z`
where `A_p` is the representative area of the individual particle, `MagTraction` is the magnitude

of the traction, and the floats `n_x`, `n_y`, and `n_z` provide the orientation of said traction. The orientation is updated with the deformation gradient, effectively describing a moving force-like term that is consistent with the deformation. Each particle with a nonzero traction contributes to the `NTraction` identified above.

B.2.10 `ParticleShape`

This base keyword is used to define the shape vectors $\mathbf{r}_1$, $\mathbf{r}_2$ and $\mathbf{r}_3$ when `CPDI` or `HybridCPDI` is used. See Figure 2.3. The input file requires the following form

`p_ID r1_x r1_y r1_z r2_x r2_y r2_z r3_x r3_y r3_z.`

This keyword is recommended when using `CPDI` or `HybridCPDI` if a modified shape is desired. If no shape data is provided, the coding framework assumes cubic particles based on initial density and supplied mass, and will automatically compute the corresponding shape vectors.

B.2.11 `ParticleVelocity` *and* `ParticleBodyForce`

These two features allow individual particle assignments of velocity and body force. When invoked they require a format consistent with

`p_ID v_x b_y b_z`

with $\mathtt{v}_i$ representing the appropriate velocity or body force component. There are situations (like a vibrating beam) that require unique, prescribed particle velocities at the outset. This feature is used with body force only for restart files and should not be used to apply something like gravity, which affects all particles. Instead use `globalBodyForce` in the analysis options.

B.2.12 Example Input Files

Examples are typically more beneficial than a written description. Two sample input files from examples appearing in this dissertation are presented in Appendix C, which includes the foundation loading analysis in Section 6.3.3 as well as the avalanche control example in Section 7.3. For length reasons particle data has been elided, but the input structure remains and shows the components needed for creating a successful analysis.

B.3 Model Analysis

The Model Analysis portion of the data flow shown in Figure B.1 accounts for the largest portion of the coding framework. The goal in this section is to provide a global overview of

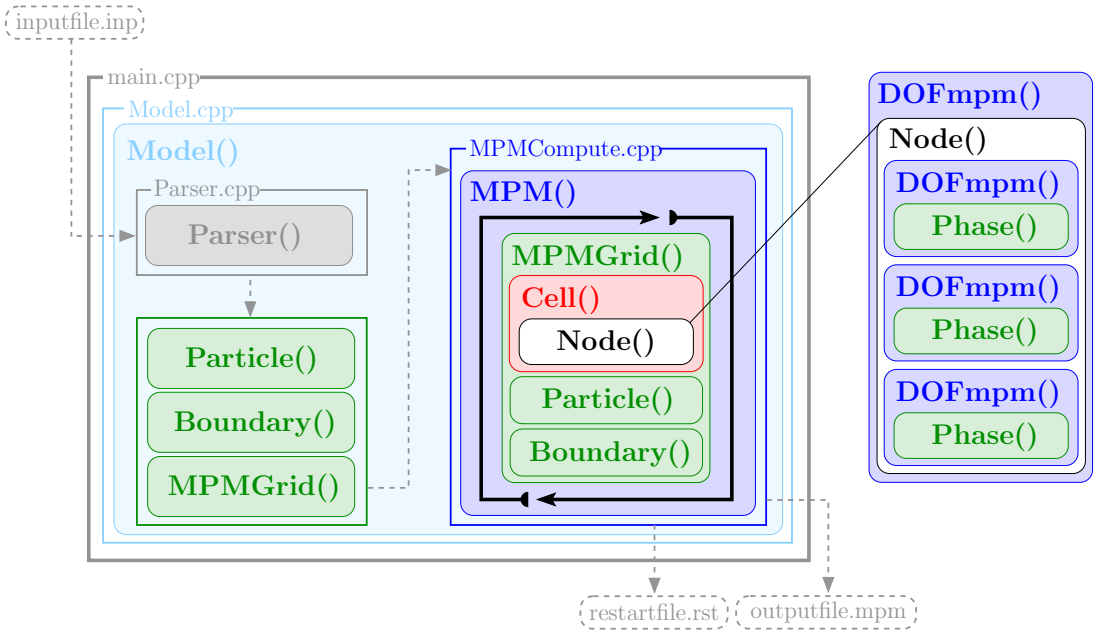

Figure B.8: Object relation and process flow chart.

the implementation, outlining the role of various objects and files along the way.

B.3.1 Object Relation and Algorithmic Flow

The analysis portion of the code is shown in detail in Figure B.8. This non-traditional flow chart highlights several aspects of the implementation, including the relationship between objects and the general flow of the algorithm. Additionally, class and file names are provided for those constructs that are not directly associated with the traditional MPM algorithm (i.e., things beyond the normal particles, grid, cell, and node). Rectangular boxes typically indicate which file these objects are instantiated in, and are labeled with `*.cpp`, with `*` serving as a general name. Individual objects names are denoted with `*()`. This notation seems to imply the constructors of these classes require no input arguments. This is not the case and the user should visit the appropriate files to see which arguments are needed for object creation.

The primary executable, `mpmdriver`, is generated by compiling `main.cpp` along with the appropriate files using the `make` utility as part of the `Makefile`. As shown in Figure B.8, the Model Analysis core consumes an `inputfile.inp` and generates at least one restart file (`restartfile.rst`) and a single `outputfile.mpm`. Certain aspects of the restart file have been discussed in Section B.2.6. The output file is outlined in additional detail shortly.

The `Model()` object serves as the global manager for all algorithmic processes. This

class instantiates all the necessary ingredients for reading and organizing the input, as well as performing the numerical analysis and writing to file. Among the first items of business is the creation of the `Parser()`, a construct written using existing C++ libraries for file parsing. The parser reads the input file line by line, storing what it finds primarily in member *list*, *vector*, and *map* objects from the standard C++ library. The `Model()` class does not attempt to build MPM related objects until the `Parser()`is done reading the contents of the entire input file since the input file can be laid out in an arbitrary order. Once the input is read the model creates the physical entities that make up the analysis, including a series of `Particle()` objects defining the body(ies), as well as the user defined `Boundary()` surfaces. The `Particle()` class itself contains a number of objects not directly mentioned here, including the `Material()` classes and the mechanics-related data types, e.g., vectors and tensors. A single instance of `MPMGrid()` rounds out this stage of the analysis.

The MPM algorithm outlined in Section 2.2.3 is managed by an instance of `MPM()`. The computational cycle shown in Figure 2.1 is indicated by the clockwise arrows surrounding the `MPMGrid()`. Within this process the grid object manages the creation of computational cells, which in turn create nodes as needed to accommodate the particles as these integration points move throughout the domain [3] . When a new node is created the object checks with the parent grid for any `Boundary()` surfaces that it may be on (or within a buffer distance related to cell size). By default nodes and cells containing no mass are destroyed by the grid object at user specified increments.

The current framework allows for multiple bodies and/or phases whose motions are captured using separate fields. From an implementation standpoint this is accomplished using not the `Node()` object itself, but a more general degree of freedom (dof) class dubbed `DOFmpm()`. Each node serves as a dof as well as a holder, or collection, of individual degrees of freedom for each phase or body present within the support of a node. This concept is illustrated in the right hand portion of Figure B.8. A collection like this might be considered inelegant from an object oriented perspective, but the current format does provide some key advantages. For example, a node can have any number of phases or bodies present and will change dynamically as needed to satisfy the current conditions. An analysis that employs three phases can—depending on particle arrangement—have nodes with only one, two, or three active phases at a given instant in time. This is more efficient than storing empty

[3]This format can be considered a cell-centered, or a cell-based, approach. Earlier implementations used a node-based approach which more easily accommodated CPDI and higher order b-spline shape functions. However, such an approach was abandoned in favor of a cell centered mapping scheme.

fields at nodes when a particular phase is not present in the support, especially near the edges of a body where a node can come in and out of existence. In the event more than one phase or body is present the nodal dof serves as the total motion of all phases/bodies, with the phase dof's capturing each individual motion. This is advantages because several of the multigrid contact algorithms rely on the common grid motion to determine the contact forces between the individual bodies/phases, and this setup lends itself naturally to these algorithms.

B.3.2 Output File Format

The `MPM()`class incrementally writes a restart file at a frequency specified by the user. By default a restart file is generated every 5000 steps as well as at the end of an analysis to capture the final state. Successive restarts appear as `*_1.rst`, `*_2.rst` ... `*_n.rst` where `n` continues to increase as many times as necessary before the analysis terminates. The format of a restart file is essentially the same as an input file. A single output file is generated for each analysis. The `MPM()`class incrementally (usually at different increments than the restart file is generated) writes particle, nodal, and boundary node data to a file with name `*.mpm`. Here `*` is taken from the input file name.

An example output file is shown in Figure B.9. The first three lines indicate the input file that generated this output, the version of the code, and the total number of particles originally read in. The initial output file listings—lines 5 through 21 in the current example—simply display the analysis options, parameters, material, and boundary objects that appear in the input file. This is done so the user can re-create an input file if need be. In future applications, should a GUI exist, these can be interpreted and trigger default view options.

The next series of lines indicate which output data is present for particles, nodes, and boundary nodes. Recalling that output data may be requested from the user in any arbitrary order, the `Model()` object identifies which category a requested output belongs to (`Particle_Output`, `Nodal_Output`, or `Boundary_Output`) when the input file is read. The size, or length, of the number string corresponding to each output type appears next to the output listing. This is critical for interpreting the output data, as the indices corresponding to a certain data type must be known in order to extract the appropriate values. The output options that can appear here are discussed in Section B.2.6.

The actual data follows the keyword `Output.` By default the initial state is written to file (usually time $t = 0.0$) as well as the very last state when the simulation ceases. The data is written between these states at user specified increments. At each file write, the

```
Created from input file:  Test.inp
Version: 1.1
Number of Particles: 3200

Input Options:

AnalysisOptions
  [...]
End
Parameters
  [...]
End
Material
  [...]
End
Boundary
  [...]
End
OutputData
   [...]
End

Particle_Output:
   ParticleVF 1
   PorePressure 1
   Stress 6
   Velocity 3
   Displacement 3

Nodal_Output:
   Velocity 3

Boundary_Output:
   Reaction_Force 3

Output:

Time 0
   Particle 3200
     [...]
   End

   Node 0
     [...]
   End

   Boundary 0
     [...]
   End
End

Time 0.000125
   Particle 3200
     [...]
   End

   Node 882
     [...]
   End

   Boundary 122
     [...]
   End
End
```

Figure B.9: Output file structure.

keywords `Time` and `End` designate the current state. The number following the `Time` keyword is the current analysis time. Within this keyword pair, particle, node, and boundary node data are written using the appropriate keyword followed by the `End` statement. Since the number of particles, nodes, and boundary nodes varies throughout the simulation, the integer following the keyword indicates the number of active entities. This information is needed for a number of reasons, including parsing the output data and creating useful output constructs as explained in the next section.

B.4 Post-Processing

The post-processing scripts are written exclusively in the Python programming language. Early implementations and examples were primarily two dimensional and consisted of less than 10,000 particles. For these cases the plotting libraries contained in the `matplotlib` and `scipy` Python modules were sufficient for data visualization, and several scripts written around these libraries were developed. However, these tools are limited to smaller simulations and are not efficient in terms of viewing all output variables in a timely fashion. Thus, recent emphasis has been placed on transitioning away from these original scripts in favor of ParaView, an open-source, multi-platform data analysis and visualization application. In an effort to be complete this section contains a detailed overview of the ParaView file format, as well as a description of the original Python scripts used for visualization.

B.4.1 ParaView and the VTK Piece Format

ParaView offers a fully three dimensional visualization environment built using the Visualization Toolkit (VTK) Library. The interactive framework allows users to create videos, snapshots, or extract quantities for plotting, and features a suite of batch processing capabilities for automation. The interface is developed to analyze extremely large datasets and utilizes distributed memory computing resources when necessary.

The VTK library consists of C++ , Tcl/Tk, Java, and Python and serves as an open source software system for three dimensional computer graphics, image processing, and visualization. ParaView can access several VTK features, including the pipeline architecture and the more general vtkObject. That being the case there are multiple options available for getting MPM data into a format that ParaView can read. In the present case the VTK Piece format is used. This is not the only option, but is the only option explored in this work.

ParaView can read and interpret XML files. An example VTK Piece format is shown in Figure B.10. This example is for a single time step and contains particle data. An

```
<?xml version="1.0"?>
<VTKFile type="UnstructuredGrid" version="0.1" byte_order="BigEndian">
<UnstructuredGrid>
<Piece NumberOfPoints="10543" NumberOfCells="10543">

<Points>
  <DataArray type="Float32" Name="Position" NumberOfComponents="3" format="ascii">
       [...]
  </DataArray>
</Points>

<PointData Scalars="Phase">
  <DataArray type="Float32" Name="Stress" NumberOfComponents="9" format="ascii">
       [...]
  </DataArray>
  <DataArray type="Float32" Name="Velocity" NumberOfComponents="3" format="ascii">
       [...]
  </DataArray>
  <DataArray type="Float32" Name="J2_Stress" NumberOfComponents="1" format="ascii">
       [...]
  </DataArray>
</PointData>

<Cells>
  <DataArray type="Int32" Name="connectivity" NumberOfComponents="1" format="ascii">
      0   1   2   3   ...   (np-1)
  </DataArray>
  <DataArray type="Int32" Name="offsets" NumberOfComponents="1" format="ascii">
      1   2   3   4   ...   np
  </DataArray>
  <DataArray type="Int32" Name="types" NumberOfComponents="1" format="ascii">
      1   1   1   1   ...   1
  </DataArray>
</Cells>

</Piece>
</UnstructuredGrid>
</VTKFile>
```

Figure B.10: XML piece data structure for use with ParaView and VTK. This example is for a single time step and contains only particle data.

equivalent file must be made for each node or boundary node data set at each time step. The file generation process is entirely automated for a single output file using a Python script that is discussed shortly. Each file must end with `*.vtu` , as ParaView interprets each file differently based on the extension. In the present case this identifies an Unstructured Grid object. `Piece` data is defined using `Points` and `Cells` (presumably connecting the `Points`). In the present case, the term *Cell* or *Cells* is needed for VTK objects and *is not* the cells in an MPM simulation. For each point listed in `Points` , `PointData` is assigned using `DataArray` brackets. Tags identify the numerical `type` and the `NumberOfComponents`. ParaView treats any 3 component object as a vector and any 9 component object as a tensor. This is nice because there are built in features available for visualizing these objects, such as attaching arrow like structures to points to visualize vector fields. This particular Unstructured Grid format treats each point as a `Cell` vtkObject. As such, it is necessary to define the `connectivity`, `offsets`, and `types` for each set of particles, nodes, or boundary

nodes. These `Cell` fields are a function only of the number of points, `np,` and are to be organized as shown in Figure B.10.

The Python script `MPMOutputToVTKOutput.py` generates *all* the necessary files and folders from a single `.mpm` output file. This primary script relies on two additional modules: `MPM2VTKFunctions.py` and the class definition `VTKFileWriter.py`. Together these scripts generate separate files for each time step consistent with the format shown in Figure B.10 for all particles, nodes, and boundary nodes (of course the XML files contain the user specified output instead of those terms shown in the example). The individual time step files are strung together with a `*.pvd` file, an XML-based structure containing the name of the individual `*.vtu` files. An example of this file type is provided in Appendix C. The user needs only to open ParaView and select the appropriate `*.pvd` file to begin viewing the data.

B.4.2 Original Visualization Scripts

Considering the convenience afforded by ParaView (or any interactive, fully three dimensional visualization environment), there is little value in continuing forward with the original series of Python scripts developed for visualization purposes. However, these scripts can still serve a purpose, as they organize the data into matrix-like structures conducive to plotting and/or analysis. That being the case each script and its capabilities are outlined below.

- `ParticlePlotter.py`: This script extracts particle data from the output file. The user may specify any number of particle IDs as well as any available output they wish to obtain. The data is either viewed as a plot, or as is more commonly done, output to file for later use. An example usage of this script was extracting the appropriate data to create the error plots in Figure 6.10.

- `NodePlotter.py`: This script extracts nodal data from the output file. The user may specify any number of node IDs as well as any available output they wish to obtain. The data is either viewed as a plot, or, as is more commonly done, output to file for later use. This script was used to extract data for Figure 6.7.

- `ParticleVisualizer.py`: This script utilizes a single MPM output file and creates a series of images used to visualize the particles. The images may be viewed individually or strung together to create a movie. The user may specify several options, including which particle value to plot. The scatter plots show data and relate the magnitude of the data via a color bar option. Despite the script name, the user may also visualize nodal location, boundary node location, as well as several nodal output quantities. As

was the case with the particles, the data at nodal locations is output as a color with corresponding magnitude obtained via the color bar. Examples plots created from this script are Figures 6.4 and 7.19.

- `NodeVisualizer.py`: This script visualizes the grid fields at user specified nodes via colored vectors. As was the case with the particle visualizer, a series of images at sequential times is created. The images may be used individually or combined to create a movie. The vector orientation and size are obtained by appropriate window scaling, whereas the magnitude is viewed via a color bar.

The above four files rely heavily on the `numpy` module, as well as several functions defined in `VisualizerFunctions.py`.

Appendix C

SAMPLE FILES

```
// This is a saturated water and solid mix with foundation loading.
AnalysisOptions
  Version 1.1
  LargeDeformation
  PlaneStrain
  VolumeConstraint
  ViscousDamping  0.5
  ConstantAntiLocking   AS1   CellBased
End
Parameters
  TimeStep   1.25e-4
  AnalysisDuration 5.0
  CellSize   1.5   1.5   1.5
  DeleteNodesEvery   10000
End
Material
 // Mat_ID        ModelName        V_Frac    Density       Params
 1 IncompressibleFluid   0.3   997.5   2.0e9      0.0      0.0
 2 LinearElasticSolid    0.7   2670.0  1.0e16     2.08e7   9.62e6
End
Boundary
  // Type    ID    l_x    l_y    l_z    n_x    n_z    n_z
  // Water boundaries
  Planar  1   0      0   0   0   1   0
  Planar  2   0      0   0   1   0   0
  Planar  3   30.0   0   0   -1  0   0
  Phase   1   1
  Phase   2   1
  Phase   3   1
  // Solid boundaries
  Planar  5   0      0   0   0   1   0
  Planar  6   0      0   0   1   0   0
  Planar  7   30.0   0   0   -1  0   0
  Phase   5   2
  Phase   6   2
  Phase   7   2
End
OutputData
  WriteToFile  250
  RestartToFile  500000
  PVolumeFraction
  PStress
  PEffectiveStress
  PPorePressure
  PVelocity
  PDisplacement
  NVelocity
  BReactionForce
End
Particles   1   1
  // p_ID     p_mass     p_x     p_y     p_z
```

```
52    1    168.328125    0.375000    0.375000    0.000000
53    2    168.328125    1.125000    0.375000    0.000000
54    3    168.328125    1.875000    0.375000    0.000000
55    4    168.328125    2.625000    0.375000    0.000000
56    //
57    // Particles 5-1600 (omitted for dissertation example)
58    //
59 End
60 Particles    2    2
61    // p_ID      p_mass      p_x      p_y      p_z
62    1601    1051.312500    0.375000    0.375000    0.000000
63    1602    1051.312500    1.125000    0.375000    0.000000
64    1603    1051.312500    1.875000    0.375000    0.000000
65    1604    1051.312500    2.625000    0.375000    0.000000
66    //
67    // Particles 1605-3200 (omitted for dissertation example)
68    //
69 End
```

```
1  // Avalanche example with mounds
2  AnalysisOptions
3    Version 1.1
4    ConstantAntiLocking  CellBased  AS1
5    LargeDeformation
6  End
7  Parameters
8    TimeStep  1.0e-3
9    AnalysisDuration  25.0
10   CellSize  1.0  1.0  1.0
11   globalPosition  0.0  0.0  -30.0
12   globalBodyForce  0.0  -10.0  0.0
13   DeleteNodesEvery 250
14 End
15 Material
16   // Mat_ID  ModelName  V_Frac  Density  Params
17   1  SmoothCapDPSolid  1  500.0  [...]
18 End
19 Boundary
20   // Type  ID  l_x  l_y  l_z  n_x  n_z  n_z
21   //
22   // Sides
23   Planar  1  0  0  0  1  0  0
24   Planar  2  36  0  0  -1  0  0
25   //
26   // Bottom
27   Planar  3  0  0  0  0  1  0
28   Fixed  4  0  0  156.0  0  1  0
29   FrictionCoefficient  3  0.3
30   Size  3  0.001  156.01  156.01
31   Size  4  0.001  156.01  156.01
32   //
33   // Mound 1
34   Planar  5  3.0  0  33.0  -1  0  0
35   Planar  6  9.0  0  33.0  1  0  0
36   Planar  7  6.0  0  30.0  0  0  -1
37   Planar  8  6.0  0  36.0  0  0  1
38   Planar  9  6.0  6.0  33.0  0  1  0
39   Size  5  0.001  12.01  6.01
40   Size  6  0.001  12.01  6.01
41   Size  7  0.001  12.01  6.01
42   Size  8  0.001  12.01  6.01
43   Size  9  0.001  6.01  6.01
44   FrictionCoefficient  9  0.3
45   //
46   // Mound 2
47   Planar  10  15.0  0  33.0  -1  0  0
48   Planar  11  21.0  0  33.0  1  0  0
49   Planar  12  18.0  0  30.0  0  0  -1
50   Planar  13  18.0  0  36.0  0  0  1
51   Planar  14  18.0  6.0  33.0  0  1  0
52   Size  10  0.001  12.01  6.01
53   Size  11  0.001  12.01  6.01
54   Size  12  0.001  12.01  6.01
55   Size  13  0.001  12.01  6.01
56   Size  14  0.001  6.01  6.01
57   FrictionCoefficient  14  0.3
58   //
59   // Mound 3
60   Planar  15  27.0  0  33.0  -1  0  0
```

```
61    Planar    16    33.0    0       33.0       1    0    0
62    Planar    17    30.0    0       30.0       0    0    -1
63    Planar    18    30.0    0       36.0       0    0    1
64    Planar    19    30.0    6.0     33.0       0    1    0
65    Size      15    0.001    12.01    6.01
66    Size      16    0.001    12.01    6.01
67    Size      17    0.001    12.01    6.01
68    Size      18    0.001    12.01    6.01
69    Size      19    0.001    6.01     6.01
70    FrictionCoefficient    19    0.3
71    //
72    // Mound 4-14 (omitted for dissertation example)
73    //
74  End
75  OutputData
76    WriteToFile    250
77    RestartToFile  500000
78    PStress
79    PPlasticStrain
80    PVelocity
81    PBodyForce
82    NVelocity
83    BArea
84    BReactionForce
85    BReactionForce_Max
86    BReactionForce_CurrentTotal
87  End
88  Particles   1   1
89    // p_ID      p_mass     p_x     p_y     p_z
90    1   45.584   0.222   0.230   0.222
91    2   45.584   0.666   0.230   0.222
92    3   45.584   1.111   0.230   0.222
93    //
94    // Particles 4-85293 (omitted for dissertation example)
95    //
96  End
97  ParticleState
98    1   [...]
99    2   [...]
100   3   [...]
101   //
102   // ParticleState 4-85293 (omitted for dissertation example)
103   //
104 End
```

```
<?xml version="1.0"?>
<VTKFile type="Collection" version="0.1" byte_order="BigEndian">

<Collection>
  <DataSet timestep="0.000000" group="" part="0" file="Sample_Particles_00001.vtu"/>
  <DataSet timestep="0.000025" group="" part="0" file="Sample_Particles_00001.vtu"/>
  <DataSet timestep="0.012525" group="" part="0" file="Sample_Particles_00002.vtu"/>
  <DataSet timestep="0.025025" group="" part="0" file="Sample_Particles_00003.vtu"/>
  <DataSet timestep="0.037525" group="" part="0" file="Sample_Particles_00004.vtu"/>
  <DataSet timestep="0.050025" group="" part="0" file="Sample_Particles_00005.vtu"/>
</Collection>

</VTKFile>
```

```
<?xml version="1.0"?>
<VTKFile type="Collection" version="0.1" byte_order="BigEndian">

<Collection>
  <DataSet timestep="0.000000" group="" part="0" file="Sample_Nodes_00001.vtu"/>
  <DataSet timestep="0.000025" group="" part="0" file="Sample_Nodes_00001.vtu"/>
  <DataSet timestep="0.012525" group="" part="0" file="Sample_Nodes_00002.vtu"/>
  <DataSet timestep="0.025025" group="" part="0" file="Sample_Nodes_00003.vtu"/>
  <DataSet timestep="0.037525" group="" part="0" file="Sample_Nodes_00004.vtu"/>
  <DataSet timestep="0.050025" group="" part="0" file="Sample_Nodes_00005.vtu"/>
</Collection>

</VTKFile>
```

```
<?xml version="1.0"?>
<VTKFile type="Collection" version="0.1" byte_order="BigEndian">

<Collection>
  <DataSet timestep="0.000000" group="" part="0" file="Sample_Boundaries_00001.vtu"/>
  <DataSet timestep="0.000025" group="" part="0" file="Sample_Boundaries_00001.vtu"/>
  <DataSet timestep="0.012525" group="" part="0" file="Sample_Boundaries_00002.vtu"/>
  <DataSet timestep="0.025025" group="" part="0" file="Sample_Boundaries_00003.vtu"/>
  <DataSet timestep="0.037525" group="" part="0" file="Sample_Boundaries_00004.vtu"/>
  <DataSet timestep="0.050025" group="" part="0" file="Sample_Boundaries_00005.vtu"/>
</Collection>

</VTKFile>
```

Figure C.1: Sample .pvd files linking the individual particle, node, and boundary node files together for visualization in ParaView.